



JAEA-Review  
2006-029

# JAEA-Review

## JAEA-Tokai TANDEM Annual Report 2005

April 1, 2005 - March 31, 2006

Department of Research Reactor and Tandem Accelerator

Nuclear Science Research Institute  
Tokai Research and Development Center

September 2006

Japan Atomic Energy Agency

日本原子力研究開発機構

本レポートは日本原子力研究開発機構が不定期に発行する成果報告書です。

本レポートの入手並びに著作権利用に関するお問い合わせは、下記あてにお問い合わせ下さい。

なお、本レポートの全文は日本原子力研究開発機構ホームページ (<http://www.jaea.go.jp/index.shtml>)  
より発信されています。このほか財団法人原子力弘済会資料センター\*では実費による複写頒布を行っ  
ております。

〒319-1195 茨城県那珂郡東海村白方白根 2 番地 4

日本原子力研究開発機構 研究技術情報部 研究技術情報課

電話 029-282-6387, Fax 029-282-5920

\*〒319-1195 茨城県那珂郡東海村白方白根 2 番地 4 日本原子力研究開発機構内

This report is issued irregularly by Japan Atomic Energy Agency

Inquiries about availability and/or copyright of this report should be addressed to

Intellectual Resources Section, Intellectual Resources Department,

Japan Atomic Energy Agency

2-4 Shirakata Shirane, Tokai-mura, Naka-gun, Ibaraki-ken 319-1195 Japan

Tel +81-29-282-6387, Fax +81-29-282-5901

© Japan Atomic Energy Agency, 2006

**JAEA-Tokai TANDEM Annual Report 2005**  
**April 1, 2005 – March 31, 2006**

**Department of Research Reactor and Tandem Accelerator**

Nuclear Science Research Institute  
Tokai Research and Development Center  
Japan Atomic Energy Agency  
Tokai-mura, Naka-gun, Ibaraki-ken

(Received August 23, 2006)

This annual report describes research activities, which have been performed using the JAEA-Tokai tandem accelerator with the energy booster from April 1, 2005 to March 31, 2006.

Summary reports of 51 papers are categorized into seven research/development fields, i.e., (1) accelerator operation and development, (2) nuclear structure, (3) nuclear reaction, (4) nuclear chemistry, (5) nuclear theory, (6) atomic physics and solid state physics, and (7) radiation effects in materials, and lists of publications, meetings, personnel and cooperative researches with universities related to these papers are contained.

JAERI (Japan Atomic Energy Research Institute) was unified with JNC (Japan Nuclear Fuel Cycle Development Institute) on October 1st, 2005 and became JAEA (Japan Atomic Energy Agency).

Keywords : JAEA-Tokai Tandem Accelerator, Operation Results, Nuclear Structure, Nuclear Reaction, Nuclear Chemistry, Nuclear Theory, Atomic Physics, Solid State Physics, Radiation Effects in Materials, Progress Report.

---

Editors : Tetsuro ISHII, Suehiro TAKEUCHI, Masumi OSHIMA, Yuichiro NAGAME,  
Satoshi CHIBA, Masao SATAKA and Akihiko OSA

原子力機構東海タンデム加速器 2005 年度年次報告

日本原子力研究開発機構  
東海研究開発センター原子力科学研究所  
研究炉加速器管理部

(2006 年 8 月 23 日受理)

本年次報告書は、原子力科学研究所の原子力機構東海タンデム加速器及びブースターを利用し、2005 年 4 月 1 日から 2006 年 3 月 31 日までの期間に実施された研究活動をまとめたものである。

その内容は、(1) 加速器の運転状況と開発、(2) 原子核構造、(3) 原子核反応、(4) 核化学、(5) 原子核理論、(6) 原子物理及び固体物理、(7) 材料の照射効果 の 7 部門に関する 51 編の研究報告とこれらに関する各種リスト（公刊文献、発表会合、関与した職員、大学等との協力研究課題）から構成されている。

なお、日本原子力研究所は、2005 年 10 月 1 日から独立行政法人日本原子力研究開発機構となり、タンデム加速器施設は、東海研究開発センター・原子力科学研究所、研究炉加速器管理部の所属となりました。

---

原子力科学研究所：☎319-1195 茨城県那珂郡東海村白方白根 2-4

編集者：石井 哲朗、竹内 末広、大島 真澄、永目 諭一郎、千葉 敏、  
左高 正雄、長 明彦

## Foreword

This report covers research and development activities with the tandem accelerator, its superconducting booster and TRIAC radioactive ion accelerator at JAEA Tokai, for the period of FY 2005 (April 1, 2005 to March 31, 2006). During this period, the tandem accelerator was operated over a total of 182 days and delivered 21 different ions over 93 beam times to the experiments in the fields of nuclear physics, nuclear chemistry, atomic physics, solid state physics and radiation effects in materials. Sixty-eight research programs were carried out in collaboration with about 180 researchers from universities and research institutes. The TRIAC started operations with  $^8\text{Li}$  beams for experiments from November. The following are some of the highlights in FY 2005.

In research at the TRIAC facility, the following three experiments were performed using  $^8\text{Li}$  beams with the intensity of  $10^5$  pps: i) Measurement of Li diffusion coefficients in the lithium ionic conductor LiGa; ii) Measurement of the reaction cross sections of  $^8\text{Li}(d,t)^7\text{Li}$  and  $^8\text{Li}(d,\alpha)^6\text{He}$  of astrophysical interest and iii) Production of a spin-polarized beam with tilted foils. The TRIAC facility has been tuned up. Stable operation of the accelerators was ensured with a newly equipped RF-amplitude controller. The duty factor of the IH-linac reached 50%. The charge breeding efficiency of CB-ECRIS with xenon elements has been 7% for the conversion of charge state from 1+ to 19+.

In the development of the tandem accelerator, in-terminal ECR ion injector was moved from the high-energy side to the low-energy side of the 180 degree bending magnet in the high voltage terminal, in order to increase the beam intensity and energy by replacing the compact ECR ion source Nanogan to a high performance ECR ion source Super-Nanogan, in the near future. The maximum terminal voltage of 19.1 MV was recorded and four-day experiments were carried out twice with very stable beams at 18.0 MV.

In research of nuclear structure, the ground-state band of the neutron-rich transuranium nucleus  $^{250}\text{Cm}$  was established up to  $12^+$  by in-beam  $\gamma$ -ray spectroscopy using a radioactive  $^{248}\text{Cm}$  target and the two-neutron transfer reaction with  $^{18}\text{O}$  beams accelerated at 18 MV. Excited states in  $^{251}\text{Fm}$  were established by the  $\alpha$ - $\gamma$  spectroscopy. By utilizing the  $\gamma$ -ray detector array, GEMINI-II, a method of projectile Coulomb excitation has been developed to extract quadrupole moments of stable Xe isotopes, which can be applied to unstable nuclear beams from TRIAC. In a systematic study on odd-odd deformed nuclei, a phenomenon of low-spin signature inversion has been observed in  $^{182,184,186}\text{Au}$  and  $^{188}\text{Tl}$  nuclei.

In research of nuclear reactions, fusion barrier distributions were measured in the  $^{70}\text{Zn}+^{208}\text{Pb}$  and  $^{209}\text{Bi}$  reactions, relating to cold fusion for production of superheavy elements  $Z=112$  and

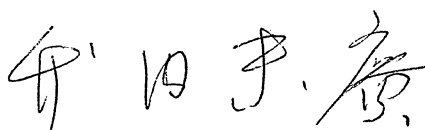
113, respectively. Astrophysical nuclear reaction rates of  ${}^8\text{Li}(d,p)$ ,  $(d,t)$  and  $(d,\alpha)$  were measured by using low-energy radioactive nuclear beams from TRIAC as well as from JAEA-RMS (Recoil Mass Separator).

In research of nuclear chemistry, aqueous chemistry of element 104, rutherfordium (Rf) produced in the reaction  ${}^{248}\text{Cm}({}^{18}\text{O}, 5n){}^{261}\text{Rf}$  was systematically investigated based on an atom-at-a-time scale. Characteristic chemical properties of Rf were observed from tributylphosphate (TBP)-extraction study in hydrochloric acid (HCl) and cation-exchange chromatography in hydrofluoric acid (HF) solutions.

In research of nuclear theory, structure of  $N=20$  isotones is investigated by a large-scale shell model calculation. It was found that the shape coexistence in sulfur region sensitively reflects the shell gap at  $N=20$ , because  $2p-2h$  configurations excited across this gap dominate the deformed state. Various decay modes of heavy and super-heavy nuclei are systematically predicted by a nuclear mass model and stability of these nuclei are revealed.

In research of atomic and solid state physics, a radio tracer method using short-lived radioactive beams from TRIAC has been developed for diffusion studies in solids. The method, using an  $\alpha$ -emitting radiotracer of  ${}^8\text{Li}$  ( $T_{1/2} = 0.8$  s), has been applied to measure the self diffusion coefficients of Li in super ionic conductors such as LiAl and LiGa. Sudden change of the diffusion coefficient attributed to order-disorder transition of vacancy was directly observed around 240 K.

A new usage program to accept direct applications from outside has been implemented for the tandem accelerator facility as well as other research facilities in JAEA. Seven experimental apparatuses are available for the program at the tandem facility. There were seven proposals for the next fiscal-year first half. The PAC adopted the proposals of requesting 21 days which corresponds to 20% of the total beam time in the period.



Suehiro Takeuchi

Deputy Director

Department of Research Reactor

and Tandem Accelerator

## Contents

1.	ACCELERATOR OPERATION AND DEVELOPMENT .....	1
1.1	Operation and Usage of Tandem Accelerator and Booster.....	3
1.2	KEK-JAEA Joint RNB Project .....	6
1.3	Ion Source Development for the JAEA-KEK Joint RNB Project .....	8
1.4	Installation of Monitoring System of Cooling Water in the Terminal .....	10
1.5	Fabrication of Low Beta Superconducting Twin Quarter Wave Resonator .....	12
1.6	Rearrangement of In-terminal ECR Ion Source Injector .....	14
1.7	New Interlock System for the Tandem Accelerator Facility .....	16
2.	NUCLEAR STRUCTURE .....	19
2.1	High-spin Gamma-ray Spectroscopy of $^{42}\text{Sc}$ .....	21
2.2	Lifetime Measurement of High-spin States in $^{144}\text{Dy}$ .....	22
2.3	Coulomb Excitation Experiment with Inverse Kinematics .....	23
2.4	Coulomb Excitation Experiment of $^{102}\text{Ru}$ .....	25
2.5	Search for Signature Inversion in the $\pi_{13/2} \otimes \nu_{13/2}$ Bands in Odd-odd Au Nuclei .....	27
2.6	Signature Inversion in the Oblate $\pi_{9/2} \otimes \nu_{13/2}$ Band of $^{188}\text{Tl}$ .....	29
2.7	Decay Studies of New Neutron-rich Isotopes $^{163,164,165}\text{Eu}$ .....	31
2.8	$Q_{\beta}$ Determinations of $^{160-165}\text{Eu}$ , $^{163}\text{Gd}$ , $^{158,159}\text{Pm}$ , $^{159,161}\text{Sm}$ and $^{166}\text{Tb}$ using a Total Absorption BGO Detector .....	33
2.9	Production of Long-lived $^{186\text{m}}\text{Re}$ for Laser Ablation Laser-induced Fluorescence Spectroscopy .....	35
2.10	In-beam $\gamma$ -ray Spectroscopy for Neutron-rich W Isotopes .....	36
2.11	Development of RI Ion Trap System .....	37
2.12	Gamma-rays in the Ground-State Band of $^{250}\text{Cm}$ .....	39
2.13	Alpha-gamma Coincidence Spectroscopy of $^{255}\text{No}$ .....	41
3.	NUCLEAR REACTIONS .....	43
3.1	Measurement of the Cross Section in the $^{12}\text{B}(\alpha, n)^{15}\text{N}$ Reaction .....	45
3.2	Study of the Neutron Transfer Reaction with Medium Mass Nucleus in Inverse Kinematics .....	47
3.3	Correlation between Fission and $\alpha$ -particle Emission in the $^{18}\text{O} + ^{244}\text{Pu}$ Reaction .....	49
3.4	Measurement of Fission Cross Sections for $^{30}\text{Si} + ^{238}\text{U}$ .....	51
3.5	Barrier Distribution of Quasi-elastic Backward Scattering of $^{70}\text{Zn}$ on $^{208}\text{Pb}$ and $^{209}\text{Bi}$ .....	53
4.	NUCLEAR CHEMISTRY .....	55
4.1	Extraction Behavior of Rf into Tributylphosphate from Hydrochloric Acid .....	57
4.2	Cation-Exchange Behavior of Rf in $\text{HNO}_3/\text{HF}$ Mixed Solution System .....	59
4.3	Chloride Complex Formation of Rf in $\text{HCl}$ and $\text{CH}_3\text{OH}$ Mixed Solution .....	61

5.	NUCLEAR THEORY .....	63
5.1	Systematic Study of Shape Coexistence in N=20 Isotones .....	65
5.2	Decay Modes of Heavy and Superheavy Nuclei Predicted by a Mass Formula .....	67
5.3	Kaonic Pasta Structures in Dense Matter .....	69
5.4	A Hybrid Approach to the Two-body Coulomb Scattering in the Momentum Space .....	71
6.	ATOMIC PHYSICS AND SOLID STATE PHYSICS .....	73
6.1	High-Resolution Zero-Degree Electron Spectroscopy of Highly Charged Oxygen Ions (III) .....	75
6.2	Charge State Distribution of Sulfur Ions after Penetration of C-foil Targets (III) .....	77
6.3	Measurement of the Diffusion Coefficients in $\beta$ -LiGa by using Short-lived Radiotracer of $^8\text{Li}$ .....	79
6.4	Vortex Imaging in Tl-1223 Superconducting Thin Films with a Scanning SQUID Microscope .....	81
6.5	Structure of Defect Cascades in Heavy Ions-irradiated Nickel by X-ray Diffuse Scattering .....	83
6.6	Effects of 100MeV Xe Ion Irradiation on Optical Properties of Al-doped ZnO Films .....	85
6.7	Electrical Conductivity Increase of Al-doped ZnO Films Induced by High Energy Heavy Ions .....	87
6.8	XRD Observation on High Energy Heavy Ion Induced Disorder in $\text{Li}_2\text{TiO}_3$ .....	89
6.9	Optical Spectroscopic Study for Sapphire Irradiated with High Energy Heavy Ions .....	91
6.10	New X-ray Diffraction Peak of Ion-irradiated $\text{TiO}_2$ at High Electronic Stopping Power Regime .....	93
6.11	Swift Heavy Ion Induced Ferromagnetic State in FeRh Alloys .....	95
6.12	Increase in Curie Temperature for Fe-Ni Alloy Thin Films by Energetic Heavy Ion Irradiation .....	97
6.13	Effect of High-energy Heavy Ion Irradiation on Magnetic Properties in Fe-Pd Invar Alloys .....	99
6.14	Electronic Excitation Effects on Secondary Ion Emission from Solid Materials Bombarded by Heavy Ions .....	101
7.	RADIATION EFFECTS IN MATERIALS .....	103
7.1	Depth Profile and Temperature Effect of Ion Tracks in $\text{CeO}_2$ under Irradiation with High Energy Ions .....	105
7.2	Radiation Effects on Mechanical Properties of Carbon Alloys and the Annealing Effects .....	107
7.3	Effects of Zr Ion Irradiation on Some Properties of Superplastic Ceramic 3Y-TZP, II .....	109
7.4	Semiconductor-metal Phase Transition of Iron Disilicide ( $\beta$ - $\text{FeSi}_2$ ) Thin Films by High Energy Heavy Ion Irradiation .....	111
7.5	Release Behavior of Implanted Xe from Zr - Implantation of Xe in Zr- .....	113
8.	PUBLICATION IN JOURNAL AND PROCEEDINGS, AND CONTRIBUTION TO SCIENTIFIC MEETINGS .....	115
8.1	Accelerator Operation and Development .....	117



8.2	Nuclear Structure .....	119
8.3	Nuclear Reactions .....	122
8.4	Nuclear Chemistry .....	125
8.5	Nuclear Theory .....	129
8.6	Atomic Physics and Solid State Physics.....	134
8.7	Radiation Effects in Materials .....	138
9.	PERSONNEL AND COMMITTEE .....	141
9.1	Personnel .....	143
9.2	Research Planning and Assessment Committee .....	146
10.	COOPERATIVE RESEARCHES LIST .....	147

目 次

<b>1. 加速器の運転状況及び開発</b> .....	1
1.1 タンデム加速器とブースターの運転と利用 .....	3
1.2 KEK-JAEA RNB 共同研究計画 .....	6
1.3 JAEA-KEK RNB 共同プロジェクトのためのイオン源の開発 .....	8
1.4 高電圧端子内冷却水監視システムの設置 .....	10
1.5 低ベータ超伝導 2 芯 1/4 波長加速空洞の製作 .....	12
1.6 高電圧端子内 ECR イオン源の移設 .....	14
1.7 タンデム加速器施設インターロックシステムの更新 .....	16
<b>2. 原子核構造</b> .....	19
2.1 $^{42}\text{Sc}$ の高スピン核分光 .....	21
2.2 $^{144}\text{Dy}$ 高スピン状態の寿命測定 .....	22
2.3 逆反応によるクーロン励起実験 .....	23
2.4 $^{102}\text{Ru}$ のクーロン励起実験 .....	25
2.5 奇々 Au 核の $\pi i_{13/2} \otimes \nu i_{13/2}$ バンドにおける指標逆転の探索 .....	27
2.6 $^{188}\text{Tl}$ 核のオブレート $\pi h_{9/2} \otimes \nu i_{13/2}$ バンドにおける指標逆転 .....	29
2.7 中性子過剰核 $^{163}, ^{164}, ^{165}\text{Eu}$ の崩壊 .....	31
2.8 全吸収 BGO 検出器を用いた $^{160-165}\text{Eu}$ , $^{163}\text{Gd}$ , $^{158, 159}\text{Pm}$ , $^{159, 161}\text{Sm}$ , $^{166}\text{Tb}$ の $Q_\beta$ 決定 .....	33
2.9 レーザーアブレーション・レーザー誘起蛍光分光のための長半減期核種 $^{186\text{m}}\text{Re}$ の生成 .....	35
2.10 中性子過剰タングステン核のインビームガンマ線核分光実験 .....	36
2.11 RI イオントラップ装置の開発 .....	37
2.12 $^{250}\text{Cm}$ の基底状態バンドの $\gamma$ 線遷移 .....	39
2.13 $^{255}\text{No}$ の $\alpha$ - $\gamma$ 同時計数測定 .....	41
<b>3. 原子核反応</b> .....	43
3.1 $^{12}\text{B} (\alpha, n) ^{15}\text{N}$ 反応断面積の直接測定 .....	45
3.2 逆運動学を用いた中重核に対する中性子移行反応の研究 .....	47
3.3 $^{18}\text{O} + ^{244}\text{Pu}$ 反応における核分裂と $\alpha$ 粒子放出の相関 .....	49
3.4 $^{30}\text{Si} + ^{238}\text{U}$ 反応の核分裂断面積の測定 .....	51
3.5 $^{70}\text{Zn} + ^{208}\text{Pb}$ , $^{209}\text{Bi}$ 反応における後方準弾性散乱の障壁分布測定 .....	53
<b>4. 核化学</b> .....	55
4.1 塩酸系における Rf のリン酸トリブチル抽出挙動 .....	57
4.2 Rf の $\text{HNO}_3/\text{HF}$ における陽イオン交換挙動 .....	59
4.3 塩酸・メタノール混合溶液における Rf の塩化物錯体形成 .....	61
<b>5. 原子核理論</b> .....	63
5.1 $N=20$ 同調体における変形共存の系統的研究 .....	65
5.2 質量公式から予想される重・超重核の原子核崩壊 .....	67
5.3 高密度物質における K 中間子 pasta 構造 .....	69

5.4	運動量空間における2体クーロン散乱に対するハイブリッド的手法	71
<b>6.</b>	<b>原子物理及び固体物理</b>	<b>73</b>
6.1	高電離酸素イオンの高分解能0度電子分光(III)	75
6.2	炭素薄膜通過後の硫黄イオンの電荷分布(III)	77
6.3	短寿命核トレーサー <sup>8</sup> Liを用いたβ-LiGa中リチウム拡散計数測定	79
6.4	走査型SQUID顕微鏡を用いたTl-1223超伝導薄膜の磁束量子	81
6.5	X線散漫散乱による重イオン照射したニッケル中の格子欠陥カスケードの構造	83
6.6	AlをドーブしたZnO薄膜の光学特性に対する100MeV Xeイオン照射効果	85
6.7	高エネルギー重イオンによるAlドーブZnO薄膜の電気伝導度上昇	87
6.8	高エネルギー重イオン照射によるLi <sub>2</sub> TiO <sub>3</sub> の無秩序化に関するX線回折観察	89
6.9	高エネルギー重イオン照射したサファイアの非晶質化と光吸収スペクトル	91
6.10	イオン照射したTiO <sub>2</sub> における高電子的阻止能領域でのX線回折ピークの出現	93
6.11	高速重イオン照射によって誘起された鉄ロジウム合金の強磁性特性	95
6.12	高エネルギー重イオン照射によるFe-Ni合金薄膜のキュリー温度の上昇	97
6.13	Fe-Pdインバー合金の磁性における高エネルギー重イオン照射効果	99
6.14	高エネルギー重イオン衝突による固体物質からの二次イオン放出における電子励起効果	101
<b>7.</b>	<b>材料の照射効果</b>	<b>103</b>
7.1	高エネルギーイオン照射によりCeO <sub>2</sub> に形成されるイオントラックの深さ分布と照射温度効果	105
7.2	カーボンアロイの機械的性質に及ぼす照射効果とその焼鈍効果	107
7.3	超塑性セラミック3Y-TZPのいくつかの特性に及ぼすZrイオン照射の効果 II	109
7.4	高エネルギー重イオン照射によるシリサイド半導体中へのナノ金属相作製	111
7.5	Zrからのイオン注入したXeの放出挙動 -Zr中の注入Xeイオン-	113
<b>8.</b>	<b>雑誌及び国際会議等の刊行物、学会発表</b>	<b>115</b>
8.1	加速器の運転状況及び開発	117
8.2	原子核構造	119
8.3	原子核反応	122
8.4	核化学	125
8.5	原子核理論	129
8.6	原子物理及び固体物理	134
8.7	材料の照射効果	138
<b>9.</b>	<b>関連課室職員及び委員会</b>	<b>141</b>
9.1	課室職員	143
9.2	委員会	146
<b>10.</b>	<b>共同・協力研究リスト</b>	<b>147</b>



## **CHAPTER 1**

### **Accelerator Operation and Development**

- 1.1 Operation and Usage of Tandem Accelerator and Booster
- 1.2 KEK-JAEA Joint RNB Project
- 1.3 Ion Source Development for the JAEA-KEK Joint RNB Project
- 1.4 Installation of Monitoring System of Cooling Water in the Terminal
- 1.5 Fabrication of Low Beta Superconducting Twin Quarter Wave Resonator
- 1.6 Rearrangement of In-terminal ECR Ion Source Injector
- 1.7 New Interlock System for the Tandem Accelerator Facility



## 1.1 OPERATION AND USAGE OF TANDEM ACCELERATOR AND BOOSTER

S. TAKEUCHI, Y. TSUKIHASHI, T. YOSHIDA, K. HORIE, I. OHUCHI,  
S. HANASHIMA, S. ABE, N. ISHIZAKI, H. TAYAMA, A. OSA, M. MATSUDA,  
Y. NAKANNOYA, H. KABUMOTO, M. NAKAMURA and K. KUTSUKAKE

The operations of the tandem accelerator and booster were given to conducting experiments over two periods, May 30 to August 14 and November 8 to March 26. The total operation time of the tandem accelerator was 4,273 hours (182 days), and 93 different beams were delivered for experiments during the operation time. In this fiscal year, the in-terminal ECR ion injector was moved from the high-energy side to the low-energy side of the 180° bending magnet, so that there was a decrease of about 20 days in the total machine time compared to the average in the past years. The experimental proposals and the usage of beam times from May 30, 2005 to March 26, 2006 are summarized in table 1 and table 2, respectively.

Table 1. Experiment Proposals.

Research Proposals accepted by the Program Committee:	
In-house Staff Proposals	8
Collaboration Proposals	43
Number of Experiments proposed	68
Number of Scientists participating in Research	
from outside	180
in-house	180
Number of Institutions presented	45

Table 2. Usage of Beam-times in Different Research Fields.

Research Fields	Beam time	Beam Delivery
Nuclear Physics	85 days 46.7 %	32 times
Nuclear Chemistry	27 18.4	13
Atomic and Solid state Physics	53 29.1	38
Radiation Damage in Materials	3 1.6	3
Accelerator Development(TRIAC)	14 7.7	7
Total	182 days	93 times

The distribution of the terminal voltages and ion species are listed in table 3 and table 4, respectively. The stable high voltage limit of the tandem accelerator was gradually increasing without very aggressive conditioning, after the whole accelerator tubes were replaced in the beginning of FY2003 to the new compressed geometry tubes which were cleaned by a high-pressure water jet[1,2,3]. The voltmeter recorded a very stable voltage of 19.1MV during a high voltage test done on January 5<sup>th</sup> in 2006 and four day experiments over a weekend were carried out twice with very stable beams at 18.0MV.

Table 3. Distribution of Terminal Voltages.

Terminal Voltage (MV)	Days	Percentage (%)
17-18	10	5.4
16-17	41	22.5
15-16	44	24.2
14-15	30	16.5
13-14	11	6.0
12-13	18	9.9
11-12	2	1.1
10-11	11	6.0
9-10	6	3.3
8 - 9	2	1.1
7 - 8	9	4.9
6 - 7	3	1.6
5 - 6	0	0

With respect to the ion beams, the accelerator provided a total of 27 different ion species for research. The ruthenium isotopes were accelerated for the first time in this facility. Most of the beams were extracted from SNICS-2 sputter sources, which were negatively charged injected into the tandem accelerator. Some hydrogen beams and multiply charged beams of nitrogen, neon and xenon were accelerated from the in-terminal ECR ion source.

Table 4. Distribution of Beam Species accelerated for Experiments.

$^1\text{H}$	19 days	$^{40}\text{Ar}$	6 days
$^{6,7}\text{Li}$	19	$^{54}\text{Cr}$	3
$^{11}\text{B}$	4	$^{56}\text{Fe}$	5
$^{12}\text{C}$	6	$^{58}\text{Ni}$	4
$^{14}\text{N}$	5	$^{64,70}\text{Zn}$	7
$^{16,18}\text{O}$	45	$^{90}\text{Zr}$	1
$^{19}\text{F}$	2	$^{100,102,104}\text{Ru}$	8
$^{22}\text{Ne}$	1	$^{124}\text{Sn}$	3
$^{27}\text{Al}$	2	$^{132,136}\text{Xe}$	24
$^{30}\text{Si}$	2	$^{197}\text{Au}$	7
$^{32}\text{S}$	9		

The  $^{16,18}\text{O}$  beams stood out most in popularity commanding over 24% of all beam time. They were mostly used for nuclear chemistry on actinides. The  $^1\text{H}$ ,  $^{6,7}\text{Li}$  and  $^{132,136}\text{Xe}$  also had a high popularity higher than 10%. The  $^1\text{H}$  and  $^7\text{Li}$  beams contributed to generating radioactive ion beams for the Tokai Radioactive Ion Accelerator Complex (TRIAC).

The super-conducting booster was operated for a total of 34 days to boost 11 different beams from the tandem accelerator. The booster also played a role of the beam transport line to the booster experimental hall for a total of 17 days. There were no big troubles in FY 2005 as before. We, however, had helium leaks from indium gaskets, which were attributed to frequent thermal cycles since 1993, and needed to re-tighten the loosened bolts or to replace indium gaskets for several super-conducting resonators in this FY as well. Forty super-conducting resonators were all in good condition to run, but the average acceleration field gradients



decreased to 4.0 MV/m at an RF input of 4 watts. The niobium surface has to be cleaned with a high-pressure water jet-spray to recover the original field gradients. The preparation for the cleaning was in progress. The ion species boosted for experiments, their boosted energies, and beam times are shown in table 5. All the boosted beams were used for nuclear physics and it means that 40% of the beam time for nuclear physics needed an energy boost.

Table 5. Boosted Ion Beams for Experiments.

<sup>18</sup> O	180 MeV	4 days
<sup>22</sup> Ne	245	1
<sup>54</sup> Cr	288	3
<sup>56</sup> Fe	280	4
<sup>64,70</sup> Zn	263-310,376	7
<sup>100,102,104</sup> Ru	435-440	8
<sup>124</sup> Sn	460	3
<sup>132</sup> Xe	400	4

The TRIAC facility, which has been installed in the tandem accelerator facility in collaboration with KEK[4,5], had a few experimental proposals for the second half of FY2005, for the first time. It has been decided that allotted time for the facility is 50 days a year which includes 10 days for R&D. That is, 25 days were allotted to the TRIAC experiments. Two experiments with <sup>8</sup>Li beams were successfully carried out, but more R&D with the accelerator system was required for effective experiments with heavy radioactive beams from fission products. There are reports about the TRIAC and its experiments elsewhere in this annual report.

## References

- [1] S. Takeuchi et al, Nucl. Instrum. Methods **A513**(2003) 429.
- [2] S. Takeuchi et al, JAERI Tandem Annu. Rep. 2002, JAERI-Review **2003-028** (2003) 6.
- [3] S. Takeuchi et al, JAERI Tandem Annu. Rep. 2003, JAERI-Review **2004-027** (2004) 6.
- [4] H. Miyatake et al, Nucl. Instrum. Methods **B204**(2003) 746.
- [5] S. Takeuchi, *Application of Accelerators in Research and Industry:17th int'l Conf.*;AIP 0-7354-0149-7/03(2003) 229.

## 1.2 KEK-JAEA JOINT RNB PROJECT

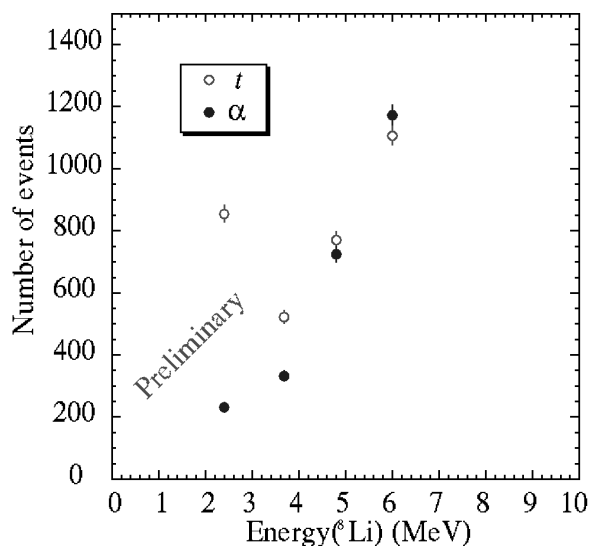
S. ICHIKAWA and H. MIYATAKE<sup>1</sup>  
for the TRIAC Collaboration

The radioactive nuclear beam (RNB) facility TRIAC (Tokai Radioactive Ion Accelerator Complex) has been jointly constructed by KEK and JAEA. From November in FY2005, the facility has started to supply RNBs for experiments. The facility is based on an isotope-separator on-line (ISOL) technique and the radioactive nuclei are produced by means of proton-induced fission of  $^{238}\text{U}$  or heavy-ion reactions with the primary beams from JAEA tandem accelerator. The produced radioactive nuclei are ionized and mass-separated with JAEA-ISOL. They are fed to a charge-breeding 18 GHz electron cyclotron resonance ion-source (CB-ECRIS), which converts singly-charged ions to multi-charged ones. The multi-charged radioactive ions are extracted and accelerated with two linear accelerators, a split-coaxial radio-frequency quadrupole (SCRFAQ) linac and an interdigital-H (IH) linac, to the energy of 1.1 MeV/A at the maximum. The following three experiments were performed in FY2005 using the  $^8\text{Li}$  beam with the intensity of  $10^5$  pps provided by TRIAC facility.

1. Measurement of Li diffusion coefficients in the lithium ionic conductor LiGa (Sun-Chan Jeong et al.)[1].
2. Measurement of the reaction cross sections of  $^8\text{Li}(d,t)^7\text{Li}$  and  $^8\text{Li}(d,\alpha)^6\text{He}$  of astrophysical interest (M. Ishiyama et al.).
3. Production of the spin-polarized beam with tilted foils (M. Hirayama and K. Matsuta et al.).

The details of the first experiment could be found in another section of this report. The preliminary results of the second and the third ones are described in the following.

All elements in the world were considered to be synthesized in the universe. The inhomogeneous big-bang model is one of theories which describe the early universe. The reactions with radioactive  $^8\text{Li}$  nuclei are key reactions to synthesize elements heavier than lithium in that model. So far we have measured the cross sections of  $^8\text{Li}(\alpha,n)^{11}\text{B}$  reaction in the temperature of  $10^9$  K, corresponding to the early universe [2]. The reactions of  $^8\text{Li}(d,t)^7\text{Li}$  and  $^8\text{Li}(d,\alpha)^6\text{He}$  are competition reactions against it. We have measured the cross sections of those reactions for the first time. The  $\text{CD}_2$  target was bombarded with the  $^8\text{Li}$  beam and emitted tritons and alpha particles together with recoil nuclei were detected by segmented silicon detectors. Figure 1 shows preliminarily the counts of detected tritons and alpha particles. The further analysis is in progress.



The tilted foil technique is a universal method to produce spin-polarized nuclear beams that are

<sup>1</sup>Institute of Particle and Nuclear Studies, KEK

applicable to any elements in principle. In order to establish the technique combined with the  $\beta$ -NMR method for the studies of nuclear spectroscopy around the double closed shell nucleus  $^{132}\text{Sn}$  as well as electromagnetic properties of various materials, a preliminary experiment with the  $^8\text{Li}$  beam was performed. The energy of the RNB was 178 keV/A. The carbon foils were tilted at an angle of 70 degrees to the beam direction. The  $^8\text{Li}$  beam passed through them was implanted in a platinum stopper. The produced nuclear spin-polarization was measured by applying the  $\beta$ -NMR technique. Figure 2 shows the produced spin-polarization as varying the number of the tilted foils, which indicates a feasibility of the future experiments.

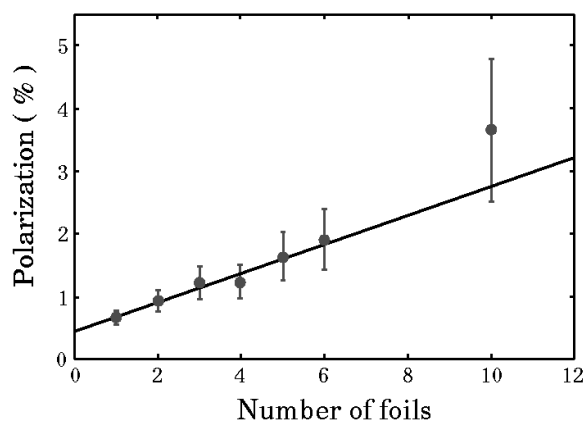


Fig. 2. Produced spin-polarization of the  $^8\text{Li}$  beam varying the number of tilted foils.

In parallel with those experiments, TRIAC facility has been tuned up continuously. The stable operation of the accelerators was ensured with a newly equipped automatic control system for the rf phase and amplitude of the radio frequencies. The duty factor of the accelerators was enlarged step by step, and has reached 50%. The facility aims for the operation with the duty factor of 100%. The research for acceleration of fragments from proton-induced fission of  $^{238}\text{U}$  was performed. For xenon element, the charge breeding efficiency of CB-ECRIS has been 7% for the conversion of charge state from 1+ to 19+.

It has been planned to connect TRIAC facility to JAEA superconducting booster in order to enhance the energy of the RNB to 5~8 MeV/A. The beam transport line between them was designed and the beam optics calculation ensured that the transportation was achieved with another two bunchers, two dipole magnets and several quadrupole magnets. A cold model of the bunchers was fabricated and has been tested. Figure 3 shows the model. The cavity has a double coaxial structure [3] with a movable partition plate to tune the resonance frequency. The resonance frequency of 51.814 MHz, which is required to match the RNBs to JAEA superconducting booster, has been achieved by adjusting the partition plate position at -1.98 mm to the calculated one. The electric field along the beam line in the cavity has been also measured and compared with the calculation.



Fig. 3. Cold model of the bunchers to transport RNBs from TRIAC facility to JAEA superconducting booster.

## References

- [1] Sun-Chan Jeong et al., *Journal of Phase Equilibria and Diffusion* **26** (2005) 472.
- [2] H. Ishiyama et al., *Proc. Intern. Symposium on the Origin of Matter and Evolution of Galaxies*, RIKEN, Saitama, Japan, 17-19 November 2003, World Scientific, Singapore, (2005) 316.
- [3] K. Yoshida et al., *Nucl. Instrum. Methods*. **A430** (1999) 189.

### 1.3 ION SOURCE DEVELOPMENT FOR THE JAEA-KEK JOINT RNB PROJECT

A. OSA, T.K.SATO, S.C. JEONG<sup>1)</sup> and S. ICHIKAWA

According to the JAEA-KEK joint radioactive nuclear beam (RNB) project, we have selected a surface ion source system to produce  $^8\text{Li}$  RNBs. This beam was provided to experiments of material science, astrophysics and condensed-matter physics.

We have chosen the  $^{13}\text{C}(^7\text{Li}, ^8\text{Li})$  neutron transfer reaction for the production of  $^8\text{Li}$  isotopes [1,2]. A 99% enriched  $^{13}\text{C}$  thick graphite disk was mounted at the catcher position of the surface ion source, working as a target and a catcher as shown in Fig.1. Some graphite disks were prepared at an enriched- $^{13}\text{C}$  density of about  $200\text{-mg/cm}^2$ . We molded disks ( $\phi=9.1\text{ mm}$ ) out of amorphous carbon (CLM-402, Cambridge Isotope Laboratories, Inc.). The disks were sintered at  $1800\sim 1900\text{ }^\circ\text{C}$  under pressure of  $70\text{MPa}$ .

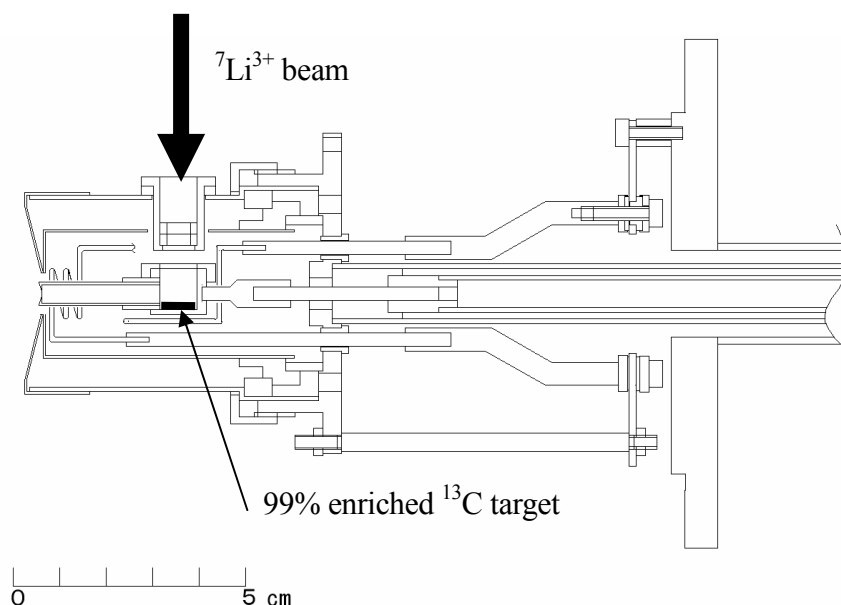


Fig.1 A schematic view of the surface ion source.

The target was bombarded with a  $67\text{-MeV } ^7\text{Li}^{3+}$  beam with intensity of about  $40\text{ pA}$ . The condition of the ion source was monitored by the separation efficiency determined with the  $^7\text{Li}$  atoms using the heavy ion implantation technique [3]. The separation efficiency of  $^7\text{Li}$  was  $13\%$ . For the separation yield measurements of  $^8\text{Li}$ , the mass separated  $^8\text{Li}$  were collected on plastic scintillation detectors that was used to the counter of  $\beta$ -ray in the decay of  $^8\text{Li}$ . The separation yield of  $^8\text{Li}$  determined with the  $\beta$ -ray counts was  $6.8 \times 10^4$  pps at the detector in the transfer tube to the ECRIS. This is fairly reasonable value in comparison with calculation from the release time [2].

---

1) High Energy Accelerator Research Organization

We expected that pure  ${}^8\text{Li}^+$  ion was ionized and separated with this ion source system, but we observed  ${}^{16}\text{O}^{2+}$  ion weakly in the mass separated beam at  $A/q=8$ . The mechanism of surface ionization is difficult to make doubly-ionized oxygen because the second ionization energy of oxygen is 35.1 eV. The ion source was heated by electron bombardment, typically 400V and 1A. So we consider that oxygen at the outside of the ionizer cause the contamination of  ${}^{16}\text{O}^{2+}$ . In fact, when the ion source was well degassed, the intensity of  ${}^{16}\text{O}^{2+}$  was decreased.

## References

- [1] L. Trache et al., Cyclotron Progress Report; 1999-2000, Texas A & M University, Available at: <http://cyclotron.tamu.edu/progress/1999-2000/sec1/section1.htm>.
- [2] S. Ichikawa et al., Nucl. Instrum. Methods. **B204** (2003) 372.
- [3] R. Kirchner, Nucl. Instrum. Methods. **B70** (1992) 186.

## 1.4 INSTALLATION OF MONITORING SYSTEM OF COOLING WATER IN THE TERMINAL

K. KUTSUKAKE, M. MATSUDA and S. HANASHIMA

The cooling water in the terminal was leaked, which disabled the tandem for applying high voltage. The leakage happened at a point connecting the cooling water pipe and the pressure-resistant hose on the transistor installation plate, which is installed in a power supply box of the 180-degree magnet. The leakage part is shown in Fig. 1. The crack of the pressure-resistant rubber hose was probably caused by the deterioration of the rubber. Every hose in the power supply box of the 180-degree magnet was replaced to new one to prevent possible crack in near future.

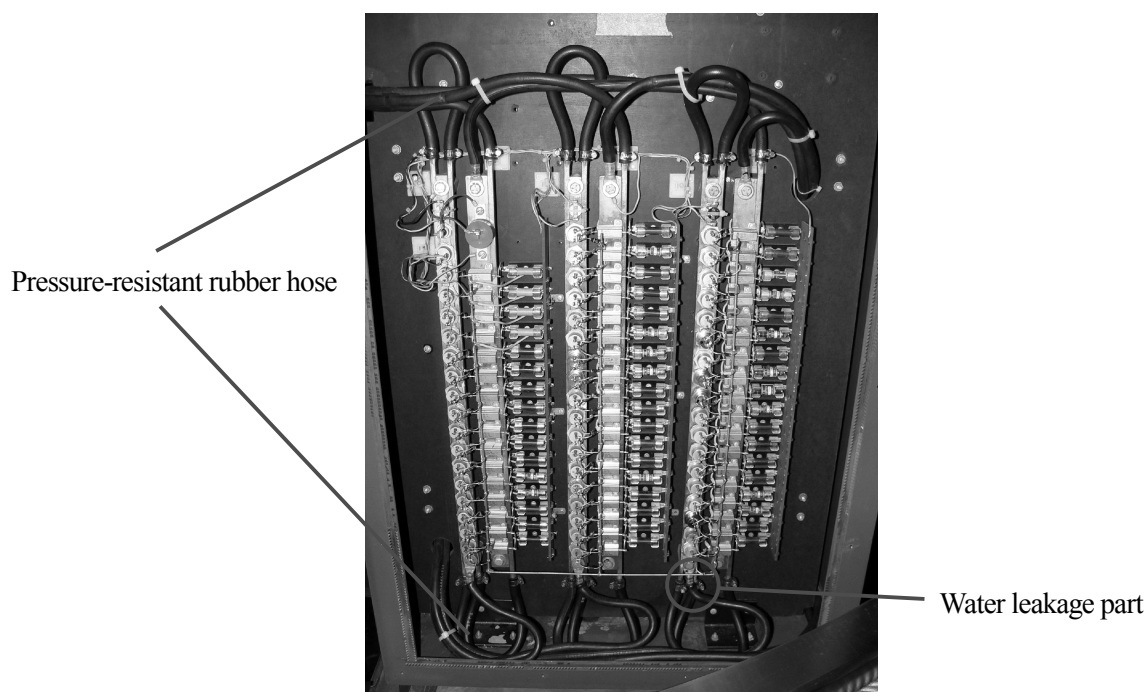


Fig. 1. Leakage part of the cooling water hose in the power supply box of the 180-degree magnet placed in the terminal.

In order to prevent a water-leakage accident, the differential pressure gauge (Nagano Keiki Co., Ltd. GC50) was installed at the terminal cooling water tank. This gauge monitors the pressure in the hoses. The terminal water cooling system is shown in Fig. 2. This monitoring also stops the water pumping when an accidental water leakage happens. The pressure range monitored by the gauge is from 0 kPa to 10 kPa, which corresponds to the water level of 0-100 cm.



## 1.5 FABRICATION OF LOW BETA SUPERCONDUCTING TWIN QUARTER WAVE RESONATOR

H. KABUMOTO, S. TAKEUCHI and M. MATSUDA

JAEA and KEK have started acceleration of radioactive nuclear beam (RNB) and stable ion beam (SNB) from TRIAC. RNB and SNB are accelerated by the split-coaxial RFQ and interdigital-H linac up to the energy of 1.1MeV/u. We were planning to re-accelerate the beams in the future by superconducting booster up to an energy of 5~8MeV/u. In order to inject the beams into superconducting booster, we need a pre-booster capable of acceleration from 1.1MeV/u to 2.0MeV/u. We have started development of a superconducting twin quarter wave resonator (twin-QWR) in FY2004, and have fabricated a prototype twin-QWR in FY2005.

Figure 1 shows a cutaway drawing of the twin-QWR. The cavity has 2 inductors and 3 acceleration gaps. The resonant frequency is designed for 130MHz same as for present QWR, and the optimum beam velocity  $\beta_{opt}$  is 6% of the light velocity ( $\sim 1.7\text{MeV/u}$ ).

These inductors are made of niobium of which Residual Resistivity Ratio (RRR) is 180~220. This outer conductor is made of niobium plate clad in copper : the lower section is oval-shaped to make evenly spaced acceleration gaps and upper section is wide-mouthed circular. The top end plate and outer conductor are connected by superconducting gasket made of niobium.

Figure 2 shows the process of fabricating twin-QWR. After mechanical processing, we have carried out some surface treatments, 80~100 $\mu\text{m}$  electro-polishing for inductors and outer conductor, and 40~60 $\mu\text{m}$  electro-polishing for niobium gasket. And then, we have carried out 600 $^{\circ}\text{C}$  1.5hours annealing for inductors and niobium gasket. We are planning to carry out a performance test of this twin-QWR after final assembling and high pressure water jet rinse in FY2006.

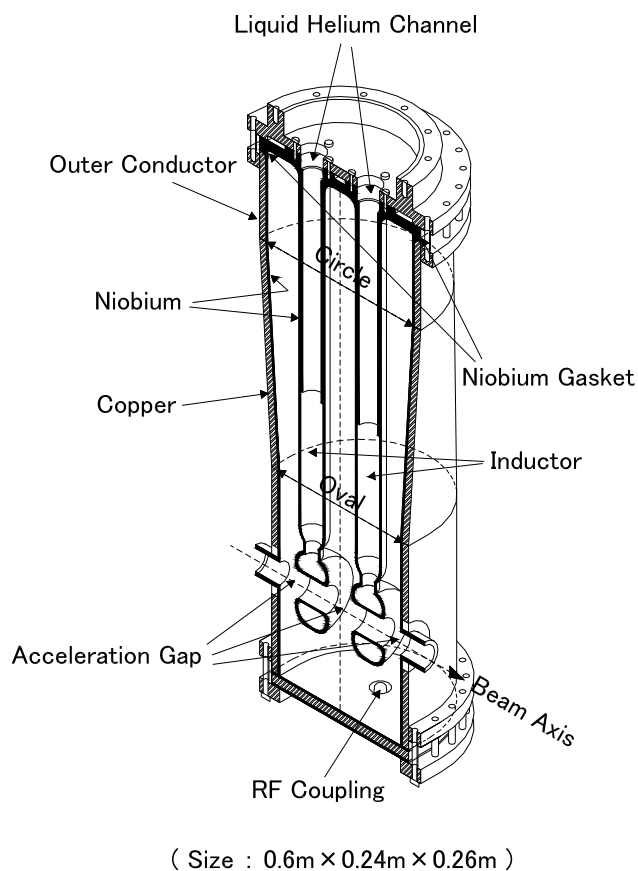


Fig. 1. Cutaway drawing of twin-QWR.



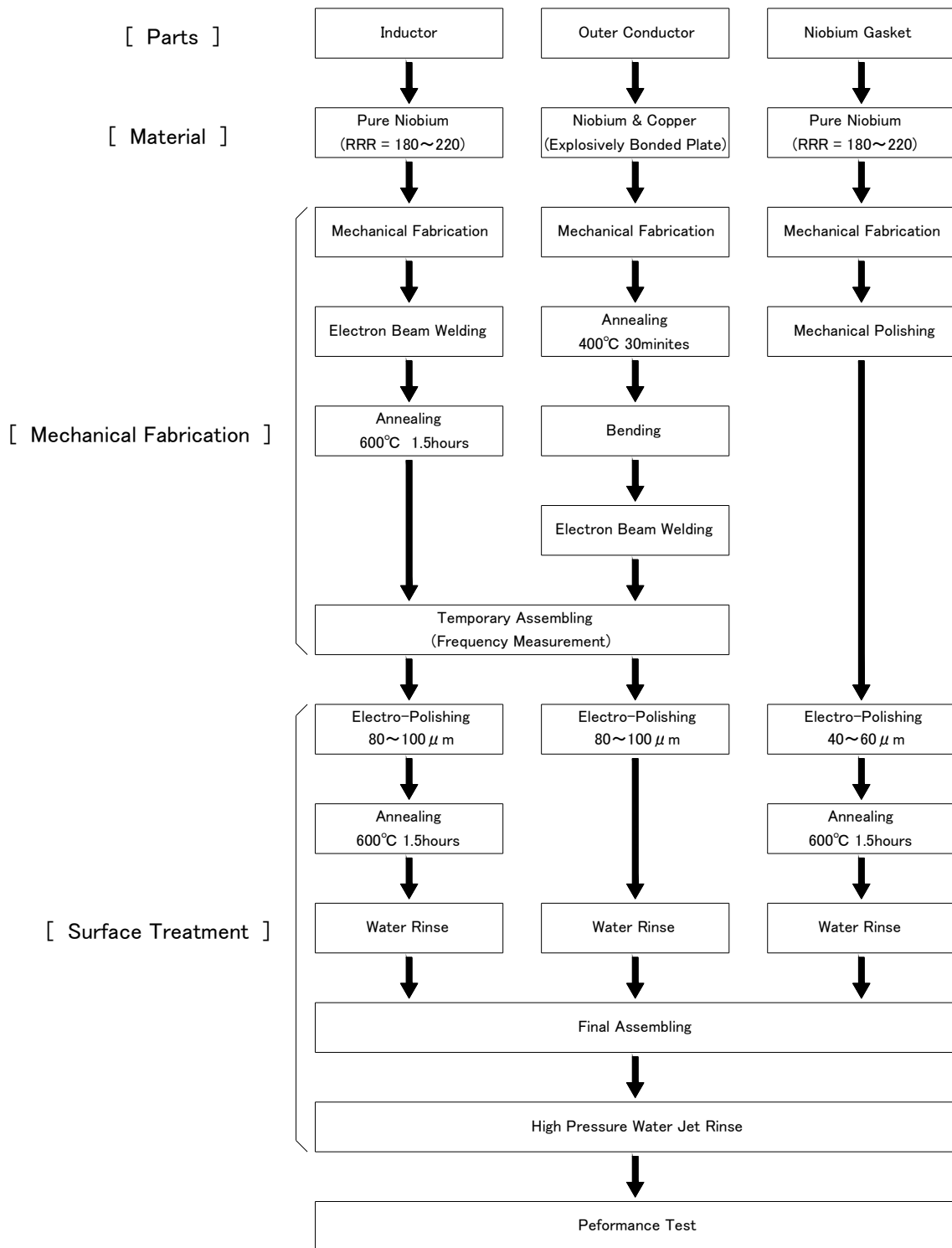


Fig. 2. Process of fabricating twin-QWR.

**References**

- [1] S. Ichikawa et al., JAERI Tandem Annu. Rep. 2004, JAEA-Review **2005-004** (2006) 6.
- [2] H. Kabumoto et al., JAERI Tandem Annu. Rep. 2003, JAERI-Review **2004-027** (2004) 13.

## 1.6 REARRANGEMENT OF IN-TERMINAL ECR ION SOURCE INJECTOR

M. MATSUDA, Y. FUJII<sup>1</sup>, T. YOSHIDA, T. NAKANOYA,  
S. TAKEUCHI and S. HANASHIMA

We are proceeding with a plan to replace the present permanent magnet type 10GHz ECR ion source by the 14.5 GHz higher performance one in order to increase the beam energy and beam intensity from the in-terminal ECR ion source (TECRIS). A new ion source will be installed in the low-energy side which is the upstream side of the 180° bending magnet in the high voltage terminal. This reason is to secure built-in space of the 14.5GHz ECR ion source and to optimize an incident beam condition to the main accelerating tube by using the 180° bending magnet for the analysis of the beam from the ion source [1].

First, we rearranged a present 10 GHz ECR ion source and the injector equipments on the low energy side and decided to confirm the improvement of the incident condition of the ion beam. The new layout of the TECRIS and injection system are shown in Fig. 1. The 90° injection magnet, the ion extractor, the einzel lens and the electrostatic steerer manufactured newly and can use those for the 14.5 GHz ECR ion source, too. The ion beams are extracted by 30kV(maximum) potential gap from the ion source, focused by einzel lens, and then the mass and charge of them are roughly selected by the 90° injection magnet ( $\rho=200\text{mm}$ , maximum magnetic field=0.4T). The horizontal beam direction is corrected by an electrostatic steerer placed just after the einzel lens. After acceleration by a 80 kV pre-accelerating tube, desired ions are selected by the 180° bending magnet. The maximum magnetic field strength and the analyzing power of the 180° bending magnet are sufficient to select the ion beams because they are  $ME/q^2=55$  and  $M/\Delta M \leq 140$  respectively. The injection condition of the ion beams into the main accelerating tube of the tandem accelerator can be optimized because there is one electrostatic quadrupole triplet (EQT) at the low energy side and there are two EQTs and one electrostatic steerer at the high energy side.

In October, 2003, the gas stripper canal and the related equipments were removed and the confirmation and the securing of the installation space for new ion source were done. Next service period, the 90° injection magnet and the both accelerating tubes of the vertical beam line were installed. A 10GHz ECR ion source, a horizontal beam line and a vacuum evacuation system which is composed of the turbo molecular pump, rotary pump and ion sputter pump were installed in service period in August, 2005. The arrangement of the ion source control devices in the high-voltage deck was changed to apply to the new ion source. The vacuum evacuation system by turbo molecular pump (TMP) for the TECRIS [2] was improved by using the new rotary pump which was exchanged at pressure-tight rotor housing in order to install into the compressed SF<sub>6</sub> gases directly. The fore-line was simplified and its pumping speed was increased, the transient vacuum deterioration which occurs in case of TMP stop was fairly suppressed. A cold cathode gauge was added newly for a monitor of the degree of vacuum of the ion source.

The improvement of the beam incident condition from TECRIS was confirmed by the beam acceleration test and the several machine-time experiments after moving. By analyzing a beam

---

<sup>1</sup> Nippon advanced technology Co. Ltd.

after pre-acceleration with the 180° bending magnet, it succeeded in the separation acceleration of the multi-charged ion of the Xe isotope with near electric charge to mass ratio. In the beneficence of the strong magnetic field which the 180° bending magnet generates, the bending of the ion beams of the low electric charge became possible without decreasing the pre-accelerating voltage. Therefore, the very heavy ion beams in the very low energy area like the neon beam with 12MeV energy became available.

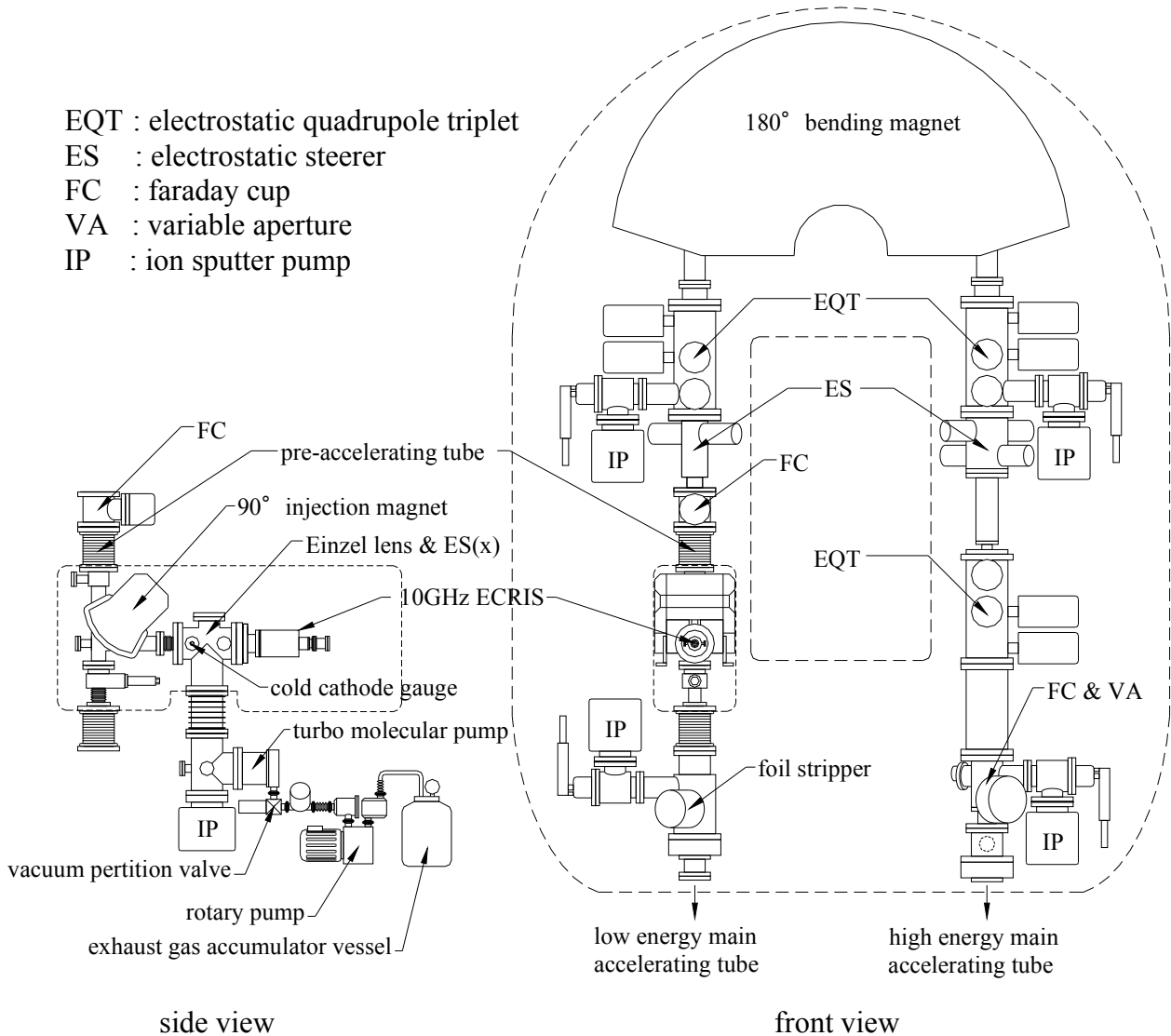


Fig. 1. The new layout of the 10GHz ECR ion source injector at the high voltage terminal.

**References**

[1] M. Matsuda et al., JAERI Tandem Annu. Rep. 2001, JAERI-Review **2002-029** (2002) 11.  
 [2] M. Matsuda et al., JAERI Tandem Annu. Rep. 2000, JAERI-Review **2001-030** (2001) 7.

## 1.7 NEW INTERLOCK SYSTEM FOR THE TANDEM ACCELERATOR FACILITY

S. HANASHIMA, N. NAKAMURA, T. YOSHIDA and T. NAKANNOYA

Modification of the interlock system for the tandem accelerator facility was required because of the installation of TRIAC. The original interlock system was very old and had problems on its maintenance. Therefore, we have developed a new interlock system. In this system, it is necessary to improve safety aspect of users getting in the target rooms. Thus, a function is added to monitor that a person goes into a controlled area and comes out of a controlled area. Emergency switches to stop the accelerator have also been installed in every section.

Fig. 1 shows block diagram of the interlock system. The new interlock system for the facility consists of two interlock systems. One of them is an interlock system for the tandem accelerator and the associated booster. The other is a system for radioactive nuclear beam (RNB) accelerators. Each system consists of a master controller, a few switch control modules, LED driver boards and entrance monitor module. One module, which generates announcements inside the facility, is shared between two interlock systems. A micro-controller (PIC18F6720) is adopted in each module. Communications among the modules are made through serial bus (RS-485), which is controlled by the master controller.

Master controllers are control centers. They execute the interlock logic. Data points showing status of entrance doors of sections etc. are switch contact inputs. The controller gets their status by the way of matrix scan. The switches are addressed with row numbers and column numbers. Signal wirings between the controller and a signal distribution box are 8 column sense lines and several row select lines. One of the master controllers can handle maximum of 8 by 16 contact inputs. Additionally the controller has an RS-232C serial interface. It is prepared for future expansions.

A central display panel for the interlock status is put in the control room of the facility. The display panel consists of a printed diagram of the facility, LED lamps and LED driver boards. LEDs are embedded in the diagram and controlled by the LED driver board. Information is put on the color of LEDs.

In our facility, we use personal dosimeters which have ID barcodes. Entrance monitor reads the barcodes. Each monitor has two readers. The one is for check in and the other is for check out. The monitor has transit sensors and a voice generator. They are used to prompt passengers to check in or out. The entrance monitor has LCD display which shows auxiliary information.

Communications between control systems of accelerators are made through switch matrix and the switch control modules.

Programs of the modules are developed by personal computers and written on the flash ROM on the micro controller chips. The development of the software has been processed setting guide lines for programming.

In March, 2005 our facility established the new license including TRIAC with the new interlock system. Until now the interlock system showed good reliability with exception of development phase of the system.

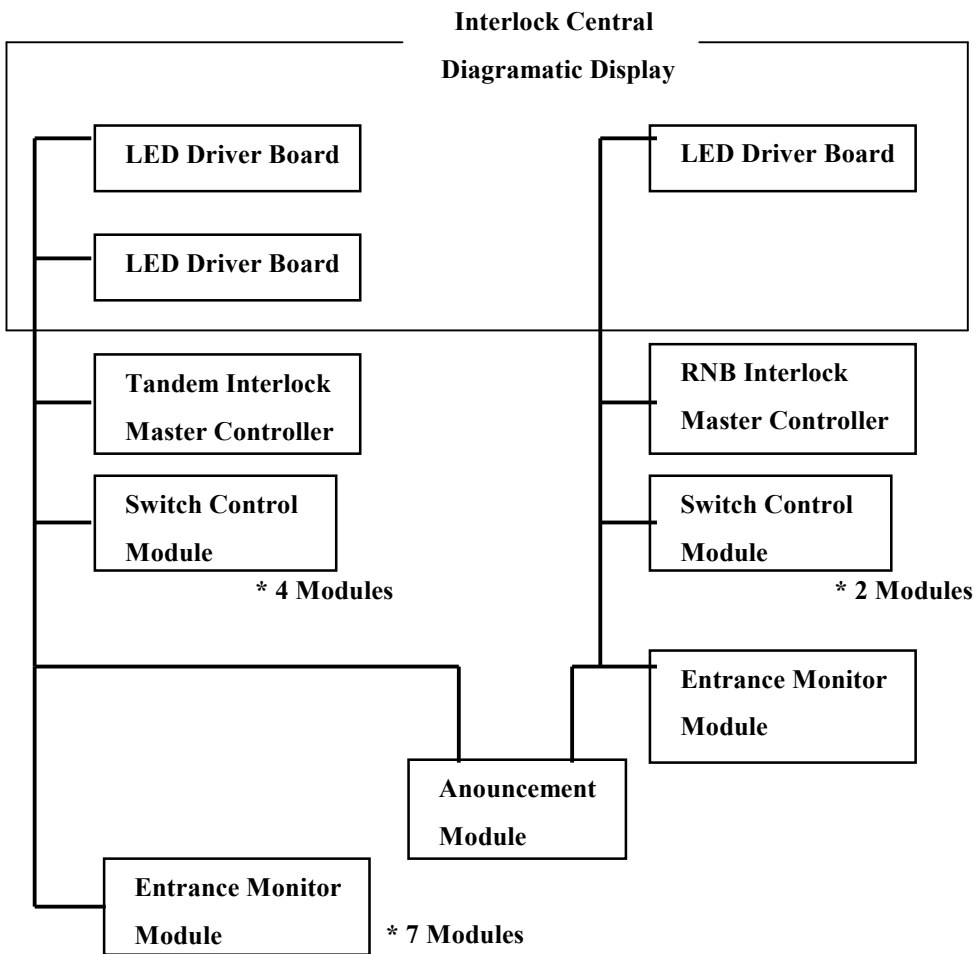


Fig. 1. Interlock system for the tandem accelerator facility.



## CHAPTER 2

### Nuclear Structure

- 2.1 High-spin Gamma-ray Spectroscopy of  $^{42}\text{Sc}$
- 2.2 Lifetime Measurement of High-spin States in  $^{144}\text{Dy}$
- 2.3 Coulomb Excitation Experiment with Inverse Kinematics
- 2.4 Coulomb Excitation Experiment of  $^{102}\text{Ru}$
- 2.5 Search for Signature Inversion in the  $\pi i_{13/2} \otimes \nu i_{13/2}$  Bands in Odd-odd Au Nuclei
- 2.6 Signature Inversion in the Oblate  $\pi h_{9/2} \otimes \nu i_{13/2}$  Band of  $^{188}\text{Tl}$
- 2.7 Decay Studies of New Neutron-rich Isotopes  $^{163, 164, 165}\text{Eu}$
- 2.8  $Q_{\beta}$  Determinations of  $^{160-165}\text{Eu}$ ,  $^{163}\text{Gd}$ ,  $^{158, 159}\text{Pm}$ ,  $^{159, 161}\text{Sm}$  and  $^{166}\text{Tb}$  using a Total Absorption BGO Detector
- 2.9 Production of Long-lived  $^{186\text{m}}\text{Re}$  for Laser Ablation Laser-induced Fluorescence Spectroscopy
- 2.10 In-beam  $\gamma$ -ray Spectroscopy for Neutron-rich W Isotopes
- 2.11 Development of RI Ion Trap System
- 2.12 Gamma-rays in the Ground-State Band of  $^{250}\text{Cm}$
- 2.13 Alpha-gamma Coincidence Spectroscopy of  $^{255}\text{No}$





## 2.1 HIGH-SPIN GAMMA-RAY SPECTROSCOPY OF $^{42}\text{Sc}$

T. MORIKAWA<sup>1</sup>, H. KUSAKARI<sup>2</sup>, M. OSHIMA, Y. TOH, M. KOIZUMI,  
 A. KIMURA, A. OSA, Y. HATSUKAWA, K. FURUTAKA, J. KATAKURA,  
 M. NAKAMURA, M. SUGAWARA<sup>3</sup>, and K. SAGARA<sup>1</sup>

The  $^{42}\text{Sc}$  nucleus is composed of one proton and one neutron coupled to the doubly magic  $^{40}\text{Ca}$  core. While its low-lying yrast levels from  $J^\pi = 0^+$  to  $J^\pi = 7^+$  can be interpreted as a member of  $\{\pi f_{7/2}\}^1 \otimes \{\nu f_{7/2}\}^1$  multiplet, high-spin states of  $J > 7$  have not been known. The negative parity levels, which should be a clear signature of the core-breaking, have scarcely been observed either. For the formation of high-spin states of  $J > 7$  in  $^{42}\text{Sc}$  nucleus, breaking of the  $^{40}\text{Ca}$  core is necessary. At the same time, the particle-hole excitation of doubly-closed core is known to lead to a sizable nuclear deformation. Hence, one can expect the onset of rotational motion of deformed state in  $^{42}\text{Sc}$  with large angular momentum. In the neighboring  $^{43}\text{Sc}$ , a rather collective rotational band based on the (core-breaking)  $J^\pi = 3/2^+$  state has been studied [1] recently up to the terminating  $J^\pi = (27/2^+)$  level.

In order to investigate the high-spin states in  $^{42}\text{Sc}$ , we undertook an experiment with a target of 11 mg/cm<sup>2</sup> PbS bombarded by the 60 MeV  $^{16}\text{O}$  beam. The  $\gamma$ - $\gamma$ -coincidence measurement with  $\pm 800$  ns time window was made by using the GEMINI-II array [2]. The data were offline sorted into  $\gamma$ - $\gamma$  correlation matrices. As presented in Fig. 1,  $\gamma$ -ray cascades of sizable multiplicity were identified as feeding to the low-lying yrast levels. Data analysis is still in progress.

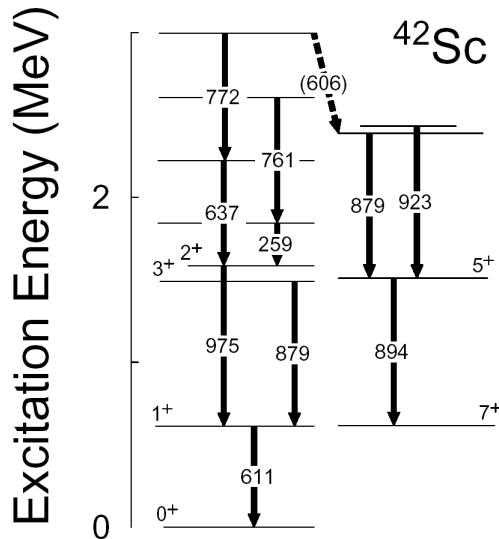


Fig. 1. A partial level scheme of  $^{42}\text{Sc}$  proposed in the present work. (tentative)

### References

- [1] T. Morikawa et al., Phys. Rev. C **70** (2004) 054323, and references therein.
- [2] K. Furuno et al., Nucl. Instrum. Methods **A421** (1999) 211.

<sup>1</sup>Department of Physics, Kyushu University

<sup>2</sup>Faculty of Education, Chiba University

<sup>3</sup>Chiba Institute of Technology

## 2.2 LIFETIME MEASUREMENT OF HIGH-SPIN STATES IN $^{144}\text{Dy}$

M. SUGAWARA<sup>1</sup>, Y. TOH, M. OSHIMA, M. KOIZUMI, A. OSA, A. KIMURA,  
Y. HATSUKAWA, H. HARADA, K. FURUTAKA, F. KITATANI,  
S. NAKAMURA, M. OHTA, K. HARA and H. KUSAKARI<sup>2</sup>,

Whereas rotational-like bands consisting of stretched dipole transitions around the spherical region have been interpreted as magnetic rotors, it was also proposed by Frauendorf[1] that a  $\Delta I=2$  band in  $^{110}\text{Cd}$ [2] being regular but having very small  $B(E2)$  values might be a candidate of an anti-magnetic rotor. In the anti-magnetic rotor, each angular momentum of the proton holes (particles) is coupled to the angular momentum of the neutron particles (holes) with  $\pm 90^\circ$  so as to produce no transverse magnetic moment differently from the magnetic rotor case. In the  $^{110}\text{Cd}$  case the relevant neutron and proton configurations to create the anti-magnetic rotor are  $\nu h_{11/2}^{-2}$  and  $\pi g_{9/2}^{-2}$  respectively.

Previously we made an in-beam  $\gamma$ -ray spectroscopy on  $^{144}\text{Dy}$  in which  $\pi h_{11/2}^{-2}$  and  $\nu h_{11/2}^{-2}$  configurations were appropriate for the anti-magnetic rotor. In that experiment, even and odd parity states were extended up to  $18^+$  and  $(19^-)$  states respectively. It was likely that two of the three quadrupole cascades above the  $10^+$  state and one dipole cascade placed upon the negative parity side band were promising candidates for the anti-magnetic rotors and the magnetic rotor respectively.

It is needed to measure the lifetimes of these states and prove that they actually have as large ratios of dynamical moment of inertia to  $B(E2)$  as in the  $^{110}\text{Cd}$  case. Therefore the lifetime measurement was made on high-spin states in  $^{144}\text{Dy}$  using the Doppler shift attenuation method through the reaction of  $^{92}\text{Mo}(^{56}\text{Fe}, 2p2n)$ . An enriched  $^{92}\text{Mo}$  foil of  $0.9 \text{ mg/cm}^2$  thickness backed with Au of  $11.6 \text{ mg/cm}^2$  thickness was bombarded with an  $^{56}\text{Fe}$  beam of 280 MeV. Emitted  $\gamma$ -rays were detected with an array of 10 HPGe detectors with BGO Compton suppressors (GEMINI-II). Total events of  $4.0 \times 10^8$  were collected for 3 days of beam time. In this reaction, the recoil velocity of  $^{144}\text{Dy}$  nucleus was estimated to be around 4 % relative to the light velocity and the energy difference between stopped and fully shifted components amounted to about 22 keV for the detector at  $\theta=144^\circ$  with respect to the beam direction. Since we have also detectors at  $\theta=47^\circ$  in GEMINI-II frame, it is possible to check the consistency of the deduced lifetimes by analyzing the  $\gamma$ -ray lineshapes of both detectors simultaneously. Detailed analysis is in progress.

### References

- [1] S. Frauendorf, Rev. Mod. Phys. **73** (2001) 463.
- [2] R. M. Clark et al., Phys. Rev. Lett. **82** (1999) 3220.

---

<sup>1</sup>Chiba Institute of Technology

<sup>2</sup>Chiba University

### 2.3 COULOMB EXCITATION EXPERIMENT WITH INVERSE KINEMATICS

M. KOIZUMI, Y. TOH, M. OSHIMA, A. OSA, A. KIMURA and Y. HATSUKAWA

Coulomb excitation is a useful method for the measurement of electromagnetic properties near the ground state of nuclei [1,2]. The information gives various clues for understanding the low-lying structures. Our systematic study revealed nuclear properties and evolutions of the structure of stable nuclei in the mass region around  $A \approx 70$  [3-10]. We are planning to explore the systematic study toward the heavy nuclei and unstable nuclei.

Although the projectile Coulomb excitation carried out at JAEA succeeded for some studies [3-10], one can not directly apply this method to the study of heavy nuclei because of the following reasons. (1) The kinetic energy of backward scattered particle becomes too low so that one cannot detect the particle with our position sensitive detectors. (2) The kinetic energy of recoiled particle is comparable with that of scattered particle. To avoid the spatial overlap of recoil and scattered particles, we proposed to introduce inverse kinematics, in which target nuclei are lighter than projectile nuclei; the heavy incident beam are scattered forward, and they pass the target chamber through a small opening.

In order to examine the usefulness of the inverse kinematics for Coulomb excitation experiments of heavy nuclei, we carried out an experiment of  $^{132}\text{Xe}$  with an aluminum target. The energy of  $^{132}\text{Xe}$  beam was 400 MeV, which is less than the Coulomb barrier, and the current was about 0.9 pA. The thickness of the aluminum target was 16  $\mu\text{m}$ . The maximum scattering

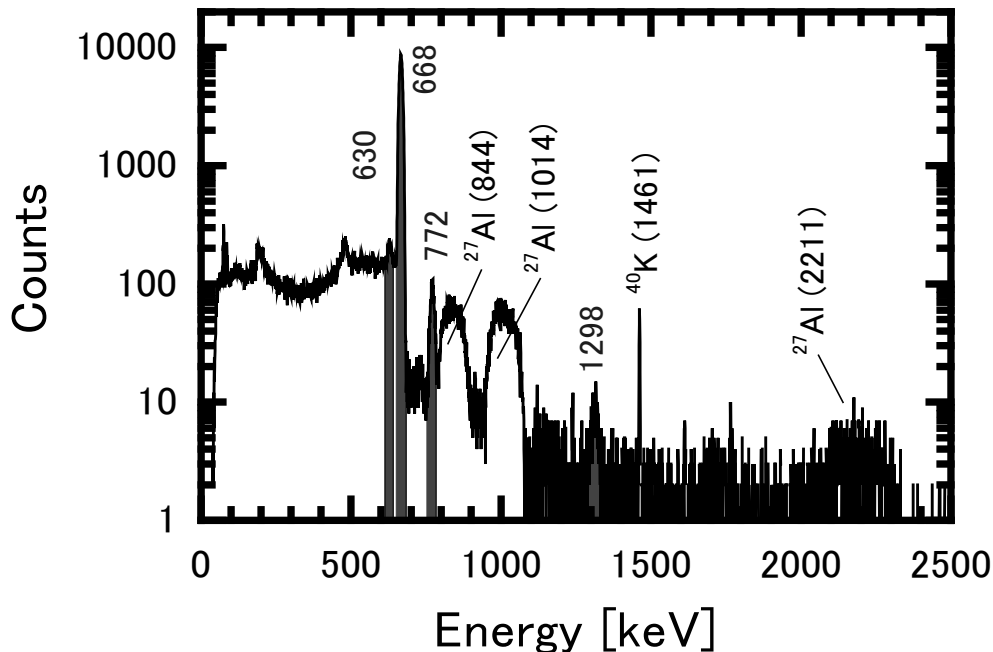


Fig. 1. A particle- $\gamma$  coincidence spectrum. No Doppler correction has been done. Because the scattered Xe particles are not dispersed, the widths of the Xe de-excitation  $\gamma$ -peaks are narrow. On the other hand, the widths of recoiled Al de-excitation  $\gamma$ -peaks are broad. The unit of the  $\gamma$ -energy given in the spectrum is keV.

angle of  $^{132}\text{Xe}$  is less than  $10^\circ$ . The experimental data were recorded event by event on magnetic tapes when one HPGe detector and one particle detector gave coincident signals. At the same time, particle singles spectrum was also taken. A particle- $\gamma$  coincidence spectrum is given in Fig. 1. No Doppler correction has been done to the spectrum. Because the scattered  $^{132}\text{Xe}$  particles are not dispersed, the widths of the  $^{132}\text{Xe}$  de-excitation  $\gamma$ -peaks are narrow. On the other hand, the widths of recoiled  $^{27}\text{Al}$  de-excitation  $\gamma$ -peaks are broad. Four peaks are identified to be the  $^{132}\text{Xe}$  de-excitation  $\gamma$ -rays: the 630-keV  $2_2^+ \rightarrow 2_1^+$  transition, the 668-keV  $2_1^+ \rightarrow 0^+$  transition, the 772-keV  $0^+ \rightarrow 4_1^+$  transition, and the 1298-keV  $2_1^+ \rightarrow 0^+$  transition. Consequently, the  $^{132}\text{Xe}$  was excited up to 1440 keV. In order to deduce the quadrupole moment of the  $2_1^+$  state, the absolute yields of both the  $2_2^+ \rightarrow 2_1^+$  transition and the  $2_2^+ \rightarrow 0^+$  transition are important. Such an analysis is in progress.

In conclusion, we have tested Coulomb excitation with inverse kinematics, and successfully excited  $^{132}\text{Xe}$  up to 1440-keV  $4^+$  state and observed four de-excitation  $\gamma$ -rays. The data analysis to deduce the quadrupole moment of the  $2_1^+$  state is in progress.

## References

- [1] K. Alder and A. Winther, Coulomb Excitation (Academic, New York, 1966).
- [2] K. Alder and A. Winther, Electromagnetic Excitation (North Holland, Amsterdam, 1975).
- [3] Y. Toh et al., J. Phys. **G27** (2001) 1475.
- [4] Y. Toh et al., Eur. Phys. J. **A9** (2000) 353.
- [5] A. Osa, T. Czosnyka, et al., Phys. Lett. **B546** (2002) 48.
- [6] M. Zielinska, T. Czosnyka, et al., Nucl. Phys. **A712** (2002) 3.
- [7] M. Koizumi, A. Seki, Y. Toh, et al., Eur. Phys. J. **A18** (2003) 87.
- [8] M. Sugawara et al., Eur. Phys. J. **A16** (2003) 409.
- [9] M. Koizumi et al., Nucl. Phys. **A736** (2003) 46.
- [10] T. Hayakawa et al., Phys. Rev. **C67** (2003) 064310.
- [11] M. Koizumi et al., JAEA-Review **2005-004** (2005) 31.
- [12] K. Furuno et al., Nucl. Instrum. Methods Phys. Res. **A421** (1999) 211.
- [13] H. Miyatake et al., NIM **B204** (2003) 746.

## 2.4 COULOMB EXCITATION EXPERIMENT OF $^{102}\text{Ru}$

Y. TOH, M. KOIZUMI, M. OSHIMA, A. OSA, A. KIMURA, Y. HATSUKAWA,  
M. MATSUDA, H. KUSAKARI<sup>1</sup>, M. SUGAWARA<sup>2</sup> and T. MORIKAWA<sup>3</sup>

Spherical and nearly spherical nuclei exhibit low-energy collective spectra with vibrational-like states, which are often called quasi-band structures. Locating at the transitional region, the chain of stable Ru isotopes exhibit the structural evolution from spherical ( $A = 96, 98$ ) to triaxial structure ( $A = 98 - 108$ ). In order to understand the structural evolution, transition probabilities and nuclear moments are important. Multiple Coulomb excitation is a useful method to deduce such electromagnetic properties without the effects of nuclear interactions [1,2]. In this study we carried out projectile Coulomb excitation experiment of  $^{102}\text{Ru}$ .

A 440 MeV  $^{102}\text{Ru}$  nuclei were excited on an about  $2 \text{ mg/cm}^2$  thick  $^{108}\text{Pb}$  target. The  $\gamma$ -ray detector array, GEMINI-II (upgraded version of GEMINI [3]), consisting of 16 HPGe detectors with BGO Compton suppression shields, was used to detect deexcitation  $\gamma$ -rays. A typical energy resolution of the Ge detectors was about 2.2 keV FWHM for the 1.3 MeV  $\gamma$ -rays from  $^{60}\text{Co}$ . The Ge detectors were placed at

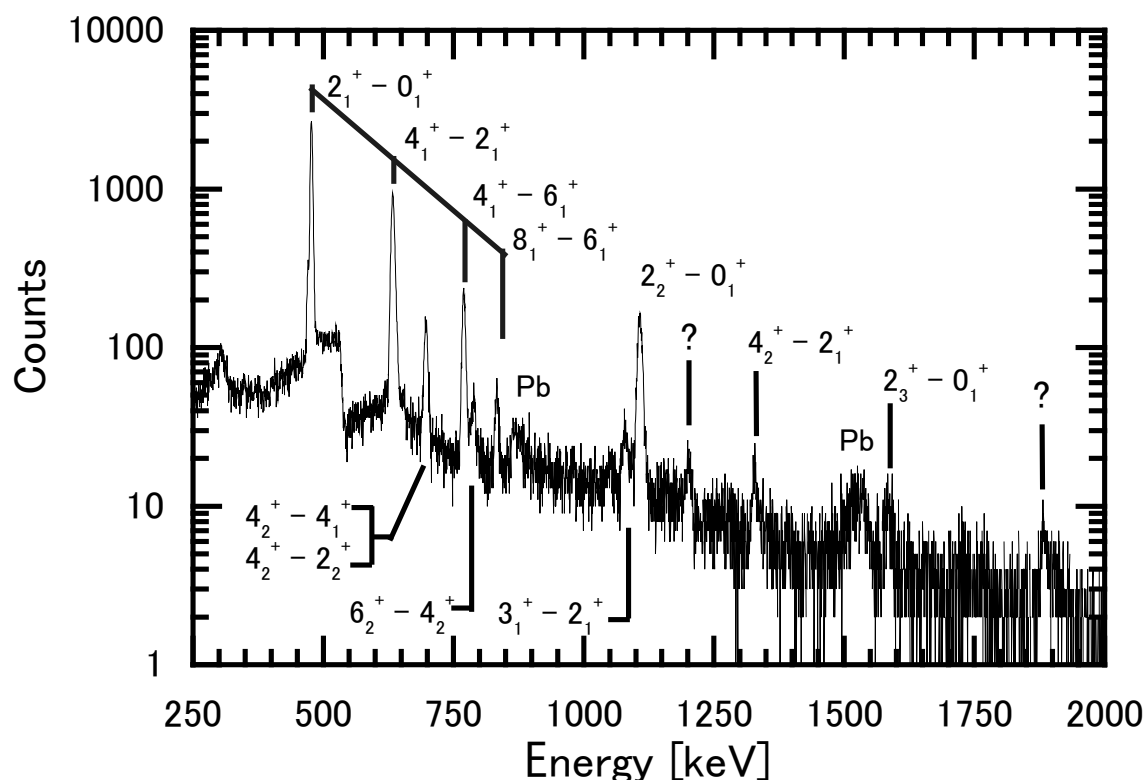


Fig. 1. Doppler corrected spectrum. Peaks with question marks are not identified.

<sup>1</sup>Chiba University

<sup>2</sup>Chiba Institute of Technology

<sup>3</sup>Kyushu University

$\theta = 47^\circ, 72^\circ, 90^\circ, 105^\circ, 147^\circ,$  and  $144^\circ$  relative to the incident beam. The scattered beam was detected with a position-sensitive particle detector system [4] with 4 photomultiplier tubes in combination with four plastic scintillators. It covered about 30% of the total solid angle, ranging from  $20^\circ$  to  $67^\circ$  and from  $113^\circ$  to  $160^\circ$  to the incident beam direction. The angular resolution was  $3.1^\circ$  FWHM near the edge of the detector and  $1.9^\circ$  at the center. The information on the particle position was used for Doppler-shift corrections of the  $\gamma$ -rays from  $^{102}\text{Ru}$ , simultaneously providing the impact-parameter dependence of the  $\gamma$ -transition intensity. The experimental data were recorded event by event on magnetic tapes when one HPGe detector and one particle detector gave coincident signals. Figure 1 gives an example of Doppler-corrected  $\gamma$ -ray spectra in coincidence with scattered particles. Ten peaks, one of which is a doublet peak, are identified as the  $\gamma$ -rays of  $^{102}\text{Ru}$ . Low-lying energy levels and transitions of  $^{102}\text{Ru}$  observed in this experiment are given in Fig. 2. Connecting the observed transitions, we can construct the ground band and quasi-gamma band structure. The detailed data analysis of this experiment is in progress with the least-squares search code GOSIA [5,6], which will reveal the  $B(E2)$  transition probabilities and some of the quadrupole moments. This will help us to understand the low-lying quasi-band structure of  $^{102}\text{Ru}$ .

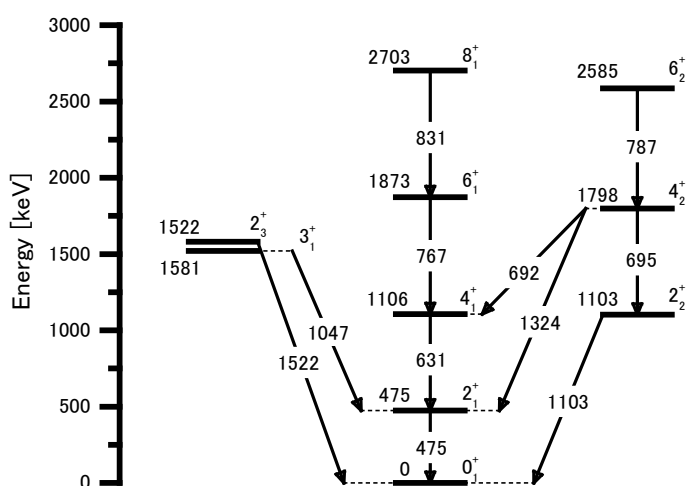


Fig. 2. Low-lying energy levels and transitions of  $^{102}\text{Ru}$  observed in this experiment.

## References

- [1] K. Alder and A. Winther, Coulomb Excitation (Academic, New York, 1966).
- [2] K. Alder and A. Winther, Electromagnetic Excitation (North Holland, Amsterdam, 1975).
- [3] K. Furuno, M. Oshima, T. Komatsubara, K. Furutaka, T. Hayakawa, M. Kidera, Y. Hatsukawa, M. Matsuda, S. Mitarai, T. Shizuma, T. Saitoh, N. Hashimoto, H. Kusakari, M. Sugawara, T. Morikawa, Nucl. Instrum. Methods Phys. Res. **A421** (1999) 211.
- [4] Y. Toh, M. Oshima, T. Hayakawa, Y. Hatsukawa, J. Katakura, M. Matsuda, H. Iimura, H. Kusakari, D. Nishimiya, M. Sugawara, Y.H. Zhang, Rev. Sci. Instrum. **73** (2002) 47.
- [5] T. Czosnyka, D. Cline, L. Hasselgren, C.Y. Wu, Nucl. Phys. **A458** (1986) 123.
- [6] T. Czosnyka, C.Y. Wu, D. Cline, Bull. Am. Phys. Soc. **28** (1983) 745.

## 2.5 SEARCH FOR SIGNATURE INVERSION IN THE $\pi i_{13/2} \otimes \nu i_{13/2}$ BANDS IN ODD-ODD Au NUCLEI

Y.H. ZHANG<sup>1</sup>, X.H. ZHOU<sup>1</sup>, J.J. HE<sup>1</sup>, Z. LIU<sup>1</sup>, Y.D. FANG<sup>1</sup>, W.T. GUO<sup>1</sup>, M. OSHIMA,  
Y. TOH, M. KOIZUMI, A. OSA, A. KIMURA, Y. HATSUKAWA, H. HAYAKAWA,  
T. SHIZUMA, J. KATAKURA, M. MATSUDA, T. MORIKAWA<sup>2</sup>,  
M. SUGAWARA<sup>3</sup>, H. KUSAKARI<sup>4</sup> and F.R. XU<sup>5</sup>

Low-spin signature inversion [1] is a very interesting phenomenon observed in a number of deformed odd-odd nuclei, and it has been attracting large experimental [2] and theoretical [3] interests. Up to date, signature inversion has been systematically observed throughout the chart of nuclides in the  $\pi g_{9/2} \otimes \nu g_{9/2}$ ,  $\pi h_{11/2} \otimes \nu h_{11/2}$ ,  $\pi h_{11/2} \otimes \nu i_{13/2}$ , and  $\pi h_{9/2} \otimes \nu i_{13/2}$  configurations of high- $j$  spherical parentage. It is thus expected that the  $\pi i_{13/2} \otimes \nu i_{13/2}$  bands may have similar inversion phenomenon. For the neutron-deficient Au isotopes, the proton Fermi surface approaches the  $1/2^+[660](i_{13/2})$  intruder orbit, rotational bands based the  $\pi i_{13/2} \otimes \nu i_{13/2}$  configuration should be easily observed experimentally using a normal  $\gamma$ -ray detector array such as the GEMINI [4] in JAEA. With this in mind, efforts have been made recently in search for the signature inversion in the  $\pi i_{13/2} \otimes \nu i_{13/2}$  bands of odd-odd  $^{182,184,186}\text{Au}$  and  $^{176,178}\text{Ir}$ . Evidence of signature inversion has been found in these nuclei, and part of the results published in references [5-7].

The in-beam  $\gamma$ -spectroscopy experiments for  $^{182}\text{Au}$  and  $^{186}\text{Au}$  have been performed in the Japan Atomic Energy Agency (JAEA) using the  $^{152}\text{Sm}(^{35}\text{Cl},5n)^{182}\text{Au}$ ,  $^{171}\text{Yb}(^{19}\text{F},4n)^{186}\text{Au}$  reactions, respectively. A study of  $^{184}\text{Au}$  has been made in LNL-INFN, Italy, via the  $^{159}\text{Tb}(^{29}\text{Si},4n)^{184}\text{Au}$  reaction. The  $\gamma$ -ray detector arrays GEMINI-II in JAEA and GASP in LNL were used for  $\gamma$ - $\gamma$  coincidence measurements. Detailed experimental conditions and data analysis procedures have been described in references. [7,8]

The  $\pi i_{13/2} \otimes \nu i_{13/2}$  band in  $^{182}\text{Au}$  has been identified for the first time, and the bands in  $^{184}\text{Au}$  and  $^{186}\text{Au}$  extended significantly. The configuration assignments are supported by the in-band  $B(M1)/B(E2)$  ratios and the quasi-particle alignments. Level schemes of the  $\pi i_{13/2} \otimes \nu i_{13/2}$  bands in  $^{182,184,186}\text{Au}$  are presented in Fig. 1. It is worth noting that the  $\pi i_{13/2} \otimes \nu i_{13/2}$  band in  $^{184}\text{Au}$  has been connected with the ground-state-band via several linking transitions, leading to a firm spin-and-parity assignment for the  $\pi i_{13/2} \otimes \nu i_{13/2}$  band. Then the level spins of the bands in  $^{182}\text{Au}$  and  $^{186}\text{Au}$  have been proposed on the basis of level spacing systematics. Our spin assignment for  $^{186}\text{Au}$  is one unit increased with respect to the previous one [9].

The signature splitting defined as  $S(I)=E(I)-E(I-1)-[E(I+1)-E(I)+E(I-1)-E(I-2)]/2$  is plotted in Fig. 2 for the  $\pi i_{13/2} \otimes \nu i_{13/2}$  bands of  $^{182,184,186}\text{Au}$ . In such a plot, the points that have negative values are energetically favored over those with positive ones. The expected favored signature is  $\alpha_f=1$  for the  $\pi i_{13/2} \otimes \nu i_{13/2}$  configuration. It can be seen in this figure that, it is the unfavored-signature branch (even spin sequence) that is favored energetically at low and medium spins rather than

<sup>1</sup>Institute of Modern Physics, P. R. China

<sup>2</sup>Department of Physics, Kyushu University

<sup>3</sup>Chiba Institute of Technology

<sup>4</sup>Chiba University

<sup>5</sup>Department of Technical Physics, P. R. China

the  $\alpha_f=1$  sequence. Such a behavior has been referred to as the low-spin signature inversion [1]. With increasing angular momentum, the inverted signature splitting becomes decreasing, and the two signature branches cross with each other around  $I^\pi=22^+$  beyond which normal signature splitting is observed. It is interesting to note that the signature inversion spin keeps constant ( $I^\pi=22^+$ ) for the three bands observed. This is different from that commonly encountered in other configurations. For example, the signature inversion spin in the  $\pi h_{9/2} \otimes \nu i_{13/2}$  bands is 2~3 unit decreased with decreasing two neutrons [8]. Further investigations are needed for a full understanding of this phenomenon.

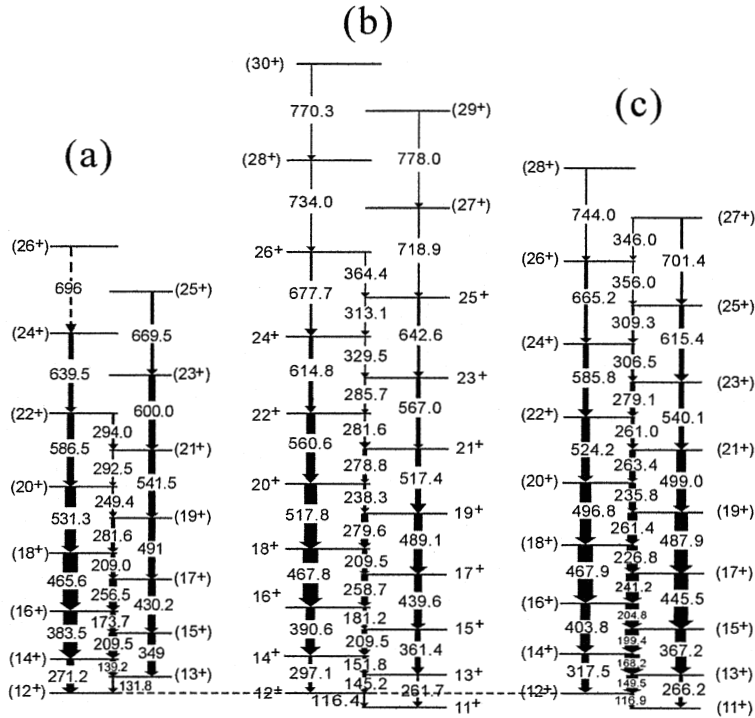


Fig. 1. Level schemes of the  $\pi i_{13/2} \otimes \nu i_{13/2}$  bands in (a)  $^{182}\text{Au}$ , (b)  $^{184}\text{Au}$  and (c)  $^{186}\text{Au}$ .

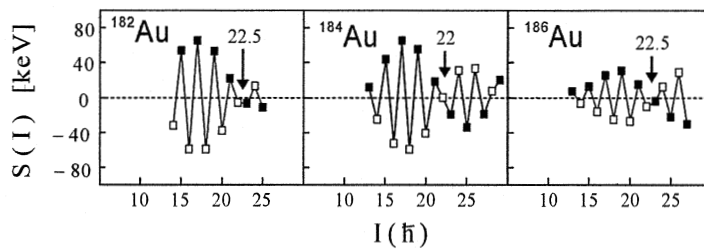


Fig. 2. Plot of signature splitting for the  $\pi i_{13/2} \otimes \nu i_{13/2}$  bands in  $^{182,184,186}\text{Au}$ .

**References**

[1] R. Bengtsson et al., Nucl. Phys. **A415** (1984) 189.  
 [2] M.A. Cadona et al., Phys. Rev. **C59** (1999) 1298.  
 [3] Z.C. Gao et al., Phys. Lett. **B634** (2006) 195 and references therein.  
 [4] K. Furuno et al., Nucl. Instrum. Methods **A421** (1999) 211.  
 [5] Y.H. Zhang et al, Eur. Phys. J. **A14** (2002) 271.  
 [6] Y.H. Zhang et al., Eur. Phys. J. **A13** (2002) 429.  
 [7] Y.H. Zhang et al., Phys. Rev. **C70** (2004) 057303.  
 [8] Y.H. Zhang et al., Phys. Rev. **C68** (2003) 054313.  
 [9] V.P. Janzen et al., Phys. Rev. **C45** (1992) 613.





configuration assignment for the band in  $^{188}\text{Tl}$  can be obtained by comparing theoretical  $B(M1)/B(E2)$  values with experimental ones. The experimental and theoretical  $B(M1)/B(E2)$  ratios have been calculated according to the description given in reference [3]. As shown in Fig. 2, the calculation, under the assumption of oblate  $\pi h_{9/2} \otimes \nu i_{13/2}$  configuration ( $\gamma = -60^\circ$ ) for the band in  $^{190}\text{Tl}$ , reproduced well the experimental results. Therefore, the band observed in  $^{188}\text{Tl}$  likely has the  $\pi h_{9/2} \otimes \nu i_{13/2}$  configuration with oblate deformation.

An interesting phenomenon concerning the oblate band in  $^{188}\text{Tl}$  is the distinctive energy staggering between the odd and even spin members, indicating an apparent energy signature splitting. If we adopted the configuration and spin-parity assignments proposed in the present work, this staggering reveals that the signature splitting in the  $\pi h_{9/2} \otimes \nu i_{13/2}$  band is inverted at low spins; the expected  $\alpha=1$  favored signature branch (odd spin sequence) lies higher in energy than the  $\alpha=0$  unfavored signature branch (even spin sequence). The signature inversion could be interpreted by the residual proton-neutron ( $p-n$ ) interaction, which attributed the staggering to a  $J$  dependence of the  $p-n$  residual interaction ( $J$  being the total intrinsic angular momentum) proposed by Kreiner et al. [6]. If a strong repulsive matrix element of the  $p-n$  residual interaction acts in the maximally aligned intrinsic state  $J=11$ , above the  $10^-$  state a further alignment of the proton and neutron intrinsic spins is energetically more costly and the system prefers to increase its total angular momentum at the expense of collective energy. As a consequence of this, the amplitude of  $J=11$  component in the wave functions for the  $11^-$  and higher states is drastically reduced and meanwhile the role of  $J=10$  component becomes dominant [6]. This leads to the energetically favored states with angular momenta of  $I=R+J=R+10=\text{even}$  and the unfavored states being  $I-1=R+10-1=\text{odd}$  ( $R=\text{even}$  is the collective angular momentum). Therefore, signature inversion occurs at low spins for this band.

## References

- [1] R. Bengtsson et al., Nucl. Phys. **A415** (1984) 189.
- [2] M. Cardona et al., Phys. Rev. **C59** (1999) 1298.
- [3] C.Y. Xie et al., Phys. Rev. **C72** (2005) 044302.
- [4] C. Plettner et al., Phys. Rev. Lett. **85** (2000) 2454.
- [5] A. Kreiner et al., Phys. Rev. Lett. **47** (1981) 1709.
- [6] A. Kreiner et al., Phys. Rev. **C22** (1980) 2570.

## 2.7 DECAY STUDIES OF NEW NEUTRON-RICH ISOTOPES $^{163,164,165}\text{Eu}$

T.K. SATO, A. OSA, K. TSUKADA, M. ASAI, H. HAYASHI<sup>1</sup>,  
Y. KOJIMA<sup>2</sup>, M. SHIBATA<sup>3</sup>, and S. ICHIKAWA

$\beta$ -decay half-lives of three new neutron-rich isotopes produced in the proton-induced fission of  $^{238}\text{U}$  have been determined to be 7.8(5) s for  $^{163}\text{Eu}$ , 4.2(2) s for  $^{164}\text{Eu}$  and 2.3(2) s for  $^{165}\text{Eu}$ , respectively, using the JAEA-ISOL with a surface ionization type integrated-target-ion source [1]. As one of the nuclear decay properties,  $\gamma$  rays associated with the  $\beta$ -decay of  $^{163}\text{Eu}$  and  $^{164}\text{Eu}$  were also assigned on the basis of x- $\gamma$ ,  $\gamma$ - $\gamma$  coincidences.

A  $^{\text{nat}}\text{U}$  target was used in the form of uranium carbide which contained 630 mg/cm<sup>2</sup>  $^{\text{nat}}\text{U}$ . The target was bombarded with the 33 MeV proton beams (24 MeV on target) with the intensity of about 400 nA. Fission products were diffused-out from the target, and then ionized in the ion source. The mass-separated ions of interest were implanted into an aluminum-coated Mylar tape in a tape transport system, and periodically transported to a measuring position. The measuring position was equipped with a sandwich-type plastic scintillator for  $\beta$ -ray measurements, a short coaxial Ge detector (ORTEC LOAX) and a coaxial Ge detector (ORTEC GAMMA-X) with 36% in relative efficiency.  $\beta$ - $\gamma$  and  $\gamma$ - $\gamma$  coincidences between these detectors were recorded event by event together with time information used in a half-life analysis.

Fig. 1 shows a  $\beta$ -coincident x/ $\gamma$ -ray spectrum gated by Gd  $K_{\alpha}$  x-ray at mass 164 fraction. The observed K x-ray following the  $\beta$ -decay of the products in the mass-separated fraction provided direct identification of isotopes. The  $\gamma$  rays with energies of 72.9 and 168.3 keV, which were assigned to the  $2^{+} \rightarrow 0^{+}$  and  $4^{+} \rightarrow 2^{+}$  transitions in the ground state band of daughter nucleus  $^{164}\text{Gd}$ , respectively, by considering their energies [2], are clearly observed. The half-life of  $^{164}\text{Eu}$  was determined to be 4.2(2) s as a weighted average of the half-life values of  $4.5 \pm 0.2\text{s}$ ,  $4.0 \pm 0.2\text{s}$  and  $4.4 \pm 0.3\text{s}$ ,  $3.9 \pm 0.4\text{s}$  for 168.3 and 72.9 keV  $\gamma$  rays measured with coaxial Ge, short coaxial Ge detectors, respectively, as shown in the inset of Fig. 1.

In the decay study of  $^{163}\text{Eu}$ , Gd K x rays were clearly observed for the A=163 fraction, and five  $\gamma$  rays, 85.8, 116, 138, 191.2, and 401 keV were assigned to those from the  $\beta$ -decay of  $^{163}\text{Eu}$  on the basis of x- $\gamma$ ,  $\gamma$ - $\gamma$  coincidence relations. The intensities of the 85.8 and 191.2 keV  $\gamma$  rays decayed with half-lives of  $7.3 \pm 0.4$ ,  $8.0 \pm 0.8$  and  $10.0 \pm 1.1$ ,  $7.9 \pm 1.1$  measured with coaxial Ge, short coaxial Ge detector, respectively. The half-life of  $^{163}\text{Eu}$  was determined to be 7.8(5) s as a weighted average of these half-life values. In addition, the decay study of  $^{165}\text{Eu}$ , the half-life was determined to be 2.7(3) s from the decay curves of Gd K x rays, but no  $\gamma$  transitions were detected.

<sup>1</sup>Graduate School of Engineering, Nagoya University.

<sup>2</sup>Graduate School of Engineering, Hiroshima University

<sup>3</sup>Radioisotope Research Center, Nagoya University

Three new isotopes observed, together with the values of their half-lives and detected x and  $\gamma$  rays are summarized in Table 1.

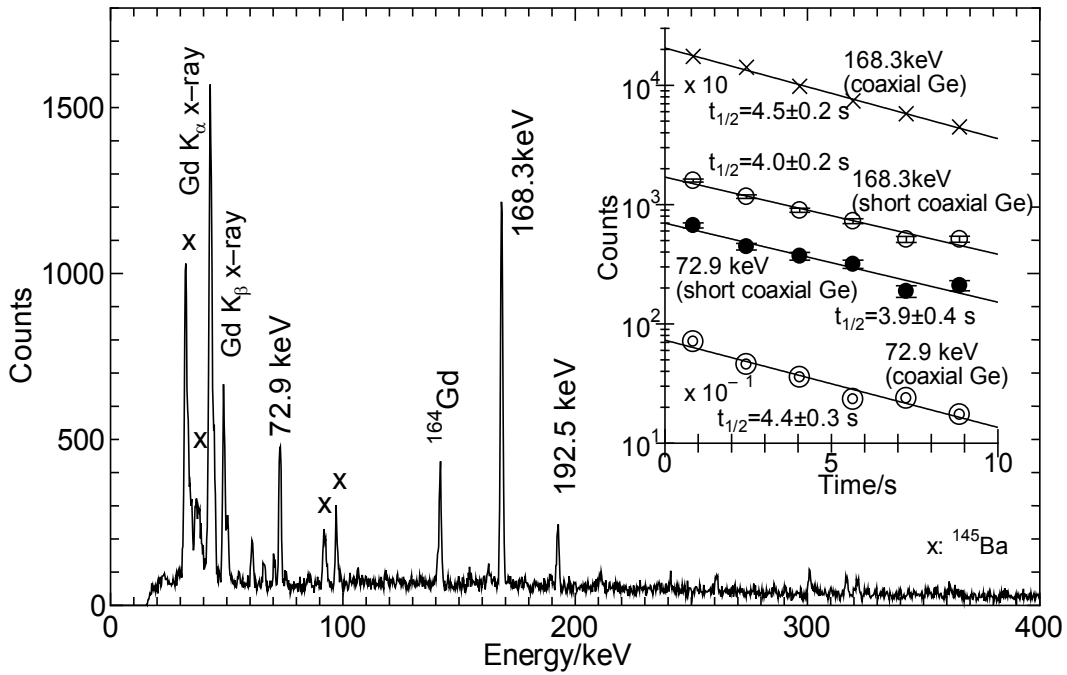


Fig. 1.  $\beta$ -coincident x/ $\gamma$ -ray spectrum measured with coaxial Ge detector for A=164. The inset shows the decay curve of the 72.9 and 168.3 keV  $\gamma$  rays.

Table 1. Measured half-lives and decay x and  $\gamma$  rays for the new Eu isotopes.

Isotope	half-life	detected x and $\gamma$ rays
$^{163}\text{Eu}$	7.8(5)s	Gd $K_{\alpha}$ x-ray , 85.8, 116, 138, 191.2 and 401 keV
$^{164}\text{Eu}$	4.2(2)s	Gd $K_{\alpha}$ x-ray , 72.9, 168.3 and 192.5 keV
$^{165}\text{Eu}$	2.3(2)s	Gd $K_{\alpha}$ x-ray

**Reference**

- [1] T. K. Sato et al. JAERI-Review **2004-027** (2004) 9.
- [2] E. F. Jones et al. J. Phys. G: Nucl. Part. Phys. **30** (2004) L43.

## 2.8 $Q_{\beta}$ DETERMINATIONS OF $^{160-165}\text{Eu}$ , $^{163}\text{Gd}$ , $^{158,159}\text{Pm}$ , $^{159,161}\text{Sm}$ AND $^{166}\text{Tb}$ USING A TOTAL ABSORPTION BGO DETECTOR

H. HAYASHI<sup>1</sup>, Y. AKITA<sup>1</sup>, M. SHIBATA<sup>2</sup>, T. K. SATO, A. OSA, M. ASAI,  
K. TSUKADA, T. ISHII, S. ICHIKAWA, Y. KOJIMA<sup>3</sup> and A. TANIGUCHI<sup>4</sup>

Beta decay energies ( $Q_{\beta}$ -values) are one of the fundamental physical quantities. The experimentally deduced  $Q_{\beta}$ -values of nuclei far from the stability can verify the reliability of the mass predictions. In order to measure low yield nuclei, the total absorption BGO detector was developed. On the last issue [1], the analyzing procedure using the Fermi-Kurie plot method was reported. In this paper, the method was applied to analyze newly measured nuclides of  $^{160-165}\text{Eu}$  and  $^{163}\text{Gd}$  and preliminary reported ones of  $^{158,159}\text{Pm}$ ,  $^{159,161}\text{Sm}$  and  $^{166}\text{Tb}$  [2].

Uranium carbide ( $\text{UC}_2$ ) target containing  $670 \text{ mg/cm}^2$   $^{238}\text{U}$  was bombarded with 32 MeV proton beams with the intensity of about 200 nA. The produced Eu isotopes of interest were separated by the on-line mass separator (Tokai-ISOL). The activities were implanted into a Mylar tape, and were transported to a detection position of the total absorption BGO detector. The counting rates of  $^{165}\text{Eu}$  and  $^{164}\text{Eu}$  were obtained 4 and 15 cps, respectively. Total absorption events of approximately  $10^{5-7}$  were accumulated during a measuring period of 0.5-16 hours for  $^{160-165}\text{Eu}$  and  $^{163}\text{Gd}$  spectrum.

Figure 1 shows a Fermi-Kurie plot of  $^{165}\text{Eu}$  (an inset of the figure shows the measured spectrum). As shown by closed circles and a solid line, a  $Q_{\beta}$ -value is deduced by fitting a line to the plot in an energy region of 1000 keV below endpoint energy. The  $Q_{\beta}$ -values of  $^{160-165}\text{Eu}$ ,  $^{163}\text{Gd}$ ,  $^{158,159}\text{Pm}$ ,  $^{159,161}\text{Sm}$  and  $^{166}\text{Tb}$  are determined with uncertainties of between 60 keV and 140 keV. In Fig. 2, these measured  $Q_{\beta}$ -values are compared with the evaluated values by the AME03 [3]. The evaluated values have large uncertainties between 100 keV and 860 keV, and, the most provable values are within the uncertainties of our  $Q_{\beta}$ -values. It means that the AME03 is reliable in a mass region of  $A \sim 160$ . In the figure, the previous analyzed values by means of the conventional root plot method are also compared with the present ones. The previous values are consistent with the present ones and the precisions of this analysis are improved for the most of nuclides.

The two-neutron separation energy ( $S_{2n}$ ) is one of the sensitive parameter related to the nuclear deformations. In Fig. 3, the experimentally deduced  $S_{2n}$ 's are compared with the evaluated ones [3]. The experimental  $S_{2n}$ 's are deduced by using a following expression with experimental value of  $Q_{\beta,\text{exp}}$  and evaluated values of  $Q_{\beta,\text{eval}}$  and  $S_{2n,\text{eval}}$ :

$$S_{2n,\text{exp}}(A,Z) = Q_{\beta,\text{eval}}(Z,A-2) - Q_{\beta,\text{exp}}(Z,A) + S_{2n,\text{eval}}(Z+1,A)$$

<sup>1</sup>Graduate School of Engineering, Nagoya University

<sup>2</sup>Radioisotope Research Center, Nagoya University

<sup>3</sup>Graduate School of Engineering, Hiroshima University

<sup>4</sup>Research Reactor Institute, Kyoto University



## 2.9 PRODUCTION OF LONG-LIVED $^{186\text{m}}\text{Re}$ FOR LASER ABLATION LASER-INDUCED FLUORESCENCE SPECTROSCOPY

H. IIMURA, M. KOIZUMI, M. MIYABE, M. OHBA,  
Y. ISHIDA<sup>1</sup> and T. HORIGUCHI<sup>2</sup>

The rhenium isotopes ( $Z=75$ ) with mass number around  $A=180$  are of particular interest because these nuclei have been theoretically predicted to have axially asymmetric deformation or  $\gamma$ -softness. Mean square charge radii obtained by high-resolution laser spectroscopy are sensitive information on the deformation of nuclei. However, the laser spectroscopy of Re isotopes have not been made except stable isotopes  $^{185,187}\text{Re}$ . Radioactive isotopes have yet to be measured mainly because Re is one of refractory elements and hard to be atomized. In this experiment we use laser ablation to atomize Re sample, and then ablated atoms are irradiated by tunable dye laser for the fluorescence detection. We set long-lived  $^{186\text{m}}\text{Re}$  ( $T_{1/2}=2\times 10^5$  y) as the first candidate to be measured by using this method. So far the known production method of  $^{186\text{m}}\text{Re}$  is thermal neutron irradiation, but this can not be used for laser spectroscopy because the irradiated sample contains stable Re isotopes which mask the fluorescence from the trace amount of  $^{186\text{m}}\text{Re}$ . Thus we use  $^{186}\text{W}(p,n)$  reaction to produce  $^{186\text{m}}\text{Re}$ . As the first step of the experiment we have estimated the production yield of  $^{186\text{m}}\text{Re}$ .

A 98.2%-enriched  $^{186}\text{W}$  powder was used as a target. It was pressed into a disk-shaped pellet with a thickness of  $650\text{ mg/cm}^2$ . The target was irradiated with 13.0 MeV protons at a beam current of approximately  $0.8\text{ }\mu\text{A}$ . The irradiation continued for a period of 20 h. After ten months decay period, gamma-ray measurements were carried out with a Ge detector. Due to extremely long half-life of  $^{186\text{m}}\text{Re}$ ,  $\gamma$ -rays in the decay of this nuclide could not be detected. Accordingly the production yield of  $^{186\text{m}}\text{Re}$  was estimated from that of  $^{184\text{m}}\text{Re}$  (165 d), which was produced simultaneously from  $^{184}\text{W}$  contained in the target with 1.7%. From the intensity of 105-keV isomeric transition in  $^{184\text{m}}\text{Re}$ , the yield of  $^{184\text{m}}\text{Re}$  after the irradiation was calculated to be  $1\times 10^9$  atoms. Since  $^{186\text{m}}\text{Re}$  has the same spin as  $^{184\text{m}}\text{Re}$  ( $J=8$ ), it could be assumed that the cross sections for the formation (p,n) reaction are roughly the same for both nuclides. Thus we obtained the yield of  $^{186\text{m}}\text{Re}$  as about  $7\times 10^{10}$  atoms, which corresponds to 1 ppb in the host  $^{186}\text{W}$ .

In order to do laser spectroscopy with this yield we are now improving the sensitivity of our set up for laser ablation laser-induced fluorescence spectroscopy. We found that the velocity of ablated atoms is about 300 m/s in 0.5 Torr Ar, which is more than one order of magnitude slower than in vacuum. It means that the laser beam can illuminate the atoms for long time and that each atom can be made to fluoresce many times. As a result the sensitivity can be much increased. By using this technique the laser spectroscopy of  $^{186\text{m}}\text{Re}$  is in progress.

---

<sup>1</sup>Institute for Physical and Chemical Research, RIKEN

<sup>2</sup>Hiroshima International University

## 2.10 IN-BEAM $\gamma$ -RAY SPECTROSCOPY FOR NEUTRON-RICH W ISOTOPES

T. SHIZUMA, T. HAYAKAWA, T. ISHII, H. MAKII, S. SHIGEMATSU<sup>1</sup>, M. MATSUDA, E.IDEGUCHI<sup>2</sup>, Y. ZHENG<sup>2</sup>, M. LIU<sup>2</sup>, T. MORIKAWA<sup>3</sup> and M. FUJIWARA<sup>4</sup>

Nuclei around the  $A = 180$  region are characterized by many high- $\Omega$  orbitals close to both the proton and neutron Fermi surfaces. High- $K(= \sum \Omega)$  multi-quasiparticle states formed by stretched coupling of these high- $\Omega$  quasiparticles compete with collectively excited states near the yrast line. Transitions depopulating such states often require large  $K$  changes, low transition energies, parity change, or combination of these, resulting in the initial state to be an isomer with a comparatively long half-life. However, high-spin studies of the heavier W nuclei have been limited due to inaccessibility by fusion-evaporation reactions with combination of stable projectile and target material. In order to populate excited states of these nuclei, we employed neutron transfer reactions induced by an  $^{18}\text{O}$  beam.

Excited states in neutron-rich  $^{187,188}\text{W}$  nuclei were populated by multi-nucleon transfer reactions using a 180-MeV  $^{18}\text{O}$  beam incident on a  $^{186}\text{W}$  target. In-beam  $\gamma$ -rays were measured by seven Ge detectors in coincidence with outgoing ions detected with four sets of Si  $\Delta E$ - $E$  detectors. An energy spectrum of  $\gamma$  rays in coincidence with  $^{16}\text{O}$  ions is shown in Fig. 1. The lowest two transitions in the ground state band of  $^{188}\text{W}$  produced by two-neutron transfer from the target nucleus can be seen. Transitions for  $^{186}\text{W}$  and  $^{187}\text{W}$  are also observed in this spectrum. Excited states of these nuclei were populated by two- or one-neutron evaporation following the two-neutron transfer. In the present study, the ground state band in  $^{188}\text{W}$  was extended up to spin  $(10) \hbar$ , and the  $K^\pi = 2^+$   $\gamma$  band was observed for the first time. The further analysis is in progress.

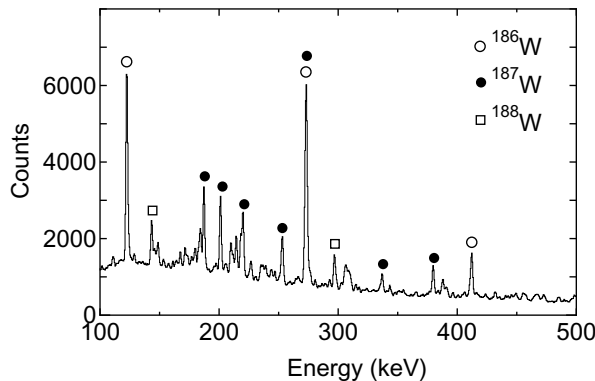


Fig. 1. An energy spectrum of  $\gamma$  rays in coincidence with  $^{16}\text{O}$  ions detected by Si  $\Delta E$ - $E$  detectors.

<sup>1</sup>Tokyo Institute of Technology

<sup>2</sup>University of Tokyo

<sup>3</sup>Kyushu University

<sup>4</sup>Osaka University



## 2. 11 DEVELOPMENT OF RI ION TRAP SYSTEM

H. MAKII, T. ISHII, S. ICHIKAWA, T. SATO and A. OSA

The low-energy low-emittance pulsed radioactive nuclear beam (RNB) is useful for the measurements of fundamental properties of nucleus such as binding energy, charge radius, and magnetization distribution with high accuracy. Construction of a new beam line and an RF linear ion trap for deceleration, bunching, and emittance improvement of RNB is now in progress at a beam line of an isotope separator on-line (ISOL). The overview of the beam line and the trap system is shown in Fig. 1. By adjusting the Einzel Lens, 10 deg. Deflector, Triplet Q-Lens, and X-Y Deflector, the continuous ion beam from an ISOL is transported to the trap. A schematic view of the trap is shown in Fig. 2. The trap is placed on a high-voltage platform as shown in Fig. 1. The transported ions are electrostatically decelerated and injected into the trap, which is filled with a buffer gas. The trap system consists of four segmented rods which provide transverse and longitudinal confinement by an oscillating electric quadrupole field and DC electric field along the axis of the system, respectively. Ions entering the trap system lose their energy due to the collision with the buffer gas, and then the cooled ions are released as bunches [1].

First on-line test was carried out using stable  $^{24}\text{Mg}^+$  and unstable  $^{25}\text{Na}^+$  ( $t_{1/2} = 59.1$  s) beams provided by the ISOL. The beam energies from the ISOL were 21 keV. Using stable  $^{24}\text{Mg}^+$  beam we determine the transmission efficiency of the trap system between the two Faraday cups. The first Faraday cup was located on a movable feed through in front of the trap and second one on a similar feed through after the trap. A current about 5.6 nA at the first Faraday cup decreased to be about 2.0 nA at the second Faraday cup. Consequently, the transmission efficiency of the trap was 36 %. To examine the trap system we stopped  $^{25}\text{Na}^+$  radioactive beam into an Al foil placed on the exit of the trap system and measured  $\gamma$ -rays emitted by daughter nuclei  $^{25}\text{Mg}$  with a Ge detector. The results are shown in Fig. 3. With the condition of the high voltage potential (HV) = 0 kV and the oscillating electric quadrupole field (RF) = 0 V<sub>p-p</sub>, the  $\gamma$ -rays emitted by the decay of  $^{25}\text{Na}$  (390 keV) was clearly observed as seen in Fig. 3(a). With the condition of HV = 19 kV and RF = 0 V<sub>p-p</sub>, the  $\gamma$ -ray peak disappeared as shown in Fig. 3(b). This is because the divergence of the beam increases with reduction of kinetic energy and beam loss occurs in

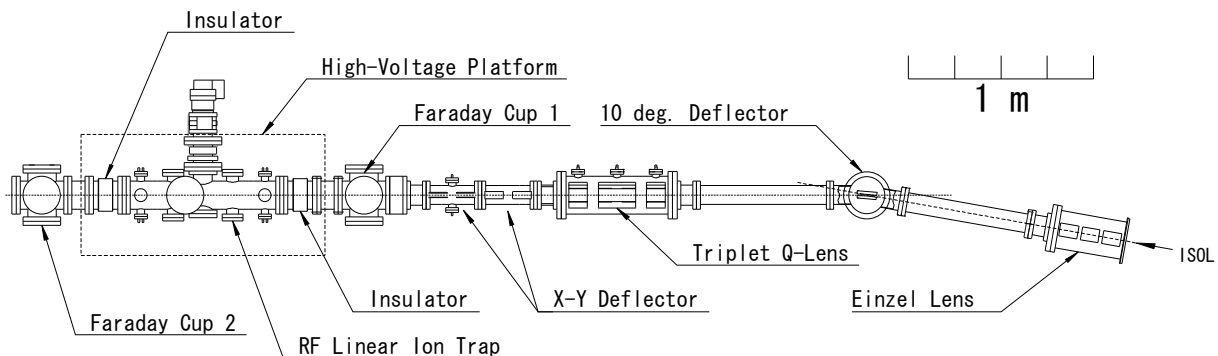


Fig. 1. Overview of new beam line and trap system.

both four segmented rods and 6 mm aperture placed inside and after the trap, respectively. By applying the RF voltages to the segmented rods the radial confinement of the beam in the trap was achieved, and therefore about a half of the  $^{25}\text{Na}^+$  beam reached the Al foil through the trap system as shown in Fig. 3(c).

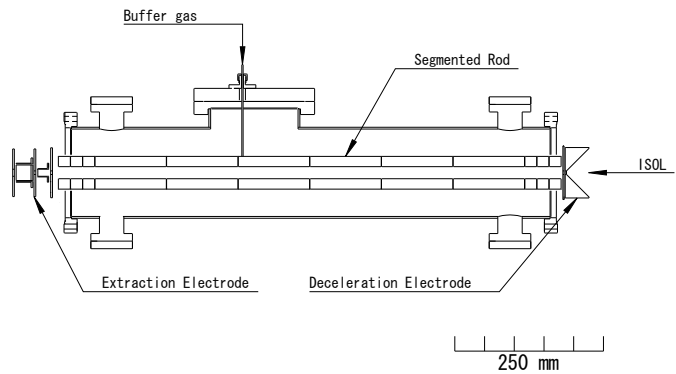


Fig. 2. Schematic view of the trap.

From the result of this on-line test, it is proved that our new trap system has enough capability to transport the RNB from the on-line mass separator ISOL to the exit of the trap. In the near future, we will examine a number of systematic investigations of the trap system to deceleration, bunching, and emittance improvement of the continuous ion beam from the ISOL.

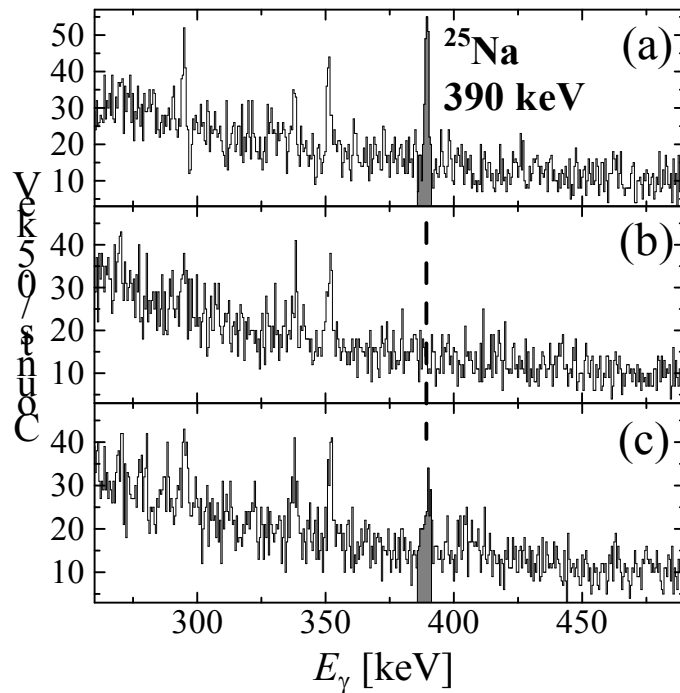


Fig. 3.  $\gamma$ -ray spectra taken by Ge detector. The spectra (a), (b), and (c) are obtained setting HV = 0 kV and RF = 0 V<sub>p-p</sub>, HV = 19 kV and RF = 0 V<sub>p-p</sub>, and HV = 19 kV and RF = 155 V<sub>p-p</sub>, respectively.

**References**

[1] F. Herfurth, J. Dilling, A. Kellerbauer, G. Bollen, S. Henry, H.-J. Kluge, E. Lamour, D. Lunney, R.B. Moore, C. Scheidenberger, S. Schwarz, G. Sikler, J. Szerypo, Nucl. Instr. and Meth. **A 469** (2001) 254.

## 2.12 GAMMA-RAYS IN THE GROUND-STATE BAND OF $^{250}\text{Cm}$

T. ISHII, S. SHIGEMATSU<sup>1</sup>, H. MAKII, M. ASAI, K. TSUKADA, A. TOYOSHIMA, M. MATSUDA, A. MAKISHIMA<sup>2</sup>, T. SHIZUMA, J. KANEKO<sup>1</sup>, I. HOSSAIN<sup>3</sup>, H. TOUME<sup>4</sup>, M. OHARA<sup>1</sup>, S. ICHIKAWA, T. KOHNO<sup>1</sup> and M. OGAWA<sup>1</sup>

We have measured in-beam  $\gamma$  rays in the neutron-rich transuranium nucleus  $^{250}_{96}\text{Cm}_{154}$  produced by the two-neutron transfer reaction of a 162-MeV  $^{18}\text{O}$  beam with a  $^{248}\text{Cm}$  target. Outgoing nuclei were detected using four sets of Si  $\Delta E$ - $E$  detectors placed at the grazing angle, and  $\gamma$  rays emitted by residual nuclei were measured using six Ge detectors in coincidence with the outgoing nuclei. Fig. 1 shows a  $\gamma$ -ray spectrum of  $^{250}\text{Cm}$  obtained by setting the gate of  $^{16}\text{O}$  particles with kinetic energies corresponding to the excitation energies in  $^{250}\text{Cm}$  below the neutron separation energy. The  $\gamma$  rays shown in Fig. 1 were found to be coincident each other. Furthermore, the in-plane to out-of-plane intensity ratios of these  $\gamma$ -rays confirm that these transitions are stretched  $E2$  types. On the basis of these results, we have established the ground-state band of  $^{250}\text{Cm}$  up to  $12^+$  as shown in Fig. 2.

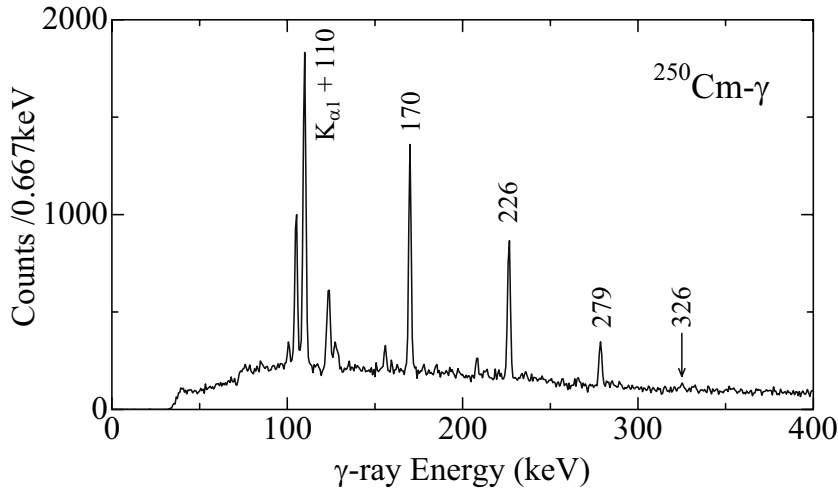


Fig. 1.  $\gamma$ -ray spectrum in coincidence with  $^{16}\text{O}$  particles whose kinetic energies correspond to the excitation energies in  $^{250}\text{Cm}$  below the neutron separation energy.  $\gamma$  peaks of  $^{250}\text{Cm}$  are labeled by energies in units of keV.

The moments of inertia  $2J_0/\hbar^2$ , which are almost the same as  $6/E_{2^+}$ , are plotted versus neutron number in Fig. 3, for the ground-state bands of even-even actinide nuclei whose excitation energies were measured precisely. In the region of well-deformed nuclei, a nucleus with a deformed shell closure is expected to have a larger moment of inertia than those of neighboring nuclei, because the pairing energy gap becomes smaller at the deformed shell gap. The present result shows that the moment of inertia of  $^{248}\text{Cm}_{152}$  is larger than that of  $^{250}\text{Cm}_{154}$  by an appreciable difference of 10%. This fact supports the existence of the  $N = 152$  deformed subshell closure in Cm isotopes. A cranking model calculation by

<sup>1</sup>Tokyo Institute of Technology  
<sup>2</sup>National Defense Medical College  
<sup>3</sup>Seoul National University  
<sup>4</sup>Ibaraki University

Sobiczewski *et al.* [1] explained the systematics of the moments of inertia of actinide nuclei by taking account of higher order deformations. They have shown that the pairing energy gap has a local minimum at  $N = 152$  in Cm isotopes and predicted that the moment of inertia of  $^{248}\text{Cm}_{152}$  is larger than that of  $^{250}\text{Cm}_{154}$ , in agreement with our experimental result.

This experiment is the first in-beam  $\gamma$ -ray study beyond  $N = 152$ , which became possible by using a small-emittance beam supplied by the tandem accelerator operated at 18 MV, a small-sized thick Cm target and high-resolution Si  $\Delta E$ - $E$  detectors. This result has been published [2].

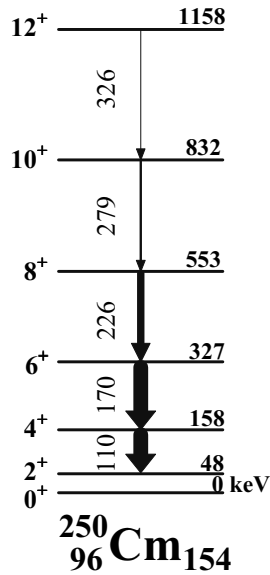


Fig. 2. Level scheme of the ground-state band of  $^{250}\text{Cm}$ . The energy of the  $2^+$  level was derived from the moment of inertia deduced from the higher levels.

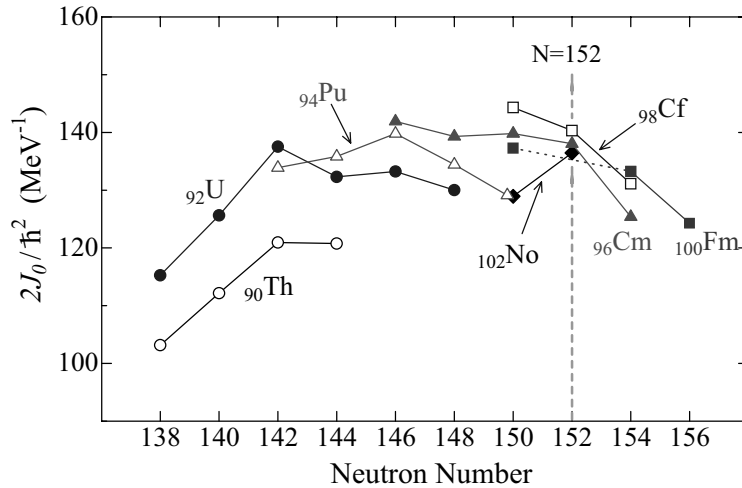


Fig. 3. Systematics of moments of inertia,  $2J_0/\hbar^2$ , for ground-state bands of even-even actinide nuclei. Because there are no accurate measurements for the moment of inertia of  $^{252}\text{Fm}_{152}$ , the data for  $^{250}\text{Fm}$  and  $^{254}\text{Fm}$  are connected by a dotted line.

### References

- [1] A. Sobiczewski, I. Muntian and Z. Patyk, Phys. Rev. C **63** (2001) 034306.
- [2] T. Ishii *et al.*, J. Phys. Soc. Jpn **75** (2006) 043201.

### 2.13 ALPHA-GAMMA COINCIDENCE SPECTROSCOPY OF $^{255}\text{No}$

M. ASAI, K. TSUKADA, H. HABA<sup>1</sup>, A. TOYOSHIMA, T. ISHII, Y. NAGAME,  
I. NISHINAKA, T. ICHIKAWA, Y. KOJIMA<sup>2</sup> and K. SUEKI<sup>3</sup>

Excited states in  $^{251}\text{Fm}$  fed by the  $\alpha$  decay of  $^{255}\text{No}$  have been studied by means of  $\alpha$ - $\gamma$  coincidence spectroscopy to establish Nilsson single-particle states in odd-mass superheavy nuclei. The nucleus  $^{255}\text{No}$  was produced by the  $^{248}\text{Cm}(^{12}\text{C}, 5n)$  reaction. The beam energy was 77 MeV on target. Reaction products were transported by a He jet into a rotating wheel  $\alpha$ - $\gamma$  detection system, and deposited on a thin foil forty of which were set on the wheel [1]. The wheel periodically rotated at 180 s intervals, and moved the deposited sources to two consecutive detector stations each of which were equipped with two Si detectors and two Ge detectors.

Figure 1 shows  $\gamma$ -ray spectra in coincidence with  $\alpha$  particles of  $^{255}\text{No}$ . The time window was set at  $-100$ – $+500$  ns from the prompt peak for the prompt coincidence spectrum and at  $0.5$ – $47.5$   $\mu\text{s}$  for the delayed one. On the basis of the  $\alpha$ - $\gamma$  coincidence relationships, the decay scheme of  $^{255}\text{No}$  has been established as shown in Fig. 2. The 200.09 keV level was found to be an isomeric state whose half-life was determined to be  $21.1(19)$   $\mu\text{s}$ . From the K X to  $\gamma$  intensity ratio, the K internal conversion coefficient of  $\alpha_K = 16.7(27)$  was derived for the 200.09 keV transition, which allows us to assign the  $M2$  multipolarity to that transition.

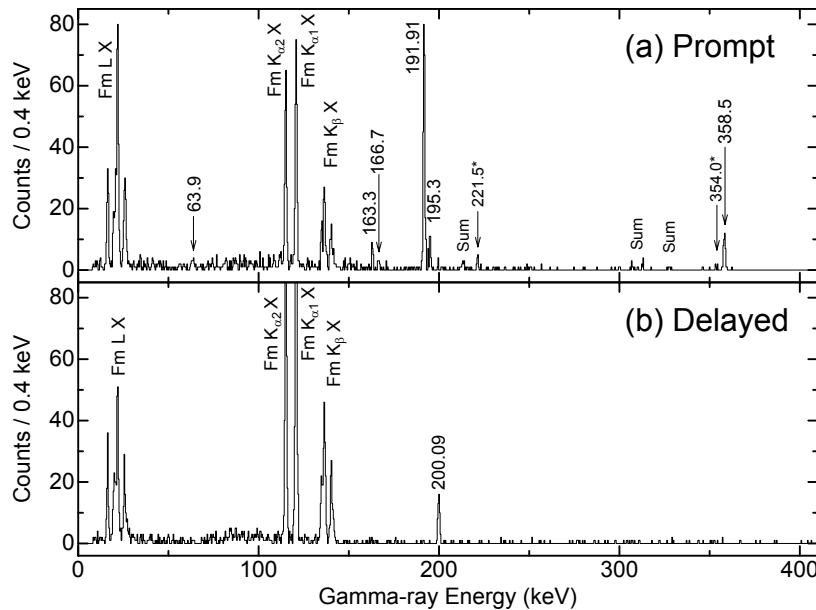


Fig. 1. Gamma-ray spectra in coincidence with  $\alpha$  particles of  $^{255}\text{No}$ . (a) The prompt coincidence spectrum obtained by setting the time window at  $-100$ – $+500$  ns from the prompt peak. (b) The delayed one obtained by setting the window at  $0.5$ – $47.5$   $\mu\text{s}$ . For assignments of the 221.5 and 354.0 keV  $\gamma$  rays, see a forthcoming paper.

<sup>1</sup>Nishina Center for Accelerator Based Science, RIKEN

<sup>2</sup>Graduate School of Engineering, Hiroshima University

<sup>3</sup>Department of Chemistry, University of Tsukuba

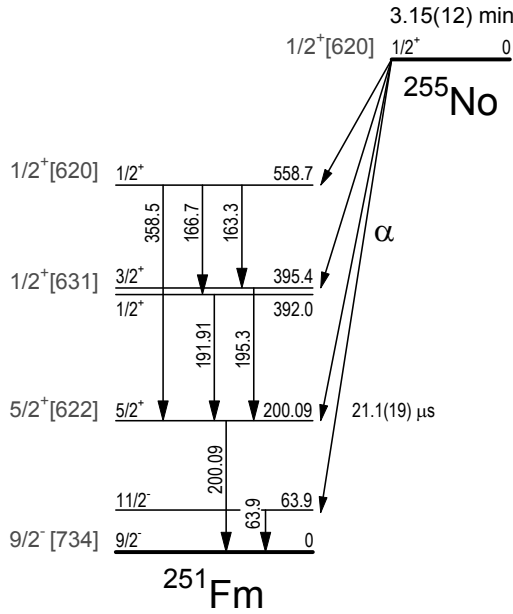


Fig. 2. Proposed decay scheme of  $^{255}\text{No}$ .

This isomeric state was previously reported by Bemis *et al.* [2] at 192 keV and with a 15.2(23)  $\mu\text{s}$  half-life; these values were derived from the  $\alpha$  fine structure measurement and the  $\alpha$ -X( $\gamma$ ) coincidence one. Very recently, Heßberger *et al.* [3] reported the  $\alpha$ - $\gamma$  coincidence results for  $^{255}\text{No}$ . Their half-life and energy of the isomeric state agree well with our data.

The ground state of  $^{251}\text{Fm}$  is known to have the  $9/2^-$  [734] configuration [4]. On the basis of the ground-state spin-parity of  $^{251}\text{Fm}$ , multiplicities of  $\gamma$  transitions derived from K X to  $\gamma$  intensity ratios, hindrance factors of  $\alpha$  transitions, and analogy of rotational band energies in neighboring nuclei, spin-parities and single-particle configurations of excited states in  $^{251}\text{Fm}$  as well as the ground state of  $^{255}\text{No}$  are suggested as shown in Fig. 2. The 392.0 and 395.4 keV levels are assigned as the  $1/2^+$  and  $3/2^+$  members of the  $1/2^+$  [631] band. These two levels were not resolved in Ref. [2], and were misassigned as the  $7/2^+$  [613] bandhead. The  $1/2^+$  [620] state populated by the favored  $\alpha$  transition is located at 558.7 keV.

The energy spacing between the  $9/2^-$  [734] orbital and the  $1/2^+$  [620] one in  $N = 151$  isotones reflects the deformed shell gap at  $N = 152$ . This energy increases with the proton number from  $Z = 96$  to 102, indicating that the  $N = 152$  deformed shell gap increases with the proton number at least up to  $Z = 102$ .

## References

- [1] M. Asai, K. Tsukada, M. Sakama, S. Ichikawa, T. Ishii, Y. Nagame, I. Nishinaka, K. Akiyama, A. Osa, Y. Oura, K. Sueki and M. Shibata, *Phys. Rev. Lett.* **95** (2005) 102502.
- [2] C. E. Bemis, Jr., D. C. Hensley, P. F. Dittner, C. D. Goodman and R. J. Silva, *ORNL-4706* (1971) 62.
- [3] F. P. Heßberger, S. Hofmann, D. Ackermann, S. Antalic, I. Kojouharov, P. Kuusiniemi, R. Mann, K. Nishio, S. Saro, B. Streicher, B. Sulignano and M. Venhart, *GSI Report 2005-1* (2005) 73.
- [4] I. Ahmad, J. Milsted, R. K. Sjoblom, J. Lerner and P. R. Fields, *Phys. Rev. C* **8** (1973) 737.

## CHAPTER 3

### Nuclear Reactions

- 3.1 Measurement of the Cross Section in the  $^{12}\text{B}(\alpha, n)^{15}\text{N}$  Reaction
- 3.2 Study of the Neutron Transfer Reaction with Medium Mass Nucleus in Inverse Kinematics
- 3.3 Correlation between Fission and  $\alpha$ -particle Emission in the  $^{18}\text{O} + ^{244}\text{Pu}$  Reaction
- 3.4 Measurement of Fission Cross Sections for  $^{30}\text{Si} + ^{238}\text{U}$
- 3.5 Barrier Distribution of Quasi-elastic Backward Scattering of  $^{70}\text{Zn}$  on  $^{208}\text{Pb}$  and  $^{209}\text{Bi}$





### 3.1 MEASUREMENT OF THE CROSS SECTION IN THE $^{12}\text{B}(\alpha, n)^{15}\text{N}$ REACTION

H. ISHIYAMA<sup>1</sup>, T. ISHIKAWA<sup>2</sup>, H. MIYATAKE<sup>1</sup>, Y.X. WATANABE<sup>1</sup>, Y. HIRAYAMA<sup>1</sup>,  
 N. IMAI<sup>1</sup>, M.H. TANAKA<sup>1</sup>, Y. FUCHI<sup>1</sup>, N. YOSHIKAWA<sup>1</sup>, S.C. JEONG<sup>1</sup>, H. KAWAKAMI<sup>1</sup>, I.  
 KATAYAMA<sup>1</sup>, T. NOMURA<sup>1</sup>, T. HASHIMOTO, S. MITSUOKA, K. NISHIO,  
 M. MATSUDA, S. ICHIKAWA, H. IKEZOE, S.K. DAS<sup>3</sup>, Y. MIZOI<sup>3</sup>, P.K. SAHA<sup>3</sup>,  
 T. FUKUDA<sup>3</sup>, K. NAKAI<sup>2</sup> and T. SHIMODA<sup>4</sup>

The  $(\alpha, n)$  reactions on light neutron-rich radioactive ( $Z < 10$ ) nuclei play important roles at the early stage of rapid-neutron (r-) process in neutron-rich environment, for example, a ‘hot-bubble’ formed in supernovae [1]. A systematic study for astrophysical reaction rates of  $(\alpha, n)$  reactions using low-energy ( $E = 1\text{-}2$  MeV/u) radioactive nuclear beams (RNB) [2, 3] is in progress at the tandem facility of JAEA. The excitation function of the  $^{12}\text{B}(\alpha, n)^{15}\text{N}$  reaction has been measured in the energy region of  $E_{\text{cm}} = 1.1 - 3.6$  MeV.

The  $^{12}\text{B}$  beam produced via the  $d(^{11}\text{B}, ^{12}\text{B})p$  reaction was separated from the primary  $^{11}\text{B}$  beam with a recoil mass separator (RMS). The typical intensity and purity of the  $^{12}\text{B}$  beam were 7.8 kpps and 98%, respectively. A detector system consists of a ‘Multi-Sampling and Tracking Proportional Chamber’ (MSTPC) and a neutron detector array. The MSTPC has high detection efficiency of almost 100%, and can measure three-dimensional tracks of charged particles as well as the energy losses along their trajectories. The MSTPC is surrounded by a neutron detector array, which consists of 28 pieces of BC408 plastic scintillators covering 31.4% solid angle of  $4\pi$ . (See the reference [2] for more details of our experimental setup.) The  $^{12}\text{B}$  beam was injected into the MSTPC filled with the gas of He + CO<sub>2</sub> (10%), which works as counter gas and a gas target. The gas pressure was set to be 18.7 kPa so as to cover the energy region of  $E_{\text{cm}} = 1.0 - 3.7$  MeV. When a nuclear reaction takes place inside the MSTPC, the energy loss ( $dE/dx$ ) changes largely due to the change of the relevant atomic numbers. Therefore, the reaction position can be determined by detecting a ‘sudden’  $dE/dx$  change ( $\Delta E$ ), and the reaction energy can be evaluated by summing up the energy losses inside the MSTPC. In order to select reaction events, the energy loss difference ( $\Delta E$ ) was set to be 80 keV. The reaction event thus selected was checked with the kinematical conditions by using all information on its reaction energy, scattering angle and the energy of ejected nuclei and neutron.

<sup>1</sup> Institute of Particle and Nuclear Studies, KEK

<sup>2</sup> Tokyo University of Sciences

<sup>3</sup> Osaka Electro-Communication University

<sup>4</sup> Osaka University

Fig. 1 shows the measured excitation function of the  $^{12}\text{B}(\alpha, n)^{15}\text{N}$  reaction. The present experiment provides the first data of the  $^{12}\text{B}(\alpha, n)^{15}\text{N}$  reaction-cross sections and the measured-energy region covers almost all of Gamow peaks from  $T_9 = 2$  to 5. The solid line in Fig. 1 indicates a theoretical estimate evaluated by a ‘black-body model’ of Fowler and Hoyle [4]. Although their model is simple, the estimate reproduces well the present result. At  $E_{\text{cm}} = 1.4 - 1.5$  MeV, there exists a resonance-like structure, whose peak value is 4 times larger than the one from the theoretical estimate. The astrophysical reaction rate of the  $^{12}\text{B}(\alpha, n)^{15}\text{N}$  reaction can be derived from our result.

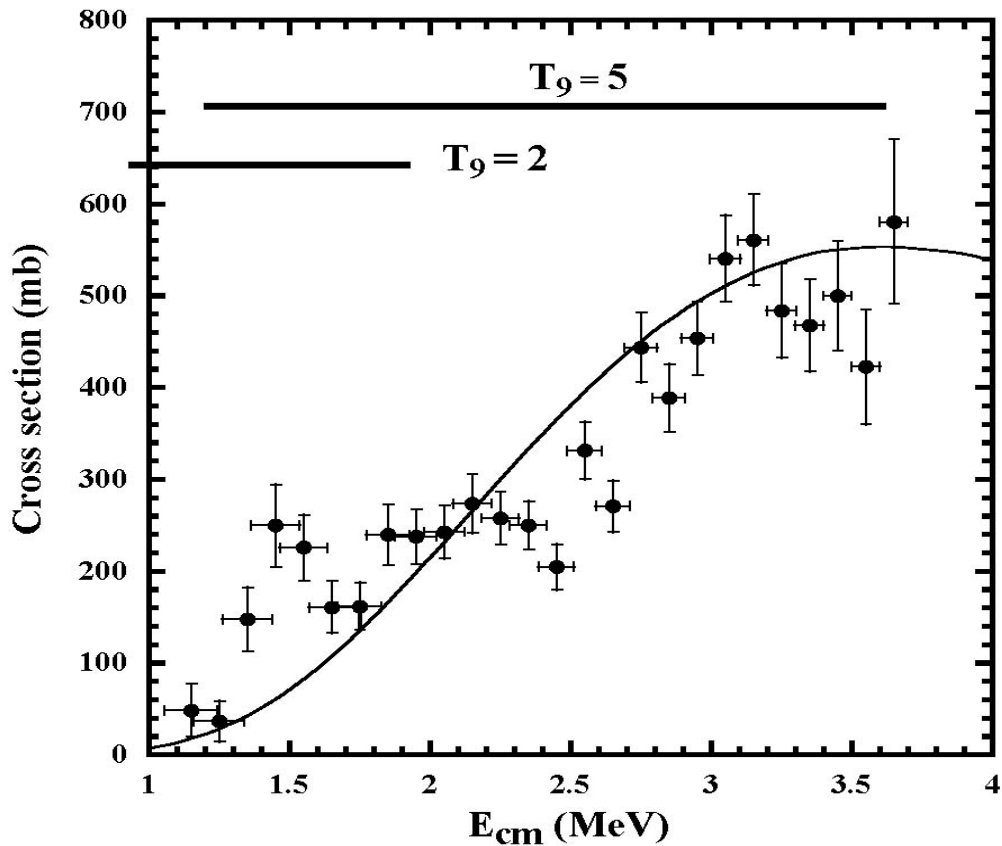


Fig. 1. Excitation function of the  $^{12}\text{B}(\alpha, n)^{15}\text{N}$  reaction.

**References**

- [1] M. Terasawa, et al., Nucl. Phys. **A688**(2001)581c.
- [2] T. Hashimoto, et al, Nucl. Instrum. Methods. **A556**(2006)339.
- [3] H. Ishiyama, et al., Nucl. Instrum. Methods. **A560**(2006)366.
- [4] W. A. Fowler and F. Hoyle, Astrophys. J. Supp. **91**(1964)201.

### 3.2 STUDY OF THE NEUTRON TRANSFER REACTION WITH MEDIUM MASS NUCLEUS IN INVERSE KINEMATICS

N. IMAI<sup>1</sup>, K. H. TSHOO<sup>2</sup>, S.C. JEONG<sup>1</sup>, H. BHANG<sup>2</sup>, S. CHOI<sup>2</sup>, J.H. HA<sup>3</sup>,  
T. HASHIMOTO, Y. HIRAYAMA<sup>1</sup>, T. ISHII, H. ISHIYAMA<sup>1</sup>, Y.K. KIM<sup>3</sup>,  
S. MITSUOKA, H. MIYATAKE<sup>1</sup>, K. NISHIO, Y.M. OH<sup>2</sup>, S.H. PARK<sup>3</sup>,  
J.S. SONG<sup>2</sup> and Y.X. WATANABE<sup>1</sup>

Once radioactive nuclear beams of around 5MeV/nucleon are available at TRIAC, we intend to study neutron capture reaction rates of around the doubly magic neutron-rich nucleus <sup>132</sup>Sn. The rates are the key reactions which play important roles to determine the path of r-process in nucleosynthesis of heavy elements. In the case of the direct radiative neutron capture reaction, the cross section mainly depends on the final state wave function, where the neutron is transferred. The wave function can be determined by a corresponding neutron transfer reaction through a distorted-wave Born approximation analysis of its differential cross sections [1].

As a test of the experiment, we have studied the <sup>124</sup>Sn(*d,p*)<sup>125</sup>Sn\* reactions in the inverse kinematics by using CD<sub>2</sub> target and <sup>124</sup>Sn beams. The same reaction was recently investigated at Oak Ridge National Laboratory with the <sup>124</sup>Sn beam of 4.7MeV/nucleon [2]. Their result suffered from the background which was thought to come from reactions with the carbon included in CD<sub>2</sub>. In the present experiment, we measured the angular distributions of the cross sections of the reaction channel emitting protons with two targets, CD<sub>2</sub> and carbon. Through the comparison of the energy spectra of protons with the two different targets, the amount of the background attributed to carbon will be determined quantitatively.

The experiment was performed at the JAEA tandem accelerator facility. The <sup>124</sup>Sn<sup>15+</sup> beams were accelerated up to 3.7 MeV/nucleon by the tandem accelerator and the super conducting booster linac. The typical beam intensity was 50 epA (10<sup>7</sup> pps). The thicknesses of CD<sub>2</sub> and carbon targets were 250 μg/cm<sup>2</sup> and 50 μg/cm<sup>2</sup>, respectively. A schematic drawing of the experimental setup is shown in Fig.1. Two SSD telescopes of 50x50 mm<sup>2</sup> were mounted to detect recoiled particles. The angular regions covered by the telescopes were from 37.4 to 82.6 degrees and from 97.4 to 142.6 degrees in the laboratory frame, respectively. The forward telescope consisted of 0.3 mm-thick SSD and 16x16-channels doubly sided striped SSD of 1mm-thickness, while the backward telescope was composed of 16-channels singly sided striped SSD of 65 μm-thickness and 0.3 mm thick SSD. In addition to the telescopes, we placed an annular type SSD of 0.3 mm thickness, which was divided to 10 strips along radial axis. This detector covered the angular region from 151.6 to 167.0 degrees. We also put a SSD of 15x15mm<sup>2</sup> at 20 degrees to monitor carbons recoiled by the elastic scattering.

---

<sup>1</sup> High Energy Accelerator Research Organization (KEK)

<sup>2</sup> Seoul National University

<sup>3</sup> Korean Energy Atomic Research Institute

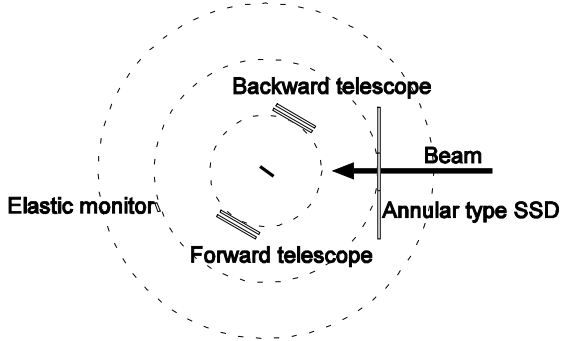


Fig. 1. A schematic view of the experimental setup.

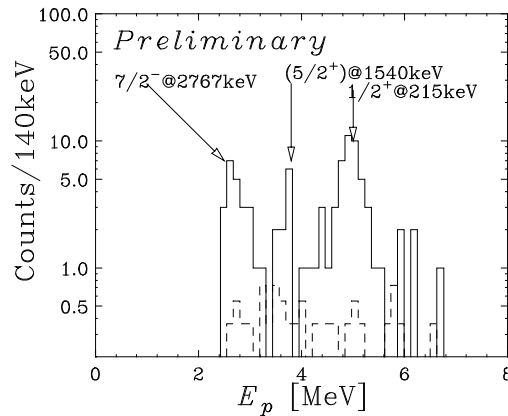


Fig. 2. Proton energy spectra measured by a strip of the backward telescope. See the text for details.

A solid line in Fig. 2 shows the proton energy spectrum measured by a strip of the backward telescope with the  $\text{CD}_2$  target, while a dashed line indicates the spectrum with the carbon target normalized by the number of the elastic scattering of carbon. It is clearly seen that energy spectrum is almost free from the background observed in Ref. [2]. This may be due to the difference of the incident energy. Further experiment to check the incident-energy dependence of the background will be performed within this year. In addition, the neutron capture reaction rate of  $^{124}\text{Sn}(n,\gamma)^{125}\text{Sn}^*$  will be estimated through the DWBA analysis of the measured angular distribution of  $^{124}\text{Sn}(d,p)^{125}\text{Sn}^*$ .

## References

- [1] N. Imai, N. Aoi, S. Kubono, D. Beaumel, X. Liu, K. Abe, K. Kumagai, H. Ohnuma, S. Kato, Y. Fuchi, P. Strasser, M. Kurokawa, H. Sakurai, T. Kubo, and M. Ishihara, *Nuclear Physics* **A688** (2001) 281.
- [2] K.L. Jones, R.L. Kozub, C. Baktash, D.W. Bardayan, J.C. Blackmon, W.N. Catford, J.A. Cizewski, R.P. Fitzgerald, M.S. Johnson, R.J. Livesay, Z. Ma, C.D. Nasaraja, D. Shapira, M.S. Smith, J.S. Thomas, and D.W. Visser, *Phys. Rev.* **C70** (2004) 067602.

### 3.3 CORRELATION BETWEEN FISSION AND $\alpha$ -PARTICLE EMISSION IN THE $^{18}\text{O} + ^{244}\text{Pu}$ REACTION

I. NISHINAKA, M. TANIKAWA<sup>1</sup>, Y. NAGAME, M. ASAI, K. TSUKADA,  
A. TOYOSHIMA, T. ICHIKAWA and A. YOKOYAMA<sup>2</sup>

Nuclear fission of heavy actinides shows anomalous properties with regard to mass and total kinetic energy  $E_k$  distributions. A drastic change to highly symmetric mass distributions with high  $E_k$  has been observed for the spontaneous fission of  $^{258}\text{Fm}$  [1, 2]. Thermal neutron induced fission of  $^{257}\text{Fm}$  produces both components of symmetric mass division with higher  $E_k$  and asymmetric one with lower  $E_k$  [3]. Excitation energy dependence of mass and  $E_k$  distributions provides information on the potential energy surface in deformation to fission. However, experiments are limited to available targets. The excitation energy dependence of competition of symmetric and asymmetric mass divisions for  $^{258}\text{Fm}$  could be studied via the incomplete fusion-fission reaction of  $^{244}\text{Pu}(^{18}\text{O},\alpha)^{258}\text{Fm}$ . The process of fission accompanied by  $\alpha$ -particle emission in heavy ion reactions is not yet completely understood. In this work, correlation between fission and  $\alpha$ -particle emission in the  $^{18}\text{O} + ^{244}\text{Pu}$  reaction has been studied experimentally. Probabilities of  $^{244}\text{Pu}(^{18}\text{O}, \alpha)^{258}\text{Fm}$  have been obtained.

Light charged particles including  $\alpha$ -particle were measured in coincident with fission fragments for the reaction  $^{18}\text{O} + ^{244}\text{Pu}$  at incident energies of 103 and 113 MeV. The  $^{244}\text{PuCl}_4$  target with thickness of  $62 \mu\text{g}/\text{cm}^2$  prepared by electrodeposition on Ni backing foil with thickness of  $89 \mu\text{g}/\text{cm}^2$  was bombarded with  $^{18}\text{O}$  beams from JAEA tandem accelerator. Light charged particles were detected with a  $\Delta E$ - $E$  telescope consisting of  $30 \mu\text{m}$  and  $2 \text{ mm}$  silicon surface barrier detectors set at  $20 \text{ deg.}$  to the beam direction. The  $\Delta E$ - $E$  telescope has a solid angle of  $0.12 \text{ msr.}$  The aluminum absorber of  $5.4 \text{ mg}/\text{cm}^2$  thickness was located in front of the  $\Delta E$  detector. Two position sensitive parallel plate avalanche counters to detect fission fragments were set at a distance of  $215 \text{ mm}$  from the target with angular ranges of  $75 - 155 \text{ deg.}$  and  $255 - 335 \text{ deg.}$ , respectively, in the reaction plane. The active area of each detector is  $(200 + 200) \times 80 \text{ mm}^2$ .

Figure 1 shows the  $\alpha$ -particle spectra measured in coincident with fission fragments in the center-of-mass system. The minimum detectable energy was  $7 \text{ MeV}$  due to the aluminum absorber. The  $\alpha$ -particle energy spectrum emitted from the compound nucleus was calculated with the statistical model code PACE2 [4] and is represented in Fig. 1(a) by dashed curve plotted in arbitrary unit. The calculated spectrum rapidly decreases with increasing energy compared with the experimental one. Thus the high energy component of  $\alpha$ -particle spectrum

---

<sup>1</sup>University of Tokyo

<sup>2</sup>Kanazawa University

does not originate from evaporation from the compound nucleus. In addition to that, the maximum energies of  $\alpha$ -particles approximately agree with the maximum energies deduced from the Q-value of preequilibrium  $\alpha$ -particle emission for  $^{244}\text{Pu}(^{18}\text{O}, \alpha)^{258}\text{Fm}$  and incident beam energies, as indicated by arrows in Fig. 1. The measured  $\alpha$ -particle spectra suggest that the preequilibrium  $\alpha$ -particle emission in the incomplete fusion-fission reaction play an important rule in the  $^{18}\text{O} + ^{244}\text{Pu}$  reaction. Fission properties of  $^{258}\text{Fm}$  at higher excitation energies will be studied in the incomplete fusion-fission reaction of  $^{244}\text{Pu}(^{18}\text{O}, \alpha)^{258}\text{Fm}$ .

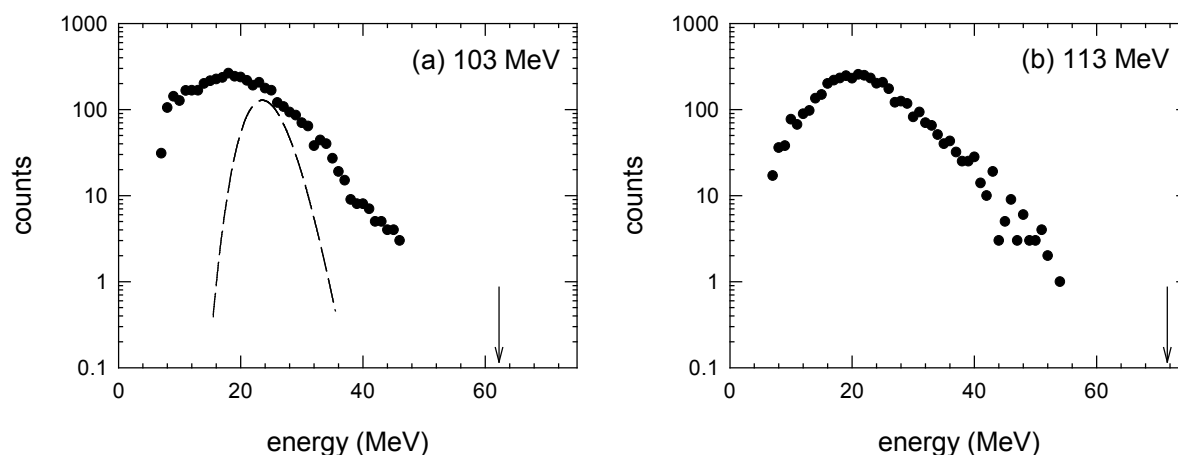


Fig.1. Energy spectra of  $\alpha$ -particles measured at 20 deg. to the beam direction in coincident with fission fragments in the  $^{18}\text{O} + ^{244}\text{Pu}$  reactions: (a) 103 MeV and (b) 113 MeV.

## References

- [1] D. C. Hoffman, J. B. Wilhelmy, J. Weber, W. R. Daniels, E. K. Hulet, R. W. Lougheed, J. H. Landrum, J. F. Wild, and R. J. Dupzyk, *Phys. Rev.* **C21** (1980) 972.
- [2] E. K. Hulet, R. W. Lougheed, J. H. Landrum, J. F. Wild, D. C. Hoffman, J. Weber, and J. B. Wilhelmy, *Phys. Rev.* **C21** (1980) 966.
- [3] W. John, E. K. Hulet, R. W. Lougheed, and J. J. Wesolowski, *Phys. Rev. Lett.* **27**(1971)45.
- [4] A. Gavron, revised version of the code PACE; see *Phys. Rev.* **C21** (1980) 230.

### 3.4 MEASUREMENT OF FISSION CROSS SECTIONS FOR $^{30}\text{Si} + ^{238}\text{U}$

K. NISHIO, H. IKEZOE, S. MITSUOKA, K. TSURUTA, Y. NAGAME, K. TSUKADA,  
M. ASAI, I. NISHINAKA and T. OHSAWA<sup>1</sup>

Recent investigation of fusion-evaporation reactions in  $^{48}\text{Ca} + ^{238}\text{U}$ ,  $^{242,244}\text{Pu}$  [1] suggest that the measured evaporation (ER) cross sections have the highest values at the bombarding energy corresponding to the Coulomb potential that the projectile touches the equatorial face of the prolately deformed nucleus. In the sub-barrier region, where contact of the projectile is limited to the polar sides of the target nucleus, the ER cross section seems to have much smaller values than expected from a statistical model calculation which takes into account the fusion enhancement in the entrance channel, caused by the lowering of the Coulomb barrier at the polar collisions. This implies that collision at the equatorial side has an advantage in forming the compound nucleus than the polar sides. On the other hand, in the reaction using light projectile,  $^{16}\text{O} + ^{238}\text{U}$  [2], measured ER cross sections at sub-barrier energies agreed with the calculation which assumes complete fusion also in the polar collisions. These results imply that only light ion can result in complete fusion in the polar collisions, whereas the equatorial collision results in fusion even for every ion. To understand the effects of deformation on fusion, it is important to measure the fission and ER cross sections systematically by changing the projectile ions. We have started investigation on the reactions involving target nucleus  $^{238}\text{U}$ . In this report, we show the results of fission cross sections for  $^{30}\text{Si} + ^{238}\text{U}$ .

The experiment was carried out by using the  $^{30}\text{Si}$  beam supplied by the JAEA-tandem accelerator. The uranium target was made by electro-deposition on a Be-foil. Fission fragments were measured in a single mode, by using dE – E detectors consisting of an ionization chamber and three silicon surface barrier detectors. Fission fragments were detected at angles of  $90^\circ$ ,  $120^\circ$  and  $150^\circ$  relative to the beam direction. Angular dependence of the fission cross section was considered. The cross sections were determined by monitoring the elastically scattered particles and referring their cross sections. The experimental results are shown in

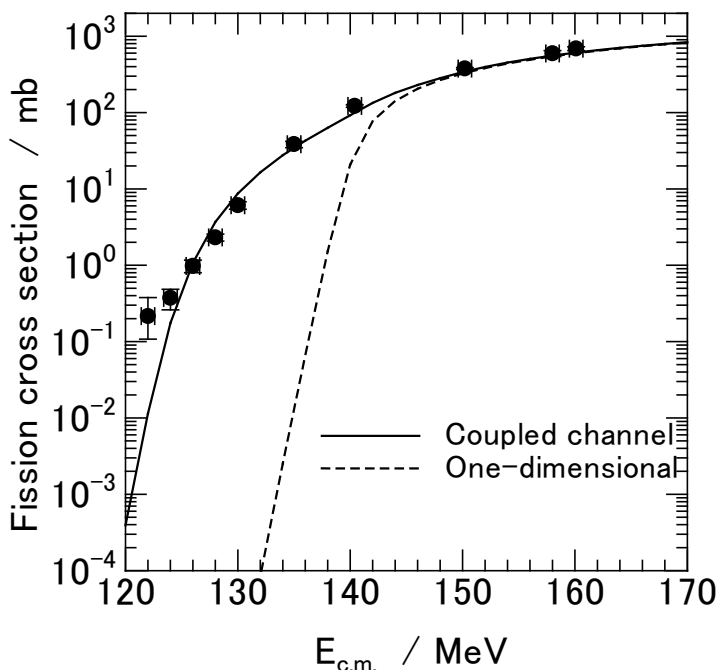


Fig. 1. Fission cross section for  $^{30}\text{Si} + ^{238}\text{U}$ .

<sup>1</sup> Kinki-University, Osaka, Japan

Fig. 1 as a function of center-of-mass energy, and are compared to a coupled channel calculation [3]. The solid curve is the result taking into account the prolate deformation of  $^{238}\text{U}$ ,  $(\beta_2, \beta_4) = (0.275, 0.05)$ . Couplings to the  $2^+$  state in  $^{30}\text{Si}$  (2.235 MeV) and  $3^-$  state in  $^{238}\text{U}$  (0.73 MeV) are also included. The dashed curve is the calculation of the one-dimensional barrier penetration model. It is found that at the sub-barrier energies the measured fission cross sections show large enhancement relative to the one-dimensional model, because of the prolate deformation of  $^{238}\text{U}$ .

## References

- [1] Yu.Ts. Oganessian *et al.*, Phys. Rev. **C69** (2004) 054607. Yu.Ts. Oganessian *et al.*, Phys. Rev. **C70** (2004) 064609.
- [2] K.Nishio *et al.*, Phys. Rev. Lett. **93** (2004) 162701.
- [3] K. Hagino (unpublished). The code is based on the CCFULL code. K.Hagino *et al.*, Computer Phys. Comm. **123** (1999) 143.



### 3.5 BARRIER DISTRIBUTION OF QUASI-ELASTIC BACKWARD SCATTERING OF $^{70}\text{Zn}$ ON $^{208}\text{Pb}$ AND $^{209}\text{Bi}$

S. MITSUOKA, H. IKEZOE, K. NISHIO, S.C. JEONG<sup>1</sup>, and Y.X. WATANABE<sup>1</sup>

The Coulomb barrier height in heavy-ion fusion reactions is an important quantity especially for the synthesis of super-heavy elements. The barrier distribution could be experimentally obtained from the first derivative of the ratio of quasi-elastic (QE) backward scattering cross section to the Rutherford cross section. We adopted this method in the reactions of  $^{70}\text{Zn}+^{208}\text{Pb}$  and  $^{70}\text{Zn}+^{209}\text{Bi}$ , relating to Pb/Bi-based cold fusion reactions for super-heavy elements 112 and 113, respectively.

A  $^{70}\text{Zn}$  beam from the tandem-booster accelerator bombarded thin strip targets of  $^{208}\text{Pb}$  and  $^{209}\text{Bi}$  with 3 mm width in horizontal plane. The QE events were detected by SSDs at the laboratory angles of 172, 168 and 162 degrees and the Rutherford scattering events were monitored at 30, 45 and 55 degrees with respect to the beam axis. The QE cross section was obtained by summing elastic, inelastic scattering and transfer yields, but excluding that of deep-inelastic scattering by using the code LINDA.

The measured QE cross section to the Rutherford cross section and the corresponding barrier distribution in  $^{70}\text{Zn}+^{208}\text{Pb}$  are shown in Figs. 1(b) and 1(c), respectively. The solid and dashed curves, respectively, are the theoretical analysis by using a coupled-channels calculation with and without coupling effects of inelastic excitations of the projectile ( $\beta_2=0.228$ ) and the target ( $\beta_3=0.110$ ). The arrow indicates the Bass barrier height, which was always higher by the amount of 4-6 MeV than our previous measured distributions of  $^{48}\text{Ti}$ ,  $^{54}\text{Cr}$ ,  $^{56}\text{Fe}$ ,  $^{64}\text{Ni} + ^{208}\text{Pb}$  reactions. The excitation function of the production cross sections of element 112 synthesized at GSI and RIKEN is also shown in Fig. 1(a), which is inconsistent with each other but both locate high energy side of the present barrier distribution.

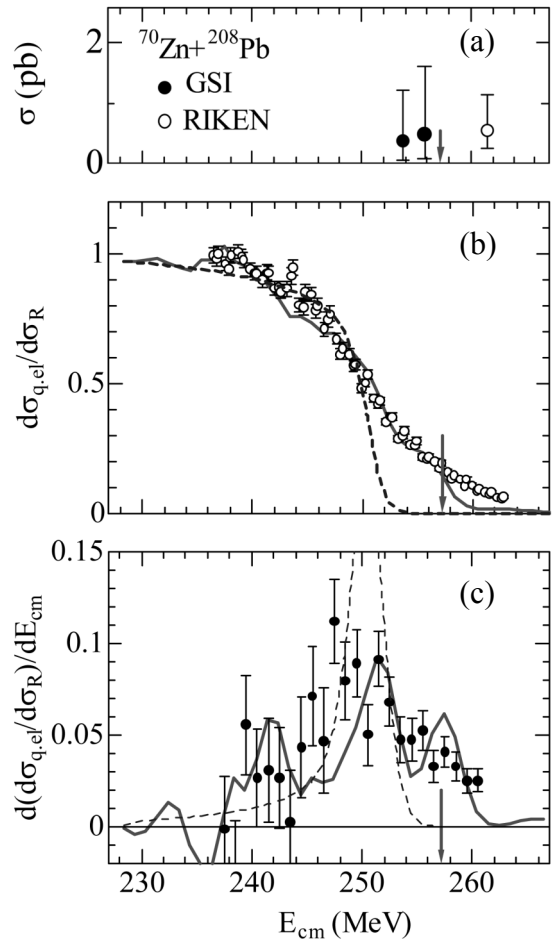


Fig. 1. (a) Production cross section of element 112 by cold fusion of  $^{70}\text{Zn}+^{208}\text{Pb}$ , (b) measured QE cross section to the Rutherford cross section and (c) the barrier distribution as a function of an effective center-of-mass energy.

<sup>1</sup> Institute of Particle and Nuclear Studies, KEK



## **CHAPTER 4**

### **Nuclear Chemistry**

- 4.1 Extraction Behavior of Rf into Tributylphosphate from Hydrochloric Acid
- 4.2 Cation-Exchange Behavior of Rf in HNO<sub>3</sub>/HF Mixed Solution System
- 4.3 Chloride Complex Formation of Rf in HCl and CH<sub>3</sub>OH Mixed Solution



#### 4.1 EXTRACTION BEHAVIOR OF Rf INTO TRIBUTYLPHOSPHATE FROM HYDROCHLORIC ACID

H. HABA<sup>1</sup>, K. TSUKADA, M. ASAI, A. TOYOSHIMA, Y. ISHII, H. TOUME, T. SATO, I. NISHINAKA, T. ICHIKAWA, S. ICHIKAWA, Y. NAGAME, W. SATO<sup>2</sup>, K. MATSUO<sup>2</sup>, Y. KITAMOTO<sup>2</sup>, Y. TASHIRO<sup>2</sup>, A. SHINOHARA<sup>2</sup>, J. SAITO<sup>3</sup>, M. ITO<sup>3</sup>, T. IKEZAWA<sup>3</sup>, M. SAKAMAKI<sup>3</sup>, S. GOTO<sup>3</sup>, H. KUDO<sup>3</sup>, H. KIKUNAGA<sup>4</sup>, M. ARAI<sup>4</sup>, S. KAMATAKI<sup>4</sup>, A. YOKOYAMA<sup>4</sup>, K. AKIYAMA<sup>5</sup>, K. SUEKI<sup>5</sup>, Y. OURA<sup>6</sup>, M. SCHADEL<sup>7</sup>, W. BRUCHLE<sup>7</sup> and J. V. KRATZ<sup>8</sup>

In our previous studies on anionic chloride complexes of element 104, Rf, we investigated the adsorption behavior of Rf and its lighter group-4 homologs Zr and Hf on an anion-exchange resin from 4.0–11.5 M HCl using the Automated Ion-exchange separation apparatus coupled with the Detection system for Alpha spectroscopy (AIDA) [1]. In addition, we measured the Extended X-ray Absorption Fine Structure (EXAFS) spectra of Zr and Hf complexes in 8.0–11.9 M HCl and those on anion-exchange resins equilibrated with 9.0–11.9 M HCl [2]. From these studies, it was suggested that Rf forms the same anionic chloride complexes as Zr and Hf,  $[\text{Rf}(\text{H}_2\text{O})_8]^{4+} \rightarrow \text{RfCl}_6^{2-}$ , and that the order of chloride complexation is  $\text{Rf} > \text{Zr} > \text{Hf}$ . Reported in this paper is our recent result of extraction experiments of Rf into tributylphosphate (TBP) to obtain further information on chloride complexation and the stability of group 4 element TBP complexes.

The isotope <sup>261</sup>Rf was produced in the <sup>248</sup>Cm(<sup>18</sup>O,5n) reaction with a 94-MeV <sup>18</sup>O beam delivered from the JAEA tandem accelerator. A <sup>248</sup>Cm target of 645 μg cm<sup>-2</sup> thickness was prepared by electrodeposition onto a 1.8 mg cm<sup>-2</sup> thick Be foil. The beam intensity was approximately 250 particle nA. As it is important to perform Rf experiments together with Zr and Hf under identical conditions to find out a different chemical behavior among the homologs, Gd (39.3%-enriched <sup>152</sup>Gd of 38 μg cm<sup>-2</sup> thickness) was admixed in the <sup>248</sup>Cm target to simultaneously produce Hf isotopes. Reaction products recoiling out of the target were transported by the He/KCl gas-jet system to AIDA. The 20 wt.% TBP loaded resin on CHP20Y [3] was filled in the 1.6 i.d. × 7.0 mm microcolumns. <sup>261</sup>Rf and <sup>169</sup>Hf deposited on the collection site of AIDA for 140 s were dissolved with 160 μL 11.5 M HCl and fed onto the column at a flow rate of 0.88 mL min<sup>-1</sup>. The effluent was discarded. Then, 210 μL of either 8.0, 7.8, 7.5, or 7.2 M HCl was pumped to the column at a flow rate of 1.0 mL min<sup>-1</sup>. The effluent was collected on a Ta disc as Fraction 1 and was evaporated to dryness using hot He gas and a halogen heat lamp. The remaining Rf and Hf in the column were finally eluted with 230 μL of 4.0 M HCl. This effluent was collected on

<sup>1</sup> Nishina Center for Accelerator Based Science, RIKEN

<sup>2</sup> Graduate School of Science, Osaka University

<sup>3</sup> Faculty of Science, Niigata University

<sup>4</sup> Faculty of Science, Kanazawa University

<sup>5</sup> Department of Chemistry, University of Tsukuba

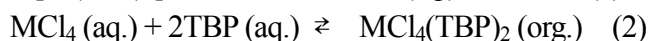
<sup>6</sup> Graduate School of Science and Engineering, Tokyo Metropolitan University

<sup>7</sup> Gesellschaft für Schwerionenforschung

<sup>8</sup> Institut für Kernchemie, Universität Mainz

another Ta disc and was evaporated to dryness as Fraction 2. The pair of Ta discs, Fractions 1 and 2, was automatically transferred to an  $\alpha$ -spectrometry station equipped with eight 600 mm<sup>2</sup> PIPS detectors. In order to investigate the behavior of Zr and Hf, <sup>85</sup>Zr and <sup>169</sup>Hf were simultaneously produced by the <sup>nat</sup>Ge(<sup>18</sup>O,*xn*) and <sup>nat</sup>Gd(<sup>18</sup>O,*xn*) reactions, respectively. The extraction experiments with <sup>85</sup>Zr and <sup>169</sup>Hf were performed at 7.0–8.0 M HCl under identical experimental conditions as in the <sup>261</sup>Rf experiments. The effluents collected in polyethylene tubes were assayed by  $\gamma$ -ray spectrometry with Ge detectors.

From the 1019 cycles of the extraction experiments, a total of 113  $\alpha$  events from <sup>261</sup>Rf and its daughter <sup>257</sup>No were registered in the energy range of 8.00–8.36 MeV, including 17 time-correlated  $\alpha$  pairs of <sup>261</sup>Rf and <sup>257</sup>No. From the activities  $A_1$  and  $A_2$  observed in Fractions 1 and 2, respectively, the %Ext values on the 20 wt.% TBP/CHP20Y resin were evaluated using the equation: %Ext = 100 $A_2$ /( $A_1$  +  $A_2$ ). The variation of the %Ext is shown in Fig. 1 as a function of [HCl]. The %Ext values of Zr are larger than those of Hf, and both increase with an increase of [HCl] from 7.0 M to 8.0 M, indicating that the concentration of the formed neutral chloride complex increases with [HCl]. The %Ext values of Rf also increase with [HCl], and they are apparently smaller than those of Zr and are almost the same as those of Hf within the experimental errors. Thus, the order of %Ext, Zr > Hf  $\approx$  Rf, is obtained in 7.2–8.0 M HCl, though the different orders of Zr > Hf > Rf [4] and Zr > Rf > Hf [5] were reported in 8 M HCl. The TBP extraction process of the group-4 elements in HCl is expressed by the following chemical equations.



The extractability of the group-4 elements into TBP is then expected to depend on both the strength of the chloride complexation and the stability of the TBP complex. As mentioned above, Rf forms the same complexes as Zr and Hf,  $[\text{Rf}(\text{H}_2\text{O})_8]^{4+} \rightarrow \text{RfCl}_6^{2-}$ , and that the strengths of the formed complexes change in the following order: Rf > Zr > Hf. As suggested from the smooth variations of the anion-exchange behavior and of the complex structures as a function of [HCl] [1, 2], we can deduce that the sequence in the strengths of  $\text{MCl}_4$  would be the same as those of  $[\text{MCl}_6]^{2-}$ . The smaller extractability of Rf in the TBP extraction then would indicate that the stability of the TBP complex of Rf chloride,  $\text{RfCl}_4(\text{TBP})_2$ , is lower than those of Zr and Hf.

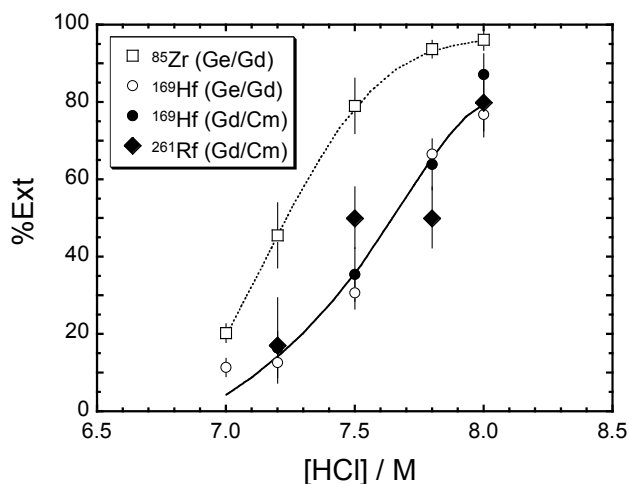


Fig. 1. Percent extractions (%Ext) of Rf, Zr, and Hf on the 20-wt.% TBP/CHP20Y resin as a function of HCl concentration, [HCl].

## References

- [1] H. Habu *et al.*: J. Nucl. Radiochem. Sci. **3** (2002) 143.
- [2] H. Habu *et al.*: *Advances in Nuclear and Radiochemistry*, S. M. Qaim and H. H. Coenen eds., Forschungszentrum Julich GmbH, Julich, Germany **3** (2004) 150.
- [3] H. Habu *et al.*: RIKEN Accel. Prog. Rep. **38** (2005) 107.
- [4] C. D. Kacher *et al.*: Radiochim. Acta **75** (1996) 127.
- [5] R. Gunther *et al.*: Radiochim. Acta **80** (1998) 121.

## 4.2 CATION-EXCHANGE BEHAVIOR OF Rf IN HNO<sub>3</sub>/HF MIXED SOLUTION SYSTEM

Y. ISHII, S. MIYASHITA<sup>1</sup>, T. MORI<sup>1</sup>, H. SUGANUMA<sup>1</sup>, Y. TASHIRO<sup>2</sup>,  
M. SAKAMAKI<sup>3</sup>, S. GOTO<sup>3</sup>, H. TOME, A. TOYOSHIMA, H. HABA<sup>4</sup>,  
K. AKIYAMA<sup>5</sup>, M. ASAI, I. NISHINAKA, K. TSUKADA, Y. OURA<sup>6</sup> and Y. NAGAME

Previously we studied distribution behavior on the anion-exchange resin of Rf and its lighter homologues Zr and Hf in the HNO<sub>3</sub>/HF mixed solution. It was found that Rf forms the hexafluoro anionic complex, [RfF<sub>6</sub>]<sup>2-</sup>, similar to the well known [ZrF<sub>6</sub>]<sup>2-</sup> and [HfF<sub>6</sub>]<sup>2-</sup>, and that the fluoride complexation of Rf is much weaker than those of Zr and Hf [1]. In this work, to enhance the understanding of the stepwise fluoride complex formation of Rf, we have investigated cation-exchange behavior of Rf and the homologues in the HNO<sub>3</sub>/HF solution.

The nuclide <sup>261</sup>Rf (*T*<sub>1/2</sub> = 78 s) produced in the <sup>248</sup>Cm(<sup>18</sup>O, 5*n*) reaction has been used for the chemical studies of Rf. A beam intensity of <sup>18</sup>O delivered from the JAEA tandem accelerator was 250 - 300 particle nA and the incident beam energy was 94 MeV on target. The 540 µg/cm<sup>2</sup> <sup>248</sup>Cm target was prepared by electrodeposition of Cm (NO<sub>3</sub>)<sub>3</sub> onto a Be foil of 1.805 mg/cm<sup>2</sup> thickness. Reaction products recoiling out of the target were transported by a He/KCl gas-jet system to the chemistry laboratory.

On-line cation-exchange chromatography was performed with Automated Ion exchange separation apparatus coupled with the Detection system for Alpha spectroscopy (AIDA). The micro columns, 1.6 mm i.d. × 7.0 mm and 1.0 mm i.d. × 3.5 mm, were filled with the cation exchange resin (MCI GEL CK08Y). The transported products were deposited on the collection site of AIDA for 130 s. Then, the products were dissolved and fed onto the column with 250 µL of 0.1 M HNO<sub>3</sub>/0.0005 - 0.1 M HF solutions at a flow rate of 0.7 mL/min. The effluent was collected on a Ta disk and evaporated to dryness using hot He or N<sub>2</sub> gas and a halogen heat lamp. The remaining products in the column were eluted with 250 µL of 0.1 M HNO<sub>3</sub>/0.1 M HF at a

---

<sup>1</sup> Radiochemical Research Laboratory, Faculty of Science, Shizuoka University

<sup>2</sup> Graduate School of Science, Osaka University

<sup>3</sup> Faculty of Science, Niigata University

<sup>4</sup> Nishina Center of Accelerator Based Science, RIKEN

<sup>5</sup> Graduate School of Pure and Applied Science, University of Tsukuba

<sup>6</sup> Department of Chemistry, Tokyo Metropolitan University

flow rate of 1.0 mL/min. The effluent was collected on another Ta disk and evaporated to dryness in the same manner. These disks were transferred to an  $\alpha$ -spectroscopy station equipped with 600 mm<sup>2</sup> PIPS detectors. These processes were automatically carried out. From observed activities, we evaluated the distribution coefficients ( $K_d$  value) of Rf on the cation-exchange resin. The Cm target contained the 39.3%-enriched <sup>152</sup>Gd of 32  $\mu\text{g}/\text{cm}^2$  in thickness to simultaneously produce short-lived Hf isotopes that are used to determine the chemical yield and the distribution behavior of Hf. After the  $\alpha$ -particle measurement, every third pair of disks was sampled and the 493 keV  $\gamma$ -ray of <sup>169</sup>Hf was measured with Ge detectors. The chemical yield of Hf was approximately 60% and no adsorption of Hf was observed on the cation exchange resin at the present conditions. The  $K_d$  values of <sup>88</sup>Zr and <sup>175</sup>Hf were also measured with a batch method in 0.1 M HNO<sub>3</sub>/10<sup>-2</sup> - 10<sup>-4</sup> M HF.

Figure 1 shows the cation-exchange behavior of Zr, Hf and Rf in 0.1 M HNO<sub>3</sub>/HF. The  $K_d$  values of Zr and Hf were decreased with increasing concentration of the fluoride ion [F<sup>-</sup>], indicating the formation of the fluoride complexes. Although the  $K_d$  values of Rf are also decreased with increasing [F<sup>-</sup>], there is about one-order of magnitude difference in [F<sup>-</sup>] between Rf and the homologues. This means that the strength of the fluoride complexation of Rf is much weaker than those of Zr and Hf, which is consistent with the result in ref. [1]. Further analyses are now in progress.

## References

[1] A. Toyoshima *et al.*, JAERI Tandem Annu. Rep. 2004, JAEA-Review **2005-004** (2006) 47.

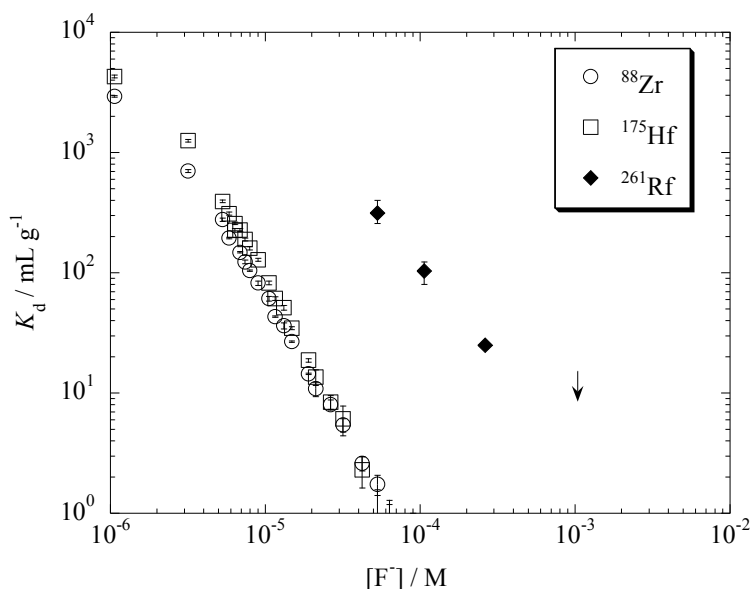


Fig. 1. Distribution coefficients of Zr, Hf and Rf on the cation exchange resin (CK08Y) in 0.1 M HNO<sub>3</sub>/HF. The data for <sup>88</sup>Zr and <sup>175</sup>Hf are obtained from the batch experiments.



### 4.3 CHLORIDE COMPLEX FORMATION OF Rf IN HCl AND CH<sub>3</sub>OH MIXED SOLUTION

K. TSUKADA, A. TOYOSHIMA, H. HABA<sup>1</sup>, M. ASAI, K. AKIYAMA<sup>2</sup>, Y. ISHII<sup>3</sup>, H. TOME<sup>4</sup>,  
I. NISHINAKA, T. SATO, S. ICHIKAWA, Y. NAGAME, T. YAITA, S. GOTO<sup>5</sup>, T. IKEZAWA<sup>5</sup>,  
W. SATO<sup>6</sup>, K. MATSUO<sup>6</sup>, Y. KITAMOTO<sup>6</sup>, Y. TASHIRO<sup>6</sup>, A. YOKOYAMA<sup>7</sup>, N. ARAI<sup>7</sup>,  
M. SAKAMA<sup>8</sup>, Y. OURA<sup>9</sup>, K. SUEKI<sup>2</sup>, A. SHINOHARA<sup>6</sup> and H. KUDO

Previously, we investigated the anion-exchange behavior of element 104, Rf, and its lighter group-4 homologues Zr and Hf in the HCl solution [1]. We also measured the Extended X-ray Absorption Fine Structure (EXAFS) spectra of Zr and Hf complexes in HCl [2]. From these studies, it was deduced that Rf forms the similar complexes to Zr and Hf,  $[\text{Rf}(\text{H}_2\text{O})_8]^{4+} \rightarrow [\text{RfCl}_6]^{2-}$ . In general, the presence of methanol expects us the enhanced formation of the anionic chloride complexes. In order to confirm the chloride complex formation, we have investigated anion-exchange behavior of Rf in the HCl and CH<sub>3</sub>OH mixed solution together with its lighter homologues Zr and Hf. The adsorption ratios of these elements on the anion-exchange resin were measured in HCl and CH<sub>3</sub>OH mixed solutions.

The isotopes <sup>261</sup>Rf, <sup>85</sup>Zr, and <sup>169</sup>Hf were produced in the <sup>248</sup>Cm(<sup>18</sup>O, 5n), <sup>nat</sup>Ge(<sup>18</sup>O, xn), and <sup>nat</sup>Gd(<sup>18</sup>O, xn) reactions, respectively, at the JAEA tandem accelerator [3]. On-line anion-exchange separations for Rf, Zr, and Hf were performed using Automated Ion exchange separation apparatus coupled with the Detection system for Alpha spectroscopy (AIDA). AIDA enables us to perform cyclic discontinuous chromatographic separations in aqueous phases and automatic detections of  $\alpha$ -particles within a typical cycle time of 1 - 2 min. The reaction products recoiling out of the target were transported by a He/KCl gas-jet system to AIDA. The transported products were dissolved with 160  $\mu$  L of hot 11.5 M HCl and were fed onto an anion-exchange column (MCI GEL CA08Y, 1.6 mm i.d.  $\times$  7.0 mm). The effluent was discarded. Then, 240  $\mu$  L of HCl and CH<sub>3</sub>OH mixed solution was eluted to the column at a flow rate of 1.0 mL/min. The effluent was collected on a Ta disk as Fraction 1 and evaporated to dryness with hot He gas and a halogen heat lamp. The products remaining in the column were eluted with 210  $\mu$  L of 4.0 M HCl. The effluent was collected on another Ta disk and evaporated to dryness as Fraction 2. Each pair of Ta disks was automatically transferred to an  $\alpha$ -spectroscopy station equipped with eight 600 mm<sup>2</sup> PIPS detectors. From the activities  $A_1$  and  $A_2$  observed in Fractions 1 and 2, respectively, the percent adsorption

<sup>1</sup> Nishina Center for Accelerator Based Science, RIKEN

<sup>2</sup> Graduate School of Pure and Applied Science, University of Tsukuba

<sup>3</sup> Graduate School of Science and Engineering, Shizuoka University

<sup>4</sup> Faculty of Science, Ibaraki University

<sup>5</sup> Graduate School of Science, Niigata University

<sup>6</sup> Graduate School of Science, Osaka University

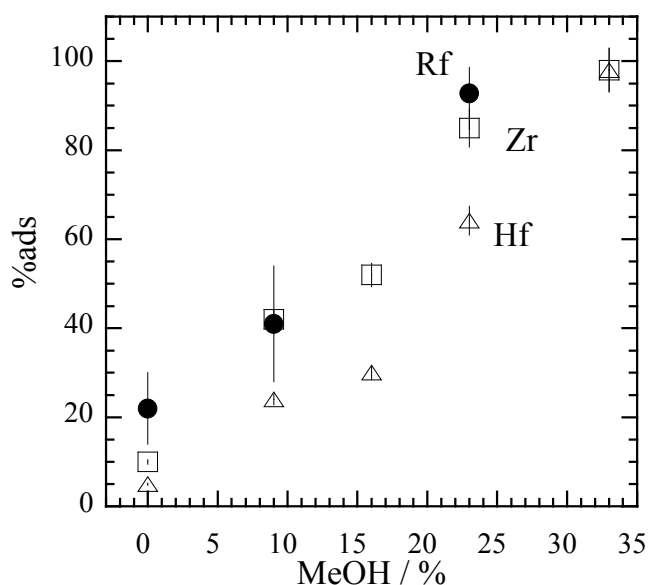
<sup>7</sup> Graduate School of National Science Technology, Kanazawa University

<sup>8</sup> School of Health Science, University of Tokushima

<sup>9</sup> Graduate School of Science and Engineering, Tokyo Metropolitan University

(%ads) on CA08Y was evaluated: %ads =  $100A_2/(A_1 + A_2)$ .

The %ads values of Rf, Hf and Zr as a function of CH<sub>3</sub>OH concentration in 7M HCl are shown in Fig. 1. It is found that the %ads values of Rf, Zr and Hf increase with increasing CH<sub>3</sub>OH concentration at the same HCl concentration; Rf behaves as same as its homologues Zr and Hf. The enhanced formation of the anionic chloride complexes shows the coordinated H<sub>2</sub>O are replaced with Cl<sup>-</sup> ion in the presence of methanol. The result indicates that the formation of the chloride complex of Rf in the HCl and CH<sub>3</sub>OH mixed solution is similar to those of its homologues. The chemical species of Zr and Hf were determined by the EXAFS method to be [MCl<sub>6</sub>]<sup>2-</sup> (M=Zr, Hf) in the HCl and CH<sub>3</sub>OH mixed solution. These results suggest that structure of the adsorbed chloride complex of Rf is expected to be [RfCl<sub>6</sub>]<sup>2-</sup>.



## References

- [1] H. Haba et al.: J. Nucl. Radiochem. Sci. **3** (2002) 143.
- [2] H. Haba et al.: Advances in Nuclear and Radiochemistry, S. M. Qaim and H. H. Coenen eds., Forschungszentrum Juelich GmbH, Juelich, Germany **3** (2004) 150.
- [3] Y. Nagame et al.: J. Nucl. Radiochem. Sci. **3** (2002) 85.

## **CHAPTER 5**

### **Nuclear Theory**

- 5.1 Systematic Study of Shape Coexistence in N=20 Isotones
- 5.2 Decay Modes of Heavy and Superheavy Nuclei Predicted by a Mass Formula
- 5.3 Kaonic Pasta Structures in Dense Matter
- 5.4 A Hybrid Approach to the Two-body Coulomb Scattering in the Momentum Space



## 5.1 SYSTEMATIC STUDY OF SHAPE COEXISTENCE IN N=20 ISOTONES

Y. UTSUNO, T. OTSUKA<sup>1,2</sup>, T. MIZUSAKI<sup>3</sup> and M. HONMA<sup>4</sup>

Recently the nuclear structure around N=20 attracts much interest in relation to the so-called disappearance of the magic number: the N=20 isotones near Z=11 displays no typical spherical ground state and are most probably deformed from the viewpoint of their low excitation energies of the first excited state and large B(E2) values. The transition from a spherical to deformed ground state appears to take place at Z=13 along the N=20 isotone chain, but at present there is no direct experimental evidence for where is the boundary. As for the mechanism of that disappearance of the magic number, we have proposed that the N=20 shell gap is not stably large in that isotone chain and narrows due to the spin-isospin dependence of the nucleus-nucleus interaction [1]. We investigated the structure of unstable nuclei with large-scale shell-model calculations using the Hamiltonian having such a shell structure [2], but still need to confirm whether or not the N=20 gap is indeed large for larger Z, which is the aim of the present study. The shape coexistence rather sensitively reflects the shell gap [3] because 2p-2h configurations excited across the N=20 shell gap dominate the deformed state. Part of the Monte Carlo shell model (MCSM) calculation was performed with the Helios computer system in Tandem.

Fig. 1 shows the energy levels of <sup>36</sup>S compared between experiment and theory. Since the sd-shell model does not reproduce the location of the 0<sup>+</sup><sub>2</sub> state, it can be interpreted as the state dominated by the 2p-2h state. With MCSM, we have obtained not only that state but also the deformed-band members which excellently accounts for the missing states (0<sup>+</sup><sub>2</sub>, 2<sup>+</sup><sub>2</sub> and 2<sup>+</sup><sub>3</sub>) in the sd-shell model. The Hamiltonian used in the present study gives the shell gap as wide as about 5 MeV for sulfur isotopes. Together with our previous results around the sodium region [2] where the shell gap must be quite narrow around 3 MeV, the shell structure should evolve quite apparently.

We also examined the importance of a fully configuration-mixed calculation in the description of the shape coexistence. In Fig. 2, the location of the 0<sup>+</sup><sub>2</sub> is compared among different truncation schemes in the shell-model calculation. Although the deformed states are dominated by the 2p-2h configurations, the excitation energy of 0<sup>+</sup><sub>2</sub> is not correctly reproduced from the calculation up to the 2p-2h configurations. This is because the effect from the 4p-4h configurations predominantly works to pull down 0<sup>+</sup><sub>2</sub> rather than the ground state: the former has much larger 2p-2h components which are easily mixed with the 4p-4h configurations. From that comparison, we emphasize that the large-scale calculation such as MCSM is essential in the discussion of the shell gap from the location of the intruder states.

<sup>1</sup>Department of Physics and Center for Nuclear Study, University of Tokyo

<sup>2</sup>RIKEN

<sup>3</sup>Institute of Natural Sciences, Senshu university

<sup>4</sup>Center for Mathematical Sciences, University of Aizu

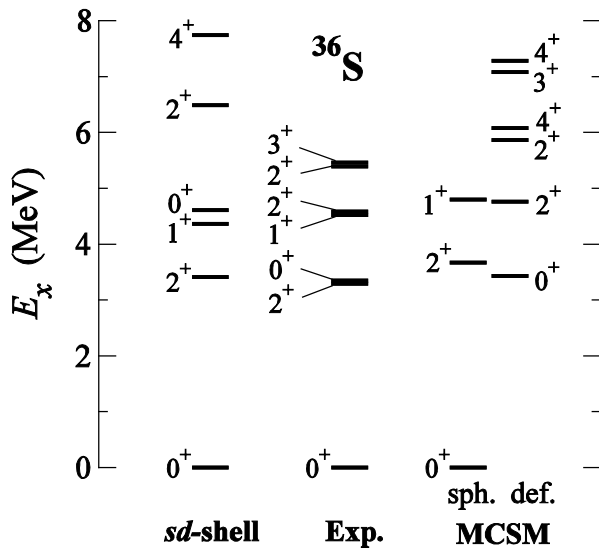


Fig. 1. Energy levels compared between experiment and shell-model calculations. The left levels are obtained from the *sd*-shell calculation using the USD interaction, while the MCSM calculation gives the right energy levels classified into spherical and deformed states based on the expectation value of  $Q \cdot Q$ .

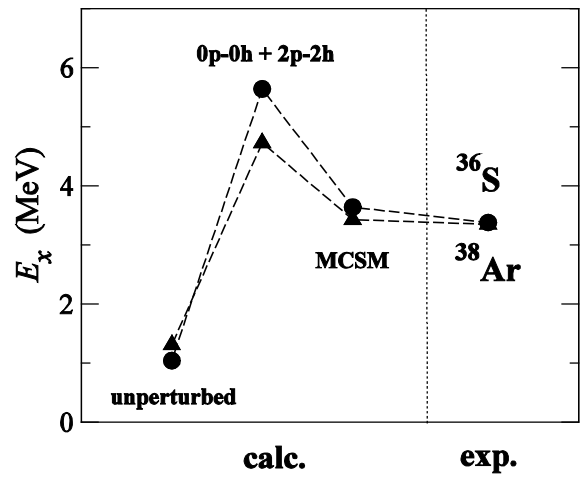


Fig. 2. The excitation energy of  $0^+_2$  state of  $^{36}\text{S}$  (circles) and  $^{38}\text{Ar}$  (triangles) compared between various truncation schemes in the shell model. The label “unperturbed” corresponds to the result in which the 0p-0h and 2p-2h states are calculated in separated spaces, “0p-0h+2p-2h” denotes the calculation including the mixing between them. The “MCSM” includes 4p-4h configurations and more.

### References

- [1] T. Otsuka, R. Fujimoto, Y. Utsuno, B.A. Brown, M. Honma, T. Mizusaki, Phys. Rev. Lett. **87** (2001) 082502.
- [2] Y. Utsuno, T. Otsuka, T. Mizusaki, M. Honma, Phys. Rev. **C70** (2004) 044307.
- [3] Y. Utsuno, T. Otsuka, T. Mizusaki, M. Honma, J. Phys.: Conf. Ser. **20** (2005) 167.

## 5.2 DECAY MODES OF HEAVY AND SUPERHEAVY NUCLEI PREDICTED BY A MASS FORMULA

H. KOURA and T. TACHIBANA<sup>1</sup>

We present a chart of decay modes for  $\alpha$ -decay,  $\beta$ -decay, proton emission and spontaneous fission ranging from light nuclei to superheavy nuclei including unknown ones by using a phenomenological atomic mass formula[1] and some decay models[2]. A bulk term of this mass formula is expressed as a function of proton number  $Z$ , neutron number  $N$  and mass number  $A$  to represent the global feature of atomic masses. Microscopic features including shell effect and deformation are calculated from a modified Woods-Saxon-type single-particle potential[3]. These calculated masses are applied to the estimation of the decay  $Q$  values of  $\alpha$ -decay,  $\beta$ -decay and proton emission. For the calculation of the decay rates of  $\alpha$ -decay, proton emission and spontaneous fission, a one-dimensional WKB method is applied[4]. Beta-decay rate is calculated using the gross theory[5].

Figure 1 shows the calculated partial half-lives of these four decays for isotopes with  $Z=101$ . One of the notable features is that spontaneous fission is quite sensitive to nucleon number because of the shell effect. The decay rates of proton emission and  $\alpha$ -decay increase with neutron number, but the proton decay rate increases more steeply. The  $\beta$ -decay line is almost flat far off the  $\beta$ -stable region in comparison with other decay modes.

Figure 2 shows estimated dominant decay modes in the nuclear chart including the superheavy nuclidic region. We find some regions of fissioning nuclei around  $Z\approx 108$ ,  $N\approx 168$ , and nuclei from  $Z\approx 100$ ,  $N\approx 190$  to heavier ones. The former one is qualitatively consistent with recent experimental  $\alpha$ -decay chains measured at Dubna, which terminate by fission, and the latter one indicates that the production of suspected double-magic super heavy nucleus  $^{298}[114]_{184}$  by the r-process nucleosynthesis in supernova is unexpected because  $\beta$  decay after the r-process near  $A\approx 300$  or more is impeded by fission in that region. (See Fig. 2.) We also calculate total half-lives in the “island of stability for the superheavy nuclei,” and obtain  $^{294}\text{Ds}_{184}$  as the  $\alpha$ -decay-dominant nucleus with the longest half-life on the  $\beta$ -stability line of our mass formula in an order of 100 years, having an ambiguity of 100 times or 1/100.

We also estimate decay modes of nuclei beyond the superheavy ones and find the next “island of stability” on  $N=228$  in the neutron-poor region. This causes from the larger fission-barrier height due to the shell closure of 228 for neutrons. Another region with similar tendency is found near  $N=126$  outside the proton-drip line. In the neutron-rich side, nuclei are almost  $\beta$ -decay dominant and relatively long total half-lives at least in the order of 1 ms. The partial half-lives of other decays are longer than that of  $\beta$ -decay.

<sup>1</sup>Advanced Research Institute for Science and Engineering, Waseda University

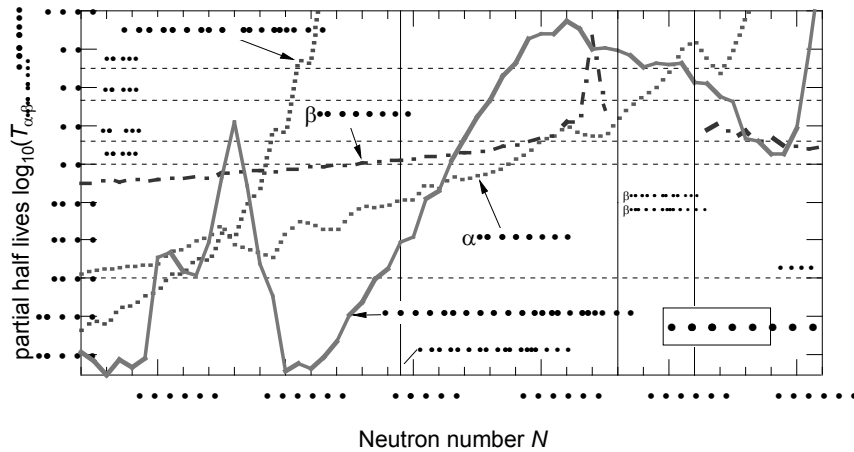


Fig.1. Transition of partial half-lives of four decay modes for isotope with  $Z=101$ .

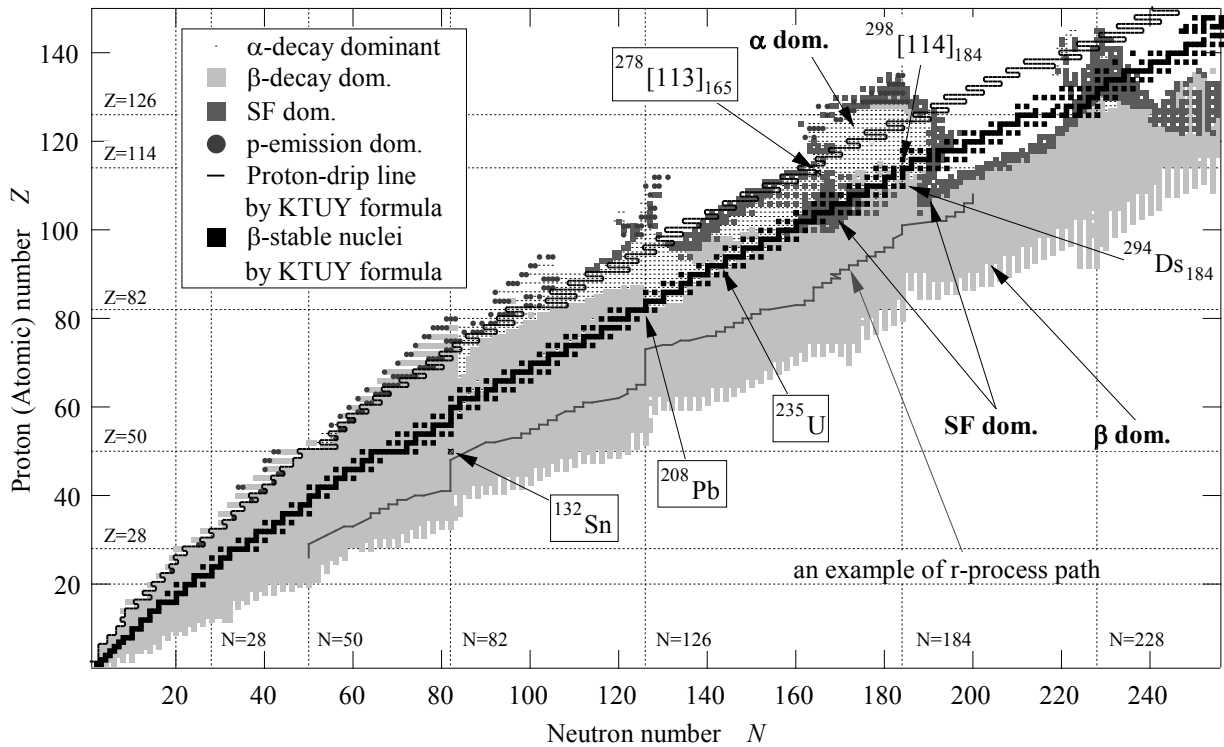


Fig. 2. Shortest partial half-lives among  $\alpha$ -decay,  $\beta$ -decay, spontaneous fission and proton emission.

**References**

[1] H. Koura, T. Tachibana, M. Uno and M. Yamada, Prog. Theor. Phys. **113** (2005) 305.  
 [2] H. Koura, T. Tachibana, Butsuri (the bulletin of the Physical Society of Japan) **60** (2005) 717.  
 [3] H. Koura, M. Uno, T. Tachibana, and M. Yamada, Nucl. Phys. **A671** (2000) 91.  
 [4] H. Koura, in *Tours Symposium on Nuclear Physics V (TOURS2003)*, ed. M. Arnould et al., AIP Conf. Proc. **704** (AIP, New York, 2004) 60.  
 [5] T. Tachibana, M. Yamada, in *Proc. Int. Conf. on exotic nuclei and atomic masses*, Arles, 1995, ed. M. de Simon and O. Sorlin (Editions Frontueres, Gif-Yvette, 1995) p.763.



### 5.3 KAONIC PASTA STRUCTURES IN DENSE MATTER

T. MARUYAMA, T. TATSUMI<sup>1</sup>, D. N. VOSKRESENSKY<sup>2</sup>  
and S. CHIBA

There have been discussed various phase transitions in nuclear matter, like liquid-gas transition, various meson condensations, hadron-quark deconfinement transition, etc. In most cases these are first-order phase transitions (FOPT). In the systems with different charged species undergoing the FOPT the structured mixed phases might appear [4]. For example, in case of the nuclear matter below the saturation density, where the liquid-gas FOPT is relevant, the “nuclear pasta” structures [1, 2, 3] have been studied by many authors. Taking charged kaon condensation as a further example, we study whether the “pasta” structures appear in the high-density neutron-star matter [5]. Kaons are the lightest mesons with strangeness, and their effective energy is much reduced by the kaon-nucleon interaction in nuclear medium. For low-energy kaons the  $s$ -wave interaction is dominant and attractive in the  $I = 1$  channel, so that negatively charged kaons appear in the neutron-rich matter once the process  $n \rightarrow p + K^-$  becomes energetically allowed. Since kaons are bosons, it causes the Bose-Einstein condensation at zero momentum [6].

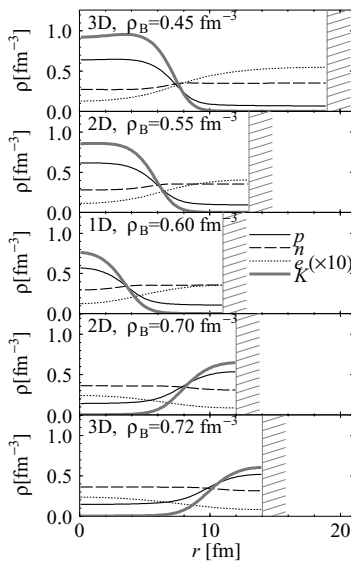


Fig. 1. Density profile of high-density nuclear matter. “3D” etc. means the geometrical dimension. The horizontal axis  $r$  is the distance from the cell center and the hatch shows the cell boundary.

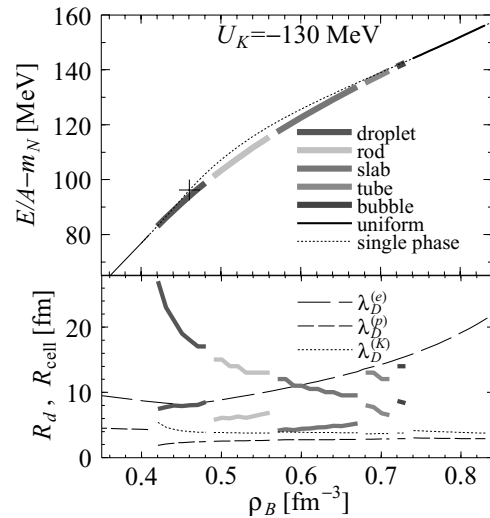


Fig. 2. Binding energies per nucleon and the structure sizes. Dotted line and the cross shows the uniform case without mixed phase and the critical point of phase transition.

We use the density functional theory (DFT) within the relativistic mean field (RMF) model [7]. We get the coupled equations of motion for meson fields (sigma, omega, rho and kaon), nucleon fields, the electron field and the Poisson equation for the electric field. Within this framework all the fields are consistently treated. The numerical solution is obtained by employing the Wigner-Seitz cell approximation and a relaxation method. Our framework

<sup>1</sup> Department of Physics, Kyoto University

<sup>2</sup> Moscow Institute for Physics and Engineering

and its ability to reproduce properties of nuclear matter and finite nuclei have been reported by the present authors [3].

We calculate the structure of the neutron star matter at zero temperature for a given average baryon density. For each baryon density, the cell radius and the geometrical dimension (indicated in Fig. 1 by “3D”, “2D”, “1D”) are chosen to satisfy the minimum of the energy. Around the critical density for kaon condensation, the matter may exhibit the structure change similar to the nuclear “pasta” phases [3]: the kaonic droplet, rod, slab, tube, bubble. Actually we observe such structures in our calculation (see Fig. 1). From the top of the figure, the matter structures correspond to droplet, rod, slab, tube, and bubble. The cluster mainly consists of kaon and proton. This is due to the strong attraction between proton and kaon. On the other hand the neutron distribution proves to be rather flat. In the upper panel of Fig. 2 we plot the energy per nucleon of the matter. Pieces of solid curves indicate the energetically favored structures, while the dotted curve shows the case for the uniform matter with a single phase. One can see the softening of matter by the appearance of “pasta” structures. In the lower panel of Fig. 2

plotted are the cluster size (radius of kaon-matter or kaon-hole) and the cell size. The dashed lines show the Debye screening lengths of the electron, the proton, and the kaon,  $\lambda_D^{(e)}$ ,  $\lambda_D^{(p)}$  and  $\lambda_D^{(k)}$ , respectively. In most cases  $\lambda_D^{(e)}$  is less than the cell size  $R_{\text{cell}}$  but it is larger than the size of the cluster  $R_d$ . However the proton and kaon Debye lengths are always shorter than  $R_d$ . When the minimal value of the Debye length inside the cluster is shorter or of the order of  $R_d$ , the charge screening effects should be pronounced. In fact, when we discard the Coulomb interaction, the density profile (see Fig. 3) and the structure size will be significantly modified. In case of the full calculation (left panel of Fig. 3) the difference between the negative charge density (of kaons and electrons) and the positive charge density of protons is smaller, indicating that the system tends to have a local charge neutrality. This charge screening effect reduces the Coulomb energy of the system and makes the structure size bigger.

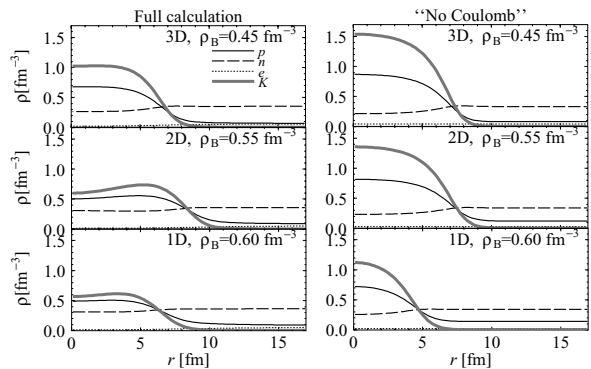


Fig. 3. Comparison of density profiles of kaonic pasta structures with (left) and without (right) the Coulomb interaction. The cell size is set to be 17 fm for all cases.

plotted are the cluster size (radius of kaon-matter or kaon-hole) and the cell size. The dashed lines show the Debye screening lengths of the electron, the proton, and the kaon,  $\lambda_D^{(e)}$ ,  $\lambda_D^{(p)}$  and  $\lambda_D^{(k)}$ , respectively. In most cases  $\lambda_D^{(e)}$  is less than the cell size  $R_{\text{cell}}$  but it is larger than the size of the cluster  $R_d$ . However the proton and kaon Debye lengths are always shorter than  $R_d$ . When the minimal value of the Debye length inside the cluster is shorter or of the order of  $R_d$ , the charge screening effects should be pronounced. In fact, when we discard the Coulomb interaction, the density profile (see Fig. 3) and the structure size will be significantly modified. In case of the full calculation (left panel of Fig. 3) the difference between the negative charge density (of kaons and electrons) and the positive charge density of protons is smaller, indicating that the system tends to have a local charge neutrality. This charge screening effect reduces the Coulomb energy of the system and makes the structure size bigger.

## References

- [1] D. G. Ravenhall, C. J. Pethick and J. R. Wilson, Phys. Rev. Lett. **50** (1983) 2066.
- [2] M. Hashimoto, H. Seki and M. Yamada, Prog. Theor. Phys. **71** (1984) 320.
- [3] T. Maruyama, T. Tatsumi, D.N. Voskresensky, T. Tanigawa and S. Chiba, Phys. Rev. **C72** (2005) 015802.
- [4] N. K. Glendenning, Phys. Rev. **D46** (1992) 1274.
- [5] T. Maruyama, T. Tatsumi, D.N. Voskresensky, T. Tanigawa, T. Endo and S. Chiba, Phys. Rev. **C73** (2006) 035802.
- [6] D. B. Kaplan and A. E. Nelson, Phys. Lett. **B175** (1986) 57; **B179** (1986) 409(E).
- [7] *Density Functional Theory*, ed. E. K. U. Gross and R. M. Dreizler, Plenum Press (1995).

## 5.4 A HYBRID APPROACH TO THE TWO-BODY COULOMB SCATTERING IN THE MOMENTUM SPACE

S. CHIBA, S. ORYU\*, S. NISHINOHARA\*, N. SHIIKI\* and Y. TOGAWA\*

The integral equation, namely the Lippmann-Schwinger (LS) equation for the 2-body scattering, has been used widely to understand nuclear reaction mechanisms and nature of the underlying interaction. It serves also as a starting point of more elaborate methods for 3-, 4- and many-body problems. However, the LS equation suffers a serious numerical difficulty in the momentum space, that is, the overlapping of the pole of Green's function and a logarithmic singularity of the Coulomb potential.

It is obvious that simple manipulation of the LS equation does not give the correct solution to the Coulomb scattering since it is naturally associated with a plane-wave boundary condition: A screened Coulomb potential does not yield a converged solution even if the screening range is increased to infinity. This difficulty in the momentum space has prohibited one to construct an exact Coulomb solution in few-body problems. This has been a long-standing issue in the scattering theories in the momentum representation[1].

In this study, we treat this problem by using an auxiliary potential with a special boundary condition. In order to pose this boundary condition, we employ a solution in the configuration space, which makes this method "hybrid". Here, we consider only the s-state of the p-p system.

Firstly we decompose the Coulomb potential,  $V^C$ , to a sum of a screened Coulomb potential  $V^R$  and the auxiliary potential  $V^\phi$ :

$$V^C = V^R + V^C - V^R = V^R + V^\phi,$$

where  $V^\phi \equiv V^C - V^R$ . The potentials are expressed in the configuration space as  $V^C = \frac{e^2}{r}$  and  $V^R(r) = \frac{e^2}{r} \exp\left(-\frac{r}{R}\right)$ . The LS equation now includes 2 potentials;

$$T^C = V^R + V^\phi + (V^R + V^\phi)G_0T^C. \quad (1)$$

When employed in the LS equation,  $V^R$  and  $V^\phi$  are expressed in the momentum representation.

Secondly, we seek for the range parameter  $R$  by solving, in the **configuration** space, the Schrödinger equation that makes the phase shift of  $V^\phi$ ,  $\phi = n\pi$ , where  $n=0, 1, \dots$ . Since  $V^\phi$  involves the Coulomb potential, this calculation was done with pure Coulomb wave functions in the asymptotic region. In this way we have incorporated the boundary condition of the Coulomb scattering. The result is shown in Fig. 1 as a function of center-of-mass-energy. It exhibits a discontinuity at the energy where the s-wave Coulomb phase shift  $\sigma_0$  becomes 0, corresponding to the change in

---

\*Tokyo University of Science

$n$ . We use the range parameter determined in this way for the calculation in the momentum space. Once determined, the range  $R$  is a definite function of energy and  $\ell$ , so no more an adjustable parameter. The choice of  $R$  to make  $\phi = n\pi$  results in a fact that the on-shell T-matrix for the potential  $V^\phi$  vanishes, since  $T^\phi(k, k; E) = -\frac{2\pi}{k\mu} \sin(\phi)e^{i\phi}$  where  $k$  denotes the on-shell momentum,  $\mu$  the reduced mass. Furthermore, it was shown that, when this condition is satisfied, the half-off shell T-matrix also vanishes;  $T^\phi(k, p; E) = T^\phi(p, k; E) = 0$  for any  $p$  (Lemma 1 of Ref. [2]).

Thirdly, we apply the 2-potential theory (2-PT) to the LS equation with the decomposed Coulomb potential. Then, we obtain the following set of equations;

$$\begin{aligned} T^C &= \bar{\omega}^\phi t^{R\phi} \omega^\phi + T^\phi, \\ t^{R\phi} &= V^R + V^R G^\phi t^{R\phi}, \\ \omega^\phi &= 1 + G_0 T^\phi, \\ \bar{\omega}^\phi &= 1 + T^\phi G_0, \text{ and} \\ G^\phi &= G_0 + G_0 T^\phi G_0. \end{aligned}$$

The on-shell component of  $T^C$  can be obtained by numerically solving the equations above. Owing to the condition posed to the range parameter, it can be shown that

$$T^C(k, k; E) = \int_0^\infty p'^2 dp' \int_0^\infty p''^2 dp'' \bar{\omega}^\phi(k, p') t^{R\phi; E}(p', p'') \omega^\phi(p'', k) + T^\phi(k, k; E) = t^{R\phi}(k, k; E),$$

since  $T^\phi(k, k; E) = 0$ ,  $\bar{\omega}^\phi(k, p')$  and  $\omega^\phi(p'', k)$  are  $\delta$ -functions. This condition facilitates numerical calculations to a great extent.

Finally the phase shift for  $V^C$  is obtained as a phase of the  $t^{R\phi}(k, k)$ , and is plotted in Fig. 2. It is noted that the present method gives the correct Coulomb phase shift down to around 1 MeV. However, we still have numerical problems in the lower energy region, so the definite conclusions are awaited.

## References

- [1] e.g., M. Yamaguchi, H. Kamada and Y. Koike, Prog. Theor. Phys. **114** (2005) 1323, and references therein.  
 [2] S. Oryu, Phys. Rev. C (in press).

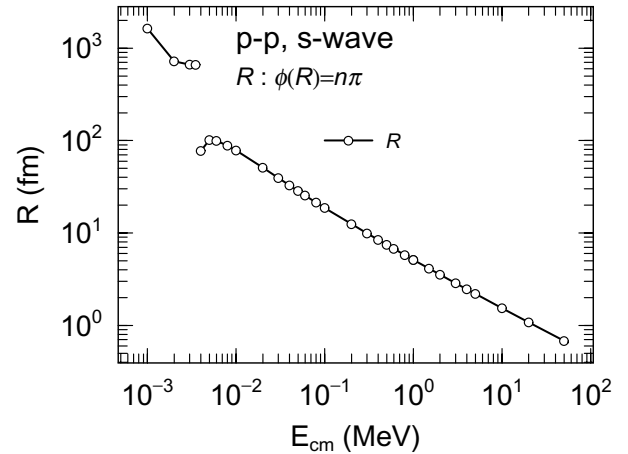


Fig. 1. Range of the screened-Coulomb potential that gives  $\phi = n\pi$ .

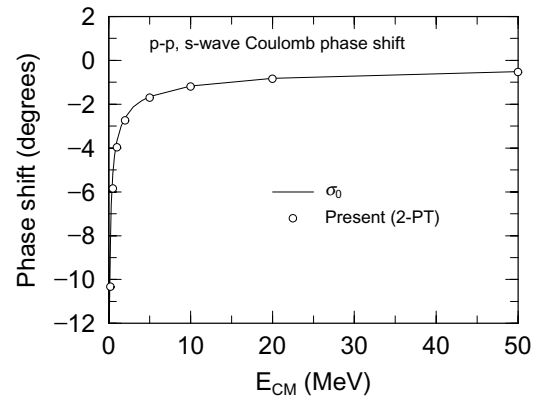


Fig. 2. Phase shift for the Coulomb potential obtained in the momentum space. The open circles denote the present result, and the solid line is the s-wave Coulomb phase shift  $\sigma_0$ .

## CHAPTER 6

### Atomic Physics and Solid State Physics

- 6.1 High-Resolution Zero-Degree Electron Spectroscopy of Highly Charged Oxygen Ions (III)
- 6.2 Charge State Distribution of Sulfur Ions after Penetration of C-foil Targets (III)
- 6.3 Measurement of the Diffusion Coefficients in  $\beta$ -LiGa by using Short-lived Radiotracer of  $^8\text{Li}$
- 6.4 Vortex Imaging in Tl-1223 Superconducting Thin Films with a Scanning SQUID Microscope
- 6.5 Structure of Defect Cascades in Heavy Ions-irradiated Nickel by X-ray Diffuse Scattering
- 6.6 Effects of 100MeV Xe Ion Irradiation on Optical Properties of Al-doped ZnO Films
- 6.7 Electrical Conductivity Increase of Al-doped ZnO Films Induced by High Energy Heavy Ions
- 6.8 XRD Observation on High Energy Heavy Ion Induced Disorder in  $\text{Li}_2\text{TiO}_3$
- 6.9 Optical Spectroscopic Study for Sapphire Irradiated with High Energy Heavy Ions
- 6.10 New X-ray Diffraction Peak of Ion-irradiated  $\text{TiO}_2$  at High Electronic Stopping Power Regime
- 6.11 Swift Heavy Ion Induced Ferromagnetic State in FeRh Alloys
- 6.12 Increase in Curie Temperature for Fe-Ni Alloy Thin Films by Energetic Heavy Ion Irradiation
- 6.13 Effect of High-energy Heavy Ion Irradiation on Magnetic Properties in Fe-Pd Invar Alloys
- 6.14 Electronic Excitation Effects on Secondary Ion Emission from Solid Materials Bombarded by Heavy Ions



## 6.1 HIGH-RESOLUTION ZERO-DEGREE ELECTRON SPECTROSCOPY OF HIGHLY CHARGED OXYGEN IONS (III)

K. KAWATSURA<sup>1</sup>, K. TAKAHIRO<sup>1</sup>, M. SATAKA, M. IMAI<sup>2</sup>,  
K. KOMAKI<sup>3</sup>, H. SUGAI and H. SHIBATA<sup>2</sup>

Energy levels of high-Rydberg states in highly charged ions and dynamical properties of the collision processes inside a solid target have been widely investigated experimentally and theoretically by our group [1-7]. Recently, we have measured high-resolution Auger and Coster-Kronig electron spectra produced in 32 MeV  $O^{q+}$  ( $q = 3, 4$ ) + He collisions. It is found that  $1s^2 2s 2pnl$  states with relatively high angular momenta  $l$  are produced in the  $O^{3+}$  ion collisions, while the  $1s^2 2pnl$  states with lower ones in the  $O^{4+}$  ion collisions [8]. The electron energies for  $1s^2 2s 2pnl - 1s^2 2s^2$  C-K transitions are also discussed and compared with quantum defect theory [9]. However, higher-resolution measurements using a wide variety of charge states of  $O^{q+}$  ions on a He target are still needed for more detailed analysis on excitation and ionization processes in high energy collision regime. The experiments were performed at the tandem accelerator facility of the JAEA-Tokai. The experimental setup for zero-degree electron spectroscopy has been presented in Refs. [1,2]. The primary  $O^{q+}$  ( $q = 1-5$ ) ion beams were produced by using the ECR ion source installed at the high-voltage terminal of the tandem accelerator.

In the present work, the high-resolution C-K electron emission spectra in collisions of 30 MeV  $O^{2+}$  ions with a He gas target have been investigated using zero-degree electron spectroscopy. Figure 1 shows zero-degree electron spectrum around the cusp energy region. The observed electron spectrum was dominated by the so-called cusp peak at around 1.05 keV and a series of C-K electron peaks was superposed on the low and high energy wings of the cusp, corresponding to the backward and forward ejected electrons respectively, from the moving projectile. The energies of these autoionization lines are determined in the projectile rest frame with high resolution.

Figure 2 shows the ejected electron spectra of autoionization lines from excited  $O^{2+}$  ions, where energy scale refers to the projectile rest frame transferred from the laboratory frame energy shown in Fig. 1, using the cusp energy  $t = 1.05$  keV. These autoionization lines for 6-electron  $O^{2+}$  ions are more complicated than for 5-electron  $O^{3+}$  and 4-electron  $O^{4+}$  ions [8,9]. Here we calculate autoionization lines arising from the Rydberg states from ground state and metastable state  $O^{2+}$  ions via single-electron excitation. Vertical bars indicate the line positions obtained by Eq. (1) given in Ref. [9], where  $n$  is the principal quantum number. The energies of C-K electrons were determined to be 1.22, 3.98, 5.47, 6.37, 6.96, 7.36 and 7.65 eV for  $n = 4$  to 10. Thus, the C-K transitions at low

<sup>1</sup> Department of Chemistry and Materials Technology, Kyoto Institute of Technology

<sup>2</sup> Department of Nuclear Engineering, Kyoto University

<sup>3</sup> Institute of Physics, Graduate School of Arts and Sciences, University of Tokyo

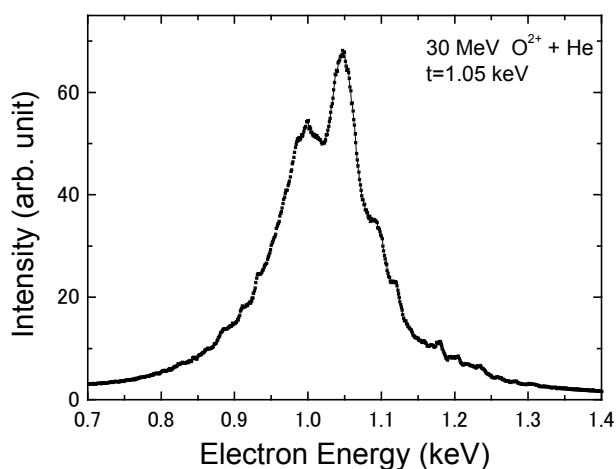


Fig. 1. Zero-degree electron spectrum around cusp energy ( $t = 1.05$  keV) in the collisions  $30$  MeV  $O^{2+} + He$ . Energy scale refers to the laboratory frame.

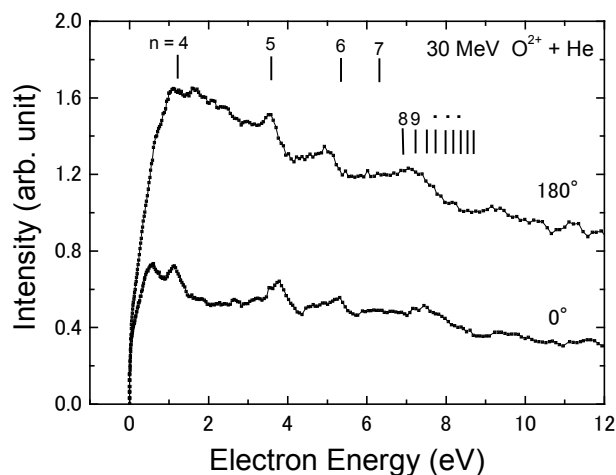


Fig. 2. High-resolution Coster-Kronig electron spectra ejected at  $0^\circ$  and  $180^\circ$  from the moving projectile in collisions of  $30$  MeV  $O^{2+} + He$ . Energy scale refers to the projectile rest frame.

energy region are found to originate in  $1s^22s2p^2(^4P)nl - 1s^22s^22p(^2P)el'$  ( $n \geq 4$ ). This means that these transitions are mainly due to the  $2s-nl$  electron transition of the ground state  $O^{2+} 1s^22s^22p(^3P)$  to the  $1s^22s2p^2(^4P)nl$  excited states and then the C-K electrons are emitted due to the decay to the  $1s^22s^22p(^2P)el'$  states.

## References

- [1] K. Kawatsura *et al.*, Nucl. Instrum. Methods Phys. Res. **B48** (1990) 103.
- [2] K. Kawatsura *et al.*, Nucl. Instrum. Methods Phys. Res. **B53** (1991) 421.
- [3] K. Kawatsura M. Sataka, M. Imai, K. Komaki, Y. Yamazaki, K. Kuroki, Y. Kanai, S. Arai and N. Stolerfoht, Nucl. Instrum. Methods Phys. Res. **B124** (1997) 381.
- [4] M. Sataka, M. Imai, K. Kawatsura, K. Komaki, H. Tawara, A. Vasilyev and U.I. Safronova, J. Phys. B: At. Mol. Opt. Phys. **35** (2002) 267.
- [5] M. Sataka, M. Imai, K. Kawatsura, K. Komaki, H. Tawara, A. Vasilyev and U.I. Safronova, Phys. Rev. **A65** (2002) 052704.
- [6] M. Imai M. Sataka, K. Kawatsura, K. Takahiro, K. Komaki and H. Shibata, Nucl. Instrum. Methods Phys. Res. **B193** (2002) 674.
- [7] M. Imai, M. Sataka, K. Kawatsura, K. Takahiro, K. Komaki and H. Shibata, Brazil. J. Phys. **36** (2006) in press.
- [8] K. Kawatsura, K. Takahiro, M. Imai, M. Sataka, K. Komaki and H. Shibata, Nucl. Instrum. Methods Phys. Res. **B205** (2003) 528.
- [9] K. Kawatsura, K. Takahiro, M. Sataka, M. Imai, K. Komaki, H. Sugai and H. Shibata, Nucl. Instrum. Methods Phys. Res. **B245** (2006) 44.



## 6.2 CHARGE STATE DISTRIBUTION OF SULFUR IONS AFTER PENETRATION OF C-FOIL TARGETS (III)

M. IMAI<sup>1</sup>, M. SATAKA, K. NISHIO, H. SUGAI,  
K. KAWATSURA<sup>2</sup>, K. TAKAHIRO<sup>2</sup>, K. KOMAKI<sup>3</sup>, and H. SHIBATA<sup>1</sup>

Charge state evolution is one of the most important aspects in ion-solid interactions. Various processes, such as electron capture, ionization, vacancy production and the consequent phenomena like energy loss and stopping, are closely related with the projectile charge state evolution in the target. Equilibrium charge state distributions for various collision systems after passing gaseous or solid target have been extensively investigated and compiled [1], although the charge state distribution somewhat changes upon exiting the target foil. As has been presented in the last annual report [2], we measured the exit charge state distributions for penetrations of S<sup>10+</sup>, S<sup>11+</sup> and S<sup>13+</sup> ions through C-foil targets of 0.9, 1.1, 1.5, 2.0, 3.0, 4.7, 6.9 and 10  $\mu\text{g}/\text{cm}^2$  in thickness and performed calculations by ETACHA code [3] to reproduce the experimental results [4].

In the ETACHA code, processes of electron capture, loss, excitation and de-excitation for sub-shells up to 3d are taken into consideration. The electron capture cross sections are derived by the Eikonal and Bethe-Salpeter approximations, respectively for non-radiative and radiative electron captures of bare ion, while the electron loss cross sections are derived by the PWB approximation for H-like ion, and the cross sections for clothed ions are scaled according to their charge states. As the ETACHA is designed to be valid for collision energies between 10 and 80 MeV/u, it underestimated the electron capture and loss cross sections in our experimental condition and the calculated charge state distribution evolved roughly two times slower with the target thickness. The mean charge state also fell a bit larger value (5%) than the experimental result [2].

We are now trying another simulation for S<sup>q+</sup> ion fractions  $F_q(x)$  at target thickness  $x$ , in which the electron transfer cross sections  $\sigma_{qq'}$  are calculated with codes applicable to the present collision energy.

It is now based only on single electron transfer processes, with solving rate equations  $dF_q/dx = \sum_{q'} F_{q'}(x)\sigma_{q'q} - F_q(x)\sum_q \sigma_{qq'}$ , where  $\sum_q F_q(x) = 1$  and  $q' = q \pm 1$ . The total electron capture cross sections are derived by summing partial cross sections calculated with CAPTURE code [5], which employs the CDW approximation and is valid for energy range  $> 0.1$  keV/u, while the total electron loss cross sections are calculated with LOSS code [6], which employs the non-relativistic PWB approximation and is valid for energy range of 1 – 100 MeV/u. In deriving the total capture cross sections, capture to the lowest unoccupied sub-shell or including also that to the second lowest one was selected, so that they balance with the loss cross sections to reproduce the experimental equilibrium charge fraction, where  $dF_q/dx$  falls on 0 [7]. The charge state evolution through C-foil target derived

<sup>1</sup> Department of Nuclear Engineering, Kyoto University

<sup>2</sup> Department of Chemistry and Materials Technology, Kyoto Institute of Technology

<sup>3</sup> Institute of Physics, Graduate School of Arts and Sciences, University of Tokyo

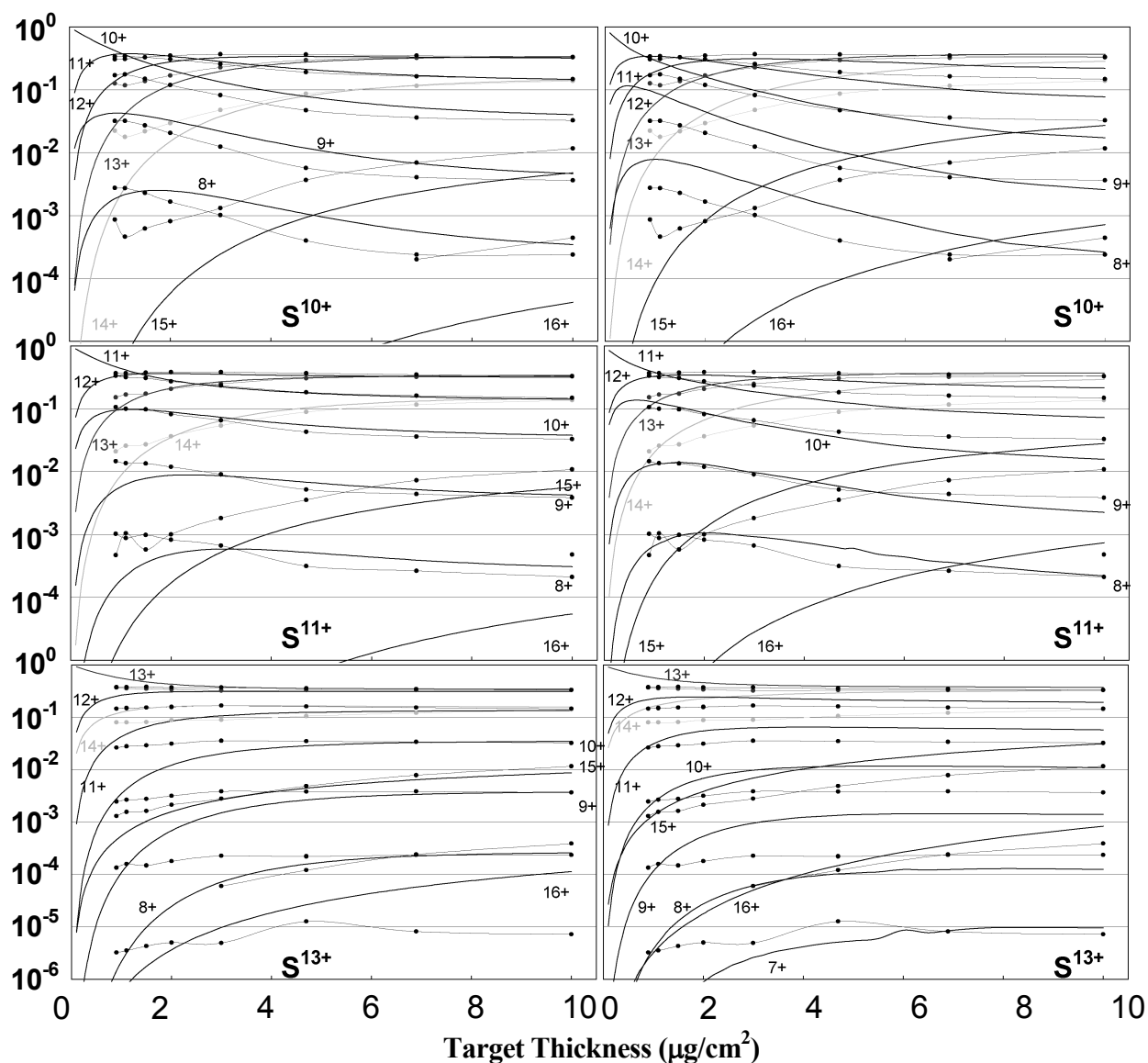


Fig. 1. Charge state distribution of 2.0 MeV/u  $S^{10+}$ ,  $S^{11+}$  and  $S^{13+}$  ions incident through carbon foil targets of 0.9 – 10  $\mu\text{g}/\text{cm}^2$  with simulated values by the present (left column) and by the ETACHA (right column) codes.

by the present and the ETACHA calculations are illustrated in Fig. 1 as a function of target thickness together with the experimental results. The present calculation improves the  $S^{10+} - S^{14+}$  ion fractions compared with the ETACHA results especially in the near-equilibrium region.

## References

- [1] A. B. Wittkower and H. D. Betz, *At. Data Nucl. Data Tables* **5** (1973) 5; K. Shima *et al.*, *At. Data Nucl. Data Tables* **34** (1986) 357; K. Shima *et al.*, *At. Data Nucl. Data Tables* **51** (1992) 173.
- [2] M. Imai *et al.*, *JAEA-Review* **2005-004** (2006) 65.
- [3] J. P. Rozet *et al.*, *J. Phys.* **B22**, 33 (1989); *Nucl. Instrum. and Method* **B107** (1996) 67.
- [4] M. Imai *et al.*, *Nucl. Instrum. Method* **B230** (2005) 63.
- [5] V.P. Shevelko, *Zh. Tekh. Fiz.* **71** (2001) 20 [*Tech. Phys.* **46** (2001) 1225].
- [6] V.P. Shevelko, I.Yu. Tolstikhina and Th. Stohlker, *Nucl. Instrum. Method* **B184** (2001) 295.
- [7] V.P. Shevelko, private communication.

### 6.3 MEASUREMENT OF THE DIFFUSION COEFFICIENTS IN $\beta$ -LiGa BY USING SHORT-LIVED RADIOTRACER OF $^8\text{Li}$

S.C. JEONG<sup>1</sup>, I. KATAYAMA<sup>1</sup>, H. KAWAKAMI<sup>1</sup>, H. ISHIYAMA<sup>1</sup>, Y. WATANABE<sup>1</sup>,  
 N. IMAI<sup>1</sup>, Y. HIRAYAMA<sup>1</sup>, H. MIYATAKE<sup>1</sup>, M. SATAKA, S. OKAYASU, H. SUGAI,  
 S. ICHIKAWA, K. NISHIO, T. NAKANOYA, S. MITSUOKA, Takashi HASHIMOTO,  
 Takanori HASHIMOTO<sup>2</sup>, M. YAHAGI<sup>2</sup>, K. TAKADA<sup>3</sup>, M. WATANABE<sup>3</sup>,  
 T. ISHIKAWA<sup>4</sup> and A. IWASE<sup>5</sup>

The  $\beta$ -LiGa is one of the Li intermetallic compounds with the NaTl structure composed of two interpenetrating sub-lattices, each forming a diamond lattice around stoichiometric atomic ratio of Li, i.e. 44~54 at. % Li. The Li compounds have been considered as possible electrode materials in Li ionic batteries because of their high diffusion coefficients at room temperature for Li ion [1]. The high diffusion coefficient in the Li compounds is associated with the constitutional vacancy concentration on the Li sub-lattice, which is large as compared to the usual metal alloy. The thermodynamic behavior of the Li vacancy has been inferred from the anomalous electrical resistivity (so-called “100K” anomaly) observed around 95K near the critical composition corresponding to the Li-deficient region of  $\beta$ -LiAl [2], which is considered as an order-disorder transition of vacancies on the Li sub-lattice [3].

In order to observe the order-disorder transition of the vacancies on the Li-site in terms of self-diffusion of Li, a detailed measurement has been performed below room temperature for the  $\beta$ -LiGa of 44 at. % Li, which is most Li-deficient in the  $\beta$ -phase of LiGa. Indeed, a sudden change in the Li self-diffusion coefficients is observed around 240 K as shown in Fig.1, at which the anomalous electrical resistivity has been observed [4]. The figure shows the temperature dependence of Li diffusion coefficients in  $\beta$ -LiGa (44 at. % Li) obtained by using short-lived radiotracer of  $^8\text{Li}$ . In the region of higher temperature, the diffusion coefficients follow Arrhenius behavior. In the lower temperature, the diffusion coefficients are observed as a constant, which is the lower limit of diffusion coefficients detectable by our method: For diffusion coefficients less than about  $10^{-10}$  cm<sup>2</sup>/s, any significant effect in the  $\alpha$ -particle yields due to the diffusing  $^8\text{Li}$  could not be observed because of the short life-time of the radiotracer.

<sup>1</sup> Institute of Particle and Nuclear Studies, KEK

<sup>2</sup> Aomori University

<sup>3</sup> National Institute of Materials Science (NIMS)

<sup>4</sup> Tokyo University of Science

<sup>5</sup> Osaka Prefecture University

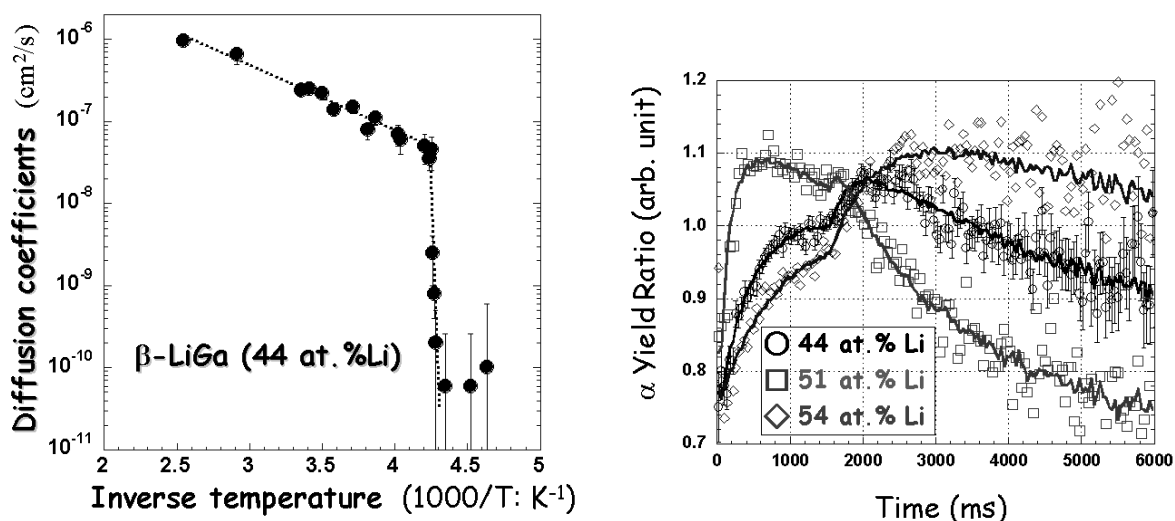


Fig.1. (left): Temperature dependence of diffusion coefficients in  $\beta$ -LiGa (44 at. % Li).

Fig.2. (right): Normalized time spectra of  $\alpha$  yields from  $\beta$ -LiGa obtained with different Li compositions as indicated in the figure. The temperature was set at room temperature. The time spectrum, more rapidly rising and falling with increasing diffusion time, corresponds to faster diffusion of Li.

In Fig.2, the time-dependent normalized  $\alpha$ -particle yields are compared for different Li compositions, i.e. 44, 51 and 54 at. % Li. Referring to the time dependence of the  $\alpha$ -particle yields,  $\beta$ -LiGa with the Li composition of 51 at. % shows fastest diffusion of Li among three. This observation is quite different from those for  $\beta$ -LiAl and LiIn, where, as the Li compositions decreases, the Li diffusion becomes faster with a minor modification due to the coexistence of the vacancies on the Li site ( $V_{Li}$ ) and the defects on the anti-site that replaced by Li ( $Li_A$ ,  $A=Al$  or In). In the case of  $\beta$ -LiGa, more constitutional vacancies on the Li site exist for a fixed Li composition as compared to those of  $\beta$ -LiAl and LiIn, and accordingly more defects of  $Li_{Ga}$  are expected to exist. The motion of the vacancies on the Li site, supposedly the carriers of Li atom, seems to be strongly promoted by the presence of anti-site defects,  $Li_{Ga}$ . In other words, the interaction between  $V_{Li}$  and  $Li_{Ga}$  might be unexpectedly large and quite repulsive than observed in  $\beta$ -LiAl and LiIn. More detailed experiments are now in progress along such an aspect.

## References.

- [1] C.J. Wen and R.A. Huggins, J. Electrochem. Soc. **128** (1981) 1636.
- [2] K. Kuriyama et al., Phys. Rev. **B24** (1981) 6158.
- [3] T.O. Brun, S. Susman, R. Dejus, B. Granelli, and K. Skold, Solid State Commun. **45** (1983) 721.
- [4] H. Hamanaka et al., Solid State Ionics **113** (1998) 19.

## 6.4 VORTEX IMAGING IN TI-1223 SUPERCONDUCTING THIN FILMS WITH A SCANNING SQUID MICROSCOPE

S. OKAYASU, M. ONO, S. SATAKA, A.IYO<sup>1</sup> and Y. TANAKA<sup>1</sup>

Multi-CuO<sub>2</sub> layered superconducting material thallium-based superconductor TlBa<sub>2</sub>Ca<sub>2</sub>Cu<sub>3</sub>O<sub>y</sub> (TI-1223) has the superconducting transition temperature T<sub>c</sub> over 100K. Multiple CuO<sub>2</sub> layers are considered as one of the origin of varieties of physics in high-T<sub>c</sub> superconducting materials. Due to high-T<sub>c</sub> and strong pinning properties, on the other hand, this material is a candidate for practical applications, such as superconducting wires, for high-T<sub>c</sub> superconductor usage. To investigate the pinning properties of this material, vortex images of the film are presented.

Sample preparation will be shown in elsewhere[1]. High energy 200MeV-Au ion irradiation was accomplished at room temperature up to the dose  $1 \times 10^{10}$  ions/cm<sup>2</sup>, corresponding the matching field B<sub>Φ</sub>=0.2 Tesla. The superconducting transition temperature T<sub>c</sub> is 102 K for both cases. Vortex imaging is obtained with a commercial scanning SQUID microscope SQM-2000 (SII nano technology). Measured temperatures are from 4 K to 120 K under a residual magnetic field (~1μT). The scanned area of the sample is 200μm×200μm and spatial sampling is every 2μm step.

The magnetic flux Φ at each vortex site can be calculated. The temperature dependence of Φ/Φ<sub>0</sub> is shown in Fig.1, here Φ<sub>0</sub> = 2.07×10<sup>-15</sup> [Wb] is flux quantum. For both cases, pristine and Au-irradiated sample, each flux at vortex site is quantized to Φ<sub>0</sub> at low temperature. The calculated Φ decreases with increase of temperature, and vanishes above T<sub>c</sub>. Under the condition which pinning is strong enough, superconducting current flows around each vortex site within the range of the penetration length. This condition is well established at lower temperature, and the shape of vortex is sharp enough. As temperature increases, the pinning force at each vortex site decreases. And it becomes impossible to flow sufficient superconducting current within the penetration length. As the result of this, the superconducting current becomes to widely spread, and the shape of the vortex broadened. This is the reason for the decrease of Φ/Φ<sub>0</sub> at higher temperatures. For Au-irradiated sample, the value of Φ/Φ<sub>0</sub> decreases above 40 K, and becomes smaller than 10 % at just below T<sub>c</sub>. The pristine sample, on the other hand, the value of Φ/Φ<sub>0</sub> begins to decrease above 60K, and keeps its value about 30 % just below T<sub>c</sub>. The difference of temperature dependence on Φ/Φ<sub>0</sub> reflects that of pinning centers, columnar defects for the Au-irradiated case and convexo-concave structure on the surface for the pristine sample. The surface roughness is the origin of the strong pinning properties of this material.

Under the measurements condition, magnetic field is low enough, and the system has reserve capacity for flowing much larger superconducting current. Therefore, we can find some vortex and anti-vortex pairs (V-A pairs) at low temperature. The contrasts from the V-A pairs are weak comparing with a single vortex. It means short distance between pair. Magnetic fluxes from a vortex and an anti-vortex located in a short distance form a small loop. And the most part of the magnetic flux goes under the pickup coil and does not pass through it. A part of the magnetic flux gives the signal through the pickup coil. To estimate the distance of the pair, we calculate the field distribution from neighboring V-A pair [3–5], and obtained the estimated distance as ~0.5μm. Short distance between V-A pair implies large attractive force, and strong pinning center is needed to maintain the pair within such a short distance.

---

<sup>1</sup>AIST, Tsukuba, Ibaraki 305-8577, Japan

In Fig.2, an example of current-induced V-A pair is shown. These images are obtained at 4 K in unirradiated region. No V-A pair can be observed for  $I=0$  A/cm<sup>2</sup> within dotted circle (Fig.2-(c)). Once any current is applied, a V-A pair appears (Fig.2-(b) and -(d)). The pair is located in the direction disassociating each other by Lorentz force. As current increases, the image of the V-A pair becomes clearly indicating that the distance between the pair becomes larger due to larger Lorentz force (Fig.2-(a) and -(e)).

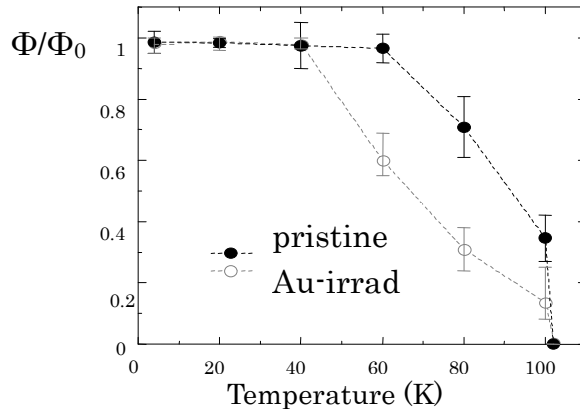


Fig. 1. Temperature dependence of mean value of magnetic flux at each vortex site. Measured temperatures are 4 K, 80 K, 100K and 103K, respectively.

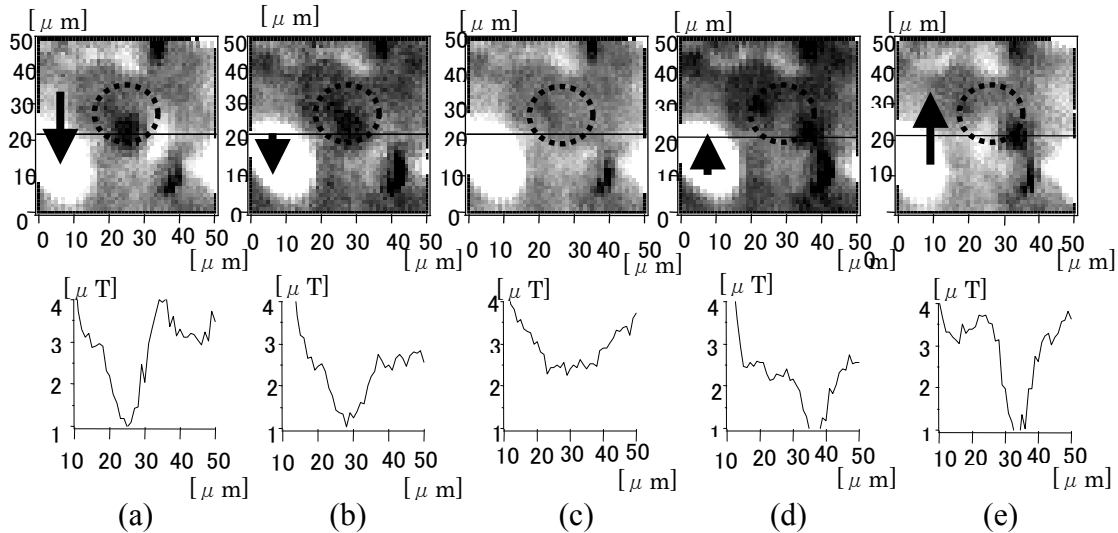


Fig.2. The upper part : Current induced vortex-antivortex pair. Arrows indicate the current directions. The applied current densities are  $-4000$ ,  $-2000$ ,  $0$ ,  $+2000$ ,  $+4000$  A/cm<sup>2</sup> from left side to right, respectively. The lower part : magnetic field distributions at the induced V-A pair.

**References**

[1] A. Iyo, Y. Tanaka, Y. Ishiura, M. Tokumoto, K. Tokiwa, T. Watanabe and H. Ihara, Supercond. Sci. Tech. **14** (2001) 504.  
 [2] A. Sundaresan, Y. Tanaka, A. Iyo, M. Kusunoki, and S. Ohshima, Supercond. Sci. Technol., **L23** (2003) 16.  
 [3] J. Pearl, Appl. Phys. Lett., **5** (1964) 65.  
 [4] J. C. Wei & T. J. Yang, Jpn. J. Appl. Phys., **35** (1996) 5696.  
 [5] G. Carneiro & E. H. Brandt, Phys. Rev. **B61** (2000) 6370.

## 6.5 STRUCTURE OF DEFECT CASCADES IN HEAVY IONS-IRRADIATED NICKEL BY X-RAY DIFFUSE SCATTERING

H. MAETA<sup>1</sup>, N. MATSUMOTO, T. KATO, H. SUGAI, H. OHTSUKA and M. SATAKA

Displacement cascade is one of the most important problems in the nuclear materials [1]. Energetic heavy ions produce point defects such as vacancy-interstitial pairs and also displacement cascades containing high local concentrations of these defects. In the study of radiation damage of solids, it is recognized that some radiation-induced defects might be mobile even below liquid hydrogen temperature (20 K). In order to retain the defects in the original configuration, it is necessary to irradiate at such as low temperature that the defects could not migrate and to observe the defects at the same low temperature. There are many measurements of the displacement cascade in the nuclear materials, but those are measured only by the transmission electron microscopy (TEM). However, few observations have been carried out at such low temperature [2]. Most of studies were carried out at high temperature at whose temperature the defects move out and change not only their original structure but also their size. Such a defect should be small size below the visibility limit of TEM. On the other hand, X-ray diffuse scattering [3] is a powerful method to observe nondestructively such a small defect in bulk specimen at low temperature below 10 K [3-5].

A cryostat has been developed for both ion irradiation below 10 K and transferring the specimen at low temperature to the X-ray diffraction measurement without any warming [6]. Single-crystalline Ni specimen (99.999 % in purity) was spark-cut from the large single crystalline grown by the Czochoralski method. The size of specimen is about  $10 \times 4 \times 1 \text{ mm}^3$ . The specimen was irradiated below 13 K with 137 MeV xenon ions ( $\text{Xe}^{10+}$ ) of fluences up to  $2.3 \times 10^{13}$  ions/cm<sup>2</sup> by the Tandem Accelerator at Tokai. After the irradiation the cryostat with the specimen was transferred to the X-ray goniometer below 20 K. The X-ray diffuse scattering measurements on the irradiated specimen were performed below 20 K with four circle diffractometer using  $\text{CuK}\alpha_1$  from an 18 kW rotating X-ray anode.

The intensity of X-ray scattering close to (111) reflection in [111] direction measured at 20 K is shown in Fig. 1. In the figure, we can see the diffuse scattering from a large area around the Bragg angle as the difference before and after irradiation. The broad diffuse scattering is associated with the disordered, i.e., amorphous-like, structure within the cascades [6]. Furthermore, the diffuse scattering intensities  $I_{D,S}$  was obtained by subtracting the background intensities (solid line in Fig. 1) from the total intensities and averaging the difference at point +q and -q in reciprocal lattice, and the q dependence of  $I_{D,S}$  is shown in Fig. 2 ( $q = \mathbf{K} - \mathbf{h}$ , where  $\mathbf{K}$  is the scattering vector and  $\mathbf{h}$  the reciprocal lattice vector). In Fig. 2, the typical  $q^{-2}$ -dependence (Huang diffuse scattering from point defects and defect clusters [3]) and the  $q^{-4}$ -dependence (Stokes-Wilson scattering from a large distorted region, dislocation loops and defect cascades [3]) are clearly demonstrated.

<sup>1</sup> Hiroshima Kokusai Gakuin University

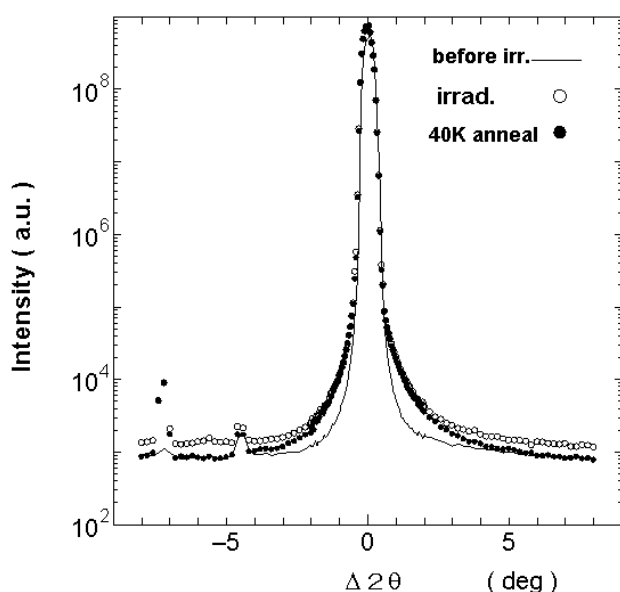


Fig. 1. Intensity of X-ray scattering from nickel irradiated with Xe ions of  $2.3 \times 10^{13}$  ions/cm<sup>2</sup> at 13 K close to (111) reflection in [111] direction. The specimens were measured at 20 K before irradiation (—), and after irradiated (○) and annealed at 40 K (●).

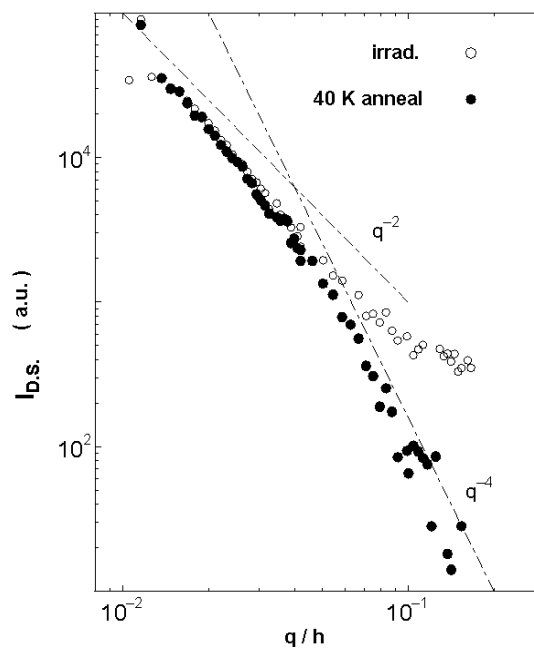


Fig. 2. The  $q$ -dependence of diffuse scattering from nickel irradiated with Xe ions of  $2.3 \times 10^{13}$  ions/cm<sup>2</sup> at 13 K. The specimens were measured at 20 K after irradiated (○) and annealed at 40 K (●).

For Ni irradiated by electron, neutron or ions, the change of electrical resistivity at recovery stage  $I_A$  is very small. Since the recovery is due to the recombination of closed Frenkel pairs at the temperatures between 20 and 40 K [7], the defects produced by the irradiation could not rearrange or migrate below 20 K. In higher  $q$ -region ( $q/h > 8 \times 10^{-2}$ ) of Fig. 2,  $I_{D.S.}$  (○) after irradiated deviates from the  $q^{-2}$ -dependence, because the diffuse scattering originated from the amorphous-like structure within cascades is dominant as mentioned in the previous paragraph [6]. Although the amorphous-like structure within cascades disappears owing to the recombination of closed Frenkel pairs by 40 K annealing, the cascades containing vacancies and interstitials remains to show the  $q^{-4}$ -dependence of diffuse scattering (●) in higher  $q$ -region. Here, the critical point  $q_0$  and the average size of cascade radius  $R_0$  satisfy  $q_0 \times R_0 = 1$  [3] and we can roughly estimate  $R_0$  to be 1 nm from Fig. 2.

## References

- [1] R.S. Averback, J. Nucl. Mater. **216** (1994) 49.
- [2] M.A. Kirk, M.L. Jemkins and H. Fukushima, J. Nucl. Mater. **276** (2000) 50.
- [3] P.H. Dederichs, J. Phys. F : Metal Phys. **3** (1973) 471; P. Ehrhart, J. Nucl. Mater. **216** (1994) 170.
- [4] B.v. Guerard, D.Grasse, J. Peisl, Phys. Rev. Lett. **44** (1980) 262.
- [5] H. Maeta and F. Ono, Mater. Sci. Forum **15-18** (1987) 1099.
- [6] H. Maeta, N. Matsumoto, T. Kato, H. Sugai, H. Ohtsuka and M. Sataka, Nucl. Instrum Methods **B 232** (2005) 312; **242** (2006) 546.
- [7] M.F. Bartels, F. Dworschak and M. Weiger, J. Nucl. Mater. **137** (1986) 130.



## 6.6 EFFECTS OF 100 MeV Xe ION IRRADIATION ON OPTICAL PROPERTIES OF Al-DOPED ZnO FILMS

N. MATSUNAMI<sup>1</sup>, O. FUKUOKA<sup>1</sup>, M. TAZAWA<sup>2</sup>, T. SHIMURA<sup>3</sup>,  
M. SATAKA, H. SUGAI and S. OKAYASU

Al-doped ZnO (AZO) is known as an n-type semiconductor with high electrical conductivity and optical transparency [1]. We have been investigating irradiation effects with high-energy ions on the properties of AZO associated with the electronic structure, i.e., optical absorption, band gap, refractive index as well as structural properties [2], searching for the electronic excitation effects due to high-energy ions other than the electronic sputtering [3].

AZO films were prepared on SiO<sub>2</sub>-glass substrates at 400°C by using an off-axis RF-magnetron-sputter deposition method [4]. According to Rutherford backscattering spectrometry (RBS) using 1.8 MeV He ions, the film thickness employed in this study ranges from 0.1 to 0.36 μm and the composition is very close to stoichiometric, i.e., O/Zn=1.0 and Al/Zn=0.04 within RBS accuracy of 10 %. In RBS analysis, the stopping power is taken from [5] with the atomic density of 4.2x10<sup>22</sup>/cm<sup>3</sup>.

Fig. 1 shows absorption spectra of an AZO film as prepared and irradiated with 100 MeV Xe at a fluence of 3.1x10<sup>12</sup> cm<sup>-2</sup>. The absorption coefficient of unirradiated AZO films at the wavelength of 310 nm (4 eV) is determined to be 154 cm<sup>-1</sup>. One sees the absorption edge (sharp increase in the absorbance) around 3.5 eV (354 nm). It is found that the slope of the absorption edge (3.3 eV<sup>-1</sup> with an accuracy of 3 % for unirradiated films) monotonically decreases with the ion fluence till ~10<sup>13</sup> cm<sup>-2</sup>, reaching minimum and stays a constant of ~2 eV<sup>-1</sup> upon further irradiation. Oscillations observed below 3 eV in Fig. 1 (spectrum in expanded scale) are due to interference between directly transmitted photon beam and reflected beam from the film-substrate interface and film surface.

The refractive index *n*, which was obtained by means of ellipsometry with an accuracy of 2 %, represented at the wavelength of 0.5μm (1.96 for unirradiated films) decreases to 1.85 at 5x10<sup>13</sup> cm<sup>-2</sup> and increases to 2.1 for the fluence > 10<sup>14</sup> cm<sup>-2</sup>. The X-ray diffraction intensity and full-width at half-maximum of the rocking curve show monotonic decrease and increase with the ion fluence, respectively.

The band gap *E<sub>g</sub>* is determined to be 3.37 eV for unirradiated films, using the formula [6]

$$(\text{Absorbance} \cdot E)^2 \propto (E - E_g), \quad (1)$$

where *E* is the photon energy. An error of *E<sub>g</sub>* is estimated to be 0.5 %, based on the sample variation. Fig. 2 shows the band-gap shift (*E<sub>g</sub>(irrad) - E<sub>g</sub>(unirrad)*) and the conductivity [7] as a function of 100 MeV Xe ion fluence. Conductivity increase originates from carrier (electron) generation due to replacement of Zn site by Al. It is suggested that the conductivity increase has more close relation with the band-gap shift. Relations between the optical properties and the increase of the carrier density and mobility, and both valence and conduction band modifications by ions are to be investigated.

<sup>1</sup> Division of Energy Science, EcoTopia Science Institute, Nagoya University

<sup>2</sup> National Institute of Advanced Industrial Science and Technology

<sup>3</sup> Nano-Materials Science Division, EcoTopia Science Institute, Nagoya University

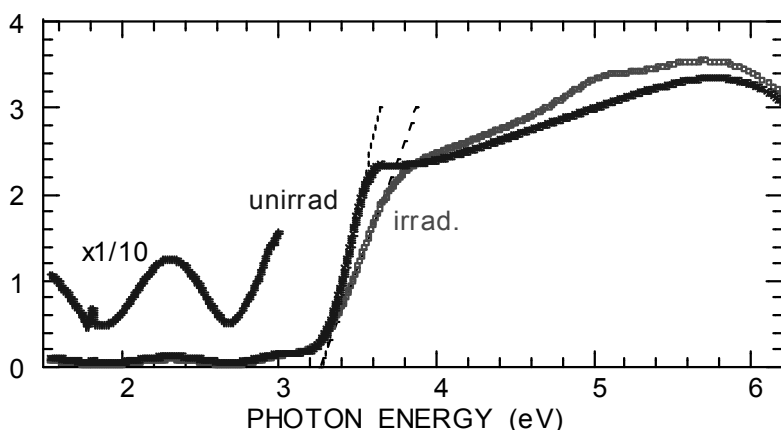


Fig. 1. Absorption spectra of an AZO film without irradiation and with irradiation by 100 MeV Xe at  $31 \times 10^{12}/\text{cm}^2$ . The dotted and dashed lines indicate the slope of the band transition for unirradiated and irradiated films. Absorbance of unirradiated film in an expanded scale is also shown.

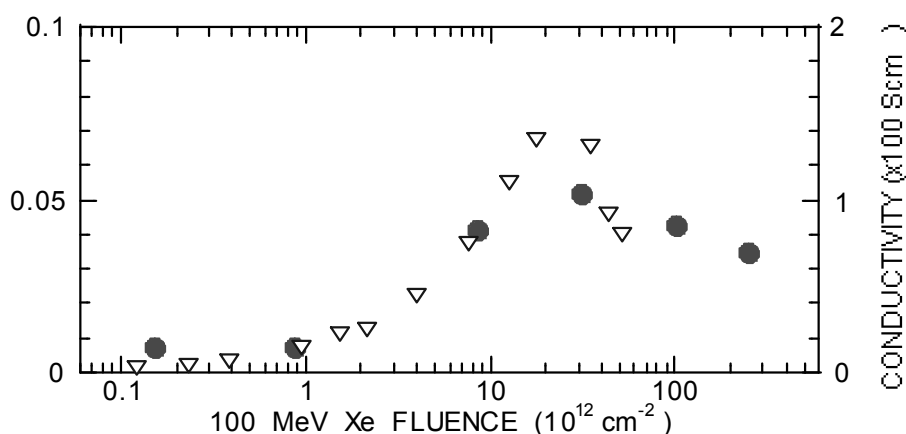


Fig. 2. Band-gap shift (closed circles) and conductivity (open triangles) after ref. [7] as a function of fluence of 100 MeV Xe ions.

## References

- [1] S. J. Pearton, D. P. Norton, K. Ip, Y. W. Heo, T. Steiner, *Prog. Mater. Sci.* **50** (2005) 293.
- [2] O. Fukuoka, N. Matsunami, M. Tazawa, T. Shimura, M. Sataka, H. Sugai, S. Okayasu, *Nucl. Instrum. Methods B* (2006 in print).
- [3] N. Matsunami, O. Fukuoka, T. Shimura, M. Sataka, S. Okayasu, *Nucl. Instrum. Methods B230* (2005) 507.
- [4] N. Matsunami, O. Fukuoka, M. Tazawa, M. Sataka, *Surf. Coatings Technol.* **196** (2005) 50. *Trans. Mater. Res. Soc. Japan* **29** (2004) 639.
- [5] J.F. Ziegler, J.P. Biersack and U. Littmark, *The Stopping and Range of Ions in Solids*, Pergamonn Press, New York (1985).
- [6] T. P. McLean, *Progress in Semiconductors*, John Wiley & Sons **5** (1960) 55.
- [7] H. Sugai, N. Matsunami, O. Fukuoka, M. Sataka, T. Kato, S. Okayasu, T. Shimura, M. Tazawa, *Nucl. Instrum. Methods B* (2006 in print).

## 6.7 ELECTRICAL CONDUCTIVITY INCREASE OF Al-DOPED ZnO FILMS INDUCED BY HIGH ENERGY HEAVY IONS

H. SUGAI, N. MATSUNAMI<sup>1</sup>, O. FUKUOKA<sup>1</sup>, M. SATAKA, T. KATO, S. OKAYASU,  
T. SHIMURA<sup>2</sup> and M. TAZAWA<sup>3</sup>

We have investigated the effects on electrical properties of Al-doped ZnO (AZO) semiconductor films induced by 90 MeV Ni, 100 MeV Xe and 200 MeV Xe ions [1]. We find that the conductivity increases by two orders of magnitude under these high-energy-heavy ion irradiation, as already observed for 100 keV Ne ion irradiation [2]. The carrier density and mobility for unirradiated and irradiated AZO films are also presented [1].

AZO films were grown on SiO<sub>2</sub>-glass substrates at 400 °C by an off-axis RF magnetron sputtering method [2]. Rutherford backscattering spectroscopy (RBS) was employed to analyze the composition and film thickness. The ratio O/Zn in AZO is 1.0 and that of Al/Zn 0.04 within the RBS accuracy of 10 %. Film thickness is ~0.26 μm. In Table 1, the electronic stopping power ( $S_e$ ), the nuclear stopping power ( $S_n$ ) and projected range calculated using TRIM1997 [3] are listed. Taking the displacement threshold energy = 57 eV [4], calculated displacement per atom (dpa) is also listed in Table 1. Since the film thickness is thin enough (~0.26 μm), the electronic and nuclear energy deposition averaged over the film thickness can be represented by the electronic and nuclear stopping powers at the film surface.

It is found that the conductivity linearly increases with ion fluence between  $10^{12}$  and  $10^{13}$  ions/cm<sup>2</sup> as shown in Fig. 1, while the conductivity for less than  $10^{12}$  ions/cm<sup>2</sup> exhibits no linear dependence on the ion fluence as shown in the inset of Fig. 1. One of the reasons for the non-linear dependence for ion fluence less than  $10^{12}$  ions/cm<sup>2</sup> is attributed to the removal of surface contaminations. In this study, we consider that the linear increase in the conductivity for ion fluence between  $10^{12}$  and  $10^{13}$  ions/cm<sup>2</sup> suggests the modification of the entire film property. The efficiency of ion irradiation effect can be represented by the slope of conductivity increase in the linear dependent region, as shown in Fig. 1. The efficiency is obtained to be  $3 \times 10^{-12}$ ,  $10 \times 10^{-12}$  and  $30 \times 10^{-12}$  Scm/ions for 90 MeV Ni, 100 MeV Xe and 200 MeV Xe ions, respectively.

Clearly, from Table 1, the efficiency does not scale with any power of  $S_n$ , but scales with  $S_e$ , as shown in Fig. 2. The exponent is obtained to be 3.7 and this is a little bit larger than the exponent for the electronic sputtering yield [5]. A reason may be that ion irradiation enhances both the carrier density and mobility, which super-linearly depend on  $S_e$ . The relation between the conductivity

<sup>1</sup> Division of Energy Science, Eco Topia Science Institute, Nagoya University

<sup>2</sup> Nano-Materials Science Division, Eco Topia Science Institute, Nagoya University

<sup>3</sup> National Institute of Advanced Industrial Science and Technology

increase and optical property modification by ion irradiation will be discussed elsewhere [6].

Table 1 Electronic ( $S_e$ ), nuclear ( $S_n$ ) stopping powers, dpa at ion fluence of  $10^{13}/\text{cm}^2$  and projected range for ZnO

Ion	Energy (MeV)	$S_e$ (keV/nm)	$S_n$ (keV/nm)	dpa	Projected range ( $\mu\text{m}$ )
Ni	90	14.5	0.0307	$3.0 \times 10^{-4}$	9.32
Xe	100	22.2	0.195	$1.9 \times 10^{-3}$	6.70
Xe	200	26.1	0.111	$1.1 \times 10^{-3}$	10.8

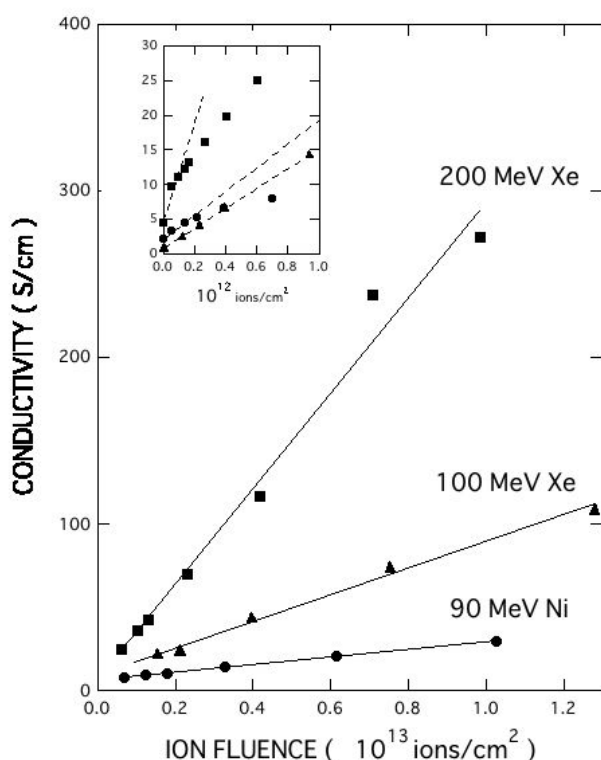


Fig. 1. Conductivity of AZO films vs ion fluence between  $10^{12}$  and  $10^{13}$  ions/cm<sup>2</sup>. Each solid line is the best fit to the data by the least-squares method. In the inset, ion-fluence dependence of the conductivities is plotted for ion fluence less than  $10^{12}$  ions/cm<sup>2</sup>. The initial slopes of the conductivity increase are shown by broken lines.

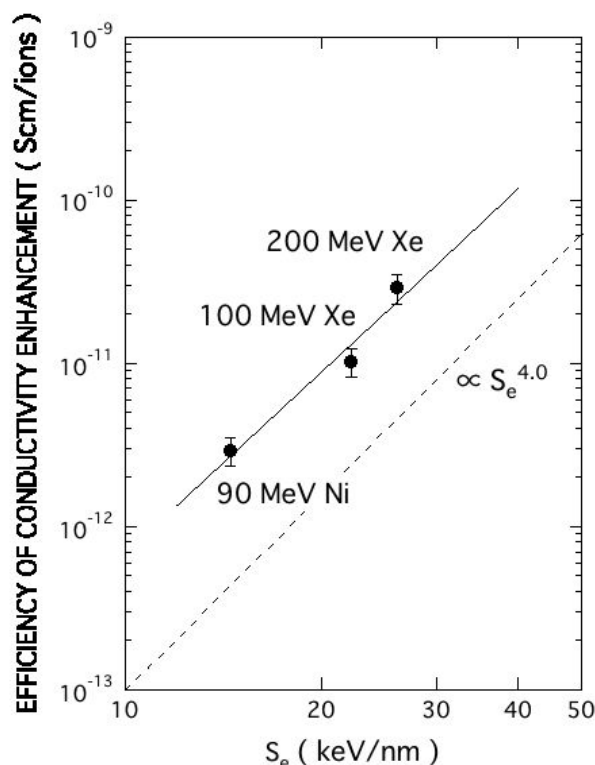


Fig. 2. Efficiency of the conductivity enhancement vs the electronic stopping power ( $S_e$ ) for 90MeV Ni, 100MeV Xe and 200MeV Xe ion irradiation. The efficiency means the slope of conductivity vs ion fluence in Fig. 1. The solid line shows a fit of  $S_e^{3.7}$  and the broken line  $S_e^4$  for reference.

### References

- [1] H. Sugai, N. Matsunami, O. Fukuoka, T. Shimura, M. Sataka, S. Okayasu and M. Tazawa, Nucl. Instrum. Methods **B** (2006) in press.
- [2] N. Matsunami, O. Fukuoka, M. Tazawa and M. Sataka, Surf. Coatings Technol. **196** (2005) 50.
- [3] J.F. Ziegler, J.P. Biersack and U. Littmark, The Stopping and Range of Ions in Solids, Pergamonn Press, New York (1985).
- [4] D.R. Locker and J.M. Meese, IEEE Trans. Nucl. Sci. **19** (1972) 237.
- [5] N. Matsunami, M. Sataka, A. Iwase and S. Okayasu, Nucl. Instrum. Methods **B209**(2003) 288.
- [6] O. Fukuoka, N. Matsunami, M. Tazawa, T. Shimura, M. Sataka, H. Sugai and S. Okayasu, Nucl. Instrum. Methods **B** (2006) in press.

## 6.8 XRD OBSERVATION ON HIGH ENERGY HEAVY ION INDUCED DISORDERING IN $\text{Li}_2\text{TiO}_3$

T. NAKAZAWA, N. OKUBO, A. NAITO, T. ARUGA, V. GRISMANOV<sup>1</sup>,  
Y. CHIMI, A. IWASE<sup>2</sup> and S. JITSUKAWA

Study on structural disorder of the breeder materials such as lithium metatitanate ( $\text{Li}_2\text{TiO}_3$ ) is essential to evaluate its irradiation performance. In this study, the structural disorder in  $\text{Li}_2\text{TiO}_3$  due to irradiation with high energy xenon (Xe) ions is examined by use of X-ray diffraction (XRD) measurements.

The irradiation conditions are listed in the table 1. The XRD patterns are obtained using a Cu-K $\alpha$  radiation for the samples before and after irradiation. During XRD measurements, samples are masked with a gold foil of 10  $\mu\text{m}$  in thickness having a square hole sized 8 by 5 millimeters in order to remove diffractions from the unirradiated portion. The intensities of diffraction peaks from samples are normalized to that of a specified diffraction peak from the gold foil.

The highest peak corresponding to the (002) supercell reflection has been observed at  $18.6^\circ$  of  $2\theta$  in the XRD patterns measured for  $\text{Li}_2\text{TiO}_3$  samples [1, 2]. The reductions in the (002) supercell peak intensities are observed for the samples irradiated with the 18-160 MeV Xe ions. The peaks are observed to be unsymmetrized for both small and large angles along with the reductions in the peak intensities due to the irradiations. The reductions mean that the destruction of long-range order of the cation arrangement in superstructure of  $\text{Li}_2\text{TiO}_3$  is caused by the irradiation. The unsymmetrized peaks indicate that the expansion and contraction of the (002) supercell are caused by the irradiation. In the concrete, the irradiation causes the disorder of the arrangement of Li and Ti cations in the superstructure of  $\text{Li}_2\text{TiO}_3$ , as the quenching does the partial site mixing between Li and Ti sites in superstructure [1, 2]. The disorder due to the irradiation is accompanied by the expansion and contraction of the (002) supercell. And also, the Li and Ti cations in  $\text{Li}_2\text{TiO}_3$  have been reported to become disordered at high temperature above  $1213^\circ\text{C}$  [2]. Thus, temperature around the trajectories of incident ions is considered to instantaneously rise above  $1213^\circ\text{C}$ .

Figure 1 shows the changes of (002) peak intensities for the accumulated electronic energy deposition  $\langle D \rangle$ . The symbol  $\langle \rangle$  of  $\langle M \rangle$  stands for the average of M as the damage parameter for the damaged region estimated with the SRIM 2000 code [3]. The peak intensities are reduced with the increase in the  $\langle D \rangle$  value. In the case of the 18 MeV Xe ion irradiations with the  $\langle S_e \rangle$  of 2.8 keV/nm, the peak intensity is drastically reduced with the increase in the  $\langle D \rangle$  value for the fluence from  $2.4 \times 10^{16}$  to  $2.4 \times 10^{17} / \text{m}^2$ . The increase in the  $\langle D \rangle$  value for the fluence from  $2.4 \times 10^{17}$  to  $4.9 \times 10^{17} / \text{m}^2$  does not cause more reduction in the peak intensities. On the other hand, the increase in  $\langle S_e \rangle$  value, which is realized by the increase in the acceleration

Table 1. Irradiation conditions of  $\text{Li}_2\text{TiO}_3$ .

Ion	Xe
E (MeV)	18 - 160
$R_p$ ( $\mu\text{m}$ )	4.4 - 17
Fluence (ions/ $\text{m}^2$ )	$2.4 \times 10^{16}$ , $2.4 \times 10^{17}$ , $4.9 \times 10^{17}$
D (GGy)	0.01 - 0.24
$S_e$ (keV/nm)	5.7 - 16.7
$S_n$ (keV/nm)	0.02 - 0.12

E: energy of ions,  $R_p$ : mean projected range, D: accumulated radiation dose,  $S_e$ : electronic stopping power at near surface,  $S_n$ : nuclear stopping power at near surface.  $R_p$ ,  $S_e$  and  $S_n$  are calculated with the SRIM2000 code [3].

<sup>1</sup>OECD Halden Reactor Project

<sup>2</sup>Division of Radiation Physics, Research Institute for Advanced Science and Technology of Osaka Prefecture University

energy, causes further reduction of the peak intensity. The (002) peak is completely disappeared by the 160 MeV Xe ion irradiation at fluence of  $2.4 \times 10^{17} / \text{m}^2$ , which gives the  $\langle D \rangle$  value of 0.29 GGy for the damaged region. No change of the (002) XRD peak intensity due to the 18 MeV Xe ion irradiation is observed while the fluence was increased from  $2.4 \times 10^{17}$  to  $4.9 \times 10^{17} / \text{m}^2$ . The independence of XRD intensity from fluence increase is considered to be due to the XRD signals being originated from the non-damaged region in depth of specimen.

The cross section ( $\alpha$ ) of disorder region, which is formed along the track of high energy ion, has been given by  $I_{\Phi}/I_0 = e^{-\alpha\Phi}$ ,  $I_{\Phi}, 0$  being XRD peak intensities at fluence  $\Phi, 0$  [4, 5]. The  $\alpha$  expressed as  $\alpha = \pi r_A^2$ , where  $r_A$  is the radius of disorder region. For the  $\text{Li}_2\text{TiO}_3$  samples irradiated by the 18 MeV Xe ions, the radius  $r_A$  of disorder region is roughly estimated to be about 2.1 nm from the XRD experimental values with the above expression. For the fluence of  $2.4 \times 10^{16} / \text{m}^2$ , about 14 % of the tracks with the mean radius of 2.1 nm overlap. For the fluences of  $2.4 \times 10^{17}$  and  $4.9 \times 10^{17} / \text{m}^2$ , about 70 and 85 % of the tracks overlap, respectively. In case of 70 and 85% of the overlapping, the damaged region is considered to be completely disordered by the irradiation because the reduction in XRD peak intensities are not observed with increase of the fluence from  $2.4 \times 10^{17}$  to  $4.9 \times 10^{17} / \text{m}^2$ . For the 39 - 160 MeV Xe ion irradiated  $\text{Li}_2\text{TiO}_3$  samples, there are not enough of the XRD experimental data to estimate the radius of track.

The results of XRD analyses indicate that the long-range order in cation arrangement in superstructure of  $\text{Li}_2\text{TiO}_3$  is easily destroyed with the increase in the values of irradiation parameters such as the  $\langle D \rangle$  and the  $\langle S_e \rangle$  of the incident ions

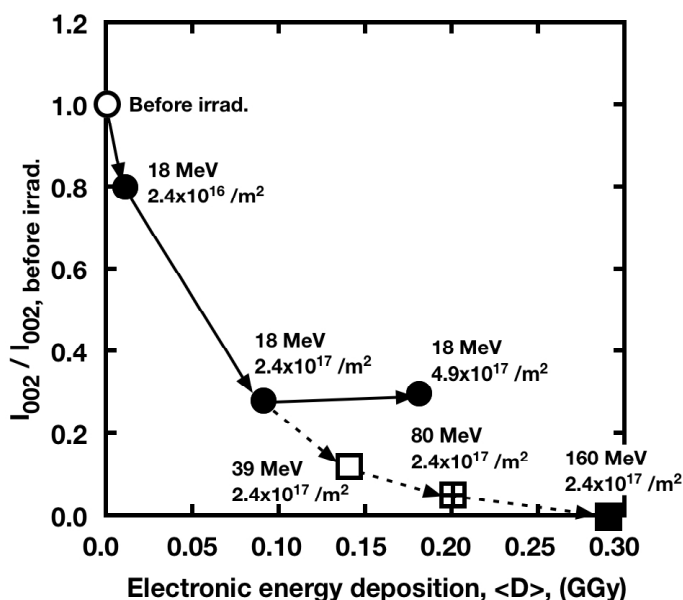


Fig. 1. Changes of X-ray diffraction peak intensities due to irradiation, plotted against accumulated electronic energy deposition,  $\langle D \rangle$ . Numerical values in figure are energies of ions and fluences.

## References

- [1] M. Castellanos and A.R. West, *J. Mater. Sci.* **14** (1979) 450.
- [2] L. Banos, M.E. Villafuerte-Castrejon, R. Valenzuela and A.R. West, *J. Chem. Soc., Faraday Trans.* **86** (1990) 2979.
- [3] J.F. Ziegler, J.P. Biersack and U. Littmark, *The Stopping and Range of Ions in Solids*, Pergamon, Oxford, 1985.
- [4] M. Toulemonde and F. Studer, *Philos. Mag.* **A58** (1988) 799.
- [5] F. Studer and M. Toulemonde, *Nucl. Instrum. Methods* **B65** (1992) 560.

## 6.9 OPTICAL SPECTROSCOPIC STUDY FOR SAPPHIRE IRRADIATED WITH HIGH ENERGY HEAVY IONS

N. OKUBO, T. NAKAZAWA, T. ARUGA, M. SATAKA and S. JITSUKAWA

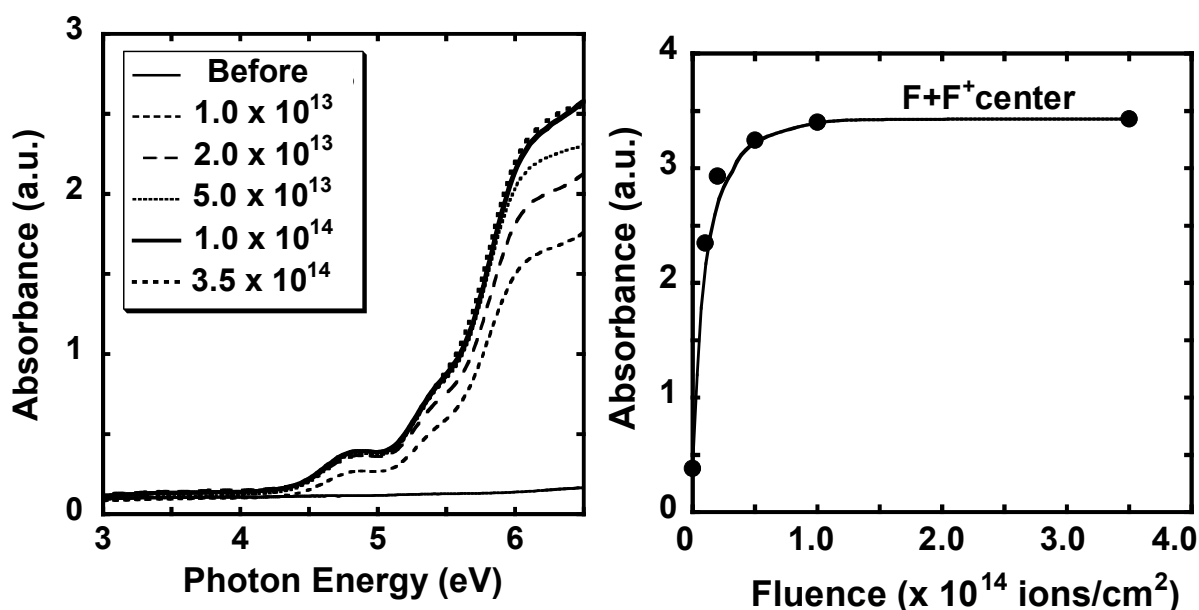
Amorphization behaviors in ceramics, such as  $\alpha$ -Al<sub>2</sub>O<sub>3</sub> induced by high energy ion irradiations, have attracted phenomenological and technological interests [1]. In our previous study, it was reported that amorphous phase was caused in polycrystalline aluminum oxide by ion irradiation with high-density electronic energy depositions ( $S_e$ ), although the lattice structure of aluminum oxide was stable against nuclear energy depositions ( $S_n$ ) [2]. The amorphization behaviors caused by high-density  $S_e$  indicated dependences on the specimen depth and grain orientation around the amorphized-crystalline region. Recently, we reported that new lattice planes, which meant lattice distorted, formed in the early stage of irradiation around the fluence of  $5.0 \times 10^{13}$  ions/cm<sup>2</sup> for single crystalline  $\alpha$ -Al<sub>2</sub>O<sub>3</sub> irradiated with 160 MeV-Xe ions [3]. Moreover, the amorphization took place by the irradiation above the fluence of  $1.0 \times 10^{14}$  ions/cm<sup>2</sup>. Detailed mechanism of the amorphization induced by ion irradiation has not been clearly understood. In this study, optical spectroscopic measurements were conducted for single crystalline  $\alpha$ -Al<sub>2</sub>O<sub>3</sub> irradiated with high energy heavy ion to obtain information on the mechanism of amorphization induced by the ion irradiation.

Single crystalline  $\alpha$ -Al<sub>2</sub>O<sub>3</sub> specimens with (0001) surface were irradiated with 160 MeV-Xe ions at ambient temperature, by using the Tandem Accelerator of JAERI. The specimens were 10 mm x 10 mm plates with 0.5 mm thickness. The fluences were in the range of  $1.0 \times 10^{13}$  to  $4.0 \times 10^{14}$  ions/cm<sup>2</sup>. The projected range ( $R_p$ ) of the Xe ions for the specimen was calculated to be 10.7  $\mu$ m with the TRIM code [4]. The electronic energy deposition ( $S_e$ ) and nuclear energy deposition ( $S_n$ ) at the surface were also calculated to be 24.5 keV/nm and 0.1 keV/nm, respectively. Optical absorbance of the specimen after irradiation was measured in a photon energy range from 1.5 to 6.5 eV, by a dual beam spectrometer.

Optical absorption spectra of the specimens before and after irradiation are shown in Fig.1. The fluence was varied from  $1.0 \times 10^{13}$  to  $3.5 \times 10^{14}$  ions/cm<sup>2</sup>. No absorption band was observed in the range of 1.0 to 4.0 eV. Two absorption bands at 4.8 and 6.05 eV appeared after irradiation and these absorption bands increased with increasing the fluence. The optical absorption bands at 4.8 and 6.05 eV were associated with the F<sup>+</sup>-center, a single electron trapped at O<sup>-2</sup> vacancy and F-center, two electron trapped similarly, respectively [5]. In Fig. 2, the absorption of F+F<sup>+</sup>-center increased rapidly up to the fluence of  $5.0 \times 10^{13}$  ions/cm<sup>2</sup> and saturated above  $1.0 \times 10^{14}$  ions/cm<sup>2</sup>. Absorption behavior of F+F<sup>+</sup> center is due to the change of oxygen-vacancy concentration produced by ion irradiation. In case of ion irradiation with high-density  $S_e$  to insulators, atomic displacement is considered to be caused around ion trajectory [1]. The saturation of the oxygen-vacancy concentration may be caused by overlapping of ion tracks, because recombination of vacancies with interstitial atoms appears to be easily caused by enhancement of ion-track overlapping. On the other hand, the fraction of formation of new

lattice planes was shown to be reduced above the fluence of  $5.0 \times 10^{13}$  ions/cm<sup>2</sup> from the XRD measurements [3]. This suggests attribution of the ion-track overlapping, where the concentration of oxygen vacancies saturated, to the formation of new lattice planes and to the following amorphization.

In summary, optical spectroscopic measurements were conducted for single crystalline  $\alpha$ -Al<sub>2</sub>O<sub>3</sub> irradiated with 160 MeV Xe ions and it was shown that the amorphization was caused around the fluence of  $1.0 \times 10^{14}$  ions/cm<sup>2</sup> through overlapping of ion tracks, where the concentration of oxygen vacancies saturated.



## References

- [1] G. Szenes, J. Nucl. Mater. **336** (2005) 81-89.
- [2] T. Aruga, Y. Katano, T. Ohmichi, S. Okayasu and Y. Kazumata, Nucl. Instrum. Methods **B 166-167** (2000) 913.
- [3] N. Okubo, T. Nakazawa, Y. Chimi, N. Ishikawa, T. Aruga and S. Jitsukawa, JAERI Tandem Annual Report, JAEA-Review **2005-004** (2006) 90.
- [4] J.F. Ziegler, J.P. Biersack, U. Littmark, The Stopping and Range of Ions in Solids, Pergamon Press, New York, Chap 8 (1985).
- [5] K.H. Lee and J.H. Crawford, J. Appl. Phys. Lett. **33** (1978) 273.



## 6.10 NEW X-RAY DIFFRACTION PEAK OF ION-IRRADIATED TiO<sub>2</sub> AT HIGH ELECTRONIC STOPPING POWER REGIME

N. ISHIKAWA, S. YAMAMOTO and Y. CHIMI

High-energy heavy ion irradiation is one of the promising tools to modify local (nanometer order) modification of the materials. Structural changes due to high-density electronic excitation have been extensively studied for various oxides irradiated with high-energy heavy ions. In this study, anatase TiO<sub>2</sub> thin film specimens were irradiated with 230 MeV <sup>136</sup>Xe ions and 200 MeV <sup>197</sup>Au ions in order to investigate possible structural changes due to high-density electronic excitation,.

The specimens were epitaxially grown single crystal thin films of TiO<sub>2</sub> with <001> TiO<sub>2</sub> // <001>SrTiO<sub>3</sub> prepared by a pulsed laser deposition method. The thickness of the films was 0.3 μm. Before irradiation, two X-ray diffraction (XRD) peaks at 2θ=37.7° and 80.4°, assigned to the (004) and (008) planes of anatase phase of TiO<sub>2</sub>, respectively, are observed. XRD patterns were measured before and after irradiation, and the irradiation-induced changes in XRD intensity and peak shape are discussed.

Firstly, we discuss the irradiation-induced decrease in XRD peak intensities in relation to track formation. The fluence dependence of XRD intensity follows an exponential function as demonstrated in Fig.1. By assuming that the ion tracks occupy part of the specimen volume according to the Poisson law, the XRD intensity can be expressed by

$$I(\Phi)=I_0\exp(-A\Phi), \quad (1)$$

where  $I(\Phi)$  is the intensity of XRD peak as a function of ion-fluence  $\Phi$ ,  $I_0$  the  $I(\Phi=0)$ , and  $A$  the area of tracks which do not contribute to XRD. Based on this recognition, the present result is explained by the formation of the cylindrical damaged regions (i.e. ion tracks) with diameters of 9.6 and 16.3nm for 230 MeV Xe and for 200 MeV Au ion irradiations, respectively. Since the electronic stopping power for the 200 MeV Au irradiation (28keV/nm) is larger than that for 230 MeV Xe irradiation (23keV/nm), we attribute the larger track diameter for the Au ion irradiation mainly to the larger electronic stopping power. Additional cause of the larger track diameter for Au ion irradiation is the higher efficiency of track formation for irradiation with lower ion velocity (so-called “velocity effect”)[1]. Possible channels for the appearance of the velocity effect are the followings: 1) Slower ion causes higher ionization which causes higher kinetic

force due to Coulomb repulsion. 2) Slower ion causes shorter range of secondary electrons which result in dense energy deposition around the ion path.

Splitting of the (004) peak is observed only for irradiation with 200MeV Au ions. The original (004)  $\text{TiO}_2$  peak remains in the same position, but the new peak shifts to higher angles as fluence increases as shown in Fig.2. The new peak observed in the present experiment does not correspond to any peaks attributable to another stable phase (rutile phase). The origin of the new peak is not clear at this moment, but it may be due to highly strained region adjacent to the large ion tracks. In contrast to the case of Xe ion irradiation, marked increases in the FWHM of the (004) reflections are observed for Au ion irradiations. This suggests the accumulation of strain due to the irradiation with 200MeV Au ions.

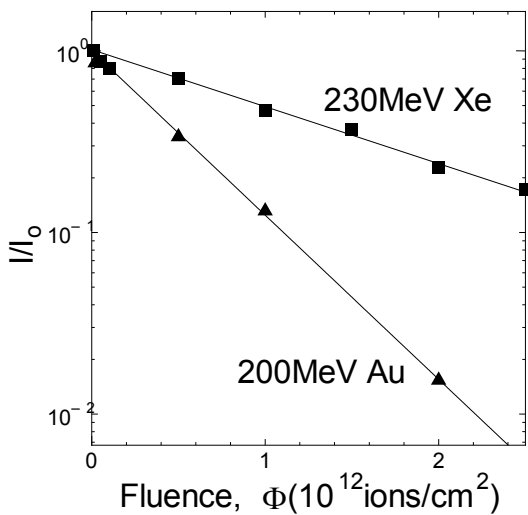


Fig.1. Intensity of (004) peak for  $\text{TiO}_2$  thin films plotted as a function of ion-fluence. The definition of  $I/I_0$  is mentioned in the text. The straight line is a fit to equation (1) assuming Poisson law.

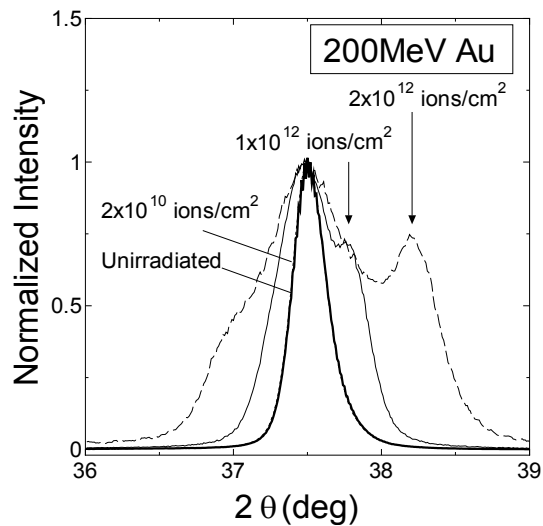


Fig.2. Evolution of (004) peak of  $\text{TiO}_2$  samples by the irradiations with 200MeV Au ions. A new peak appears in the fluence range of  $1-2 \times 10^{12}$  ions/cm<sup>2</sup>.

**Reference**

[1] A. Meftah et al., Phys. Rev. **B48** (1993) 920.

## 6.11 SWIFT HEAVY ION INDUCED FERROMAGNETIC STATE IN FeRh ALLOYS

A. IWASE<sup>1</sup>, M. FUKUZUMI<sup>1</sup>, Y. ZUSHI<sup>1</sup>, F. HORI<sup>1</sup>, Y. CHIMI and N. ISHIKAWA,

We have reported that high-energy electron irradiation decreases the ferromagnetic-antiferromagnetic transition temperature in Fe-50at.%Rh alloy[1]. In this report, we show that the swift heavy ion irradiation stabilizes the ferromagnetic state of Fe-50at.%Rh even at 20K [2,3].

Fe-50at.%Rh alloys were prepared by induction melting in vacuum, and then were cut into  $5 \times 5 \times 0.2 \text{ mm}^3$ . The specimens were irradiated with 200 MeV  $^{136}\text{Xe}$  ions to the fluence of  $5 \times 10^{12}$ ,  $1 \times 10^{13}$ ,  $5 \times 10^{13}$ ,  $1 \times 10^{14}$  and  $1 \times 10^{15} / \text{cm}^2$  at room temperature using the JAEA tandem accelerator. After and before the irradiations, the magnetization was measured at 20K as a function of external magnetic field by using Quantum Design SQUID magnetometer. The scanning range of magnetic field was from -0.6 T to +0.6 T.

In Fig. 1, we plot the magnetization- external magnetic field curves at 20 K for unirradiated Fe-50at.%Rh and those irradiated with 200 MeV Xe ions. The figure shows that the ferromagnetic state is induced by the irradiation. Figure 2 shows the saturated values of magnetization as a function of ion-fluence. The ferromagnetism develops until the fluence around  $5 \times 10^{13} / \text{cm}^2$ , and then the magnetization decreases with the increase of ion-fluence.

To estimate the defect concentration primarily produced by Xe irradiation, we performed Doppler-broadening experiments for unirradiated Fe-50at.%Rh alloy and that irradiated with 200 MeV  $^{136}\text{Xe}$  ions by using a slow positron beam[4]. The S-parameter increases gradually with increasing the ion-fluence up to  $5 \times 10^{12}$  ions /  $\text{cm}^2$ . Above  $5 \times 10^{12}$  ions /  $\text{cm}^2$ , the values of S-parameter are saturated. From the dependence of S-parameter on ion-fluence, we have calculated the concentration of vacancy-type defects surviving in the specimen, which is much smaller than that estimated by TRIM-code. The result implies that anti-site type defects dominantly remain in the irradiated specimen, which stabilize the ferromagnetic state in Fe-50at.%Rh alloy. In heavily irradiated specimens, the XRD profiles show that the B2- lattice structure is destroyed, leading to the decrease in magnetization.

The authors would like to thank Dr. A. Kawasuso for the S-parameter measurements using positron beam.

---

<sup>1</sup> Osaka Prefecture University

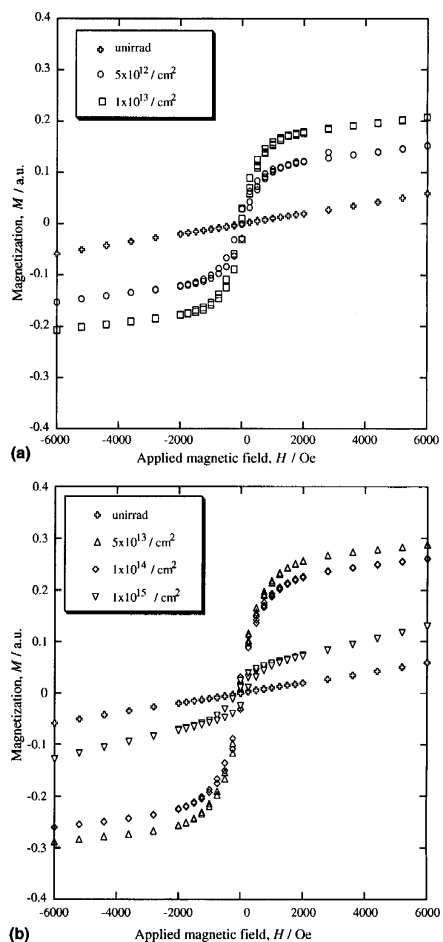


Fig. 1. Magnetization of unirradiated and Xe ion irradiated Fe-50%Rh alloys at 20 K as a function of external magnetic field.

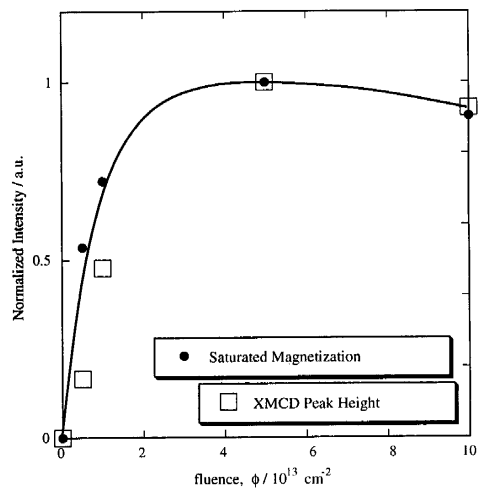


Fig. 2. Dependence of magnetization at 20 K on Xe ion-fluence. In the figure, XMCD result is also plotted, which is, however, not mentioned in this report.

**References**

[1] M. Fukuzumi, R. Taniguchi, S. Komatsu, F. Ono and A. Iwase, *Mat. Res. Soc. Symp. Proc.* **792** (2004) 393.  
 [2] M. Fukuzumi, Y. Chimi, N. Ishikawa, F. Ono, S. Komatsu and A. Iwase, *Nucl. Instrum. Methods* **B230** (2005) 269.  
 [3] M. Fukuzumi, Y. Chimi, N. Ishikawa, M. Suzuki, M. Takagaki, J. Mizuki, F. Ono, R. Neumann and A. Iwase, *Nucl. Instrum. Methods* **B245** (2006) 161.  
 [4] M. Fukuzumi, A. Kawasuso, Y. Zushi, Y. Chimi, N. Ishikawa, A. Iwase and F. Hori, *Physica B*, to be published.

## 6.12 INCREASE IN CURIE TEMPERATURE FOR Fe-Ni ALLOY THIN FILMS BY ENERGETIC HEAVY ION IRRADIATION

Y. CHIMI, N. ISHIKAWA, A. IWASE<sup>1</sup> and F. ONO<sup>2</sup>

We have studied effects of high-energy heavy ion irradiation on magnetic properties in Fe-Ni invar alloys [1-4]. So far, we have found that the Curie temperature,  $T_C$ , for Fe-Ni invar alloys increases by the irradiation. This result indicates that the irradiation induces ferromagnetic regions in the paramagnetic phase above  $T_C$  for Fe-Ni invar alloys. In our previous papers [1-4], the cause of this phenomenon was discussed on the electronic excitation as well as on the elastic displacement, but it still remains unclear. Since the projected ranges of the ions were so short in our bulk alloys that not only the electronic excitation but also the elastic displacement could occur in the same specimen, we could not determine which process was dominant for the phenomenon. In order to clarify the cause of the phenomenon, therefore, the single parameter experiment by using thin film specimens is indispensable. In the present work, we have investigated the increase in  $T_C$  for Fe-Ni alloy thin films by several kinds of energetic heavy ion irradiation, and tried to determine the cause of the phenomenon.

The specimens of Fe-Ni (Ni concentration of ~32 at.%) alloy thin films (~500 nm in thickness) were irradiated at room temperature with 200-MeV <sup>197</sup>Au or <sup>136</sup>Xe ions to the fluence of  $1 \times 10^{11}$ - $1 \times 10^{14}$  cm<sup>-2</sup>. The energy of the incident ions to the specimen was degraded to ~1.9-34.9 MeV by penetrating into Al foils with 12.5-19.0 μm thick. Moreover, for precise detection of the change in  $T_C$ , a half of the specimen was unirradiated by means of a masking technique and both irradiated and unirradiated regions were produced in the same specimen. After the irradiation, measurements of AC-susceptibility of the specimen were performed up to ~500 K and the change in  $T_C$  for each irradiation was detected.

Figure 1 shows the temperature dependence of the normalized AC-susceptibility,  $\chi_{AC}$ , for 200-MeV and 20.7-MeV Au ion irradiations. Although no change in  $T_C$  was detected in the case of 200-MeV Au ion irradiation, a large increase in  $T_C$  of ~20 deg. was observed for 20.7-MeV Au ion irradiation. In the present analyses, the value of  $T_C$  was defined as the peak temperature of the temperature derivative of the AC-susceptibility. For 20.7-MeV Au ion irradiation, the value of nuclear stopping power,  $S_n$ , of 3.0 MeV/(mg/cm<sup>2</sup>) is larger than that for 200-MeV Au ion irradiation of 0.56 MeV/(mg/cm<sup>2</sup>), though the electronic stopping power,  $S_e$ , decreases as ion energy decreases in this energy range (54 MeV/(mg/cm<sup>2</sup>) and 8.0 MeV/(mg/cm<sup>2</sup>) for 200-MeV and 20.7-MeV Au ion irradiations, respectively). This result implies that the phenomenon is caused mainly by the elastic displacements.

The change in  $T_C$ ,  $\Delta T_C$ , by several kinds of ion irradiations is shown in Fig. 2 as a function of the total deposited energy by (a) the electronic excitation,  $\Phi \times S_e$ , and by (b) the elastic displacement,  $\Phi \times S_n$ . As can be seen in the figure, increase in  $T_C$  does not depend on the electronic energy deposition, but on the elastic energy deposition. This result also suggests that the elastic displacement is dominant process for the phenomenon.

<sup>1</sup>Department of Materials Science, Osaka Prefecture University

<sup>2</sup>Department of Physics, Okayama University

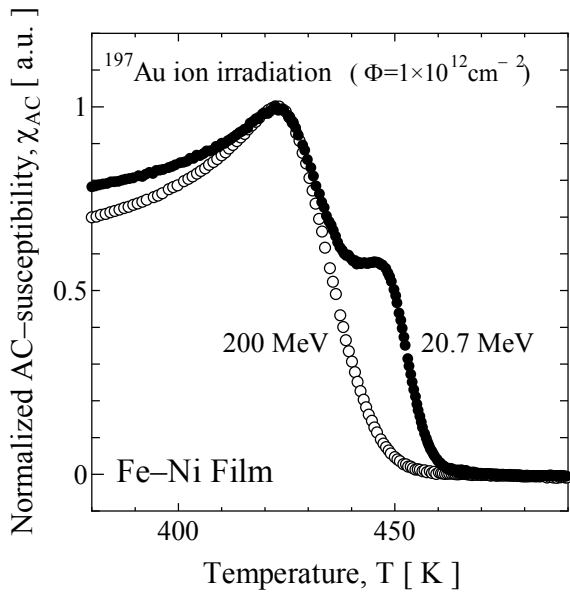


Fig. 1. Temperature dependence of normalized AC-susceptibility,  $\chi_{AC}$ , for 200-MeV and 20.7-MeV Au ion irradiations.

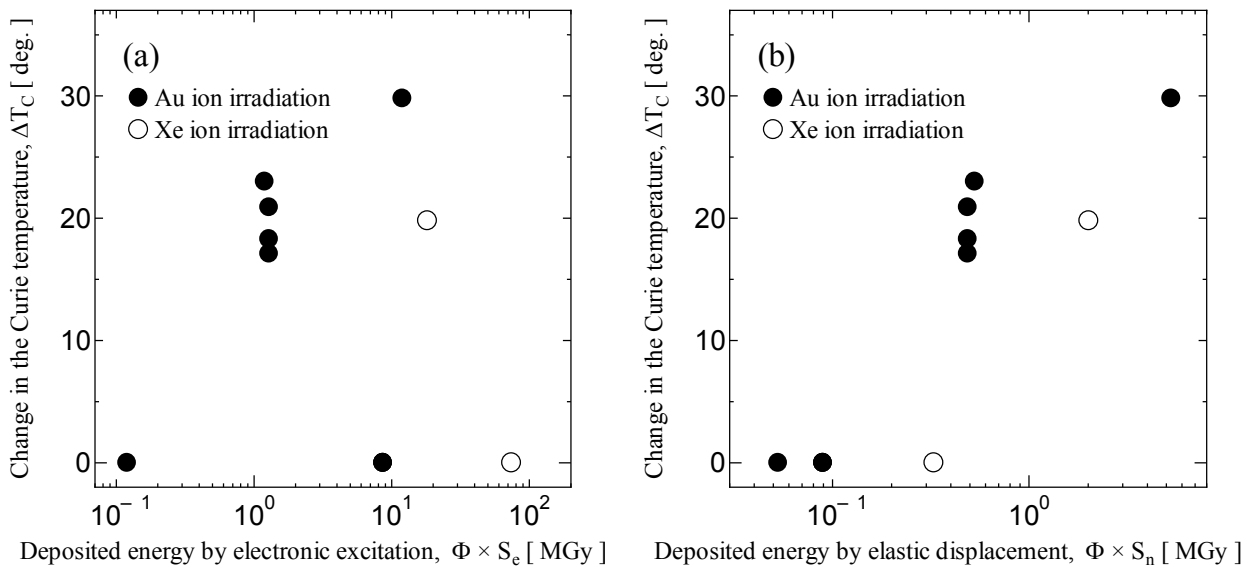


Fig. 2. Change in the Curie temperature,  $\Delta T_C$ , as a function of total deposited energy by (a) electronic excitation,  $\Phi \times S_e$ , and by (b) elastic displacement,  $\Phi \times S_n$ .

## References

- [1] F. Ono, Y. Hamatani, Y. Mukumoto, S. Komatsu, N. Ishikawa, Y. Chimi, A. Iwase, T. Kambara, C. Muller and R. Neumann, Nucl. Instrum. Methods **B206** (2003) 295.
- [2] A. Iwase, Y. Hamatani, Y. Mukumoto, N. Ishikawa, Y. Chimi, T. Kambara, C. Muller, R. Neumann and F. Ono, Nucl. Instrum. Methods. **B209** (2003) 323.
- [3] F. Ono, S. Komatsu, Y. Chimi, N. Ishikawa, T. Kambara and A. Iwase, Mat. Res. Soc. Symp. Proc. **792** (2004) 441.
- [4] F. Ono, S. Komatsu, Y. Chimi, N. Ishikawa, A. Iwase and T. Kambara, Nucl. Instrum. Methods. **B230** (2005) 279.

### 6.13 EFFECT OF HIGH-ENERGY HEAVY ION IRRADIATION ON MAGNETIC PROPERTIES IN Fe-Pd INVAR ALLOYS

F. ONO<sup>1</sup>, H. KANAMITSU<sup>1</sup>, N. Q. SUN<sup>1</sup>, Y. MATSUSHIMA<sup>1</sup>, A. IWASE<sup>2</sup>, Y. CHIMI,  
N. ISHIKAWA and T. KAMBARA<sup>3</sup>

Fe-Pd alloys around the Pd-composition of 30-35at.% are known to show low or even negative thermal expansion in low temperature region [1]. This anomaly in thermal expansion is also seen in Fe-Ni and Fe-Pt alloys with nearly the same concentration of the second element, and has been understood as a result of the instability of the band ferromagnetism in fcc phase. The concentrations of the second element of those alloys are close to the boundary of the martensitic phase transition [2]. Our group has made high-energy ion irradiation on Fe-Ni Invar alloys [3-7]. We found that the Curie temperature  $T_C$  increases almost 100 K by an irradiation with 200 MeVXe-ions to the fluence of  $10^{14}$  ions/cm<sup>2</sup>. In Fe-Pt Invar alloy, however, a decrease of  $T_C$  of about 15 K was observed after the irradiation [8]. Therefore, it seems interesting to investigate the irradiation effect on Fe-Pd Invar alloy that exhibits the same type of Invar anomalies as seen in Fe-Ni and Fe-Pt alloys.

Specimens of disordered Fe-34 at.%Pd Invar alloy were in a form of thin rectangular discs of  $3 \times 3$  mm<sup>2</sup> and the thickness of 240  $\mu$ m. They were irradiated with 200 MeV Xe-ions to the fluency up to  $10^{14}$  ions/cm<sup>2</sup>. AC-susceptibility measurements were made using a specially designed apparatus for rapid temperature variation. The range of the Xe-ions was 9  $\mu$ m, which was much smaller than the thickness of the sample.

Observed AC-susceptibility versus temperature curves before and after the high-energy Xe-ion irradiation are shown in Fig. 1. As seen in this figure the curve has two steps. The first step corresponds to the  $T_C$  for non-irradiated part, while the second step indicate that of the irradiated part. The Curie temperature increased 12 K by the irradiation of  $10^{13}$  ions/cm<sup>2</sup>. The decrease of the Curie temperature is about 10K at the irradiation of  $10^{14}$  ions/cm<sup>2</sup>. The amount of the shift of  $T_C$  in Fe-Pd Invar alloy is just in the middle of the irradiation effect between Fe-Ni Invar alloy where a large increase was observed and Fe-Pt Invar alloy where a decrease of  $T_C$  was found.

It was found that the type of modification of the magnetic properties is quite different from one another among three typical Fe-based Invar alloys. A possibility for an application as high-density magnetic memory and giant magneto-resistance materials seems to remain only in Fe-Ni Invar alloys.

By comparing those three different experimental results in Fe-Ni, Fe-Pt and Fe-Pd Invar alloys, it is concluded that there exist at least two factors that contribute to the shift of the Curie temperature. One, which contributes to increase  $T_C$ , is acting as a negative pressure introduced through the expansion of the crystal lattice by the irradiation. Another possible factor which contributes to the decrease of  $T_C$  is selective knocking

<sup>1</sup> Graduate School of Natural Science (Department of Physics), Okayama University

<sup>2</sup> Graduate School of Engineering, Osaka Prefecture University

<sup>3</sup> Atomic Physics Laboratory, The Institute of Physical and Chemical Research

out of atoms that have larger atomic radius.

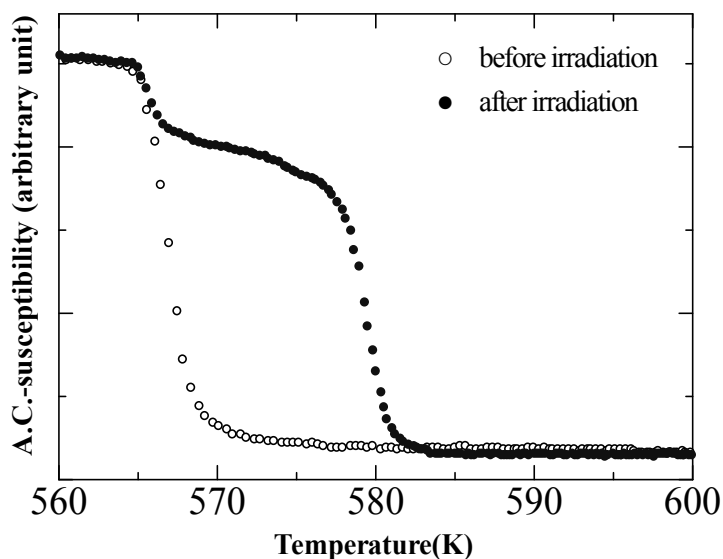


Fig. 1. AC-susceptibility-temperature curves in Fe-Pd Invar alloy before ( $\circ$ ) and after ( $\bullet$ ) the irradiation of 200MeV Xe to the fluence of  $10^{13}$  ions/cm<sup>2</sup>.

## References

- [1] For example, see “*The Invar Effect: A Centennial Symposium*” ed. by J. Wittenauer, The Minerals, Metals and Materials Society (1997).
- [2] F. Ono, L. Bang and H. Maeta, in [1], p.197.
- [3] F. Ono, Y. Hamatani, Y. Mukumoto, S. Komatsu, N. Ishikawa, Y. Chimi, A. Iwase, T. Kambara, C. Muller and R. Neumann, Nucl. Instrum. Methods Phys. Res. **B206** (2003) 295.
- [4] A. Iwase, Y. Hamatani, Y. Mukumoto, N. Ishikawa, Y. Chimi, T. Kambara, C. Muller, R. Neumann and F. Ono, Nucl. Instrum. Methods Phys. Res. **B209** (2003) 323.
- [5] F. Ono, S. Komatsu, Y. Chimi, N. Ishikawa, T. Kambara and A. Iwase, Mat. Res. Soc. Symp. Proc. **792** (2004) 441.
- [6] Y. Matsushima, F. Ono, H. Kanamitsu, S. Komatsu, A. Iwase, Y. Chimi, N. Ishikawa and T. Kambara, JAEA-Review **2004-027** (2004) 86.
- [7] F. Ono, S. Komatsu, Y. Chimi, N. Ishikawa, A. Iwase and T. Kambara, Nucl. Instrum. Methods Phys. Res. **B230** (2005) 279.
- [8] F. Ono, H. Kanamitsu, Y. Matsushima, Y. Chimi, N. Ishikawa, T. Kambara and A. Iwase, Nucl. Instrum. Methods Phys. Res. **B245** (2006) 166.



## 6.14 ELECTRONIC EXCITATION EFFECTS ON SECONDARY ION EMISSION FROM SOLID MATERIALS BOMBARDED BY HEAVY IONS

T. SEKIOKA<sup>1</sup>, M. TERASAWA<sup>1</sup> and M. SATAKA

The interaction between swift heavy ions and solids has been an active research area. We have been studying secondary ion mass spectrometry from thin conductive solid targets irradiated with heavy ion beams from the JAERI tandem accelerator in the energy region where the electronic stopping power is dominant. A thin Cu or Au foil target of 1000 to 2000 Å thickness evaporated on C-foils of  $8.5\mu\text{g}/\text{cm}^2$  was irradiated with high-energy heavy ion beams from the tandem accelerator. The secondary ions ejected from the front surface of the target were collected by a time of flight (TOF) mass spectrometer by applying an acceleration voltage of  $-500\text{V}$  and detected by an electron multiplier. Secondary electrons from the back side of the target were detected by another electron multiplier and this signal was used as the start signal of the TOF. Using this TOF system, we have investigated the dependence of the yield of the secondary ions of  $\text{Cu}^+$  from Cu target on the electronic stopping power, and it is found that the secondary ion yield shows a significant increase with increasing electronic stopping power, which has approximately  $S_e^2$ -dependence. This suggests that even in the conductive materials, the electronic excitation effects play an important role in the secondary ion sputtering [1]. The yield of the  $\text{Au}^+$  secondary ions from Au target is very small as compared with the yield of the  $\text{Cu}^+$  secondary ions from Cu target. Although immediately before the secondary ions measurement, we maintained the temperature of the Au target about  $500^\circ\text{C}$  by infrared radiation heating for two hours in the vacuum of  $1.6 \times 10^{-6}$  Pa, the target cleaning is still insufficient to obtain the reproducible data on the secondary  $\text{Au}^+$  ion yield from Au target.

It is important to study the secondary ion mass spectroscopy in a wide range of electronic stopping power with various combinations of projectiles and conductive targets under low background. We are now developing a new TOF system which is shown in fig. 1. The secondary electrons emitted from a thin C-foil located at the upper stream of the target are detected by an electron multiplier. This signal is used as the start signal for the TOF. The secondary ions are detected by a multiple channel plate (MCP) in the TOF with a flight pass of 20 cm, which is much longer than the old TOF system. The target cleaning is carried out by a few keV ion beams which are expected to be more efficient than the infrared radiation heating. So far, the targets we studied have been limited to thin foils. However with this new TOF system, we can study the

---

<sup>1</sup> Graduate School of Engineering, University of Hyogo

electronic excitation effect in conductive materials which is difficult to make a thin foil, and also we can widen the scope of our study to the electronic excitation effect in semiconductor and insulator target materials bombarded by swift heavy ions beam.

### New Experimental Setup

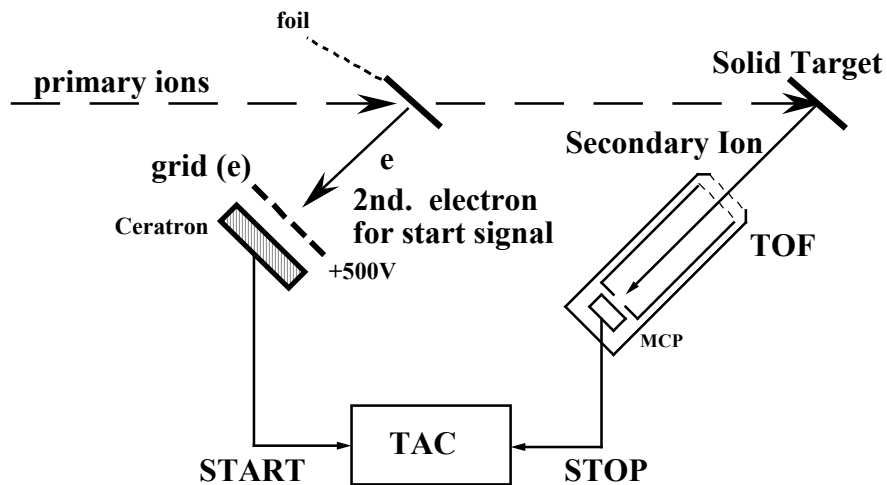


Fig.1. The schematic drawing of the new experimental setup.

### References

- [1] T. Sekioka, M. Terasawa, M. Sataka, S. Kitazawa and M. Niibe, Nucl. Instrum. Methods **B193** (2002) 751.

## **CHAPTER 7**

### **Radiation Effects in Materials**

- 7.1 Depth Profile and Temperature Effect of Ion Tracks in  $\text{CeO}_2$  under Irradiation with High Energy Ions
- 7.2 Radiation Effects on Mechanical Properties of Carbon Alloys and the Annealing Effects
- 7.3 Effects of Zr Ion Irradiation on Some Properties of Superplastic Ceramic 3Y-TZP, II
- 7.4 Semiconductor-metal Phase Transition of Iron Disilicide ( $\beta\text{-FeSi}_2$ ) Thin Films by High Energy Heavy Ion Irradiation.
- 7.5 Release Behavior of Implanted Xe from Zr - Implantation of Xe in Zr -



## 7.1 DEPTH PROFILE AND TEMPERATURE EFFECT OF ION TRACKS IN CeO<sub>2</sub> UNDER IRRADIATION WITH HIGH ENERGY IONS

T. SONODA<sup>1</sup>, M. KINOSHITA<sup>1</sup>, N. ISHIKAWA, Y. CHIMI, M. SATAKA and A. IWASE<sup>2</sup>

In order to progress high burnup extension of LWR fuels, formation and growth mechanism of a crystallographic re-structuring in the periphery region of high burnup fuel pellets, as named “rim structure” [1] should be clarified. This structure is characterized by the existence of highly dense small sub-grains whose size is approximately 200 nm, and the accumulation of small pores with average size around 1 μm. The structure shall be formed by the accumulation and mutual interactions of radiation damages, fission products (FPs) and electronic excitations deposited partially by nuclear fissions [2].

In order to clarify the electric excitation effects in fluorite structure ceramics, especially to understand the properties and accumulation effects of ion tracks that are formed by high dense electronic excitation, 70 – 210 MeV FP ions (Xe, I, Zr) irradiation examinations on CeO<sub>2</sub>, as a simulation of fluorite ceramics of UO<sub>2</sub>, have been done at JAEA-Tandem facility. Microstructural evolutions in the irradiated samples are observed in a 300kV FE-TEM (HF-3000) at CRIEPI. This study was financially supported by the Budget for Nuclear Research of the Ministry of Education, Culture, Sports, Science and Technology, based on the screening and counseling by the Atomic Energy Commission.

High dense electronic excitation effects by high energy ions irradiation produce a typical radiation damage, “ion tracks”, in CeO<sub>2</sub>. Fig. 1 indicates the mean diameter of ion tracks by 100 MeV Xe<sup>+14</sup> and 210 MeV Xe<sup>+14</sup> ion irradiation as a function of irradiation temperature (°C) with the typical bright field images. This figure shows that the mean diameter decreased around 23% at 800°C. Though the inner structure seems to be slightly recovered at around 600°C, the image of ion tracks are still clearly observed till 800°C. This result indicates that the temperature range from room temperature to 800°C does not significantly affect annealing of ion tracks.

The affected area of electronic excitation by fissions in CeO<sub>2</sub> has been clarified to be around 5 ~ 7 nm φ [3]. In order to take the high dense electronic excitation effects into a kinetic equation of radiation damage behavior under nuclear fission, the length of ion tracks, that is the information of depth profile of ion tracks, should be needed. Fig. 2 (a) shows the depth profile of an electronic stopping power (S<sub>e</sub>) and nuclear stopping power (S<sub>n</sub>) of 210 MeV Xe<sup>+14</sup> ion in CeO<sub>2</sub>, that was estimated by SRIM 2003 code [4]. Fig. 2 (b) indicate the typical cross-sectional microstructures of CeO<sub>2</sub> under irradiation with 210 MeV Xe ions to a fluence of 1 x 10<sup>14</sup> ions/cm<sup>2</sup>, whose specimen is sampled by the focused ion beam (FIB) method. Four images in Fig. 2 (b) show the typical TEM images at a depth of ~ 2.7μm (i), ~7.0μm (ii-iii) and ~10.3μm (iv), respectively. At a depth of ~ 2.7μm, ion tracks are clearly observed (Fig. 2 (b-i)). The diameter of ion tracks become decreasing as the position becomes deeper and deeper, and the images of ion tracks become invisible at the depth of ~ 7.0 μm, as shown in Fig. 2 (b-ii, iii). At the depth of ~10.3μm (Fig. 2 (b- iv)) whose S<sub>e</sub> was decreased and S<sub>n</sub> became bigger, relatively, high dense defect clusters were observed. These figures indicate that the length of ion track will be ~ 7.0 μm in case of 210 MeV Xe<sup>+14</sup> irradiation in CeO<sub>2</sub>. This result suggests that the threshold S<sub>e</sub> of ion track formation in CeO<sub>2</sub> will be ~ 16 keV/nm.

<sup>1</sup> Sector, Nuclear Power Generation Technology, Nuclear Technology Research Laboratory, Central Research Institute of Electric Power Industry (CRIEPI)

<sup>2</sup> Department of Materials Science, Osaka Prefecture University

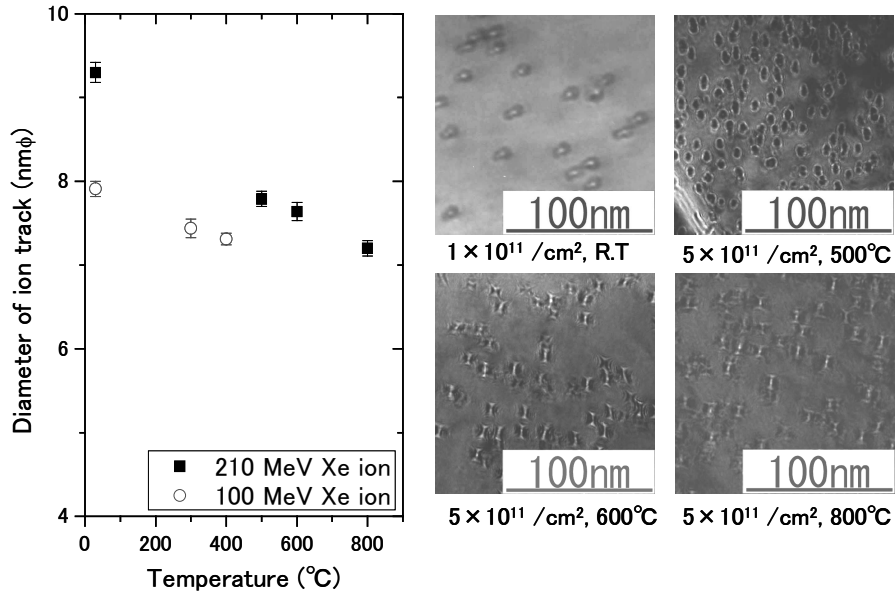


Fig. 1. Mean diameter of ion tracks by 210 MeV and 100 MeV Xe ion irradiation as a function of irradiation temperature (°C), and the typical TEM images.

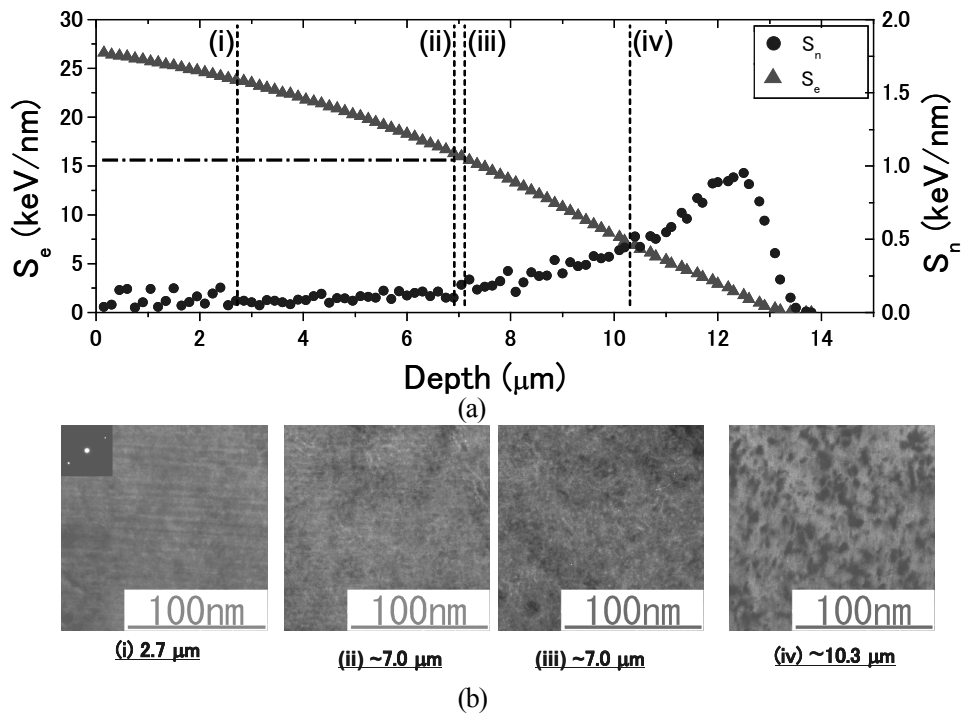


Fig. 2. Depth profile of an electronic stopping power ( $S_e$ ) and nuclear stopping power ( $S_n$ ) of 210 MeV Xe ion in  $CeO_2$  (a), and the typical cross-sectional microstructures of  $CeO_2$  under irradiation with 210 MeV Xe ions to a fluence of  $1 \times 10^{14}$  ions/cm<sup>2</sup>(b).

**References**

[1] J.O. Barner, M.E. Cunningham, M.D. Freshley, and D.D. Lanning, HBEP-61, 1990, Battelle Pacific Northwest Laboratories.  
 [2] T. Sonoda, M. Kinoshita, I.L.F. Ray, T. Wiss, H. Thiele, D. Pellottiero, V.V. Rondinella and Hj. Matzke, Nucl. Instrum. Methods. **B191** (2002) 622.  
 [3] T. Sonoda, M. Kinoshita, Y. Chimi, N. Ishikawa, M. Sataka and A. Iwase, Nucl. Instrum. Methods. **B** (2006), in press.  
 [4] J.F. Ziegler, J.P. Biersack and U. Littmark, “The stopping and Range of Ions of Solids”, Pergamon Press, New York (1985).

## 7.2 RADIATION EFFECTS ON MECHANICAL PROPERTIES OF CARBON ALLOYS AND THE ANNEALING EFFECTS

A. KURUMADA<sup>1</sup>, Y. IMAMURA<sup>1</sup>, T. OKU<sup>2</sup>,  
K. SAWA, T. SHIBATA, S. BABA, J. AIHARA and S. HANAWA

Carbon materials have been taken as one of the candidate materials for core structural components of the high temperature gas cooled reactors and for plasma facing components of the fusion experimental devices, since they have good nuclear characteristics, high thermal conductivity and excellent mechanical properties at high temperatures. Their material properties, however, change due to radiation damage and their thermal conductivities at high temperatures are not sufficient in order to apply them for the high performance reactors and the next fusion devices. Therefore, it is necessary to study on the changes of the material properties and the microstructures due to radiation damage and to develop the excellent carbon composite materials that have more stable properties to radiation damage and higher thermal conductivity at high temperatures. Recently, carbon/copper-based materials with high thermal conductivity and good stability at high temperatures, which are named carbon alloys, have been developed by adding a small amount of titanium.[1] In this study, high energy ions of nickel are irradiated to the carbon alloys and the changes of the mechanical properties are evaluated. And the recovery phenomenon of the mechanical properties is also examined by the heat treatment at high temperatures after irradiation.

Materials tested in this study are two kinds of carbon alloys with high thermal conductivity and good stability at high temperatures. The isotropic fine-grained nuclear grade graphite and the felt type C/C composite have been impregnated by copper (10-18 vol.%) and titanium (0.5-0.8 vol.%).[1] The samples from the IG-430U/CuTi and the CX-2002U/CuTi carbon alloys are polished to a mirror finish so as to easily distinguish copper grains from carbon matrix. Nickel ions ( $\text{Ni}^{13+}$ ) of 200 MeV with 0.4  $\mu\text{A}$  are irradiated to the samples of carbon alloys by the TANDEM accelerator in Tokai, JAEA. The maximum radiation damage and the range of nickel ions calculated by TRIM-98 code are 0.45 dpa and 28.6  $\mu\text{m}$  for the carbon material of 1.9  $\text{g}/\text{cm}^3$ , respectively. For the copper material, they have been calculating now.

Mechanical properties are evaluated by a dynamic ultra micro hardness tester (DUH-201) made by Shimadzu Co. The dynamic hardness (DH) is corresponding to the Vickers hardness and is defined as follows.[2] We can evaluate the change of the mechanical properties at the surface area of several  $\mu\text{m}$ .

$$\text{DH} = \alpha L/h^2 \quad (\alpha ; \text{shape factor of } 3.8584, \quad L; \text{load}, \quad h; \text{depth of indenter})$$

---

<sup>1</sup> Faculty of Engineering, Ibaraki University

<sup>2</sup> Honorary Professor, Ibaraki University

Fig.1 shows the changes of the dynamic hardness at copper (a) and carbon (b) parts in the carbon alloys, respectively. In the case of copper parts (a) in the carbon alloys, the dynamic hardness increases about 15% by Ni ion irradiation, and recovers to the similar value of the original material due to a heat treatment at 673 K for 100 minutes after irradiation. One of the reasons is considered that lattice defects due to irradiation are moved easily and disappear at copper parts in the carbon alloys by the heat treatment because copper materials begin recrystallization from about 473 K. In the case of carbon parts (b) in the carbon alloys, the dynamic hardness increases about 75% by Ni ion irradiation. The mechanical properties of carbon parts increase more than that of copper parts in the carbon alloys. And the properties recover little due to the heat treatment at 673 K for 100 minutes after irradiation. One of the reasons is considered that the temperature of the heat treatment is too low for carbon materials because the interstitial atoms and pores due to irradiation begin disappearing from about 1573 K. These tendencies of the changes of the CX-2002U/CuTi carbon alloy are similar to that of the IG-430U/CuTi carbon alloy. However, the dynamic hardness in this study has been measured at the surface area of several  $\mu\text{m}$ , the radiation damage at the tip area of the indenter is investigated in detail from now. And the radiation effect on mechanical properties of each component of the carbon alloys is planned to be evaluated finally.

**References**

- [1] T. Oku, A. Kurumada, T. Sogabe, T. Oku, T. Hirooka and K. Kuroda, J of Nuclear Materials, **257** (1998) 59.
- [2] Shimadzu Co., Handling Explanatory Node of Dynamic Ultra Micro Hardness Tester, p.5-1.

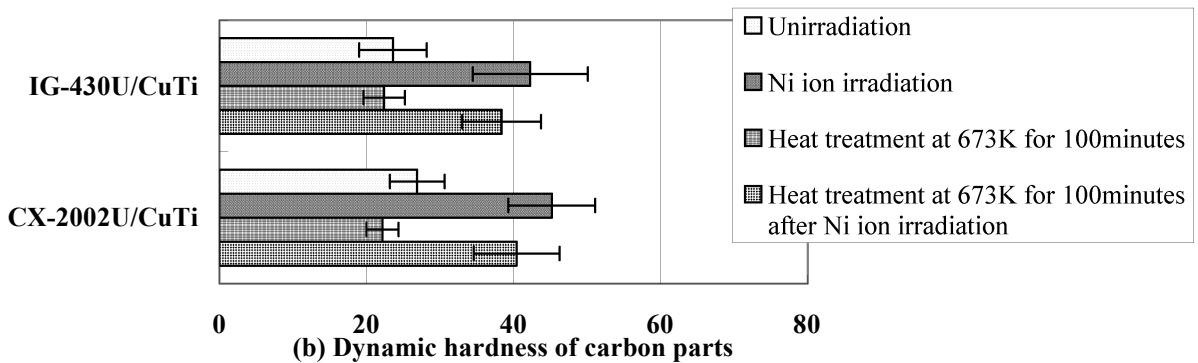
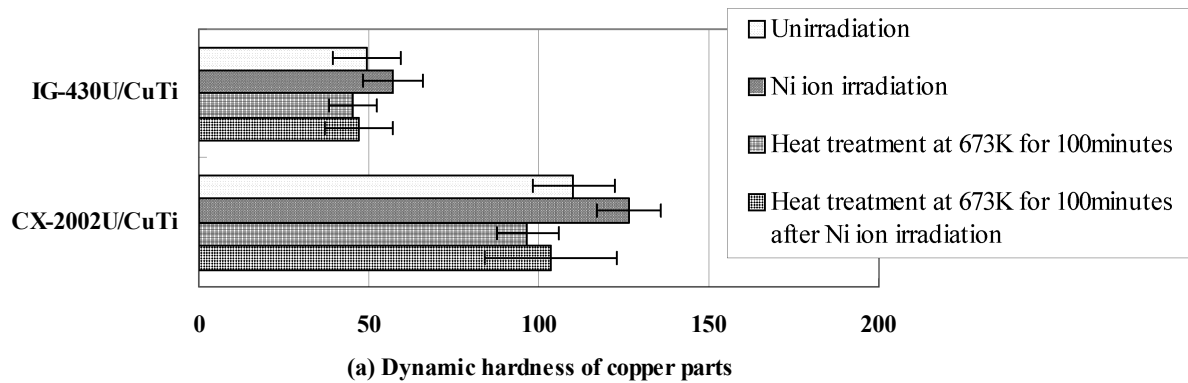


Fig.1. Changes of dynamic hardness due to ion irradiation and heat treatment.



### 7.3 EFFECTS OF Zr ION IRRADIATION ON SOME PROPERTIES OF SUPERPLASTIC CERAMIC 3Y-TZP, II

Y.MOTOHASHI<sup>1</sup>, T.SAKUMA<sup>1</sup>, T.SHIBATA, S.BABA, J.AIHARA and K.SAWA

Superplastic ceramics usually possess high heat-, high oxidative-, and high wear- resistance as well as potential ability to be formed into complicated shapes by means of plastic working under superplastic state. Although the application of the superplastic ceramics to nuclear energy field is very promising, there have been only a few studies relating to the irradiation effects on them [1-6]. Tetragonal ZrO<sub>2</sub> polycrystal containing 3mol% Y<sub>2</sub>O<sub>3</sub> (3Y-TZP) is well known as a typical superplastic ceramic. We have investigated some superplastic characteristics of Zr-ion irradiated 3Y-TZP, and have shown in previous works [2,4] that the flow stress and apparent activation energy for the superplastic deformation of the 3Y-TZP are increased by the Zr-ion irradiation. In addition, we studied the effects of Zr-ion irradiation and subsequent annealing on room temperature mechanical and microstructural properties of the 3Y-TZP. Only lately, we have carried out Zr ion irradiation with higher fluence than that performed in previous works [5,6] to 3Y-TZP. In the present study, some effects on mechanical properties of the 3Y-TZP of Zr-ion irradiation with higher fluence are evaluated and the results are compared and discussed briefly with the previous results [3,5,6].

Chemical composition of the 3Y-TZP is ; Y<sub>2</sub>O<sub>3</sub>=5.15, HfO<sub>2</sub>=1.7, Al<sub>2</sub>O<sub>3</sub>≤0.10, SiO<sub>2</sub>≤0.02, Fe<sub>2</sub>O<sub>3</sub>≤0.01, Na<sub>2</sub>O≤0.04 and ZrO<sub>2</sub> = bal., in mass%. The shape of the 3Y-TZP specimens is a rectangular thin plate with the dimension of 1×2×20mm<sup>3</sup>. One of the widest side surfaces (2×20mm<sup>2</sup>) of the specimen was polished to mirror-like plane, and the Zr<sup>+11</sup> ions were irradiated normal to this polished plane. They were irradiated using 130MeV Zr<sup>+11</sup> ions at the TANDEM accelerator facility. Irradiation was performed with the fluence of 1.5×10<sup>14</sup> and 2.1×10<sup>13</sup> ions/cm<sup>2</sup>. The latter is the same amount of fluence as one of the irradiations used in previous works [2-6] so that we can use it as a reference. The irradiation induced displacements per atom (dpa) was estimated from Monte Carlo simulations using the TRIM code [7] and are shown in Fig.1. The TRIM simulations indicate that the peak damage emerges at a depth of approximately 10μm from the irradiated surface. Room temperature hardness and fracture toughness were measured by a Vickers Micro-hardness tester and by the Indentation Fracture (IF) method, respectively.

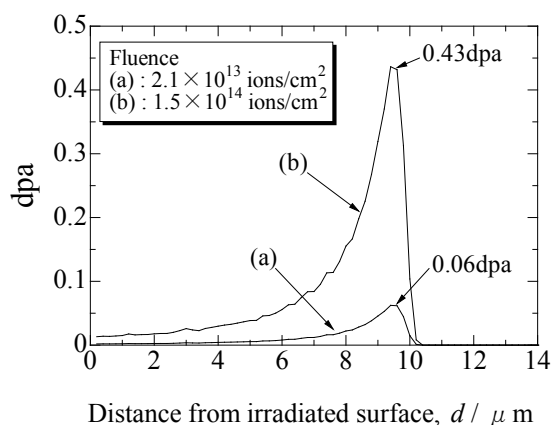


Fig.1. Displacement per atom(dpa) as a function of distance from irradiated surface.

Figures 2 and 3 show variations in Vickers hardness and fracture toughness, measured on the irradiated planes of the specimens, as a function of the amount of fluence. Since the indentation traces formed were around 27μm in diagonal length and around 5.5μm in depth at the apex of the indenter, it is certain that the hardness values measured would be affected by the peak damage. It is seen that the hardness and fracture toughness values were increased with the amount of fluence, i.e., the amount of irradiation. We have already shown that compressive residual stress, the magnitude of which depends on the amount of irradiation, is produced in the irradiated surface region. The irradiated ions lose their energy by electronic excitation of the target material, and then lose it by atomic displacements [8]. The near-surface compressive stress must be generated by these

processes, and then it resulted in the increase of the hardness and toughness.

<sup>1</sup>The Research Center for Superplasticity, Faculty of Engineering, Ibaraki University.

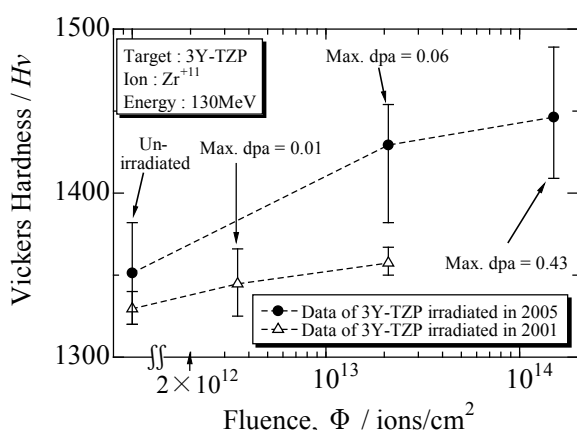


Fig.2. Variation in hardness with amount of fluence.

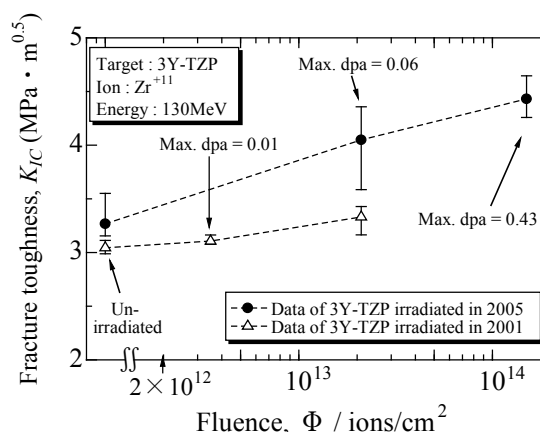


Fig.3. Variation in fracture toughness with amount of fluence.

Fig. 4 shows the amount of implanted Zr-ions as a function of the distance from the irradiated surface. It is evident that the implanted Zr-ions are accumulated in a region about 10 μm in depth from the irradiated surface. The contribution of the implanted Zr-ions, knocked-on ions and electronic excitation to the compressive stress generation is not evaluated quantitatively at present.

It should be noted that the hardness and fracture toughness values obtained for the 3Y-TZP specimens irradiated in 2005 are higher than those irradiated in 2001. It appears that these differences are due to the differences of impurities, grain sizes, residual pores and so forth of the 3Y-TZP specimens irradiated in 2001 and those in 2005, since they were made at different times, i.e., have difference in their batches.

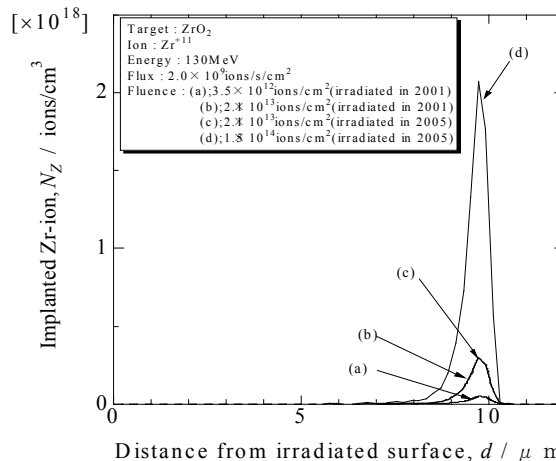


Fig.4. Implanted Zr-ions as a function of distance from irradiated surface.

As stated above, we were able to confirm with the present result that the main cause of the increases in the hardness and fracture toughness values due to the irradiation must be the residual compressive stresses left in the irradiated surface region of the specimen.

## References

- [1] T. Shibata, Y. Motohashi, M. Ishihara, S. Baba and K. Hayashi, JAERI-Review **2000-008** (2000) 1.
- [2] T. Shibata, M. Ishihara, Y. Motohashi, S. Baba T. Hoshiya T. Kobayashi, S. Harjo and T. Sakuma, Nucl. Instrum. Methods **B206** (2003) 139.
- [3] Y. Motohashi, T. Kobayashi, S. Harjo, T. Sakuma, T. Shibata, M. Ishihara, S. Baba and T. Hoshiya, Nucl. Instrum. Methods **B206** (2003) 144.
- [4] T. Shibata, M. Ishihara, Y. Motohashi, S. Baba, T. Sakuma and T. Hoshiya, Mater. Sci. Forum **426-432** (2003) 2813.
- [5] Y. Motohashi, T. Kobayashi, S. Harajo, T. akuma, T. Shibata, M. Ishihara, S. Baba and T. Hoshiya, JAERI-Review **2002-029** (2002) 101.
- [6] Y. Motohashi, T. Shibata, S. Harajo, T. Sakuma, M. Ishihara, S. Baba and K. Sawa, JAERI-Review **2005-004** (2005) 83.
- [7] J.F.Ziegler, Instruction manual for TRIM-95, IBM-Research, (1995).
- [8] K.E.Sickafus, et al. :J. Nucl. Mater. **274** (1999) 66.

## 7.4 SEMICONDUCTOR-METAL PHASE TRANSITION OF IRON DISILICIDE ( $\beta$ -FeSi<sub>2</sub>) THIN FILMS BY HIGH ENERGY HEAVY ION IRRADIATION

M. SASASE<sup>1</sup> and S. OKAYASU

$\beta$ -FeSi<sub>2</sub> is a direct transition type semiconductor with band gap of 0.87 eV and high absorption coefficient ( $>10^{-5}$  cm<sup>-1</sup>) [1]. Furthermore,  $\beta$ -FeSi<sub>2</sub> consists of resource elements of Fe and Si, which are harmless to the human bodies and the environment [2]. Another attractive feature of  $\beta$ -FeSi<sub>2</sub> is that it can be transformed to the metal phase  $\alpha$ -FeSi<sub>2</sub> when heated above 937 °C [3]. Since the bulk  $\alpha$ -FeSi<sub>2</sub> has electric resistivity as low as  $2.5 \times 10^{-4}$   $\Omega$  cm [4], one may consider if a small part of  $\beta$ -FeSi<sub>2</sub> can be transformed into  $\alpha$ -FeSi<sub>2</sub> selectively, it can be used as the electrode of a  $\beta$ -FeSi<sub>2</sub> based device.

When the high-energy heavy ions are irradiated into materials, most of their energies are dissipated through an electronic excitation [5]. This leads to strong localization of the dissipated energy along the projectile path. The density of energy deposition is high enough, compared with bond or displacement energy of the target materials, structural changes take place such as amorphization and phase transformation etc. We attempted to perform phase transition from  $\beta$ -FeSi<sub>2</sub> into  $\alpha$  phase by the high-energy heavy-ion irradiation.

The specimens used in this study were iron disilicides ( $\beta$ -FeSi<sub>2</sub>) films. The  $\beta$ -FeSi<sub>2</sub> film is fabricated with the Ion Beam Sputter Deposition (IBSD) method by deposition of Fe on Si(100) substrates at certain temperatures [6]. The specimens were irradiated by 95 MeV Ni<sup>9+</sup> ions and 180 MeV Fe<sup>11+</sup> at room temperature with a fluence of  $1.0 \times 10^{12}$  ions•cm<sup>-2</sup> using the Tandem accelerator at Japan Atomic Energy Agency (JAEA). The range and deposited ions in  $\beta$ -FeSi<sub>2</sub> films were calculated by using the TRIM98 code [7]. Irradiation damage was observed by using transmission electron microscope (TEM, JEOL JEM-3000F) with a field emission gun operated at 300 keV.

If the phase transition from  $\beta$ -FeSi<sub>2</sub> to  $\alpha$  phase takes place by the high-energy heavy ion irradiation, it is expected that some structural changes in the nano-region are observed from TEM images. No significant changes were observed in TEM images by 95 MeV Ni<sup>9+</sup> irradiation. On the other hand, contrast changes corresponded to defects, induced by ion irradiation were observed from TEM images at 180 MeV Fe<sup>11+</sup>. This result is shown in Fig. 1. The image in this figure was observed along the direction perpendicular to the a-axis of  $\beta$ -FeSi<sub>2</sub>. The arrows indicate the columnar defect produced by the Fe<sup>11+</sup> ion passing along this direction. These defects have an average diameter of 2 nm as a shape of column, which is amorphous.

---

<sup>1</sup> The Wakasa-wan energy research center (WERC)

The columnar defects were formed by the thermal spike effect due to the energy dissipation through electronic excitation. We calculated the electronic energy loss ( $S_e$ ) in  $\beta$ -FeSi<sub>2</sub> for each irradiating condition using the TRIM code [7]. On the basis of the results, the  $S_e$  is about 12.2 keV/nm at 180 MeV Fe<sup>11+</sup> and 8.7 keV/nm at 95 MeV Ni<sup>9+</sup>, respectively. Observed difference on the defects formation and the calculated results imply that the dominant defect formation mechanism might be changed around the  $S_e$  of 12 keV/nm. This value can be regarded as the threshold energy to produce the columnar defects on  $\beta$ -FeSi<sub>2</sub> films. These results are consistent with the reported ones for YBCO superconductor obtained by Hensel et al. [8].

Although the phase transition of  $\beta$ -FeSi<sub>2</sub> to  $\alpha$  phase is not confirmed yet, our results showed the structural change by swift heavy ion irradiation. We will intend to observe the microstructure of defects and phase transitions in the irradiated films precisely by using both high resolution TEM and micro-diffraction.

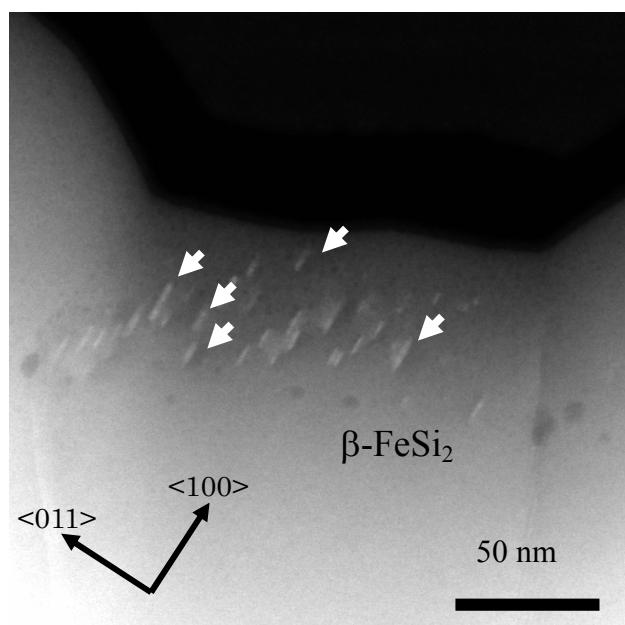


Fig. 1. Columnar defects introduced with 180 MeV, Fe<sup>11+</sup> ( $1.0 \times 10^{12}$  ions/cm<sup>2</sup>) in  $\beta$ -FeSi<sub>2</sub> crystal observed by cross sectional TEM image.

## References

- [1] K. Yamaguchi and K. Mizushima, Phys. Rev. Lett., **25** (2001) 6006.
- [2] K. Miyake, Y. Makita, Y. Maeda and T. Suemasu(Eds.), Thin Solid Films **381** (2001) 2.
- [3] H. Lange, Phys. Stat. Sol. **B201** (1997) 3.
- [4] K. Max and M van Rossum, Properties of Metal Silicides, INSPEC-IEE, London (1995).
- [5] M. Toulemonde, S. Bouffard and F. Studer, Nucl. Instrum. Method **B91** (1994) 108.
- [6] M. Sasase, T. Nakanoya, H. Yamamoto and K. Hojou, Thin Solid Films **401** (2001) 73.
- [7] J. F. Ziegler, "Handbook of Stopping Cross Section for Energetic Ions in All Elements", Pergamon Press, New York (1980).
- [8] B. Hensel, B. Roas, S. Henke, R. Hopfengartner, M. Lippert, J.P. Strobel, M. Vildic, G. Saemann-Ischenko and S. Klaumunzer, Phys. Rev. **B42** (1990) 4135.

## 7.5 RELEASE BEHAVIOR OF IMPLANTED Xe FROM Zr - IMPLANTATION OF Xe IN Zr-

H. OGAWA, I. IOKA, K. KIUCHI, Y. ISHIJIMA and Y. NAKAHARA

The gas release behavior of heavy rare gases such as Xe and Kr formed as fission products in nuclear fuel oxides are very important for understanding the pellet – clad interactions on fuel elements at high burn-up. The accumulation of these gases in the gap of fuel elements by gas release acts to decreasing the thermal conductivity and increasing the fuel temperature and internal pressure. Moreover, the swelling due to the void formation of these gases in oxide fuels is one of the most important problems for attaining ultra-high burn-up with respect to economical requirement. However, the release mechanism of these gases is not basically clarified. From the practical experiences in nuclear oxide fuels, the gas release temperature of heavy elements such as Xe and Kr is higher than it of light elements such as He. The fuel temperature for LWRs at the present normal operation is controlled less than 1500°C for inhibiting gas release. However, the modified fuel design applied to the advanced LWRs are required to enhance the fuel temperature for attaining ultra-high burn-up, controlling the low neutron energy spectrum and applying super critical pressurized water for high temperature operation. Therefore, it is very important to evaluate their release mechanism from the pellet. In previous study, Xe<sup>14</sup> ion with 180MeV was irradiated into porous CeO<sub>2</sub> test piece instead of UO<sub>2</sub> fuel pellet. Though the depth profile of Xe in the test piece was measured by EDX. The analyzers could not detect implanted Xe. This might be caused by CeO<sub>2</sub> of the pore or the low fluence of Xe.

In this study, metallic zirconium (Zr) without pores was selected as a target. The fluence was increased about three times in comparison with the last examination. Xe<sup>14+</sup> ion with 180MeV was irradiated into Zr test piece (1<sup>t</sup>x10<sup>w</sup>x10<sup>L</sup> mm) for about eight hours at room temperature using the TANDEM. The fluence was about 3.6x10<sup>16</sup> ions/cm<sup>2</sup>. The depth profile of Xe in the test piece was evaluated by SIMS. Xe content was also calculated by SRIM<sup>[1]</sup> code, and it was estimated that the content was about 0.6 at% in the test piece around the depth of about 12 μm as shown in Fig.1. However, the signal of Xe in the test piece was almost the same as that of background. The implanted Xe could not detect with SIMS. SIMS has enough precision for the content of implanted Xe. For the reason that Xe was not able to detect, it is believed that it is caused by the fact that ionization rate of Xe at the time of analysis is low.

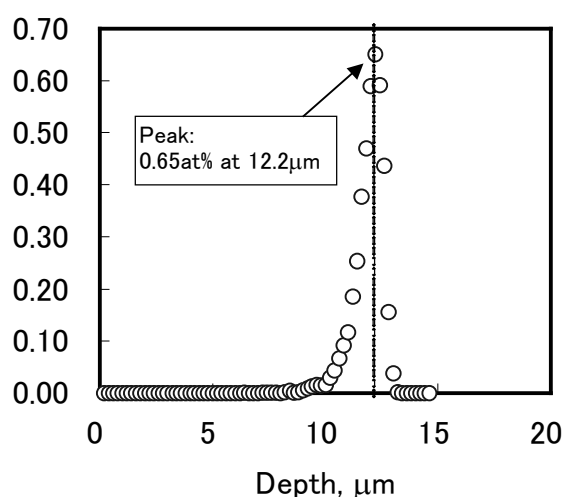


Fig.1. Xe as a function of depth from irradiated surface.

### Reference

[1] J.F.Zinger et al., “The Stopping and Range of Ion in Solids”, vol.1, Pergamon Press, New York (1985).



## **CHAPTER 8**

### **Publication in Journal and Proceedings, and Contribution to Scientific Meetings**

- 8.1 Accelerator Operation and Development
- 8.2 Nuclear Structure
- 8.3 Nuclear Reactions
- 8.4 Nuclear Chemistry
- 8.5 Nuclear Theory
- 8.6 Atomic Physics and Solid State Physics
- 8.7 Radiation Effects in Materials





## 8.1 Accelerator Operation and Development

### Journal/Proceedings

H. Miyatake

*Present Status of the KEK-JAERI joint RNB Project*

Proc. of the Int. Symp. on Exotic Nuclei 2004, Peterhof, Russia, July 5-12, 2004, World Scientific (2005) 636.

H. Miyatake, S. Arai, Y. Arakaki, Y. Fuchi, Y. Hirayama, N. Imai, H. Ishiyama, S.C. Jeong, I. Katayama, H. Kawakami, K. Niki, T. Nomura, M. Okada, M. Oyaizu, M.H. Tanaka, E. Tojyo, M. Tomizawa, Y.X. Watanabe, N. Yoshikawa, S. Abe, M. Asai, S. Hanashima, K. Horie, S. Ichikawa, H. Iimura, H. Ikezoe, T. Ishii, N. Ishizaki, H. Kabumoto, S. Kanda, T. Kaneko, M. Koizumi, M. Matsuda, S. Mitsuoka, Y. Nagame, T. Nakanoya, K. Nishio, I. Ohuchi, A. Osa, M. Oshima, M. Sataka, S. Takeuchi, H. Tayama, K. Tsukada, Y. Tsukihashi and T. Yoshida

*Present Status of the KEK-JAERI joint RNB Project*

Proc. of the 5th Italy-Japan Symp. on Recent Achievements and Perspective in Nuclear Physics, Naples, Italy, Nov. 3-7, 2004, World Scientific (2005) 547.

M. Matsuda, S. Takeuchi, Y. Tsukihashi, K. Horie, I. Ohuchi, S. Hanashima, S. Abe, N. Ishizaki, H. Tayama, T. Nakanoya, H. Kabumoto, T. Sato, M. Nakamura, S. Kanda and T. Yoshida

*Status Report of the JAERI Tandem Accelerator*

Proc. of the 18th Workshop of the Tandem Accelerator and their Associated Technology, Fukuoka, Jul. 1-2, 2005, (2005) 11.

S. Hanashima, M. Nakamura, T. Nakanoya and T. Yoshida

*New Interlock System for the JAERI Tandem Accelerator Facility*

Proc. of the 18th Workshop of the Tandem Accelerator and their Associated Technology, Fukuoka, Jul. 1-2, 2005, (2005) 84.

### Meetings

A. Osa, T. Sato, S. Ichikawa, M. Matsuda, K. Tsukada, M. Asai, S.C. Jeong, and I. Katayama,

*Development of FEBIAD-type Integrated-uranium-target-ion Source System*

The 47th Symp. on Radiochemistry in Kanazawa, Kanazawa (Sep. 28-30, 2005).

M. Matsuda, S. Takeuchi, Y. Tsukihashi, K. Horie, I. Ohuchi, S. Hanashima, S. Abe, N. Ishizaki, H. Tayama, T. Nakanoya, H. Kabumoto, T. Sato, M. Nakamura, S. Kanda and T. Yoshida

*Status Report of the JAERI Tandem Accelerator*

The 18th Workshop of the Tandem Accelerator and their Associated Technology, Fukuoka (Jul. 1-2, 2005).

S. Hanashima, M. Nakamura, T. Nakanoya and T. Yoshida

*New Interlock System for the JAERI Tandem Accelerator Facility*

The 18th Workshop of the Tandem Accelerator and their Associated Technology, Fukuoka (Jul. 1-2, 2005).

## 8.2 Nuclear Structure

### Journal/Proceedings

T. Shizuma, T. Hayakawa, S. Mitarai, T. Morikawa and T. Ishii

*Identification of the  $K^\pi=11/2^+$  Isomer in Neutron Rich  $^{187}W$*

Phys. Rev. C **71** (2005) 067301.

T. Morikawa, M. Nakamura, T. Sugimitsu, H. Kusakari, M. Oshima, Y. Toh, M. Koizumi, A. Kimura, J. Goto, Y. Hatsukawa and M. Sugawara

*High-spin Yrast Structure of  $^{43}Sc$*

J. Phys., Conference Series **20** (2005) 191.

T. Ishii, S. Shigematsu, M. Asai, A. Makishima, M. Matsuda, J. Kaneko, I. Hossain, S. Ichikawa, T. Kohno and M. Ogawa

*In-beam  $\gamma$ -ray Spectroscopy of  $^{240}U$  using the ( $^{18}O, ^{16}O$ ) Reaction*

Phys. Rev. C **72** (2005) 021301(R) (1-5).

M. Asai, K. Tsukada, M. Sakama, S. Ichikawa, T. Ishii, Y. Nagame, I. Nishinaka, K. Akiyama, A. Osa, Y. Oura, K. Sueki and M. Shibata

*Experimental Identification of Spin-parities and Single-particle Configurations in  $^{257}No$  and Its  $\alpha$ -decay Daughter  $^{253}Fm$*

Phys. Rev. Lett. **95** (2005) 102502.

Y.H. Zhang, G. Song, X.H. Zhou, L. Ma, M. Oshima, Y. Toh, M. Koizumi, A. Osa, A. Kimura, Y. Hatsukawa, M. Sugawara and H. Kusakari

*Observation of High-j Two-Quasiparticle Bands in Odd-odd  $^{174}Re$*

Chin. Phys. Lett. **22** (2005) 2788.

Y.H. Zhang, Y.D. Fang, G. de Angelis, N. Marginean, A. Gadea, D.R. Napoli, M. Axotis, C. Rusu, T. Martinez, H.L. Wang, X.H. Zhou, W.T. Guo, M.L. Liu, Y.X. Guo, X.G. Lei, M. Oshima, Y. Toh and F.R. Xu

*High-spin States of Odd-odd  $^{184}Au$  Nucleus*

J. Phys. G **31**, Nucl. Part. Phys. (2005) S1545.

H. Wang, H. Ohba, M. Saeki, M. Miyabe, T. Shibata, H. Miyatake and H. Iimura

*Velocity and Metastable State Population Distributions of Neodymium Atoms Produced by Laser Ablation*

Appl. Phys. **B81** (2005) 1127.

F.P. Hessberger, S. Antalic, B. Streicher, S. Hofmann, D. Ackermann, B. Kindler, I. Kojouharov, P. Kuusiniemi, M. Leino, B. Lommel, R. Mann, K. Nishio, S. Saro and B. Sulignano

*Energy Systematics of Low-lying Nilsson Levels in Odd-mass Einsteinium Isotopes*  
 Eur. Phys. J. **A 26** (2005) 233.

A.N. Andreyev, S. Antalic, D. Ackermann, S. Franchoo, F.P. Hessberger, S. Hofmann, M. Huyse, I. Kojouharov, B. Kindler, P. Kuusiniemi, S.R. Leshner, B. Lommel, R. Mann, G. Munzenberg, K. Nishio, R.D. Page, J.J. Ressler, B. Streicher, S. Saro, B. Sulignano, P. Van Duppen, and D.R. Wiseman  
*Alpha-decay Spectroscopy of the New Isotope  $^{192}\text{At}$*   
 Phys. Rev. **C 73** (2006) 024317.

## Meetings

T. Ishii  
*In-beam  $\gamma$ -ray Spectroscopy of Neutron-rich U Nuclei Produced by the Multi-nucleon Transfer Reaction*  
 RIKEN RIBF Int. Workshop "Collective Motions in Unstable Nuclei -Experiments vs. Theories", RIKEN, Wako (May 24-26, 2005).

H. Iimura  
*Laser Spectroscopy for the Study of Nuclear Charge Radii*  
 Int. Workshop on "Nuclear Physics with RIBF", Wako (Mar. 16, 2006).

T. Ishii, S. Shigematsu, M. Asai, A. Makishima, M. Matsuda, J. Kaneko, I. Hossain, S. Ichikawa, T. Kohno and M. Ogawa  
*In-beam  $\gamma$ -ray Spectroscopy of a Neutron-rich Nucleus of  $^{240}\text{U}$*   
 Hawaii 2005: the 2nd Joint Meeting of the Nuclear Physics Division of the APS and JPS, Kapalua (Sep. 18-22, 2005).

H. Iimura, M. Koizumi, M. Miyabe, M. Oba, T. Shibata, N. Shinohara, Y. Ishida, T. Horiguchi and H.A. Schuessler  
*Nuclear Moments of the Neutron-Deficient Lanthanum Isotopes by Collinear Laser Spectroscopy*  
 Hawaii 2005: the 2nd Joint Meeting of the Nuclear Physics Division of the APS and JPS, Kapalua (Sep. 18-22, 2005).

M. Asai, K. Tsukada, T. Ishii, Y. Nagame, I. Nishinaka, K. Akiyama, A. Toyoshima, S. Ichikawa, T. Ichikawa, M. Sakama, H. Haba, K. Sueki, M. Shibata, Y. Kojima and Y. Oura  
*Alpha-gamma Decay Studies of  $^{261}\text{Rf}$  and  $^{257}\text{No}$*   
 Hawaii 2005: the 2nd Joint Meeting of the Nuclear Physics Division of the APS and JPS, Kapalua (Sep. 18-22, 2005).

M. Asai  
 *$\alpha$ - $\gamma$ (e) Spectroscopy of  $^{261}\text{Rf}$  and  $^{257}\text{No}$*

Pacificchem 2005: Int. Chemical Congress of Pacific Basin Societies, Honolulu (Dec. 15-20, 2005).

T. Ishii, S. Shigematsu, H. Makii, M. Asai, K. Tsukada, A. Toyoshima, M. Matsuda, A. Makishima, T. Shizuma, J. Kaneko, I. Hossain, H. Tome, M. Ohara, S. Ichikawa, T. Kohno and M. Ogawa  
*In-beam  $\gamma$ -ray Measurement of the Neutron-rich Nucleus  $^{250}_{96}\text{Cm}_{154}$*   
 The 61st Annual Meeting of the Physical Society of Japan, Matsuyama (Mar. 27-30, 2006).

S. Shigematsu, T. Ishii, H. Makii, M. Asai, K. Tsukada, A. Toyoshima, M. Matsuda, A. Makishima, T. Shizuma, J. Kaneko, I. Hossain, H. Tome, M. Ohara, S. Ichikawa, T. Kohno and M. Ogawa  
*In-beam  $\gamma$ -ray Spectroscopy of Nuclei in the Region of Transuranium Elements using the ( $^{18}\text{O}, ^{16}\text{O}$ ) Reaction*  
 The 61st Annual Meeting of the Physical Society of Japan, Matsuyama (Mar. 27-30, 2006).

M. Asai, K. Tsukada, M. Sakama, H. Haba, T. Ishii, Y. Nagame, I. Nishinaka, K. Akiyama, A. Toyoshima, T. Ichikawa, S. Ichikawa, K. Sueki, M. Shibata, Y. Kojima and Y. Oura  
*Alpha-gamma Spectroscopy of  $^{261}\text{Rf}$*   
 The 61st Annual Meeting of the Physical Society of Japan, Matsuyama (Mar. 27-30, 2006).

H. Hayashi, Y. Akita, M. Shibata, T.K. Sato, M. Asai, A. Osa, K. Tsukada, T. Ishii, S. Ichikawa and Y. Kojima  
 *$Q_{\beta}$  Measurements for Neutron-rich Isotopes of Eu using a Total Absorption BGO Detector*  
 The 61st Annual Meeting of the Physical Society of Japan, Matsuyama (Mar. 27-30, 2006).

H. Iimura

*Nuclear Moments Studied by Collinear Laser Spectroscopy*

Symp. on the Structure of Unstable Nuclei Studied by Electromagnetic Moments and Low-energy Nuclear Spectroscopy, Wako (Mar. 1, 2006).

M. Koizumi, Y. Toh, A. Osa, A. Kimura, Y. Utsuno, M. Oshima, T. Hayakawa, Y. Hatsukawa, J. Katakura, M. Matsuda, T. Shizuma, A. Seki, T. Morikawa, M. Sugawara, H. Kusakari, J. Goto, T. Czosnyka and M. Zielinska  
*Coulomb Excitation Experiments at JAEA Tandem Facility for the Study of Nuclear Structure*  
 RCNP-JAEA Workshop on Nuclear Photon Science, "Hadron-nuclear physics probed by photon", JAEA, Kizu (Feb. 16-18, 2006).

H. Hayashi, Y. Akita, M. Shibata, M. Asai, T.K. Sato, S. Ichikawa, K. Tsukada, A. Osa, T. Ishii, Y. Kojima, A. Taniguchi and T. Tachibana  
 *$Q_{\beta}$  Measurements using the ISOL*  
 The 2nd TRIAC Workshop, JAEA-Tokai (Mar. 7-8 2006).

### 8.3 Nuclear Reactions

#### Journal/Proceedings

T. Hashimoto, H. Ishiyama, T. Ishikawa, T. Kawamura, K. Nakai, Y.X. Watanabe, H. Miyatake, M.H. Tanaka, Y. Fuchi, N. Yoshikawa, S.C. Jeong, Y. Matsuyama, I. Katayama, T. Nomura, T. Furukawa, S. Mitsuoka, K. Nishio, M. Matsuda, H. Ikezoe, T. Fukuda, S.K. Das, P.K. Saha, T. Fukuda, K.Y. Mizoi, T. Komatsubara, M. Yamaguchi and Y. Tagishi

*Gated Multiple-sampling and Tracking Proportional Chamber New Detector System for Nuclear Astrophysical Study with Radioactive Nuclear Beams*

Nucl. Instrum. Methods. Phys. Res. **A556** (2006) 339.

H. Ishiyama, T. Ishikawa, T. Hashimoto, Y.X. Watanabe, Y. Hirayama, N. Imai, H. Miyatake, M.H. Tanaka, Y. Fuchi, N. Yoshikawa, S.C. Jeong, H. Kawakami, I. Katayama, T. Nomura, S. Mitsuoka, K. Nishio, M. Matsuda, P.K. Saha, H. Ikezoe, S.K. Das, Y. Mizoi and T. Fukuda

*Production of a Low-energy Radioactive Nuclear Beam with High Purity using JAERI-RMS*

Nucl. Instrum. Methods. Phys. Res. **A560** (2006) 366.

K. Satou, H. Ikezoe, S. Mitsuoka, K. Nishio, C.J. Lin and S.C. Jeong

*Measurements of Evaporation Residue Cross Sections for the Fusion Reactions  $^{86}\text{Kr}+^{134}\text{Ba}$  and  $^{86}\text{Kr}+^{138}\text{Ba}$*

Phys. Rev. **C 73** (2006) 034609.

H. Ishiyama, T. Hashimoto, T. Ishikawa, Y.X. Watanabe, Y. Hirayama, H. Miyatake, M.H. Tanaka, N. Yoshikawa, S.C. Jeong, Y. Matsuyama, Y. Fuchi, I. Katayama, T. Nomura, H. Kawakami, K. Nakai, S.K. Das, P.K. Saha, T. Fukuda, K. Nishio, S. Mitsuoka, H. Ikezoe, M. Matsuda, S. Ichikawa, T. Furukawa, H. Izumi, T. Shimoda, Y. Mizoi, M. Terasawa and T. Sasaqui

*Direct Measurement of the Astrophysical  $^8\text{Li}(\alpha, n)^{11}\text{B}$  Reaction*

Recent Achievement and Perspective in Nuclear Physics, Proc. of the 5th Italy-Japan Symp., World Scientific Publishing Co. Pre. Ltd. (2005) 379.

K. Nishio and H. Ikezoe

*Exploring the Fusion Reaction Involving Deformed Nucleus  $^{238}\text{U}$*

Nuclear Data News **81** (2005) 52.

#### Meetings

S.K. Das, T. Fukuda, Y. Mizoi, H. Ishiyama, H. Miyatake, Y.X. Watanabe, Y. Hirayama, M.H. Tanaka, N. Yoshikawa, S.C. Jeong, Y. Fuchi, I. Katayama, T. Nomura, T. Ishikawa, K. Nakai, T. Hashimoto, S. Mitsuoka, K. Nishio, P.K. Saha, M. Matsuda, S. Ichikawa, H. Ikezoe, T. Furukawa, H. Izumi, T. Shimoda and T. Sasaqui

*A New Measurement of the  $^8\text{Li}(\alpha, n)^{11}\text{B}$  Reaction for Astrophysical Interest*

Int. Symp. on Origin of Matter and Evolution of Galaxies (OMEG05), Tokyo (Nov. 8-11, 2005).

H. Ishiyama, H. Miyatake, Y.X. Watanabe, Y. Hirayama, N. Imai, M.H. Tanaka, N. Yoshikawa, S.C. Jeong, Y. Fuchi, I. Katayama, T. Nomura, T. Ishikawa, K. Nakai, S.K. Das, Y. Mizoi, T. Fukuda, T. Hashimoto, K. Nishio, S. Mitsuoka, H. Ikezoe, M. Matsuda, S. Ichikawa, P.K. Saha, T. Shimoda, M. Terasawa and T. Sasaqui

*Study of Astrophysical ( $\alpha, n$ ) Reactions on Light Neutron-rich Nuclei using Low-energy Radioactive Nuclear Beams*

Int. Symp. on Origin of Matter and Evolution of Galaxies (OMEG05), Tokyo (Nov. 8-11, 2005).

S. Mitsuoka, H. Ikezoe, K. Nishio, K. Tsuruta, S.C. Jeong and Y.X. Watanabe

*Probing Fusion Barrier Distributions with Large-angle Quasielastic Scattering of  $^{48}\text{Ti}$ ,  $^{56}\text{Fe}$  and  $^{64}\text{Ni}$  on  $^{208}\text{Pb}$*   
Hawaii 2005: the 2nd Joint Meeting of the Nuclear Physics Division of the APS and JPS, Kapalua (Sep. 18-22, 2005).

T. Ishikawa, K. Nakai, H. Ishiyama, H. Miyatake, Y.X. Watanabe, Y. Hirayama, N. Imai, M.H. Tanaka, N. Yoshikawa, S.C. Jeong, Y. Fuchi, I. Katayama, T. Nomura, T. Hashimoto, S. Mitsuoka, K. Nishio, P.K. Saha, M. Matsuda, S. Ichikawa, H. Ikezoe, Y. Mizoi, S.K. Das, T. Fukuda and T. Shimoda

*Direct Measurement of the  $^{12}\text{B}(\alpha, n)^{15}\text{N}$  Astrophysical Reaction Rate*

The 61st Annual Meeting of the Physical Society of Japan, Matsuyama (Mar. 27-30, 2006).

S. Mitsuoka, H. Ikezoe, K. Nishio, K. Tsuruta, S.C. Jeong and Y.X. Watanabe

*Measurement of Fusion Barrier Distribution for Cold Fusion Reactions*

The 61st Annual Meeting of the Physical Society of Japan, Matsuyama (Mar. 27-30, 2006).

S. Mitsuoka

*Nuclear Astrophysical Experiment using Radioactive Beams from JAERI-RMS and TRIAC*

The 18th Workshop of the Tandem Accelerator and their Associated Technology, Fukuoka, Kyusyu university (July. 1-2, 2005).

K. Nishio, H. Ikezoe, Y. Nagame, M. Asai, K. Tsukada, S. Mitsuoka, K. Tsuruta, S. Satou, C.J. Lin and T. Ohsawa

*Evidence of Complete Fusion in the Sub-barrier  $^{16}\text{O}+^{238}\text{U}$  Reaction*

Frontiers in the Physics of Nucleus 2005, Peterhof, St. Petersburg (Jun. 27-Jul. 1, 2006).

S. Hofmann, D. Ackermann, S. Antalic, H.G. Burkhard, R. Dressler, F.P. Hessberger, B. Kindler, I. Kojouharov, P. Kuusiniemi, M. Leino, B. Lommel, R. Mann, G. Munzenberg, K. Nishio, A.G. Popeko, S. Saro, H.J. Schott, B. Streicher, B. Sulignano, J. Uusitalo and A. V. Yeremin

*Synthesis of SHE at SHIP*

Carpathian Summer School of Physics 2005 “Exotic Nuclei and Nuclear/Particle Astrophysics”, Mamaia-Constanta, Romania (Jun. 13-24, 2005).

K. Nishio

*Planned Fusion Reaction  $^{30}\text{Si}+^{238}\text{U}$*

Workshop on Superheavy Elements, Schloss Rauischholzhausen, Germany, (Sep.6, 2005).

T.K. Sato, M. Asai, A. Osa, K. Tsukada, H. Hayashi, M. Shibata, Y. Kojima and S. Ichikawa

*Identification of New Neutron-rich Isotopes  $^{163-165}\text{Eu}$*

The 61st Annual Meeting of the Physical Society of Japan, Matsuyama (Mar. 27-30, 2006).



## 8.4 Nuclear Chemistry

### Journal/Proceedings

Y. Nagame, K. Tsukada, M. Asai, A. Toyoshima, K. Akiyama, Y. Ishii, T. Kaneko-Sato, M. Hirata, I. Nishinaka, S. Ichikawa, H. Haba, S. Enomoto, K. Matsuo, D. Saika, Y. Kitamoto, H. Hasegawa, Y. Tani, W. Sato, A. Shinohara, M. Ito, J. Saito, S. Goto, H. Kudo, H. Kikunaga, N. Kinoshita, A. Yokoyama, K. Sueki, Y. Oura, H. Nakahara, M. Sakama, M. Schadel, W. Bruchle and J. V. Kratz

*Chemical Studies on Rutherfordium (Rf) at JAERI*

Radiochim. Acta **93** (2005) 519.

Y. Nagame

*Radiochemical Studies of the Transactinide Element, Rutherfordium (Rf) at JAERI*

J. Nucl. Radiochem. Sci. **6** (2005) A21.

T.K. Sato, K. Tsukada, M. Asai, K. Akiyama, H. Haba, A. Toyoshima, S. Ono, T. Hirai, S. Goto, S. Ichikawa, Y. Nagame and H. Kudo

*Simultaneous Observation of Volatility of Zr, Hf, and Rf Chlorides*

J. Nucl. Radiochem. Sci. **6** (2005) N1.

Y. Nagame

*Production and Chemistry of Transactinide Elements*

J. Nucl. Radiochem. Sci. **6** (2005) 205.

Y. Nagame, H. Haba, K. Tsukada, M. Asai, A. Toyoshima, K. Akiyama, T. Kaneko, T. Hirai, S. Goto, M. Hirata, I. Nishinaka and S. Ichikawa

*Few Atom Chemistry of the Transactinide Element Rutherfordium (Rf)*

Proc. of the Int. Conf. on Applications of High Precision Atomic and Nuclear Methods, Neptun, Romania, September 2-6, 2002, Editura Academiei Romane (2005) 334.

Y. Nagame, K. Tsukada, M. Asai, A. Toyoshima, K. Akiyama, Y. Ishii, I. Nishinaka, T.K. Sato, M. Hirata, T. Ichikawa, H. Haba, S. Goto and M. Sakama

*Atom-at-a-time Chemistry of the Transactinide Element, Rutherfordium (element 104) –Towards Experimental Verification of Relativistic Effects in Chemical Properties-*

Proc. of the 5th Italy-Japan Symp., Recent Achievements and Perspectives in Nuclear Physics, Naples, Italy, November 3-7, 2004, World Scientific (2005) 295.

Y. Nagame and H. Nakahara

*Authorization of New Elements*

BUTSURI **60** (2005) 707.

A. Shinohara, K. Tsukada and Y. Nagame

*Chemistry of Superheavy Elements*  
BUTSURI **60** (2005) 709.

Y. Nagame  
*Transactinide Element Research – Present Status and Perspectives*  
RADIOISOTOPES **54** (2005) 555.

## Meetings

Y. Nagame  
*Production and Chemistry of Transactinide Elements*  
Int. Symp. on Technetium – Science and Utilization – Oarai (May 24-27, 2005).

K. Tsukada, A. Toyoshima, H. Haba, M. Asai, K. Akiyama, Y. Ishii, T.K. Sato, I. Nishinaka, Y. Nagame, K. Sueki, M. Ito, J. Saito, S. Goto, H. Kudo and Y. Oura  
*Chloride Complex Formation of Rf in HCl and CH<sub>3</sub>OH Mixed Solution*  
Actinides 2005, Manchester (Jul. 4-8, 2005).

Y. Nagame  
*Aqueous Chemistry of Element 104, Rutherfordium (Rf)*  
Gesellschaft Deutscher Chemiker (GDCh)-Jahrestagung 2005, Dusseldorf (Sep. 11-14, 2005).

K. Tsukada, A. Toyoshima, H. Haba, M. Asai, K. Akiyama, Y. Ishii, H. Tome, I. Nishinaka, T.K. Sato, T. Ichikawa, S. Ichikawa, M. Hirata, Y. Nagame, T. Yaita, S. Goto, T. Ikezawa, W. Sato, K. Matsuo, Y. Kitamoto, Y. Tashiro, A. Yokoyama, N. Arai, M. Sakama, Y. Oura, K. Sueki, A. Shinohara, H. Kudo and M. Schadel  
*Formation of Anionic Chloride Complex of Rutherfordium (Rf)*  
The 49th Symp. on Radiochemistry, Kanazawa (Sep. 28-30, 2005).

A. Toyoshima, H. Haba, K. Tsukada, K. Akiyama, M. Asai, Y. Ishii, H. Toume, I. Nishinaka, T. Ichikawa, T.K. Sato, S. Ichikawa, Y. Nagame, W. Sato, K. Matsuo, Y. Kitamoto, Y. Tashiro, A. Shinohara, T. Ikezawa, M. Sakamaki, S. Goto, H. Kudo, M. Arai, S. Kamataki, A. Yokoyama, Y. Oura, and K. Sueki  
*Reversed-phase Extraction Chromatography of Rutherfordium in the TBP-HCl System*  
The 49th Symp. on Radiochemistry, Kanazawa (Sep. 28-30, 2005).

A. Toyoshima, H. Haba, K. Tsukada, M. Asai, K. Akiyama, S. Goto, Y. Ishii, W. Sato, K. Matsuo, D. Saika, Y. Kitamoto, A. Yokoyama, M. Sakama, Y. Oura, I. Nishinaka, T.K. Sato, T. Ichikawa, M. Hirata, S. Ichikawa, K. Sueki, A. Shinohara, H. Kudo, Y. Nagame, H. Nakahara and M. Schadel  
*Fluoride Complexation of Rutherfordium*  
The 49th Symp. on Radiochemistry, Kanazawa (Sep. 28-30, 2005).

Y. Ishii, H. Suganuma, H. Haba, K. Akiyama, A. Toyoshima, M. Asai, K. Tsukada and Y. Nagame  
*Cation Exchange Behavior of Zr and Hf Fluoride – Model Experiments for Chemical Characterization of Super Heavy Element Rutherfordium*

The 49th Symp. of Radiochemistry, Kanazawa (Sep. 28-30, 2005).

K. Akiyama, K. Tsukada, M. Asai, H. Haba, K. Sueki, A. Toyoshima, T. Yaita and Y. Nagame  
*Structural Study of Nb and Ta in HF Solution for Chemical Characterization of Dubnium*

The 49th Symp. on Radiochemistry, Kanazawa (Sep. 28-30, 2005).

Y. Nagame

*Radiochemical Studies of the Transactinide Elements at JAERI*

Asia-Pacific Symposium on Radiochemistry-05, Beijing (Oct. 17-21, 2005).

Y. Nagame

*Nuclear Chemistry of Heavy Elements at JAERI*

Int. Workshop on Heavy Elements, Lanzhou (Oct. 23-26, 2005).

Y. Nagame

*Aqueous Chemistry of Rutherfordium (Rf) at JAERI*

The 2005 Int. Chemical Congress of Pacific Basin Societies, Honolulu (Dec. 15-20, 2005).

A. Toyoshima, K. Tsukada, M. Asai, H. Haba, K. Akiyama, Y. Ishii, I. Nishinaka, T.K. Sato, M. Hirata, Y. Nagame, W. Sato, K. Matsuo, D. Saika, Y. Kitamoto, A. Shinohara, S. Goto, H. Kudo, A. Yokoyama, M. Sakama, K. Sueki, H. Nakahara, M. Schadel, W. Bruchle and J.V. Kratz

*Fluoride Complexation of Rutherfordium*

The 2005 Int. Chemical Congress of Pacific Basin Societies, Honolulu (Dec. 15-20, 2005).

K. Tsukada, A. Toyoshima, H. Haba, M. Asai, K. Akiyama, Y. Ishii, T.K. Sato, I. Nishinaka, Y. Nagame, K. Sueki, S. Goto, H. Kudo, W. Sato, Y. Kitamoto, K. Matsuo, Y. Tashiro and Y. Oura

*Chemical Behavior of Rf and its Homologues in the TBP/HCl System*

The 2005 Int. Chemical Congress of Pacific Basin Societies, Honolulu (Dec. 15-20, 2005).

K. Akiyama, H. Haba, K. Tsukada, M. Asai, K. Sueki, A. Toyoshima, T. Yaita and Y. Nagame  
*Structural Study for the 4th and 5th Group of Elements in Hydrofluoric Acid Solution*

The 2005 Int. Chemical Congress of Pacific Basin Societies, Honolulu (Dec. 15-20, 2005).

M. Hirata, K. Tanaka, Y. Nagame, T. Bastug, J. Anton and B. Fricke

*Prediction of Ionic Radii of Nobelium Ions,  $No^{2+}$  and  $No^{3+}$*

The 2005 Int. Chemical Congress of Pacific Basin Societies, Honolulu (Dec. 15-20, 2005).

A. Toyoshima, H. Haba, K. Tsukada, M. Asai, K. Akiyama, Y. Ishii, H. Toume, I. Nishinaka, T.K. Sato, T.

Ichikawa, Y. Nagame, W. Sato, K. Matsuo, Y. Kitamoto, Y. Tashiro, A. Shinohara, T. Ikezawa, M. Sakamaki, S. Goto, H. Kudo, M. Arai, S. Kamataki, A. Yokoyama, Y. Oura and K. Sueki  
*Reversed-phase Extraction Chromatography of Rutherfordium in the HCl-TBP System*  
The 86th Spring Meeting of the Chemical Society of Japan, Funabashi (Mar. 27-30, 2006).

Y. Ishii, H. Suganuma, H. Haba, K. Akiyama, H. Tome, A. Toyoshima, M. Asai, K. Tsukada and Y. Nagame  
*Cation Exchange Behavior of Zr and Hf in HNO<sub>3</sub>/HF Mixed Solution System – Model Experiments for Chemical Characterization of Superheavy Element Rutherfordium*  
The 86th Spring Meeting of the Chemical Society of Japan, Funabashi (Mar. 27-30, 2006).

K. Tsukada, A. Toyoshima, H. Haba, M. Asai, K. Akiyama, Y. Ishii, H. Tome, I. Nishinaka, T.K. Sato, T. Ichikawa, S. Ichikawa, M. Hirata, Y. Nagame, T. Yaita, S. Goto, M. Sakamaki, T. Ikezawa, W. Sato, K. Matsuo, Y. Kitamoto, Y. Tashiro, A. Yokoyama, N. Arai, S. Kamataki, M. Sakama, Y. Oura, K. Sueki, A. Shinohara and H. Kudo  
*Formation of Anionic Chloride Complex of Rutherfordium (Rf)*  
The 86th Spring Meeting of the Chemical Society of Japan, Funabashi (Mar. 27-30, 2006).

## 8.5 Nuclear Theory

### Journal/Proceedings

H. Koura and T. Tachibana

*How Far Does the Area of Superheavy Elements Extend? -Decay Modes of Heavy and Superheavy Nuclei Predicted by a Mass Formula-*  
 BUTSURI **60** (2005) 717.

Y. Utsuno

*Anomalous Magnetic Moment of C and Shell Quenching in Exotic Nuclei*  
 Eur. Phys. J. A **25**, Suppl. **1** (2005) 209.

Y. Utsuno, T. Otsuka, T. Mizusaki and M. Honma

*Shape Coexistence and Mixing in N~20 Region*  
 J. Phys., Conf. Ser. **20** (2005) 167.

Y. Utsuno, T. Otsuka, T. Mizusaki and M. Honma

*Shell Structure and Correlation Studied by Large-scale Shell-model Calculations*  
 Proc. of the 5th Italy-Japan Symp. on Recent Achievements and Perspectives in Nuclear Physics, Singapore, World Scientific (2005) 19.

T. Maruyama, T. Tatsumi, D.N. Voskresensky, T. Tanigawa and S. Chiba

*Nuclear "Pasta" Structures and the Charge Screening Effect*  
 Phys. Rev. C **72** (2005) 015802.

T. Endo, T. Maruyama, S. Chiba and T. Tatsumi

*Charge Screening Effect in the Hadron-quark Mixed Phase*  
 Prog. Theor. Phys. **115** (2006) 337.

Y. Akimura, T. Maruyama, N. Yoshinaga and S. Chiba

*Molecular Dynamics Simulation for the Baryon-quark Phase Transition at Finite Baryon Density*  
 Eur. Phys. J. A **25** (2005) 405.

T. Maruyama, T. Tatsumi, D.N. Voskresensky, T. Tanigawa, T. Endo and S. Chiba

*Finite Size Effects on Kaonic Pasta Structures*  
 Phys. Rev. C **73** (2006) 035802.

T. Endo, T. Maruyama, S. Chiba and T. Tatsumi

*Charge Screening Effect on Hadron-quark Mixed Phase in Compact Stars*  
 Proc. of Science (JHW2005) 019, the 29th Johns Hopkins Workshop on Current problems in Particle Theory : Strong Matter in the Heavens, 1-3 August, Budapest.

T. Maruyama, T. Tatsumi, D.N. Voskresensky, T. Endo and S. Chiba

*Coulomb and Surface Effects on the Pasta Structure in Nuclear Matter*

Proc. of Science (JHW2005) 024, the 29th Johns Hopkins Workshop on Current Problems in Particle Theory : Strong Matter in the Heavens, 1-3 August, Budapest.

S. Chiba, T. Kawano, H. Koura, T. Nakagawa, T. Tachibana, T. Kajino, S. Oryu, T. Haytakawa, A. Seki, T. Maruyama, T. Tanigawa, Y. Watanabe, T. Ohsaki, T. Murata and K. Sumiyoshi  
*Nuclear Data for Astrophysical Nucleosynthesis : A Japanese + LANL Activity*  
 AIP Conf. Proc. **769** (2005) 1339.

V. Tripathi, S.L. Tabor, P.F. Mantica, C.R. Hoffman, M. Wiedeking, A.D. Davies, S.N. Liddick, W.F. Mueller, T. Otsuka, A. Stolz, B.E. Tomlin, Y. Utsuno and A. Volya  
*<sup>29</sup>Na: Defining the Edge of the Island of Inversion for Z = 11*  
 Phys. Rev. Lett. **94** (2005) 162501.

P. Mason, N. Marginean, S. M. Lenzi, M. Ionescu-Bujor, F. Della Vedova, D.R. Napoli, T. Otsuka, Y. Utsuno, F. Nowacki, M. Axiotis, D. Bazzacco, P.G. Bizzeti, A. Bizzeti-Sona, F. Brandolini, M. Cardona, G de Angelis, E. Farnea, A. Gadea, D. Hojman, A. Iordachescu, C. Kalfas, Th. Kroll, S. Lunardi, T. Martinez, C.M. Petrache, B. Quintana, R.V. Ribas, C. Rossi Alvarez, C.A. Ur, R. Vlastou and S. Zilio  
*High Spin Structure of <sup>34</sup>S and the Proton-neutron Coupling of Intruder States*  
 Phys. Rev. C **71** (2005) 014316.

T.K. Onishi, A. Gelberg, H. Sakurai, K. Yoneda, N. Aoi, N. Imai, H. Baba, P. von Brentano, N. Fukuda, Y. Ichikawa, M. Ishihara, H. Iwasaki, D. Kameda, T. Kishida, A.F. Lisetskiy, H. J. Ong, M. Osada, T. Otsuka, M.K. Suzuki, K. Ue, Y. Utsuno and H. Watanabe  
*Gamow-Teller Decay of the T = 1 Nucleus <sup>46</sup>Cr*  
 Phys. Rev. C **72** (2005) 024308.

M. Belleguic, F. Azaiez, Zs. Dombradi, D. Sohler, M.J. Lopez-Jimenez, T. Otsuka, M.G. Saint-Laurent, O. Sorlin, M. Stanoiu, Y. Utsuno, Yu.-E. Penionzhkevich, N.L. Achouri, J.C. Angelique, C. Borcea, C. Bourgeois, J.M. Daugas, F. De Oliveira-Santos, Z. Dlouhy, C. Donzaud, J. Duprat, Z. Elekes, S. Grevy, D. Guillemaud-Mueller, S. Leenhardt, M. Lewitowicz, S.M. Lukyanov, W. Mittig, M.G. Porquet, F. Pougheon, P. Roussel-Chomaz, H. Savajols, Y. Sobolev, C. Stodel and J. Timar  
*Search for Neutron Excitations Across the N = 20 Shell Gap in <sup>25-29</sup>Ne*  
 Phys. Rev. C **72** (2005) 054316.

M. Ionescu-Bujor, A. Iordachescu, D.R. Napoli, S.M. Lenzi, N. Marginean, T. Otsuka, Y. Utsuno, R.V. Ribas, M. Axiotis, D. Bazzacco, A.M. Bizzeti-Sona, P.G. Bizzeti, F. Brandolini, D. Bucurescu, M.A. Cardona, G de Angelis, M. De Poli, F. Della Vedova, E. Farnea, A. Gadea, D. Hojman, C.A. Kalfas, Th. Kroll, S. Lunardi, T. Martinez, P. Mason, P. Pavan, B. Quintana, C. Rossi Alvarez, C.A. Ur, R. Vlastou and S. Zilio  
*High Spin Structure and Intruder Configurations in <sup>31</sup>P*  
 Phys. Rev. C **73** (2006) 024310.

R. Capote, E. Sh. Soukhovitskii, J.M. Quesada and S. Chiba  
*Is a Global Coupled-channel Dispersive Optical Model Potential for Actinides Feasible?*  
 Phys. Rev. C **72** (2005) 064610.

T. Nakagawa, S. Chiba, T. Hayakawa and T. Kajino  
*Maxwellian-averaged Neutron-induced Reaction Cross Sections and Astrophysical Reaction Rates for  $kT = 1$  keV to 1 MeV Calculated from Microscopic Neutron Cross Section Library JENDL-3.3*  
 Atomic Data and Nuclear Data Tables 91 (2005) 77.

K. Sumiyoshi, S. Yamada, H. Suzuki, H. Shen, S. Chiba and H. Toki  
*Postbounce Evolution of Core-collapse Supernovae: Long-term Effects of the Equation of State*  
 Astrophys. J. **629** (2005) 922.

T. Hayakawa, T. Shizuma, T. Kajino, S. Chiba, N. Shinohara, T. Nakagawa and T. Arima  
*New S-process Path and its Implication for  $^{187}\text{Re}$ - $^{187}\text{Os}$  Nucleo-cosmochronometer*  
 Astrophys. J. **628** (2005) 533.

E. Sh. Soukhovitskii, R. Capote, J.M. Quesada and S. Chiba  
*Dispersive Coupled-channel Analysis of Nucleon Scattering from  $^{232}\text{Th}$  up to 200 MeV*  
 Phys. Rev. C **72** (2005) 024604.

T. Kawano, S. Chiba and H. Koura  
*Phenomenological Nuclear Level Densities Using the KTUY05 Nuclear Mass Formula for Applications Off-Stability*  
 J. Nucl. Sci. Technol. **43** (2006) 1.

S. Oryu, S. Nishinohara, K. Sonoda, N. Shiiki, Y. Togawa, and S. Chiba  
*A Novel Three-charged-particle Faddeev-type Equation in Momentum Space*  
 AIP Conf. Proc. **768** (2005) 433.

E.S. Soukhovitskij, S. Chiba and J. Y. Lee  
*Soft-Rotator Coupled Channels Global Optical Potential for  $A=24$ -122 Mass Region Nuclides up to 200-MeV Incident Nucleon Energies*  
 AIP Conf. Proc. **769** (2005) 1100.

L. Cui, A. Iwamoto, J. Q. Lian, H. Neoh, T. Maruyama, Y. Horikawa and K. Hiramatsu  
*Novel Mechanism of Antibiotic Resistance Originating in Vancomycin-Intermediate Staphylococcus Aureus*  
 Antimicrobial Agents and Chemotherapy **50** (2006) 428.

## Meetings

H. Koura, T. Tachibana and S. Chiba  
*Fission Properties of Superheavy Nuclei and a Limit of Existence of Nuclei*  
 Asia-Pacific Symp. on Radiochemistry (APSORC2005), Beijing (Oct. 17-21,2005).

H. Koura, T. Tachibana and S. Chiba  
*Systematical Calculation of Fission Barriers in the Heavy and Superheavy, Neutron-rich Nuclidic Region*  
 The 61st Annual Meeting of the Physical Society of Japan, Matsuyama (Mar. 27-30, 2006).

Y. Utsuno, T. Otsuka, T. Mizusaki and M. Honma

*Deformation and Shape Coexistence of Neutron-rich Mg Isotopes*

RIKEN RIBF Workshop, Collective motions in unstable nuclei –experiments vs. theories– , Wako (May. 24-26, 2005).

Y. Utsuno

*Exotic Structure of Unstable Nuclei from the Nuclear Moment Study*

The 2nd Joint Meeting of the Nuclear Physics Divisions of the APS and JPS, Hawaii (Sep. 18-22, 2005).

Y. Utsuno

*Shell Model Description of Unstable Nuclei*

YITP Workshop on Binding Mechanism and New Dynamics in Weakly Bound Systems, Kyoto (Dec. 12-14, 2005).

Y. Utsuno, T. Otsuka, T. Mizusaki and M. Honma

*Structure of Unstable Nuclei Studied by the Monte Carlo Shell Model*

CNS Workshop on Past, Present and Future of the Nuclear Shell Model, Wako (Jan. 26-28, 2006).

Y. Utsuno, T. Otsuka, T. Mizusaki and M. Honma

*Structure of Unstable Nuclei by Large-scale Shell-model Calculations*

KEK 2005 Numerical Simulation Workshop on Perspectives of Computational Physics Exploited by Massively Parallel Computer, Tsukuba (Feb. 6-8, 2006).

Y. Utsuno

*Disappearance of the Magic Number and Nuclear Moment*

RIKEN Symposium on Structure of unstable nuclei exploited from electromagnetic moment and low-energy nuclear spectroscopy, Wako (Mar. 1, 2006).

Y. Utsuno, T. Otsuka, T. Mizusaki and M. Honma

*Structure of Exotic Nuclei in the  $Sd$ - $pf$  Shell Region and its Relation to the Effective Interaction*

Int. Symp. on Structure of Exotic Nuclei and Nuclear Forces, Tokyo (Mar. 9-12, 2006).

Y. Usuno

*Shell Model Understanding for Shell Evolution*

RIKEN Int. Workshop on Physics with RIBF, Wako (Mar. 13-17, 2006).

Y. Utsuno, T. Otsuka, T. Mizusaki and M. Honma

*Shell Model Calculation of Unstable Nuclei with an Interaction Including Tensor Force*

The 61st annual meeting of Physical Society of Japan, Matsuyama (Mar. 27-30, 2006).

T. Maruyama, T. Endo, T. Tatsumi, D.N. Voskresensky, T. Tanigawa and S. Chiba

*Coulomb and Surface Effects on the Pasta Structures in Nuclear Matter*

The 29th Johns Hopkins Workshop in Theoretical Physics (Strong matter in the heavens), Budapest (Aug. 1-3, 2005).



T. Endo, T. Maruyama, S. Chiba and T. Tatsumi

*Charge Screening Effect on Hadron-quark Mixed Phase in Compact Stars*

The 29th Johns Hopkins Workshop in Theoretical Physics (Strong matter in the heavens), Budapest (Aug. 1-3, 2005).

T. Endo, T. Maruyama, S. Chiba and T. Tatsumi

*Impact of the Coulomb Screening on the Hadron-quark Deconfinement Transition*

The 18th Int. Conf. on Ultrarelativistic Nucleus-Nucleus Collisions (QM2005), Budapest (Aug. 4-9, 2005).

Y. Akimura, T. Maruyama, N. Yoshinaga and S. Chiba

*Properties of Baryon and Quark Matter Studied with a Molecular Dynamics*

The 18th Int. Conf. on Ultrarelativistic Nucleus-Nucleus Collisions (QM2005), Budapest (Aug. 4-9, 2005).

T. Maruyama, T. Endo, T. Tatsumi, D.N. Voskresensky, T. Tanigawa and S. Chiba

*Non Uniform Structure in the First-order Phase Transition*

Int. Workshop on The New Physics of Compact Stars, Trento (Sep. 12-16, 2005).

T. Maruyama, T. Tatsumi and S. Chiba

*Bulk Structure and Bulk Property of Kaonic Nuclei*

The 61st Annual Meeting of the Physical Society of Japan, Matsuyama (Mar. 27-30, 2006).

Y. Akimura, T. Maruyama, N. Yoshinaga and S. Chiba

*Viscosity of Quark Matter Studied with Molecular Dynamics*

The 61st Annual Meeting of the Physical Society of Japan, Matsuyama (Mar. 27-30, 2006).

T. Endo, T. Maruyama, D.N. Voskresensky, S. Chiba and T. Tatsumi

*Hadron-quark Mixed Phase in Hybrid Star*

The 61st Annual Meeting of the Physical Society of Japan, Matsuyama (Mar. 27-30, 2006).

## 8.6 Atomic Physics and Solid State Physics

### Journal/Proceedings

K. Kawatsura, K. Takahiro, M. Sataka, M. Imai, K. Komaki, H. Sugai and H. Shibata  
*Ejected-electron Spectra from Rydberg States in High-energy Collisions of  $O^{3+}$  Ions with He*  
 Nucl. Instrum. Methods Phys. Res. **B245** (2006) 44.

S.C. Jeong, I. Katayama, H. Kawakami, Y. Watanabe, H. Ishiyama, H. Miyatake, M. Sataka, S. Okayasu, H. Sugai, S. Ichikawa, K. Nishio, T. Nakanoya, N. Ishikawa, Y. Chimi, T. Hashimoto, M. Yahagi, K. Takada, B.C. Kim, M. Watanabe, A. Iwase, Takashi Hashimoto and T. Ishikawa  
*Measurement of Diffusion Coefficients in Solids by the Short-lived Radioactive Beam of  $^8Li$*   
 Nucl. Instrum. Methods **B230** (2005) 596.

S.C. Jeong, I. Katayama, H. Kawakami, Y. Watanabe, H. Ishiyama, N. Imai, Y. Hirayama, H. Miyatake, M. Sataka, S. Okayasu, H. Sugai, S. Ichikawa, K. Nishio, S. Mitsuoka, T. Nakanoya, M. Yahagi, T. Hashimoto, K. Takada, M. Watanabe, T. Ishikawa and A. Iwase  
*Measurements of Self-diffusion Coefficients in Li Ionic Conductors by using the Short-lived Radiotracer of  $^8Li$*   
 J. PHASE EQUILIBRIA and DIFFUSION **26** (2005) 472.

M. Imai, M. Sataka, K. Kawatsura, K. Takahiro, K. Komaki, H. Shibata, H. Sugai and K. Nishio  
*Charge State Distribution and its Equilibration of 2MeV/u Sulfur Ions Passing through Carbon Foils*  
 Nucl. Instrum. Methods **B230** (2005) 63.

M. Fukuzumi, Y. Chimi, N. Ishikawa, M. Suzuki, M. Takagaki, J. Mizuki, F. Ono, R. Neumann and A. Iwase  
*Effects of Swift Heavy Ion Irradiation on Magnetic Properties of Fe-Rh Alloy*  
 Nucl. Instrum. Methods **B245** (2006) 161.

S. Okayasu, T. Nishio, M. Ono, T. Mashimo, Y. Tanaka and A. Iyo  
*Vortex Observation in Tl-based Superconductors with a Scanning SQUID Microscopy*  
 Physica **C437-438** (2006) 239.

N. Matsunami, O. Fukuoka, T. Shimura, M. Sataka and S. Okayasu  
*A Multi-exciton Model for the Electronic Sputtering of Oxides*  
 Nucl. Instrum. Methods **B230** (2005) 507.

T. Sueyoshi, S. Inada, T. Ueno, N. Jyodai, T. Fujiyoshi, K. Miyahara, T. Ikegami, K. Ebihara, R. Miyagawa, Y. Chimi, and N. Ishikawa  
*Effect of Controlled Densities of Columnar Defects on Pinning Parameters in  $YBa_2Cu_3O_{7-\delta}$  Thin Films*  
 Physica **C 424** (2005) 153.

T. Sueyoshi, S. Inada, T. Fujiyoshi, K. Miyahara, T. Ikegami, K. Ebihara, R. Miyagawa, Y. Chimi, and N. Ishikawa

*Effect of Inclined Magnetic Field on Pinning Parameters in YBaCuO Thin Films with Columnar Defects*  
*Physica C* **426-431** (2005) 83.

F. Ono, S. Komatsu, Y. Chimi, N. Ishikawa, A. Iwase and T. Kambara  
*Effect of GeV-ion Irradiation on Magnetic Properties of Fe-Ni Invar Alloys*  
*Nucl. Instrum. Methods B* **230** (2005) 279.

Y. Matsushima, N.Q. Sun, H. Kanamitsu, M. Matsushita, A. Iwase, Y. Chimi, N. Ishikawa, T. Kambara and F. Ono  
*Pressure Dependence of the Irradiation-induced Ferromagnetism in Fe-Ni Invar Alloys*  
*J. Magn. Magn. Mater.* **298** (2006) 14.

Y. Chimi, A. Iwase, N. Ishikawa, M. Kobiyama, T. Inami, T. Kambara and S. Okuda  
*Swift Heavy Ion Irradiation Effects in Nano-crystalline Gold*  
*Nucl. Instrum. Methods B* **245** (2006) 171.

F. Ono, A. Kanamitsu, Y. Matsushima, Y. Chimi, N. Ishikawa, T. Kambara and A. Iwase  
*Effect of High-energy Ion Irradiation on Magnetic Properties in Fe-Pt Invar Alloys*  
*Nucl. Instrum. Methods B* **245** (2006) 166.

H. Maeta, N. Matsumoto, O. Fukuoka, T. Kato, H. Sugai, H. Ohtsuka and M. Sataka  
*Structure of Defect Cascades in Heavy Ions-irradiated Nickel by X-ray Diffuse Scattering*  
*Nucl. Instrum. Methods B* **242** (2006) 546.

## Meetings

K. Kawatsura, K. Takahiro, M. Sataka, M. Imai, K. Komaki, H. Sugai and H. Shibata  
*Ejected-electron Spectra from Rydberg States in High-energy Collisions of  $O^{3+}$  Ions with He*  
 The 6th Int. Symp. on Swift Heavy Ions in Matters, Aschaffenburg Germany (May 29-Jun. 1, 2005).

M. Imai, M. Sataka, K. Kawatsura, K. Takahiro, K. Komaki, H. Shibata, H. Sugai and K. Nishio  
*Non-equilibrium Charge State Distribution of 2MeV/u S Ions through C-foils*  
 The 61st Annual Meeting of the Physical Society of Japan, Matsuyama (Mar. 27-30, 2006).

T. Nakazawa, A. Naito, T. Aruga, V. Grismanovs, Y. Chimi, A. Iwase, N. Okubo and S. Jitsukawa  
*High Energy Heavy Ion Induced Structural Disorder in  $Li_2TiO_3$*   
 The 12th Int. Conf. on Fusion Reactor Materials, Santa Barbara, California, USA (Dec. 4-9, 2005).

M. Fukuzumi, Y. Chimi, N. Ishikawa, M. Suzuki, M. Takagaki, J. Mizuki, F. Ono, R. Neumann and A. Iwase  
*Effects of Swift Heavy Ion Irradiation on Magnetic Properties of Fe-Rh Alloy*  
 Int. Symp. on Swift Heavy Ions in Matter, Aschaffenburg, Germany (May. 2005).

Y. Zushi, M. Fukuzumi, N. Ishikawa, Y. Chimi, M. Suzuki, M. Takagaki, J. Mizuki, T. Kambara, H. Tsuchida and A. Iwase

*Low Temperature Ferromagnetism in FeRh Induced by Swift Heavy Ion Irradiation*

Annual Meeting of the Physical Society of Japan, Kyoto (Sep. 21, 2005).

M. Fukuzumi, Y. Zushi, N. Ishikawa, Y. Chimi, M. Suzuki, M. Takagaki, J. Mizuki, T. Kambara, H. Tsuchida and A. Iwase

*Ferromagnetic-antiferromagnetic Transition Induced by Swift Heavy Ion Irradiation in FeRh*

Annual Meeting of the Physical Society of Japan, Kyoto (Sep. 22, 2005).

S. Okayasu, T. Nishio, M. Ono, T. Mashimo, Y. Tanaka and A. Iyo

*Vortex Observation in TI-based Superconductors with a Scanning SQUID Microscopy*

The 4th Int. Conf. on Vortex Matter in Nano-structured Superconductors, Crete (Sep. 8, 2005).

S. Okayasu, T. Nishio, M. Ono, T. Mashimo, Y. Tanaka and A. Iyo

*Vortex Imaging in TI-based Superconductors with a Scanning SQUID Microscopy*

International Symposium on Superconductivity 2005, Tsukuba (Oct. 25, 2005).

N.S. Shinde, N. Matsunami, T. Shimura, M. Sataka, S. Okayasu, T. Kato and M. Tazawa

*Alignment of Grain Orientation in Polycrystalline-SiO<sub>2</sub> Films Induced by High-Energy Heavy Ions*

The 6th Int. Symp. Swift Heavy Ions in Matter (SHIM) 2005, Aschaffenburg, Germany (May 28-31, 2005).

O. Fukuoka, N. Matsunami, M. Tazawa, T. Shimura, M. Sataka, H. Sugai and S. Okayasu

*Ion Irradiation Effects on Optical Properties of Al-doped ZnO Films*

The 13th Int. Conf. Radiation Effects in Insulators, Santa Fe, New Mexico, USA (Aug. 28- Sep. 2, 2005).

N.S. Shinde, N. Matsunami, T. Shimura, M. Sataka, S. Okayasu and M. Tazawa

*Modifications of Polycrystalline-SiO<sub>2</sub> Films by High-Energy Heavy Ions*

Fall Meeting of the Physical Society of Japan, Kyoto (Sept, 2005).

N. Ishikawa, S. Yamamoto and Y. Chimi

*Structural Changes in Anatase TiO<sub>2</sub> Thin Films Irradiated with High Energy Heavy Ions*

The 13th Int. Conf. on Radiation Effects in Insulators, Santa Fe, New Mexico, USA (Aug. 30, 2005).

N. Ishikawa, S. Yamamoto and Y. Chimi

*Electronic Excitation Effects in Anatase TiO<sub>2</sub> Irradiated with High Energy Ions*

Fall Meeting of the Physical Society of Japan, Kyoto (Sep. 19, 2005).

N. Ishikawa

*Modification of Oxide Materials by Irradiation with High-Energy Heavy Ions*

Int. Symp. on Application of Quantum Beam 2005, Kobe (Oct. 18, 2005).

N. Ishikawa

*Ionization-induced Defect Creation in Oxides Irradiated with Light, Ion and Cluster Beams*

Sectional Meeting of The Japanese Society of Microscopy, Nagoya (Mar. 6, 2006).

N. Okubo, T. Nakazawa, Y. Chimi, N. Ishikawa, T. Aruga, M. Sataka and S. Jitsukawa  
*The Initial Stage of Amorphization of Single Crystalline  $\alpha$ -Al<sub>2</sub>O<sub>3</sub> Irradiated with High Energetic Ions*  
Fall Meeting of the Japan Institute of Metals, Hiroshima (Sep. 28, 2005).

H. Sugai, N. Matsunami, O. Fukuoka, M. Sataka, T. Kato, S. Okayasu, T. Shimura and M. Tazawa  
*Electrical Conductivity Increase of Al-doped ZnO Films Induced by High-Energy-Heavy Ions*  
The 13th Int. Conf. on Radiation Effects in Insulators, Santa Fe, New Mexico (Aug. 30, 2005).

H. Sugai, N. Matsunami, O. Fukuoka, M. Sataka, T. Kato, S. Okayasu, T. Shimura and M. Tazawa  
*Irradiation Effects of High-Energy Heavy Ions in Electrical Properties of Al-doped ZnO Films*  
Fall Meeting of the Physical Society of Japan, Kyoto (Sep. 19, 2005).

Y. Chimi, A. Iwase, N. Ishikawa, M. Kobiyama, T. Inami, T. Kambara and S. Okuda  
*Swift Heavy Ion Irradiation Effects in Nano-crystalline Gold*  
The 6th Int. Symp. on Swift Heavy Ions in Matter, Aschaffenburg (Bavaria), Germany (May 28, 2005).

F. Ono, A. Kanamitsu, Y. Matsushima, Y. Chimi, N. Ishikawa, T. Kambara and A. Iwase  
*Effect of High-energy Ion Irradiation on Magnetic Properties in Fe-Pt Invar Alloys*  
The 6th Int. Symp. on Swift Heavy Ions in Matter, Aschaffenburg (Bavaria), Germany (May 30, 2005).

Y. Matsushima, H. Kanamitsu, N.Q. Sun, D. Kaneda, F. Ono, Y. Chimi, N. Ishikawa and A. Iwase  
*Change in Magnetic Properties of Fe-Pd Invar Alloys by High-Energy Heavy Ion Irradiation*  
2005 Annual Meeting of the Physical Society of Japan and the Japan Society of Applied Physics,  
Chugoku-Shikoku Branch, Shimane (Jul. 30, 2005).

N.Q. Sun, D. Kaneda, Y. Matsushima, N. Ishikawa, Y. Chimi, A. Iwase and F. Ono  
*Effect of Ion Irradiation on the Magnetic Properties of Ni<sub>3</sub>Mn Alloys*  
2005 Annual Meeting of the Physical Society of Japan and the Japan Society of Applied Physics,  
Chugoku-Shikoku Branch, Shimane (Jul. 30, 2005).

Y. Chimi, N. Ishikawa, S. Komatsu, D.T.N. Minh, F. Ono, A. Iwase, T. Kambara, A. Dunlop, C.J. van der Beek, R. Neumann and C. Muller  
*Modification of Magnetic Properties in Fe-Ni Alloys Induced by Swift Heavy-ion Irradiation*  
2005 Fall Meeting of the Physical Society of Japan, Kyoto (Sep. 19, 2005).

## 8.7 Radiation Effects in Materials

### Journal/Proceedings

A. Kurumada, Y. Imamura, T. Oku, M. Ishihara, K. Sawa, T. Shibata, S. Baba and J. Aihara  
*Ion Irradiation Effects on Electric Resistivity and Microstructures of Carbon Fibers*  
 JAEA-Review **2005-004** (2006) 101.

A. Kurumada and Y. Imamura  
*Ion Irradiation Effects on Microstructures and Properties of Joining Materials between Tungsten and Copper*  
 The Joint-use Institute Research Reports, Research Institute for Applied Mechanics, Kyushu University  
 (2006) 156.

M. Sasase, K. Shimura, H. Yamamoto, K. Yamaguchi, S. Shamoto and K. Hojou  
*Cross Sectional Transmission Electron Microscope (XTEM) Observation of Interface Structure of  $\beta$ -FeSi<sub>2</sub>/Si (100) Prepared by Ion Beam Sputter Deposition (IBSD) Method*  
 J. Appl. Phys. **45** (2006) 4929.

### Meetings

A. Kurumada, Y. Imamura and Y. Motohashi  
*Irradiation Damage Effects on Properties and Microstructures of Materials for HTGR*  
 Oarai Research Reports, Institute for Materials Research, Tohoku University (Aug. 25-26, 2005).

A. Kurumada, Y. Imamura, T. Oku, M. Ishihara, T. Shibata, K. Sawa, S. Baba, J. Aihara and T.D. Burchell  
*Effects of Ion Irradiations on the Electrical Resistivity and Mechanical Properties of Carbon Fibers*  
 The 6th Int. Nuclear Graphite Specialists Meeting, Chamonix, France (Sep. 19-21, 2005),

M. Sasase, K. Shimura, K. Yamaguchi, H. Yamamoto, S. Shamoto and K. Hojou  
*Interface Structure of  $\beta$ -FeSi<sub>2</sub> Thin Film Fabricated on Si and SIMOX Substrate*  
 Spring Meeting of the Japan Society of Applied Physics, Tokyo (Apr. 1, 2005).

M. Sasase, K. Shimura, K. Yamaguchi, H. Yamamoto, S. Shamoto and K. Hojo  
*Interface Structure of  $\beta$ -FeSi<sub>2</sub> Thin Film Fabricated on Si and SIMOX Substrate*  
 Surface Modification of Materials by Ion Beam (SMMIB2005), Turkey Kusadasu (Sep. 3-11, 2005).

T. Sonoda  
*High Energy Ion Irradiation Examination as Simulations of Fission Field in Nuclear Fuels*  
 The 20th Nuclear Fuel Summer Seminar of the Atomic Energy Society of Japan, Yamagata (July 8, 2005).

T. Sonoda, M. Kinoshita, Y. Chimi, N. Ishikawa, M. Sataka and A. Iwase  
*Electronic Excitation Effects in CeO<sub>2</sub> under Irradiations with High-energy Ions of Typical Fission Products*  
The 13th Int. Conf. on Radiation Effects in Insulators, Santa Fe, New Mexico (Aug. 30, 2005).

T. Sonoda, M. Kinoshita, Y. Chimi, N. Ishikawa, M. Sataka, A. Iwase and H. Abe  
*Irradiation Temperature and Energy Dependence on Microstructural Evolution in CeO<sub>2</sub> under High Energy Ion Irradiation*  
Fall Meeting of Japan Institute of Metals, Hiroshima (Sep. 28, 2005).

H. Abe, T. Mihara and T. Sonoda  
*Irradiation Enhanced Mobility of Defect Clusters in CeO<sub>2</sub>*  
Fall Meeting of Japan Institute of Metals, Hiroshima (Sep. 28, 2005).

K. Yasunaga, K. Funamoto, K. Yasuda, S. Matsumura and T. Sonoda  
*Structure of Planar Defects in CeO<sub>2</sub> under Irradiation with Electrons and Heavy Ions*  
Fall Meeting of Japan Institute of Metals, Hiroshima (Sep. 29, 2005).

T. Sonoda, S. Matsumura, K. Yasuda, K. Yasunaga, H. Abe, A. Iwase, N. Ishikawa, Y. Chimi and M. Sataka  
*Review of Experimental Approach in NXO Project to Clarify the Formation Mechanism of a Crystallographic Re-structuring (rim structure) in High Burnup LWR Fuels*  
New Cross Over Project International Workshop II, Kyoto (Oct. 7, 2005).





## **CHAPTER 9**

### **Personnel and Committee**

- 9.1 Personnel
- 9.2 Research Planning and Assessment Committee



## 9.1 Personnel

### Department of Materials Science (Apr.-Sep.)

Hiroshi	Ikezoe	Director
Atsushi	Yokoyama	Deputy Director
Yoshiyuki	Ozeki	Administrative Manager

### Department of Research Reactor and Tandem Accelerator (Oct.-Mar.)

Fumio	Sakurai	Director
Kiyonobu	Yamashita	Deputy Director
Suehiro	Takeuchi	Deputy Director
Shigeru	Mori	Manager of Administration Section

### Department of Research Reactor and Tandem Accelerator

#### *Tandem Accelerator Section ( \*General Manager )*

##### *Scientific Staff*

Suehiro	Takeuchi*
Susumu	Hanashima
Akihiko	Osa
Makoto	Matsuda

##### *Technical Staff*

Yoshihiro	Tsukihashi
Shin-ichi	Abe
Nobuhiro	Ishizaki
Hidekazu	Tayama
Takamitsu	Nakanoya
Hiroshi	Kabumoto
Masahiko	Nakamura
Ken-ichi	Kutsukake
Susumu	Kanda (Apr.-Sep.)
Tadashi	Yoshida
Katsuzo	Horie
Isao	Ohuchi

##### *Entrusted Operators*

Akihiko	Iijima
Takahiro	Yoshida
Takahiro	Usami
Tetsusi	Hida
Hisashi	Sakurayama
Hikaru	Nisugi
Nobuo	Seki
Teruo	Onodera

*Entrusted Assistants*

Yoshio Fujii  
Teruo Kozawa

**Department of Radiation Protection**

***Facility Radiation Control Section I***

Takashi Nakazawa (Oct.-Mar.)  
Takehisa Ohkura  
Kenji Yamane  
Hiroshi Shimada (Apr.-Mar.)

**Advanced Science Research Center**

***Research Group for Shell Structure and Reaction Properties of Heavy Nuclei far from Stability***

( \*Group Leader )

Hiroari Miyatake\*  
Tetsuro Ishii  
Shin-ichi Ichikawa  
Satoshi Chiba  
Toshiki Maruyama  
Shin-ichi Mitsuoka  
Katsuhisa Nishio  
Hiroyuki Koura  
Yutaka Utsuno  
Tetsuya Sato  
Kaoru Tsuruta (Post Doc.)  
Takashi Hashimoto (Post Doc.)  
Hiroyuki Makii (Post Doc.)  
Yuka Akimura (Student)  
Soichiro Shigematsu (Student)

**Advanced Science Research Center**

***Research Group for Nuclear chemistry of the Heaviest Elements ( \*Group Leader )***

Yuichiro Nagame\*  
Kazuaki Tsukada  
Ichiro Nishinaka  
Masato Asai  
Takatoshi Ichikawa (Post Doc.)  
Atsushi Toyoshima (Post Doc.)  
Yasuo Ishii (Student)

**Advanced Science Research Center**

***Mega Gravity Research Group***

Satoru Okayasu

**Nuclear Science and Engineering Directorate**

***Innovative Nuclear Science Research Group ( \*Group Leader )***

Masumi	Oshima*	
Hideo	Harada	Sub Leader (Oct.-Mar.)
Hideki	Iimura	
Mitsuo	Koizumi	
Kazuyoshi	Furutaka	(Oct.-Mar.)
Tetsuya	Hirade	(Apr.-Sep.)
Yuichi	Hatsukawa	
Akihiko	Osa	(Apr.-Sep.)
Fumito	Kitatani	(Oct.-Mar.)
Shoji	Nakamura	(Oct.-Mar.)
Yutaka	Utsuno	(Apr.-Sep.)
Yosuke	Toh	
Atsushi	Kimura	
Kaoru	Hara	(Post Doc., Oct.-Mar.)
Masayuki	Ohta	(Post Doc., Oct.-Mar.)

**Nuclear Science and Engineering Directorate**

***Research Group for Irradiation Field Materials ( \*Group Leader )***

Shirou	Jitsukawa*
Masao	Sataka
Hideo	Ohtsuka
Hiroyuki	Sugai
Nariaki	Okubo
Teruo	Kato
Norito	Ishikawa
Yasuhiro	Chimi
Takeo	Aruga
Tetsuya	Nakazawa
Daijyu	Yamaki

**Nuclear Science and Engineering Directorate**

***Corrosion Resistant Materials Development Group ( \*Group Leader )***

Kiyoshi	Kiuchi*
Ikuo	Ioka
Hiroaki	Ogawa
Yukio	Nakahara

Yasuhiro Ishijima  
**Nuclear Science and Engineering Directorate**  
***High Temperature Fuel and Material Group ( \*Group Leader )***

Kazuhiro Sawa\*  
 Shin-ichi Baba  
 Jun Aihara

**Quantum Beam Science Directorate**  
***Environment and Industrial Materials Research Division***

Toshio Hirao

**Quantum Beam Science Directorate**  
***Research Group for Laser Accelerator***

Takehito Hayakawa  
 Toshiyuki Shizuma

## 9.2 Research Planning and Assessment Committee

<i>Chairman</i>	Shigeru Kubono	(Professor, The University of Tokyo)
<i>Vice Chairman</i>	Ken-ichiro Komaki	(Professor, The University of Tokyo)
<i>Member</i>	Tadashi Kambara	(Senior Scientist, RIKEN)
	Kenji Kimura	(Professor, Kyoto University)
	Noriaki Matsunami	(Associate Professor, Nagoya University)
	Tetsuo Noro	(Professor, Kyushu University)
	Tsutomu Ohtsuki	(Associate Professor, Tohoku University)
	Tadashi Shimoda	(Professor, Osaka University)
	Kazuhiro Yabana	(Associate Professor, Tsukuba University)
	Yuichi Hatsukawa	(A-Senior Researcher, Quantum Beam Science Directorate)
	Shiro Jitsukawa	(Group Leader, Nuclear Science and Engineering Directorate)
	Motoharu Mizumoto	(S-Senior Researcher, Quantum Beam Science Directorate)
	Kazumasa Narumi	(Group Leader, Advanced Science Research Center)
<i>Organizer</i>	Hiroshi Ikezoe	(Deputy Director, Advanced Science Research Center)
	Suehiro Takeuchi	(Deputy Director, Dep. Research Reactors and Accelerator)
<i>Secretary</i>	Akihiko Osa	(A-Senior Researcher, Tandem Accelerator Section)
	Susumu Hanashima	(Tandem Accelerator Section)

## **CHAPTER 10**

### **Cooperative Researches List**





Title	Contact Person Organization
1. Study on the shape coexistence in $^{70}\text{Ge}$ and the coexisting phenomena of magnetic and anti-magnetic rotors	Masahiko SUGAWARA Chiba Institute of Technology
2. Gamma-ray spectroscopy for super-heavy nuclei	Keisuke SUEKI University of Tsukuba
3. Ion source development for the JAEA on-line isotope separator	Sun-Chan Jeong High Energy Accelerator Research Organization
4. Producing heavy elements by heavy-ion fusion reaction using actinide target and the measurement of the fission properties	Takaaki OHSAWA Kinki University
5. In-beam gamma-ray spectroscopy in the trans-uranium region by the transfer reaction	Masao OGAWA Tokyo Institute of Technology
6. Study of excited states beyond the high-spin isomer	Kenji SAGARA Kyushu University
7. Decay study on neutron-rich nuclei of fission products of $^{238}\text{U}$ using the on-line mass separator JAEA-ISOL	Michihiro SHIBATA Nagoya University
8. Nuclear spectroscopy using lasers for refractory element isotopes in Re region	Takayoshi Horiguchi Hiroshima International University
9. Study of nuclear fission from excited states of Fermium isotopes produced by break-up fusion reactions	Akihiko YOKOYAMA Kanazawa University
10. Aqueous chemistry of the heaviest elements on an atom-at-a-time basis	Atsushi SHINOHARA Osaka University
11. Study of nuclear deformation by Coulomb excitation	Yoshifumi SHIMIZU Kyushu University
12. Systematic study of signature inversion and deformation phenomena in high-spin states of deformed nuclei	Masahiko SUGAWARA Chiba Institute of Technology
13. Nuclear structure study in the Hf-W-Os region by deep inelastic collisions	Mamoru FUJIWARA Osaka University
14. Ionic radius of the heavy actinide elements produced in heavy ion fusion reaction	Hisaaki KUDO Niigata University

- |   |   |
|---|---|
| 15. Experimental study of fusion barrier distribution for super-heavy element synthesis   | Sun-Chan Jeong<br>High Energy Accelerator Research Organization                 |
| 16. Neutron orbit radii of Sn isotopes from sub-coulomb transfer reaction   | Hiroari MIYATAKE<br>High Energy Accelerator Research Organization               |
| 17. Study of the nuclear synthesis under an explosive condition in the universe by using radioactive nuclear beams  | Hiroari MIYATAKE<br>High Energy Accelerator Research Organization               |
| 18. Atomic mixing induced by electronic excitation at metal-oxide, oxide-oxide and metal-semiconductor interface  | Akihiro IWASE<br>Osaka Prefecture University                                    |
| 19. Ion-velocity effect for crystalline structure change in oxides irradiated with high-energy ions   | Osamu MICHIKAMI<br>Iwate University   |
| 20. Study on recovery phenomenon of material properties of new carbon composite materials and carbon fibers with radiation damage resistance due to high heat treatment after irradiation | Akira KURUMADA<br>Ibaraki University  |
| 21. Atomic displacements induced by high-density electronic excitation in iron-based ferromagnetic alloys   | Fumihisa ONO<br>Okayama University  |
| 22. Diffusion studies in Li ionic conductors using the short-lived Li radioisotope of $^8\text{Li}$   | Sun-Chan Jeong<br>High Energy Accelerator Research Organization                 |
| 23. Electronic excitation effects on secondary ion emission from solid materials bombarded by high energy heavy ions  | Tsuguhisa SEKIOKA<br>University of Hyogo  |
| 24. Electronic sputtering of non-metals by high-energy ions   | Noriaki MATSUNAMI<br>Nagoya University  |
| 25. Heavy ion structure and electronic processes studied with zero degree electron spectroscopy   | Ken-ichiro KOMAKI<br>University of Tokyo  |
| 26. Charge changing processes of multi-charged ion in matter  | Kiyoshi KAWATSURA<br>Kyoto Institute of Technology                              |
| 27. Study of ion irradiation effect of superconducting properties for the over-doped $\text{YSr}_2\text{Cu}_3\text{Cu}_{7+\delta}$  | Hijiri KITO<br>National Institute of Advanced Industrial Science and Technology |

- |   |   |
|---|---|
| 28. Micro-structural evolution process in nuclear fuels and fluorite structure ceramics under the irradiation of high energy fission products | Takeshi SONODA<br>Central Research Institute of Electric Power Industry |
| 29. Semiconductor-metal phase transition of iron disilicide ( $\beta$ -FeSi <sub>2</sub> ) thin films by high energy heavy ion irradiation    | Masato SASASE<br>The Wakasa Wan Energy Research Center                  |
| 30. Effects of ion irradiation on a zirconia-base superplastic-ceramic material   | Yoshinobu MOTOHASHI<br>Ibaraki University                               |



- |   |   |
|---|---|
| 28. Micro-structural evolution process in nuclear fuels and fluorite structure ceramics under the irradiation of high energy fission products | Takeshi SONODA<br>Central Research Institute of Electric Power Industry |
| 29. Semiconductor-metal phase transition of iron disilicide ( $\beta$ -FeSi <sub>2</sub> ) thin films by high energy heavy ion irradiation    | Masato SASASE<br>The Wakasa Wan Energy Research Center                  |
| 30. Effects of ion irradiation on a zirconia-base superplastic-ceramic material   | Yoshinobu MOTOHASHI<br>Ibaraki University                               |



# 国際単位系 (SI)

表1. SI 基本単位

基本量	SI 基本単位	
	名称	記号
長さ	メートル	m
質量	キログラム	kg
時間	秒	s
電流	アンペア	A
熱力学温度	ケルビン	K
物質の量	モル	mol
光度	カンデラ	cd

表2. 基本単位を用いて表されるSI組立単位の例

組立量	SI 基本単位	
	名称	記号
面積	平方メートル	m <sup>2</sup>
体積	立方メートル	m <sup>3</sup>
速度	メートル毎秒	m/s
加速度	メートル毎秒毎秒	m/s <sup>2</sup>
波数	毎メートル	m <sup>-1</sup>
密度 (質量密度)	キログラム毎立方メートル	kg/m <sup>3</sup>
質量体積 (比体積)	立法メートル毎キログラム	m <sup>3</sup> /kg
電流密度	アンペア毎平方メートル	A/m <sup>2</sup>
磁界の強さ	アンペア毎メートル	A/m
(物質の)濃度	モル毎立方メートル	mol/m <sup>3</sup>
輝度	カンデラ毎平方メートル	cd/m <sup>2</sup>
屈折率	(数の) 1	1

表5. SI 接頭語

乗数	接頭語	記号	乗数	接頭語	記号
10 <sup>24</sup>	ヨタ	Y	10 <sup>-1</sup>	デシ	d
10 <sup>21</sup>	ゼタ	Z	10 <sup>-2</sup>	センチ	c
10 <sup>18</sup>	エクサ	E	10 <sup>-3</sup>	ミリ	m
10 <sup>15</sup>	ペタ	P	10 <sup>-6</sup>	マイクロ	μ
10 <sup>12</sup>	テラ	T	10 <sup>-9</sup>	ナノ	n
10 <sup>9</sup>	ギガ	G	10 <sup>-12</sup>	ピコ	p
10 <sup>6</sup>	メガ	M	10 <sup>-15</sup>	フェムト	f
10 <sup>3</sup>	キロ	k	10 <sup>-18</sup>	アト	a
10 <sup>2</sup>	ヘクト	h	10 <sup>-21</sup>	ゼプト	z
10 <sup>1</sup>	デカ	da	10 <sup>-24</sup>	ヨクト	y

表3. 固有の名称とその独自の記号で表されるSI組立単位

組立量	SI 組立単位			
	名称	記号	他のSI単位による表し方	SI基本単位による表し方
平面角	ラジアン <sup>(a)</sup>	rad		m <sup>2</sup> ・m <sup>-1</sup> =1 <sup>(b)</sup>
立体角	ステラジアン <sup>(a)</sup>	sr <sup>(c)</sup>		m <sup>2</sup> ・m <sup>-2</sup> =1 <sup>(b)</sup>
周波数	ヘルツ	Hz		s <sup>-1</sup>
力	ニュートン	N		m <sup>2</sup> ・kg <sup>2</sup> ・s <sup>-2</sup>
圧力, 応力	パスカル	Pa	N/m <sup>2</sup>	m <sup>-1</sup> ・kg <sup>2</sup> ・s <sup>-2</sup>
エネルギー, 仕事, 熱量	ジュール	J	N・m	m <sup>2</sup> ・kg <sup>2</sup> ・s <sup>-2</sup>
工率, 放射束	ワット	W	J/s	m <sup>2</sup> ・kg <sup>2</sup> ・s <sup>-3</sup>
電荷, 電気量	クーロン	C		s <sup>2</sup> ・A
電位差 (電圧), 起電力	ボルト	V	W/A	m <sup>2</sup> ・kg <sup>2</sup> ・s <sup>-3</sup> ・A <sup>-1</sup>
静電容量	ファラド	F	C/V	m <sup>-2</sup> ・kg <sup>-1</sup> ・s <sup>4</sup> ・A <sup>2</sup>
電気抵抗	オーム	Ω	V/A	m <sup>2</sup> ・kg <sup>2</sup> ・s <sup>-3</sup> ・A <sup>-2</sup>
コンダクタンス	ジーメン	S	A/V	m <sup>-2</sup> ・kg <sup>-1</sup> ・s <sup>3</sup> ・A <sup>2</sup>
磁束	ウェーバ	Wb	V・s	m <sup>2</sup> ・kg <sup>2</sup> ・s <sup>-2</sup> ・A <sup>-1</sup>
磁束密度	テスラ	T	Wb/m <sup>2</sup>	kg <sup>2</sup> ・s <sup>-2</sup> ・A <sup>-1</sup>
インダクタンス	ヘンリー	H	Wb/A	m <sup>2</sup> ・kg <sup>2</sup> ・s <sup>-2</sup> ・A <sup>-2</sup>
セルシウス温度	セルシウス度 <sup>(d)</sup>	°C		K
光照射度	ルーメン	lm	cd・sr <sup>(c)</sup>	m <sup>2</sup> ・m <sup>-2</sup> ・cd=cd
(放射性核種の)放射能	ベクレル	Bq	lm/m <sup>2</sup>	m <sup>2</sup> ・m <sup>-1</sup> ・cd=m <sup>2</sup> ・cd
吸収線量, 質量エネルギー分与, カーマ線量当量, 周辺線量当量, 方向性線量当量, 個人線量当量, 組織線量当量	グレイ	Gy	J/kg	s <sup>-1</sup>
	シーベルト	Sv	J/kg	m <sup>2</sup> ・s <sup>-2</sup>

- (a) ラジアン及びステラジアンの使用は、同じ次元であっても異なった性質をもった量を区別するときの組立単位の表し方として利点がある。組立単位を形作る際のいくつかの用例は表4に示されている。
- (b) 実際には、使用する時には記号rad及びsrが用いられるが、習慣として組立単位としての記号“1”は明示されない。
- (c) 測光学では、ステラジアンの名称と記号srを単位の表し方の中にそのまま維持している。
- (d) この単位は、例としてミリセルシウス度m°CのようにSI接頭語を伴って用いても良い。

表4. 単位の中に固有の名称とその独自の記号を含むSI組立単位の例

組立量	SI 組立単位		
	名称	記号	SI 基本単位による表し方
粘着力のモーメント	パスカル秒	Pa・s	m <sup>-1</sup> ・kg <sup>2</sup> ・s <sup>-1</sup>
表面張力	ニュートンメートル	N・m	m <sup>2</sup> ・kg <sup>2</sup> ・s <sup>-2</sup>
角速度	ニュートン毎メートル	N/m	kg <sup>2</sup> ・s <sup>-2</sup>
角加速度	ラジアン毎秒	rad/s	m <sup>2</sup> ・m <sup>-1</sup> ・s <sup>-1</sup> =s <sup>-1</sup>
熱流密度, 放射照度	ラジアン毎平方メートル	rad/s <sup>2</sup>	m <sup>2</sup> ・m <sup>-1</sup> ・s <sup>-2</sup> =s <sup>-2</sup>
熱容量, エントロピー	ワット毎平方メートル	W/m <sup>2</sup>	kg <sup>2</sup> ・s <sup>-3</sup>
質量熱容量 (比熱容量), 質量エントロピー	ジュール毎キログラム	J/K	m <sup>2</sup> ・kg <sup>2</sup> ・s <sup>-2</sup> ・K <sup>-1</sup>
質量エネルギー (比エネルギー)	ジュール毎キログラム	J/(kg・K)	m <sup>2</sup> ・s <sup>-2</sup> ・K <sup>-1</sup>
熱伝導率	ワット毎メートル毎ケルビン	W/(m・K)	m <sup>2</sup> ・kg <sup>2</sup> ・s <sup>-3</sup> ・K <sup>-1</sup>
体積エネルギー	ジュール毎立方メートル	J/m <sup>3</sup>	m <sup>-1</sup> ・kg <sup>2</sup> ・s <sup>-2</sup>
電界の強さ	ボルト毎メートル	V/m	m <sup>2</sup> ・kg <sup>2</sup> ・s <sup>-3</sup> ・A <sup>-1</sup>
体積電荷	クーロン毎立方メートル	C/m <sup>3</sup>	m <sup>-3</sup> ・s <sup>2</sup> ・A
電気変位	クーロン毎平方メートル	C/m <sup>2</sup>	m <sup>-2</sup> ・s <sup>2</sup> ・A
誘電率	ファラド毎メートル	F/m	m <sup>-3</sup> ・kg <sup>-1</sup> ・s <sup>4</sup> ・A <sup>2</sup>
透磁率	ヘンリー毎メートル	H/m	m <sup>2</sup> ・kg <sup>2</sup> ・s <sup>-2</sup> ・A <sup>-2</sup>
モルエネルギー	ジュール毎モル	J/mol	m <sup>2</sup> ・kg <sup>2</sup> ・s <sup>-2</sup> ・mol <sup>-1</sup>
モルエントロピー, モル熱容量	ジュール毎モル毎ケルビン	J/(mol・K)	m <sup>2</sup> ・kg <sup>2</sup> ・s <sup>-2</sup> ・K <sup>-1</sup> ・mol <sup>-1</sup>
照射線量 (X線及びγ線)	クーロン毎キログラム	C/kg	kg <sup>-1</sup> ・s <sup>2</sup> ・A
吸収線量	グレイ毎秒	Gy/s	m <sup>2</sup> ・s <sup>-3</sup>
放射強度	ワット毎ステラジアン	W/sr	m <sup>4</sup> ・m <sup>-2</sup> ・kg <sup>2</sup> ・s <sup>-3</sup> =m <sup>2</sup> ・kg <sup>2</sup> ・s <sup>-3</sup>
放射輝度	ワット毎平方メートル毎ステラジアン	W/(m <sup>2</sup> ・sr)	m <sup>2</sup> ・m <sup>-2</sup> ・kg <sup>2</sup> ・s <sup>-3</sup> =kg <sup>2</sup> ・s <sup>-3</sup>

表6. 国際単位系と併用されるが国際単位系に属さない単位

名称	記号	SI 単位による値
分	min	1 min=60s
時	h	1 h=60 min=3600 s
日	d	1 d=24 h=86400 s
度	°	1°=(π/180) rad
分	'	1'=(1/60)°=(π/10800) rad
秒	"	1"=(1/60)'=(π/648000) rad
リットル	l, L	1 l=1 dm <sup>3</sup> =10 <sup>-3</sup> m <sup>3</sup>
トン	t	1 t=10 <sup>3</sup> kg
ネーパ	Np	1 Np=1
ベル	B	1 B=(1/2) ln10 (Np)

表7. 国際単位系と併用されこれに属さない単位でSI単位で表される数値が実験的に得られるもの

名称	記号	SI 単位であらわされる数値
電子ボルト	eV	1 eV=1.60217733(49)×10 <sup>-19</sup> J
統一原子質量単位	u	1 u=1.6605402(10)×10 <sup>-27</sup> kg
天文単位	ua	1 ua=1.49597870691(30)×10 <sup>11</sup> m

表8. 国際単位系に属さないが国際単位系と併用されるその他の単位

名称	記号	SI 単位であらわされる数値
海里	海里	1 海里=1852m
ノット	ノット	1 ノット=1 海里毎時=(1852/3600)m/s
アール	a	1 a=1 dam <sup>2</sup> =10 <sup>2</sup> m <sup>2</sup>
ヘクタール	ha	1 ha=1 hm <sup>2</sup> =10 <sup>4</sup> m <sup>2</sup>
バール	bar	1 bar=0.1 MPa=100kPa=1000hPa=10 <sup>5</sup> Pa
オングストローム	Å	1 Å=0.1 nm=10 <sup>-10</sup> m
バール	b	1 b=100fm <sup>2</sup> =10 <sup>-28</sup> m <sup>2</sup>

表9. 固有の名称を含むCGS組立単位

名称	記号	SI 単位であらわされる数値
エール	erg	1 erg=10 <sup>-7</sup> J
ダイン	dyn	1 dyn=10 <sup>-5</sup> N
ポアズ	P	1 P=1 dyn・s/cm <sup>2</sup> =0.1 Pa・s
ストークス	St	1 St=1 cm <sup>2</sup> /s=10 <sup>-4</sup> m <sup>2</sup> /s
ガウス	G	1 G=10 <sup>4</sup> T
エルステッド	Oe	1 Oe=(1000/4π) A/m
マクスウェル	Mx	1 Mx=10 <sup>-8</sup> Wb
スチル	sb	1 sb=1 cd/cm <sup>2</sup> =10 <sup>4</sup> cd/m <sup>2</sup>
ホト	ph	1 ph=10 <sup>4</sup> lx
ガリ	Gal	1 Gal=1 cm/s <sup>2</sup> =10 <sup>-2</sup> m/s <sup>2</sup>

表10. 国際単位に属さないその他の単位の例

名称	記号	SI 単位であらわされる数値
キュリー	Ci	1 Ci=3.7×10 <sup>10</sup> Bq
レントゲン	R	1 R=2.58×10 <sup>-4</sup> C/kg
ラド	rad	1 rad=1cGy=10 <sup>-2</sup> Gy
レム	rem	1 rem=1 cSv=10 <sup>-2</sup> Sv
X線単位	X unit	1 X unit=1.002×10 <sup>-4</sup> nm
ガンマ	γ	1 γ=1 nT=10 <sup>-9</sup> T
ジャンスキー	Jy	1 Jy=10 <sup>-26</sup> W・m <sup>-2</sup> ・Hz <sup>-1</sup>
フェルミ	fem	1 fem=1 fm=10 <sup>-15</sup> m
メートル系カラット	metric carat	1 metric carat=200 mg=2×10 <sup>-4</sup> kg
トル	Torr	1 Torr=(101 325/760) Pa
標準大気圧	atm	1 atm=101 325 Pa
カリ	cal	1 cal=4.184 J
マイクロン	μ	1 μ=1um=10 <sup>-6</sup> m

